Experimental Investigation on Patterning of Anchored and Unanchored Aligned Carbon Nanotube Mats by Fluid Immersion and Evaporation

Thesis by

Elijah Bodhi Sansom

In Partial Fulfillment of the Requirements

for the Degree of

Doctor of Philosophy

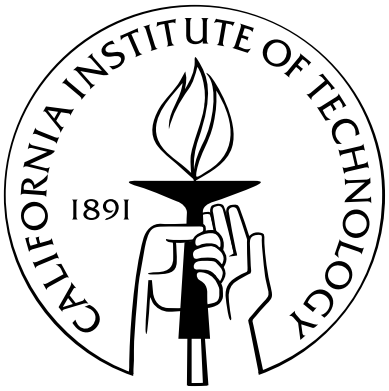

California Institute of Technology

Pasadena, California

2007

(Defended December 15, 2006)

I dedicate this creation to my parents, Richard and Hopi, who have always known I could do anything I choose, and also to my grandparents, George, Louise, Sam, Marcia, and Karl, who have all passed during my time here.

Acknowledgements

My advisor, Mory Gharib, has stood by me and my project throughout the years, especially when things looked bad, and I am deeply grateful. We were partners on this, and I learned many, many things from him.

I am thankful to Flavio Noca, my former JPL advisor, for his guidance, assistance, and leadership in tackling nanotube work as well as the start of Bioengineering at Caltech. He helped me learn the value of the research chat.

I thank the rest of committee: Sandra Troian, Chiara Daraio, and Scott Fraser, who have made the time to critique my research.

To my roommates during my years at Caltech: Ben Hebert, Eddie Branchaud, and Pete Kekenes-Huskey, thank you. You have been my friends, my partners in crime, and my support system.

I thank my first set of friends at Caltech: Eddie Branchaud, Carl Gold, and Jordan Katz. You helped me see that maybe it wouldn't be that bad.

I thank and acknowledge Ariana Hall, because of whom my life will forever be altered.

I thank all the bioengineering students from the "early days" when we were all trying to figure it out together. And also the aero students from the same time. I felt as if I were in both options at once.

I thank the Beer Hour crew, past and present. You have given me some of my favorite memories at Caltech.

I especially thank Derek Rinderknecht for being an awesome labmate and friend. We built that lab together, and I'm proud to have done it with you.

I thank Lydia Trevino for working with me on building the nanotube facility and

being a great person throughout everything.

The whole Gharib group, past and present, has been wonderful to me over the years. I could never have wished for a nicer, more accepting, or more supportive group of people to work with.

I thank Michael Bronikowski for his generous help and advice over the years, especially in advising me on getting the nanotube furnace up and running. He turned out to be oh so right about the timeline.

I sincerely thank Jijie Zhou for sharing results from her parallel project on wicking in nanocarpets, and for being an inaugural bioengineering program classmate of mine. We had many useful conversations about all the things we didn't understand about nanocarpets, and we also braved the flames that were the Caltech bioengineering option in its early days.

I thank Anna Hickerson, Reza Miraghaie, and Jim Sterling at Keck Graduate Institute for being generous enough to lend their sputter-coater and Anna's time so that this work could be done.

Thanks to others at Caltech who have been helpful in conducting this work. Chi Ma in the GPS analytical facility helped me learn how to use the SEM. Bahram Valiferdowsi helped with building the nanotube facility. Joseph Shepherd assisted with the design of the nanotube growth facility safety system.

Thanks to Emily McDowell for proofreading a half-done draft of this manuscript.

I thank Uekuma-sensei, Sean Mauch, Dana Dabiri, Meyer Pesenson, John Lin, and all the rest of the wonderful kenshi I have had the pleasure of knowing in my practice of Shorinji Kempo. I will always be thinking of what Shorinji Kempo means to me. Arigato-gozaimashita.

I thank Casey Schell, who has helped me more than she or I know.

I thank and appreciate the readers of my blog, the Grayworld, which has been an incredible support for me and an amazing outlet and inspiration.

I am truly blessed to have many caring and supportive friends far too numerous to mention here. My friends have often been my lifeline to my humanity. Thank you all for being that for me.

Every day, I appreciate my family more. My family has always loved me and seen me as so much more than any fears or doubts I might have. The appreciation and gratitude I feel is not fit for words.

Abstract

Pattern formation by capillary forces in a nanoscale system was studied experimentally. Densely packed, vertically aligned mats of order 100 μm in height comprised of 20 nm diameter multi-walled carbon nanotubes were fabricated and treated with various liquids. The carbon nanotubes deflected and rearranged under the action of surface tension as the liquids evaporated, and remained fixed once dried. The size analysis of the resulting patterns in these experiments and in the literature showed they are distributed within one standard deviation from the mean, and there are, in general, many more small sizes than large ones within a pattern.

Preexisting defects in the mats were found to play a significant role in the pattern formation process, both in this work and in the literature, whereas the properties of the specific liquid used and the height of the mats did not.

A novel method for anchoring the aligned mats within another material using spin-coating was developed. An anchored mat made in this way was successfully held in place even under the application of a 5.5 m/s water jet.

The anchoring method allowed the first known investigation of the role of boundary conditions in this pattern formation process. Under identical experimental conditions to cases where patterns are formed in the unanchored mats, it was found that no pattern formation occurs in the anchored mats.

A population balance model based on conservation of area was applied to the pattern formation process, but sufficient details are lacking to make predictions.

The anchoring method and its prevention of pattern formation is a very important finding, and is relevant to applications of the aligned mats, such as field emission displays, supercapacitors, tissue culture scaffolds, and friction drag reducing surfaces.

Contents

List of Figures

List of Tables

Chapter 1

Introduction

1.1 Context of the Present Work

The seminal paper of Iijima [1], which was the first study to carefully characterize carbon nanotubes (CNT) and is considered to represent their discovery, has been cited 5554 times as of this writing. Both Terrones [2] and de Heer [3] note the trend of exponential increase in CNT publications since 1991. De Heer also shows that although academic interest is very high, relatively few CNT-based technologies have been brought to market as viable products. This is because most of these technologies are not ready to come out of the lab.

In a broad sense, the results of this thesis are related to the many technical issues that CNT-based technologies face and will continue to face. Densely packed aligned mats of CNTs rearrange into patterns upon contact with liquid-air interfaces during liquid wetting and drying processes, and this is foreseen as potentially both a desirable outcome and a drawback, depending on viewpoint. This process is investigated experimentally in this thesis. The ability to anchor large numbers of CNTs within a material and thereby hold them onto a surface while leaving them partially and controllably exposed is conceived and demonstrated as part of this thesis. This anchoring method could prove very useful for improving the ease of handling of CNTs in general as well as improving their usefulness in many specific technological applications. Further insight into the pattern formation process in aligned CNT mats is provided by attempting to create patterns in mats that have been anchored using

the method described in this thesis. Rather surprisingly, it is found that patterns do *not* form in anchored mats under the same experimental conditions as would form patterns for unanchored mats. This has implications for mechanism as well as the use of the anchoring method in any applications that involve CNTs contacting liquids.

The development of the fabrication of densely packed aligned mats of CNTs, which are fabricated and used in this work, may be traced back to studies in the early to mid-90s. However, the synthesis of the CNT mats themselves is not the focus of this work, though it is a necessary component in order to generate the raw materials to perform the studies described. As other researchers had recognized before, it was noted early on in this work that detailed study of the synthesis of the mats is rather complicated and required infrastructure and expertise that were not available during the course of this work. Rather, the focus herein is on the use of the CNT mats as a nanostructured material in which self-assembled patterns may form during the experiments. Working with a delicate nanostructured material created a need for a more handleable and robust version of the material that preserved the desired functionality, and consequently this is also a major focus of this work. Though the experiments in this work are conducted solely with CNTs, the findings may also be applicable to other nanostructures.

The contribution that this thesis represents is the identification and characterization of several aspects of pattern formation in CNTs, which should prove useful in their many foreseen applications.

1.2 Background

Efforts at manipulating and controlling objects in the mesoscale range of nanometers to microns can be divided into those which aim to work serially with the individual objects and those which are designed to affect large numbers of objects in parallel. Self-assembly is a term taken here to mean a spontaneous assembly process due to the correct conditions, and this is a common goal of parallel manipulation and control methods. The self-assembly of CNTs by capillary forces due to the presence of liquids

is the subject of this work. Capillary forces are considered to be a "long-range force" [4, 5, 6], and are very significant at the nanometer to micron length scales. Thus, it is already expected that capillary forces may have significant effects on CNTs.

CNTs have a multitude of interesting and potentially useful properties. For this work, however, only a few have been of interest. In particular, the CNTs used in this work are multi-walled carbon nanotubes (MWNT) of about 10–20 nm in diameter, with edge-to-edge spacings of 50–100 nm, and range in length from 4 μm to about 200 μm, which means their aspect ratios of length to diameter are on the order of 10^4. Even though CNTs have been reported to have a very high elastic modulus of around 1 TPa [2], they are also very flexible and resilient, and can be subjected to 180° bends without fracture [7]. The very long, slender CNTs in this work are shown to be bent and flexed by capillary forces.

The wetting and nonwetting of CNTs by liquids is a major field of study, and is described sufficiently for this work in appendix A. It has not been of major importance in this work because the experiments require the wetting of the CNTs and it is achieved.

The pattern formation process of study in this thesis is viewed as a nucleation and growth process. Homogeneous and heterogeneous nucleation are terms used for discussing the ways in which patterns can be originated and formed over time.

In order to make this project tractable, the focus must be narrowed significantly. This is done primarily through the presentation of negative results and continually refining the interest.

1.3 Definition of Nanocarpets and Nanocarpet Patterns

The term nanocarpet is used throughout this thesis for convenience. It is meant to refer to any densely packed and vertically aligned array of CNTs resembling an ordinary carpet in appearance, but of much smaller scale. The term refers only to

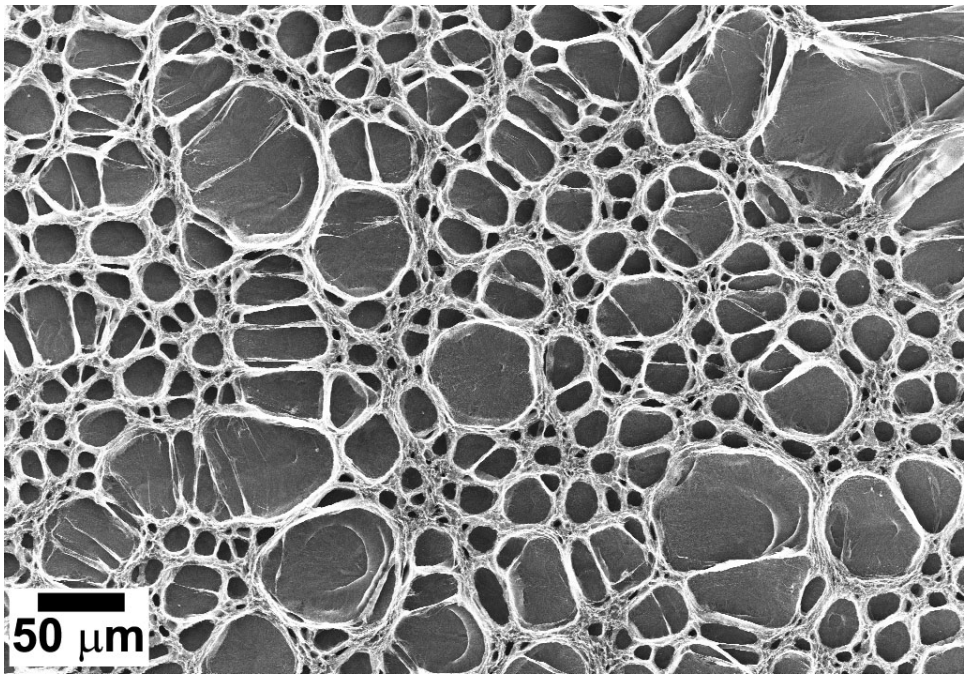

Figure 1.1: Example of a pattern created by application of liquid to an aligned mat of carbon nanotubes followed by ambient drying of the liquid. The image was taken in the scanning electron microscope, viewed from directly above the sample, and the sample is fully dried.

the CNTs themselves in the densely packed and vertically aligned configuration, not their substrates, and is specific to this morphology, meaning that a random array of CNTs or single freestanding CNTs would *not* be called a nanocarpet. Occasionally results of other workers will be mentioned and discussed, and their CNT arrays will also be referred to as nanocarpets if they are of similar configuration. The synthesis of nanocarpets for this work is described in detail in chapter 2.

An example of a pattern created in a nanocarpet by the wetting and drying of a liquid is given in figure 1.1. Often a whole pattern in a nanocarpet such as this will be referred to herein simply as a "nanocarpet pattern." The patterns are composed of many "pattern elements," as they are termed herein, which are defined as contiguous areas surrounded by a border of adjacent CNT tips and are occasionally also called cells, nests, craters, valleys, or cavities in this thesis. One should picture bowls with their cavities facing upward. Two examples of an *individual* pattern element are

shown in figure 1.2 and together with figure 1.1 illustrate the multiscaled nature of the subject.

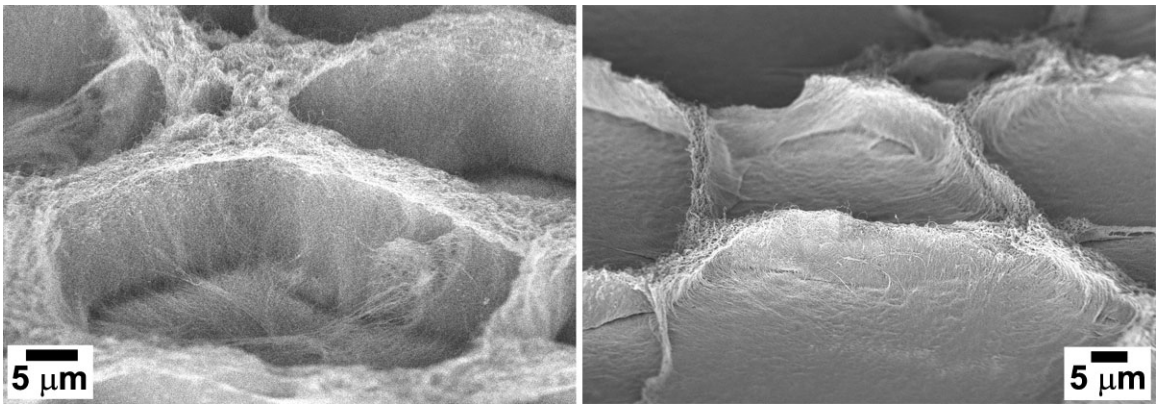

Figure 1.2: Examples of individual pattern elements (though surrounded by neighbors) in liquid-induced patterns within an aligned mat of carbon nanotubes. Individual CNTs are visible at this scale, and are the small hairlike fibers making up the floor and walls of the pattern elements, with their tips defining the upper surface of the walls. The scanning electron microscope images were taken at a 60° tilt angle.

1.4 Prior Related Studies

Several studies have been published that contain pattern formation in nanocarpets as at least some portion of their results. They are each discussed in detail here for comparison, reference, and creating additional context and introduction for this thesis.

1.4.1 Discussion of Chakrapani et al.

The most well-known paper dealing with nanocarpets patterned by evaporating liquids is the 2004 work of Chakrapani et al. [8]. The authors grow their nanocarpets by a different thermal chemical vapor deposition (CVD) method [9] than is used in this work, with no catalyst applied to the substrate surface, but rather iron (often used as a catalyst on substrates for CNT growth) is present in the ferrocene gas ($Fe(C_5H_5)_2$)

which is coflowed with xylene (C_8H_{10}) during the CVD. Thus the CNTs which make up the nanocarpets are grown from gaseous interaction with the silicon substrates. Their CNTs are multiwalled and should be of similar dimensions as those in this work. From the one low magnification scanning electron microscope (SEM) image of an unpatterned nanocarpet in the paper, shown in figure 1.3, it would appear that the morphology is fairly similar to those of this thesis. Examples of nanocarpets in this thesis are given in §2.8.

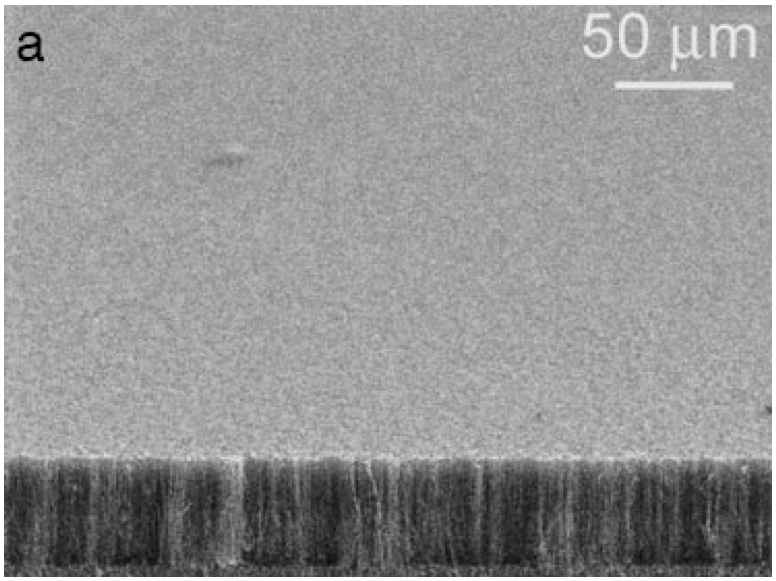

Figure 1.3: A tilted-view SEM image of an as-grown nanocarpet from Chakrapani et al., described as "substrate-grown, vertically aligned MWNT array with an average nanotube diameter of 30 nm." Image reused with permission from Proceedings of the National Academy of Sciences of the United States of America, 101(12):4009, Copyright 2004 National Academy of Sciences, U.S.A. [8].

In Chakrapani et al., an oxygen plasma treatment is required to alter CNT surface chemistry and render the nanocarpets water wettable because as-grown nanocarpets are highly hydrophobic. The effect of this technique on water wettability of nanocarpets has also been observed during experiments related to this work. Chakrapani et al. apply various liquids to their nanocarpets, including water, acetone, toluene, dimethylformamide, tetrahydrofuran, and methanol, and they do so by immersing their nanocarpet samples within the liquid used. This is also the preferred method

for achieving the most uniform and reproducible patterns in this thesis. Their patterns are reported to be stable once formed, as are the patterns in this thesis, even upon rewetting and drying by evaporation, which is presumed to also be true for this work. The patterns of CNTs remain fixed because of significant van der Waals forces between the CNTs [10] after they are brought into close contact by surface tension forces due to the air-liquid interfaces. It is also reported that freeze-drying of wetted nanocarpets does not produce patterns, and this is cited as evidence that evaporation of liquids from the nanocarpet is required to produce patterns. This may be somewhat misleading, since it is more likely that the presence of air-liquid interfaces and surface tension is required, but not necessarily the evaporation of liquids. For example, if liquids were to be removed from a wetted nanocarpet in a way other than evaporation, it is an unanswered question as to whether patterns would form. The authors discount both Marangoni convection and nucleation-and-growth mechanisms as the source of their patterns because they claim both should result in regular polygonal networks while the most prominent pattern features they obtain are generally quite elongated. Marangoni convection is further discounted simply because the "nanotubes cannot convect." Presumably this is assumed because of the small (10–100 nm) spacings between the as-grown CNTs. It is noted that coalescence and cell division is not observed in their patterns, and this is also true of the patterns in this work. Time scales of initial pattern formation are seconds, but minutes are required for the patterns to mature. Though it is not stated clearly, this is probably only true for the slower evaporating liquids like water, but not for more volatile liquids such as acetone.

Chakrapani et al. cite a 1995 paper [11] on the well-known microlithography issue of so-called resist collapse. This phenomenon occurs when the height-to-width aspect ratio of silicon nanoline features is such that deflections and breakage occurs due to surface tension effects during rinse and dry steps. Using Laplace's law for a cylindrically shaped air-liquid interface, $\Delta P = \gamma \cos\theta / r$, and assuming complete wetting ($\theta = 0$), Chakrapani et al. estimate the capillary underpressure in the water between two CNTs spaced 50 nm apart to be 6 MPa (though they do not show their

calculation). Further assuming this pressure difference to be distributed along the entire length of a cantilevered CNT they calculate that a deflection at the free end of 50 μm would require only a 5 kPa pressure difference. This is used to illustrate that capillary forces are significant enough at these length scales to cause the observed deformations.

The assumption of a cylindrically shaped air-liquid interface between two cylinders in close proximity is a poor one. The paper of Namatsu et al. [11] deals with line structures having smooth, long in-plane walls, and in that case the assumption of a cylindrical interface between them makes sense. A comparison of the *curvature* of the deformed line structures of Namatsu et al. with the deformed CNTs of Chakrapani et al. is very telling. Figure 1.4 compares structures shown in both works. Chakrapani et al. claim that although the height of the liquid in the system should be decreasing as it evaporates, the bending of the CNTs compensates for this and results in the air-liquid interface always being at the upper tips of the CNTs (they use the term "film" in referring to the CNT array). Together with the cantilevered beam assumption, this should result in the *opposite curvature* from what is observed. Thus at least one of the several assumptions being made here is incorrect. From observations in the present work, the air-liquid interface does *not* always remain at the CNT tips, but rather the liquid film height continues to decrease with the CNT tips eventually protruding from its surface. Chapter 6 in this thesis deals with pattern formation in nanocarpets that have been anchored to a substrate, thereby ensuring a cantilevered boundary condition, and it is observed that patterns do not form at all, while bending curvatures similar to those of the line structures of Namatsu et al. are in fact observed.

A better model for the behavior of air-liquid interface interaction with CNTs is likely the so-called lateral capillary force [12] most prominently used in the formation of colloidal crystals [13, 14]. In this model, a pair of particles, whether spheres or cylinders, pierce the air-liquid interface and are drawn together regardless of their hydrophobicity or hydrophilicity as long as they have identical character (they repel each other if they are of opposite character). This is illustrated in figure 1.5. Importantly, there is a resultant lateral attractive force *as well as* a downward force, which

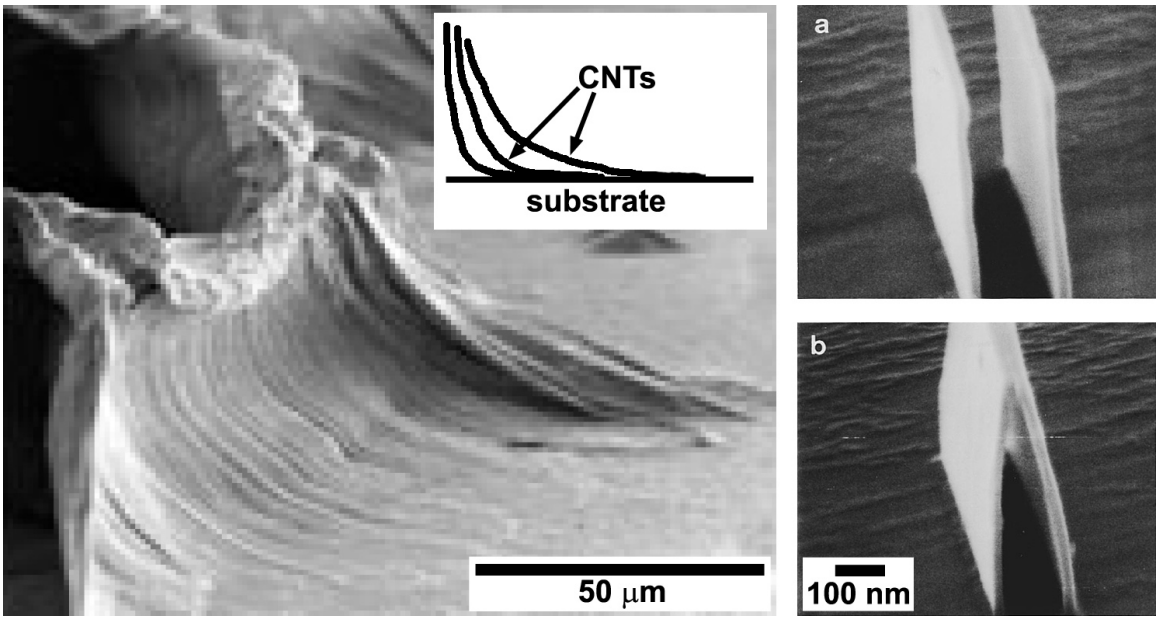

Figure 1.4: A comparison of curvatures for structures in Chakrapani et al. and Namatsu et al. Left: tilted-view SEM image of the wall of a canyon in a patterned nanocarpet from Chakrapani et al. Left inset: schematic illustrating CNT curvatures and that they lie flush against the substrate. Right: silicon nanoline features from Namatsu et al. before (upper) and after (lower) water rinsing, shown at the same scale. Left image reused with permission from Proceedings of the National Academy of Sciences of the United States of America, 101(12):4009, Copyright 2004 National Academy of Sciences, U.S.A. [8]. Right images reused with permission from Hideo Namatsu, Applied Physics Letters, 66(20):2655, Copyright 1995, American Institute of Physics [11]. Schematic and scale bars added by the thesis author.

better explains the downward and inward collapsed curvature observed in patterned nanocarpets.

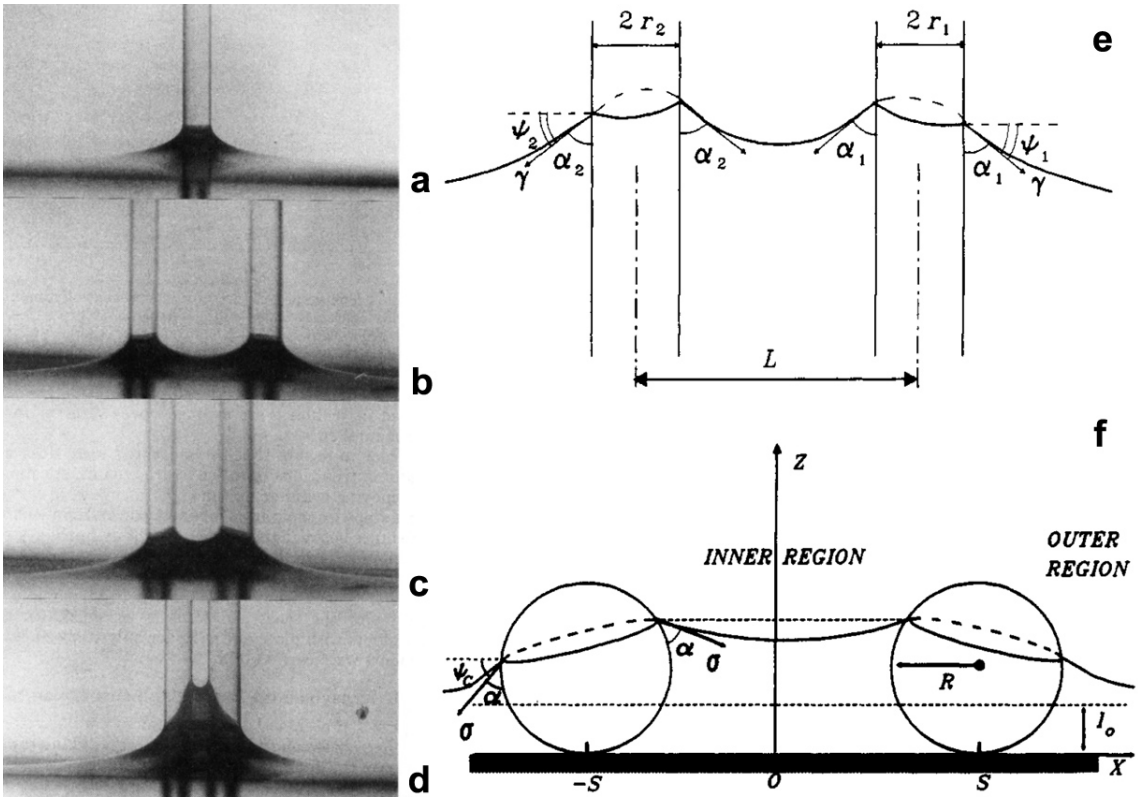

Figure 1.5: The menisci and geometry of particles at an air-liquid interface as described by the lateral capillary force model. The force is attractive if the particles have the same wettability type. (a) A single hydrophilic 630 μm diameter capillary piercing a 0.08 M sodium dodecyl sulfate solution. (b-d) Two hydrophilic capillaries, 630 μm diameter (left) and 740 μm diameter (right), piercing the same liquid and at progressively smaller spacings. (e) Geometry for two cylinders. (f) Geometry for two spheres supported on a substrate. Images reused with permission from Langmuir 8(12):3183, Copyright 1992 American Chemical Society [13] and Langmuir 9(12):3702, Copyright 1993 American Chemical Society [12].

In analyzing their patterns, Chakrapani et al. look solely at the widths obtained because there is large variation in the lengths of their "canyons," as they refer to them. Though convenient, this likely neglects important factors. Additionally, no mention is made of the smaller features confined between the rims of the larger canyons. Both the canyons and the small features are indicated in the SEM image in figure 1.6,

adapted from Chakrapani et al. The pattern analysis results presented in chapter 4

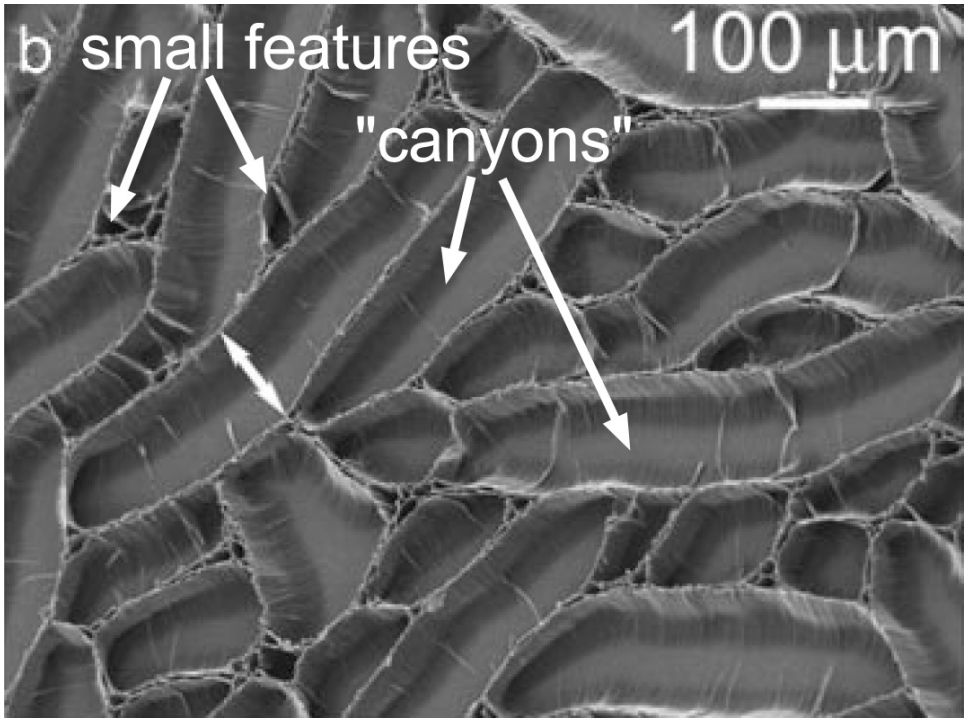

Figure 1.6: SEM image of a patterned nanocarpet in Chakrapani et al., showing both the large, elongated "canyons" and the small features confined between them. Image reused with permission from Proceedings of the National Academy of Sciences of the United States of America, 101(12):4009, Copyright 2004, National Academy of Sciences, U.S.A. [8]. Text and arrows added by the thesis author.

of this thesis include this pattern from the paper of Chakrapani et al., and consider widths only for the large canyons as they do, but diameters for the small features. In the supplemental figure of Chakrapani et al., average canyon *width* data in the range of about 20 to 375 µm (obtained from 14 nanocarpet samples) is plotted against their prepatterned heights, which range from about 20 to 200 µm. This relationship is linear with a slope of 2 µm canyon width per 1 µm of unpatterned height. Thus a 50 µm tall nanocarpet should have canyons with a mean width of 100 µm. This means one of two things. Either the base of the canyon is covered with CNTs that are lying completely horizontally, with the nanocarpet being "parted" like hair along the canyon's centerline, or there is detachment of the CNTs from the central region

of the canyon. The SEM images of the canyon patterns seem to indicate that the parted case is occurring, but the optical micrographs at different time steps in the formation process (particularly the first) seem to show visible bare substrate in the central region of the canyons. Still, appeal is made to adhesion of the CNTs at their base to their growth substrate as the cause of inhomogeneous shrinkage and stress accumulation, which is then supposedly relieved by crack formation. An initial pattern of long cracks is said to form quickly, followed by a much slower widening of these long cracks under the influence of capillary forces. Because the distribution of the cracks would presumably be relatively uniform in order to relieve local stresses everywhere in the nanocarpet, it follows that all the cracks would then have relatively equal amount of real estate within the nanocarpet to widen to equal final widths, and thus the widths of the canyons are described as uniform. Again, it is important to draw attention to the neglect of the smaller pattern features between the canyons within this crack-based description. Finally, by using different relative humidity levels during the drying portion of the experiments, it is found that faster evaporation "favors crack formation," (assumed to mean favoring the number of cracks formed) and leads to a decrease in canyon width (because there is less time for the growth process to occur). Conversely, a slower evaporation rate leads to increased canyon widths, and the relationship between evaporation rate and canyon *width* is stated as being linear, though no data are shown.

A very important point must be made about the crack formation and resulting canyons. Nowhere is it mentioned nor shown that high magnification, same location, before and after SEM characterization was carried out. This sort of characterization is required in order to determine if microcracks were *preexisting* and were merely opened up and widened by capillary forces. Such defects can easily be caused in nanocarpet growths by contamination (fibers or particles), microfractures within the silicon substrates, or poor handling of substrates. Defects will be shown in this thesis to very significantly influence the pattern formation. It would seem that such defects could not be the sole source of their canyons, however, since the canyons do cover the entire surface and are apparently quite reproducible. One other unmentioned factor

that could influence the formation of elongated structures (canyons) of very different scale from the smaller patterns between the canyon rims is that of flow effects. In this thesis, it is shown that flow effects can cause directionality in patterns, as well as larger structures superposed with much smaller ones.

Finally, Chakrapani et al. demonstrate the less-than-surprising effect of forced vacancies (bald spots) in their nanocarpets by prepatterning their substrates and consequently the resulting nanocarpet growth. Interestingly, they *do* now obtain polygonal patterns of the rims surrounding the vacancies, which can be thought of as heterogenous nucleation sites in a nucleation and growth process. If one looks closely at the image shown in figure 1.7, it is also evident that there are much smaller, but still visible, spaces (pattern elements) present where the rims of these patterns intersect. This would indicate that there are other sources of patterns in these samples in addition to the predefined holes in the nanocarpet growth.

Though patterns are clearly created in the work of Chakrapani et al. , many debatable assumptions are made in attempting to understand them. Underlying all of their work is the fact that the CNTs are grown during *gaseous* interaction with the substrate. Without strength of adhesion measurements to prove otherwise, it is unclear whether there is any significant adhesion greater than stiction (van der Waals) forces involved. The formation of cracks and their subsequent widening during drying is clearly evident, but the presence of (much smaller) patterns in addition to the cracks indicates there may be two separate modes of pattern formation at play, with the crack-forming mode dominating in their results. Discounting the presence of nucleation and growth mechanisms out of hand because regular polygonal networks are not the dominant pattern observed is incorrect, as their own results from the experiments containing bald spots (heterogeneous nucleation sites) indicate.

The notion of multiple possible modes of pattern formation in nanocarpets is important to this work. A model for pattern formation based upon nucleation and growth is outlined in chapter 7 and the nanocarpet pattern results obtained throughout this work differ significantly from those of Chakrapani et al. . The results of this work indicate that nucleation and growth is indeed one plausible explanation for

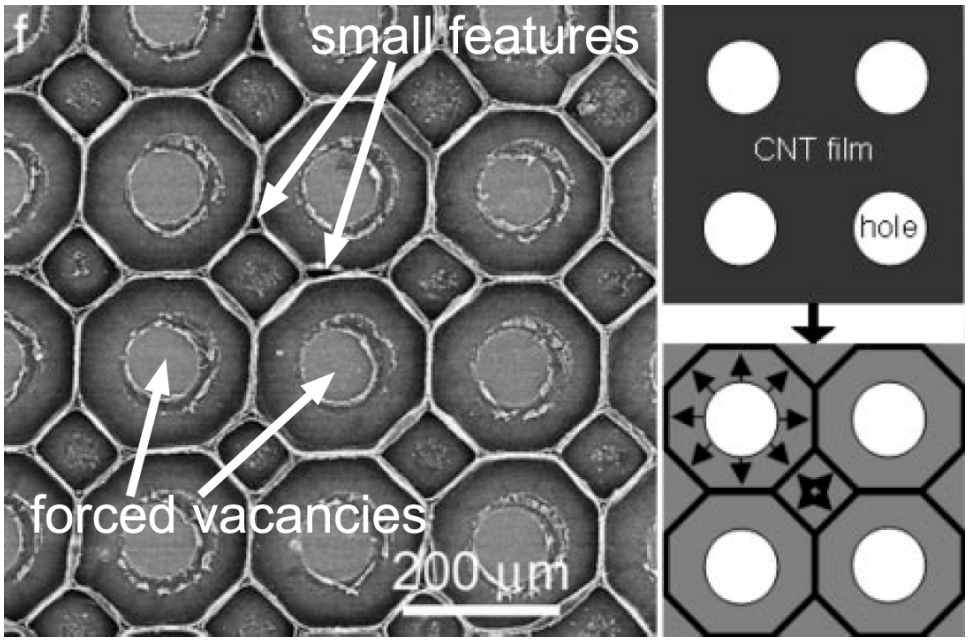

Figure 1.7: SEM image and schematics of a patterned nanocarpet with forced vacancies in Chakrapani et al., showing polygonal patterns and smaller features confined between the polygonal pattern elements. Image reused with permission from Proceedings of the National Academy of Sciences of the United States of America, 101(12):4009, Copyright 2004, National Academy of Sciences, U.S.A. [8]. Text and arrows added by the thesis author.

nanocarpet pattern formation. It seems nucleation and growth may also be superposed with other modes of pattern formation, for example with cracks forming first as in Chakrapani et al. in conjunction with nucleation and growth of additional features. The fabrication process used in forming the anchored nanocarpets in chapter 6 makes the nanocarpets strongly well-adhered, enforcing a cantilevered boundary condition on the CNTs, and still no cracklike patterns form when treated with liquids and dried as observed by Chakrapani et al.

1.4.2 Discussion of Liu et al.

In the 2004 paper of Liu et al. [15], the authors claim to report the first use of the capillary force in the formation of patterns in an aligned CNT film (nanocarpet) through a "water spreading method." They note the importance of low density regions and vacancies within the nanocarpet, which is also clearly shown throughout this work.

Liu et al. grow their nanocarpets using a different method of thermal CVD than either Chakrapani et al. or the simple thermal CVD method used in this work. In describing their growth process, which is based on pyrolysis of iron(II) phthalocyanine (FePc), they reference a 2000 work by Wang et al. [16] where a complicated mixture of "metal salts, phthalandione, urea, and ammonium molybdate" were roasted to make a product called nickel-cobalt phthalocyanine. In the works of Liu et al. and Wang et al., clean quartz glass pieces are placed within a tube furnace (also used for the CNT growth by thermal CVD in this work) and once desired conditions are reached, the nickel-cobalt phthalocyanine, in the case of Wang et al., or the iron(II) phthalocyanine, in the case of Liu et al., is placed upstream of the quartz glass. A mixture of argon and hydrogen gases are continuously being flowed through the furnace. Wang et al. produce "honeycomb-like alignments of carbon nanotubes," which they describe as being densely packed vertical arrays of CNTs that are spread outward into honeycomb patterns at the very tops of the arrays. The as-grown patterns are shown in figure 1.8. No explanation is given in Wang et al. for why the

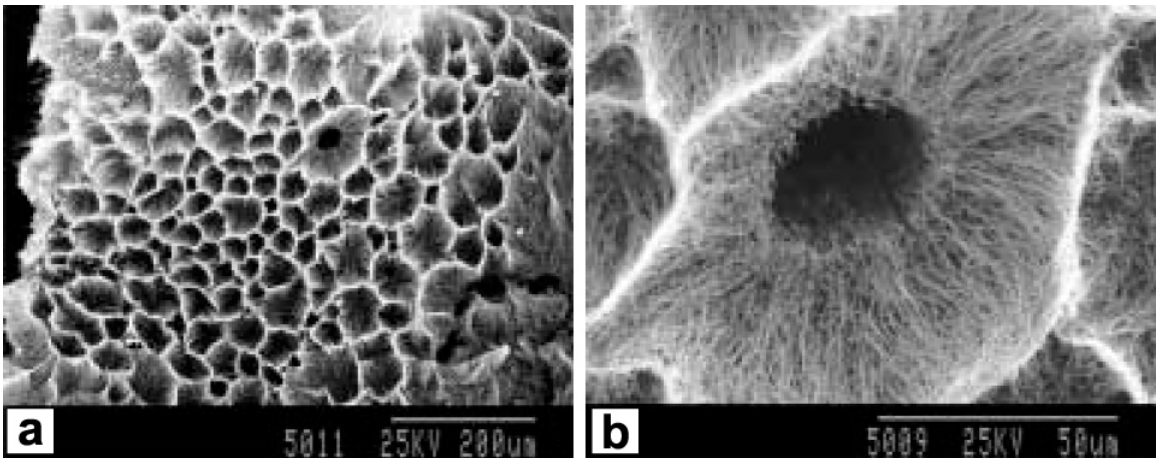

Figure 1.8: SEM images of *as-grown* honeycomb patterns in nanocarpets from Wang et al. (a) Lower magnification image. (b) Higher magnification image of a large cell within (a). Figure reproduced from Applied Physics A, Materials Science and Processing, Vol 71(3), 2000, pgs 347–348, Honeycomb-like alignments of carbon nanotubes synthesized by pyrolysis of a metal phthalocyanine, X. B. Wang, Y. Q. Liu, and D. B. Zhu, Fig 2, Copyright 2000, with kind permission from Springer Science and Business Media [16].

honeycomb-like alignments are produced instead of continuously packed arrays as in this work or many other CNT growth papers. In figure 1.8(b) from Wang et al., there is a central "hollow inner cavity" of about 30 μm diameter shown within a typical honeycomb cell of 80 μm diameter. This is a region where apparently no CNTs were formed. Thus, there is a void within the nanocarpet in the center of the honeycomb cell.

Like Wang et al., there is a work by Zhang et al. [17] that also demonstrates honeycomb alignments of *as-grown* CNTs. Ferrocene and xylene are coflowed to produce the CNTs, which is the same method used by Chakrapani et al. Zhang et al. explain that a prolonged deposition time results in a densely packed array of CNTs (no honeycomb alignments), while a shorter deposition time results in a honeycomb alignment with regularly arranged void regions throughout the array. The two growth methods of Wang et al. and Zhang et al. are similar in that neither involves the catalyst being placed directly on the substrate, but rather the catalyst

is gas-borne during either transfer from the upstream source (in the case of Wang et al.) or entirely (Zhang et al.). This similarity lends further support to the possibility that Liu et al. may also have honeycomb-like alignment in their nanocarpets due to the growth process itself.

Liu et al. make no mention of the honeycomb-like alignments in the nanocarpet growths produced by Wang et al., even though Liu et al. claim to be using the same growth method. No image or description of their nanocarpets prior to water treatment are given. In their supplementary info, there is one top view SEM image showing a 10 μm wide section that seems to indicate that their nanocarpets are densely packed and similar to those of this work, though this is highly questionable given the growth method used and the work of Wang et al. 10 μm is less than one-third of the typical diameter of the pattern elements of Liu et al. and is not sufficient to prove there is no preexisting honeycomb alignment. The diameter range of the post-water spreading honeycomb pattern elements reported by Liu et al., shown in figure 1.9, is 30–60 μm, which is very similar to the diameter range (15–80 μm) of honeycombs formed at the

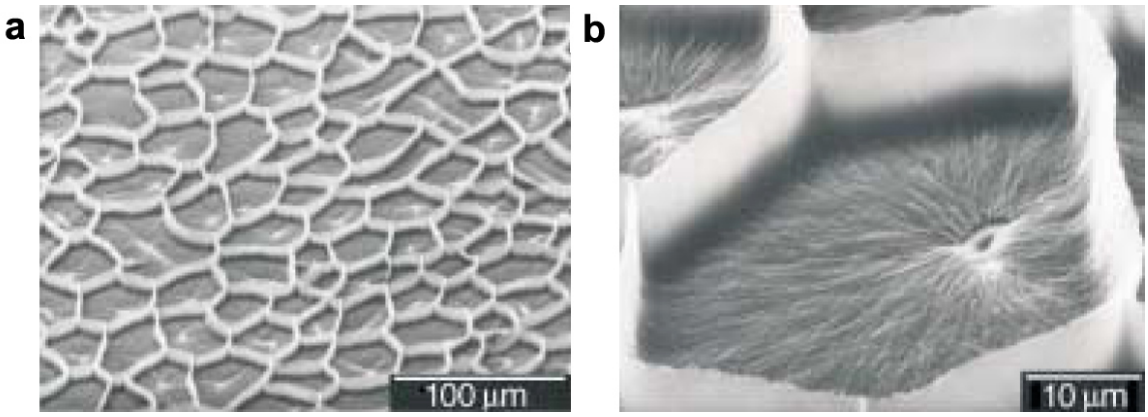

Figure 1.9: SEM images of nanocarpet patterns obtained by water treatment as reported by Liu et al. (a) Lower magnification image. Almost every pattern element contains a central "bald spot." (b) Higher magnification image of a single pattern element within (a). Images reused with permission from Angewandte Chemie International Edition, 43(9):1146, Copyright 2004, John Wiley and Sons [15].

tips of the nanocarpets *during growth* by Wang et al. If indeed there are honeycomb alignments in the nanocarpets of Liu et al. prior to water treatment, then the patterns

they obtain are caused by the preexisting voids, as will be shown in this work.

Liu et al. explain that water is able to permeate within the CNTs and reach their quartz substrate where it is then able to spread easily because quartz is hydrophilic. All interspaces between CNTs are said to be soaked.

Liu et al. construct a 2-D model of their nanocarpet using hexagonally packed rods, and appear to be thinking of an integration of surface tension around the diameter of a protruding CNT when speaking of the "capillary force supplied by a single nanotube of radius r" and writing the expression $2\pi r\gamma_w \cos\phi_{nt}$, where γ_w is the surface tension of water and ϕ_{nt} is the contact angle made with the CNT. By considering their hexagonal packing arrangement, they derive something they call the "hydrostatic dilation stress," which appears to be similar to the capillary pressure due to Laplace's law. The packing density (volume fraction) of CNTs is considered as the ratio r^2/R^2, where R is half the center-to-center distance between neighboring CNTs. Next they estimate the variation of this hydrostatic dilation stress with packing density, and show that the stress is very high, on the order several MPa, for high packing density of CNTs. After an interesting statement that SEM images show that the CNT densities are not homogeneous and there are low- and high-density regions present in their nanocarpets, an estimate is made to show that capillary forces are significant enough to deflect CNTs. As deflection occurs, the capillary forces have greater effect, deflecting the CNTs further. Low-packing-density regions are seen to originate features that grow outward until they contact similar outward growing regions from neighboring low-packing-density regions. The statement that there are heterogeneities in the packing density may indicate the presence of honeycomb-type alignment *before* water treatment and the formation of patterns.

Liu et al. demonstrate (as also did Chakrapani et al.) the effect of forced vacancies by etching the surface with a pulsed laser, shown in figure 1.10. These vacancies are said to be 2–3 μm in diameter and are made into various patterns. Following water treatment and evaporation, the lines bisecting the distance between vacancy centers are marked by the CNT tips. The authors note there are two regions observed. One is the "controlled assembling region" in which the laser etched vacancy is the

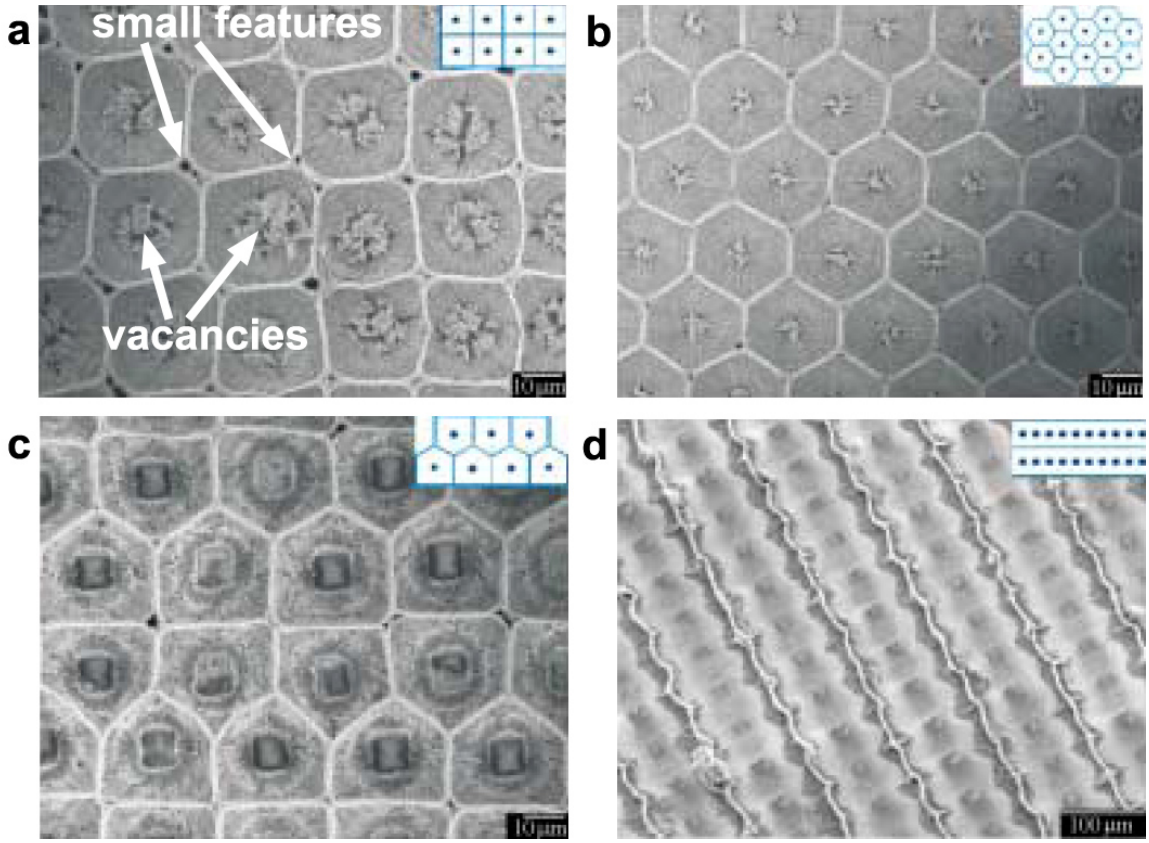

Figure 1.10: SEM images of nanocarpet patterns created by laser etching of vacancies followed by water treatment as reported by Liu et al. Insets are the etch patterns used. (a) Square lattice pattern, with vacancies and small features within the rims indicated. (b-d) Further etch pattern results. Images reused with permission from Angewandte Chemie International Edition, 43(9):1146, Copyright 2004, John Wiley and Sons [15]. Text and arrows added by the thesis author.

center. The other is the "freely assembling region," which contains pattern formation presumably controlled by the packing density of the CNTs in the nanocarpet. Liu et al. demonstrate that if the forced vacancies are placed close enough (about 40 μm), the freely assembling region is minimized. However, it is still clearly visible in their SEM images that small features are present within the rims bounding the vacancy-induced features. Chakrapani et al. showed the same effect by creating nanocarpet material in line regions of narrow enough width (about 100 μm) that no features were formed by wetting and drying with acetone.

A final point about the paper of Liu et al. must be made. In the only SEM image shown of patterns formed by water spreading *without* forced vacancies, there are central "bald spots" within every single feature. These could very well have been present prior to the water treatment, and could be the motivation for their statement that CNT densities within the nanocarpet are not homogeneous. A review paper was published in 2006 by a subset of the same authors [18] and contains additional images of their patterns, but no significant new findings.

The patterns of Liu et al. are more similar to those obtained in this thesis than are the patterns of Chakrapani et al. However, the results of Liu et al. are rather unclear, especially due to not being able to rule out significant preexisting defects (vacancies) in their nanocarpets.

In this thesis, it will be shown in detail throughout that the influence of voids, vacancies, and similar defects can have a dominant effect on pattern formation in nanocarpets. These types of defects are usually due to the CNT growth step itself, but can also be induced, as others have shown. It will be shown that nanocarpets that are anchored at their base do *not* form patterns, even in the presence of such defects.

1.4.3 Discussion of Correa-Duarte et al.

In the 2004 paper of Correa-Duarte et al. [19], the authors are interested in demonstrating that mouse fibroblast cells can grow on a patterned nanocarpet, whose 3-D

topology and multiple length scales of microns for the cavities and nanometers for the CNTs are expected to be useful as a cell growth scaffold. Correa-Duarte et al. obtain their nanocarpets from NanoLab (Newton, MA) and reference a paper by the group of a NanoLab cofounder, Z. F. Ren [20] for the nanocarpet growth. The type of nanocarpet growth described therein is more similar to the thermal CVD method used in this work than the works of Chakrapani et al. and Liu et al. In the paper by Ren's group, and presumably also in the formation of the nanocarpets obtained from NanoLab by Correa-Duarte et al., thermal CVD is carried out with acetylene and ammonia. The catalyst is a fine powder composed of iron nanoparticles formed by a sol-gel process followed by drying.

Because Correa-Duarte et al. are interested in chemically functionalizing their CNTs to prepare them as cell-growth scaffolds, they use a solution of nitric and sulfuric acid in a 1:3 ratio. It will be shown in this work that many different liquids can be used to create patterns in nanocarpets as long as the liquid wets the nanocarpet sufficiently.

In the short ≈5 μm nanocarpets shown in Correa-Duarte et al. and in figure 1.11(B), the CNTs are observed to bundle together under the action of surface tension. A bundled pattern created in a ≈7 μm nanocarpet obtained from NanoLab is also shown later in this thesis (figure 4.10). In Correa-Duarte et al., for the longer nanocarpets of 35 and 50 μm, a pattern of cavities is formed that look similar to the patterns obtained in this work. An important feature to note is that the thickness of the rims between the cavities in Correa-Duarte et al. is quite small compared to many that will be shown in this work. Perhaps the pattern obtained in this work that is most similar to those of Correa-Duarte et al. is shown in figure 4.4, where the nanocarpet is quite sparsely packed. The as-grown nanocarpets in Correa-Duarte et al. are also sparsely packed when compared with those in this work.

Correa-Duarte et al. form cavities of diameters ranging 5–60 μm in nanocarpets of 50 μm in height, and cavity diameters of 5–15 μm in nanocarpets of 35 μm in height. It is not described how these diameter ranges are estimated. Since they are interested in growing cells on their nanocarpets and not in the mechanism of pattern formation,

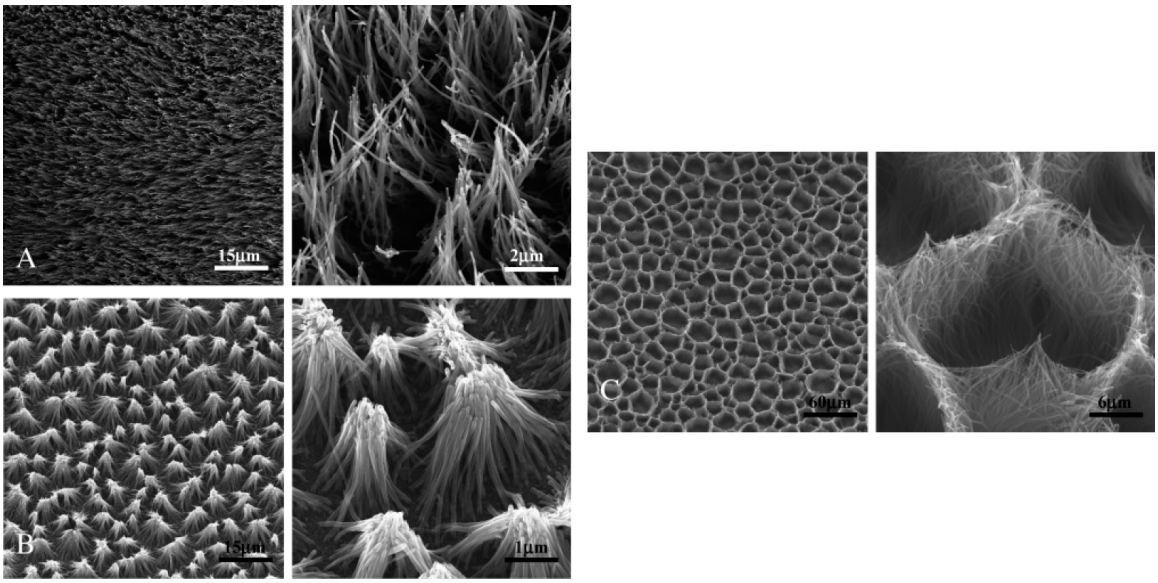

Figure 1.11: SEM images of nanocarpet patterns created by acid solution treatment as reported by Correa-Duarte et al. (A) As-grown nanocarpet at low and high magnification. (B) Short nanocarpet patterned into bundles following treatment, at low and high magnification. (C) Cavity patterns in a taller nanocarpet following treatment, at low and high magnification. Images reused with permission from Nano Letters, 4(11):2233, Copyright 2004, American Chemical Society [19].

they do not investigate the pattern formation process in detail. They reference the previously discussed paper of Liu et al., the so-called hydrostatic dilation stress, and regions of low packing density as the source of their patterns. There does not appear to be any obvious presence of defects or voids in the nanocarpets used by Correa-Duarte et al., but rather the sparseness of their nanocarpets before patterning likely results in the patterns created.

1.4.4 Discussion of Patil et al.

In the 2005 paper of Patil et al. [21], the authors are interested in obtaining field emission from surface-modified aligned CNT arrays (nanocarpets). They grow their nanocarpets using the pyrolysis of iron(II) phthalocyanine in an argon and hydrogen flow in a thermal CVD process as did Liu et al. This again raises the question of whether there is honeycomb-like alignment of their *as-grown* nanocarpets prior to any liquid treatments, but this is not adequately addressed in the paper. Following growth, they transfer the nanocarpets to gold substrates, which are used as electrodes in the field emission measurements. The transfer is carried out using a 30%–40% HF solution. In an additional step, they keep their nanocarpets in distilled water for 30 minutes and then allow them to dry in air. A honeycomb pattern is produced, though the pattern is much less pronounced than any in this work. In a figure in their paper and reproduced in figure 1.12, a nanocarpet on a gold substrate is shown without placement in the distilled water bath. The nanocarpet has extensive voids and gaps, which likely originate the formation of the patterns during the water treatment and air drying. Patil et al. simply attribute the pattern formation to the "capillary effect" and reference a paper by Feng et al. [22] that deals with creating a microscale mesh film with special wettability characteristics, but is unrelated to any capillary effect-based pattern formation.

Patil et al. obtain better field emission characteristics from their nanocarpets that have been patterned into honeycombs by water treatment, and this is a promising application for this work as well.

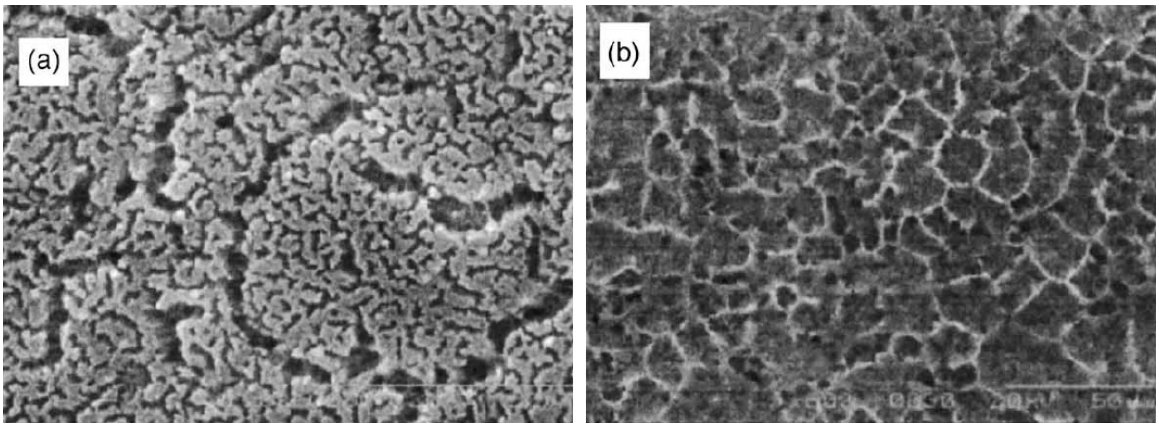

Figure 1.12: SEM images of nanocarpets as reported by Patil et al. (a) Nanocarpet following transfer via an HF solution to a gold substrate. The large number of voids in the nanocarpet is clearly visible. (b) Honeycomb structure in the nanocarpet following water treatment and air drying. Figures were published in Synthetic Metals, Vol 154(1–3), A. Patil, R. Vaia, and L. Dai, Surface Modification of Aligned Carbon Nanotube Arrays for Electron Emitting Applications, pgs 229–232, Copyright Elsevier 2005 [21].

1.4.5 Discussion of Sheng et al.

In the 2005 paper of Sheng et al. [23], the authors are also interested in field emission from nanocarpets that have been patterned by liquids. The concept is that the pattern formation process leaves many more CNTs at edges, and therefore with fewer neighboring CNTs. A major issue in field emission devices constructed of CNTs is that of the "screening effect" where electric fields are not concentrated sharply at CNT tips as desired in order for field emission of electrons to occur, but are screened by their neighbors. Through patterning, the increased number of CNTs at edges could decrease screening and lead to better field emission characteristics.

For their CNT growth, Sheng et al. use a thermal CVD method that is nearly the same as the method used in this work. Thin (5 nm) iron films were deposited by electron beam evaporation onto silicon substrates and ethylene gas was flowed at 700 °C. The average height of the nanocarpet was said to be 160 μm. Ethanol was used as the liquid for their pattern formation, which adds further evidence to a finding of this work—many different liquids can be used to form patterns in nanocarpets. The

authors state that the nanocarpet "shrank and split" into cells separated by walls. The description given by the authors of the pattern formation process is worth quoting in full.

> "When the CNT array was immersed into the ethanol, the liquid was guided into the spaces between the aligned tubes. When the array was taken out, firstly, cracks were formed at sparse regions during the evaporation of liquid from the nanotube film. Then the array shrank and the CNTs bent. Finally, the open self-assembly structures were formed."

By "open self-assembly structures," it is assumed they are referring generically to all their structures, not just a particular type. Examining the low magnification SEM image of their nanocarpet prior to treatment, reproduced in figure 1.13, it is obvious that there are several very large voids (defects) of 200 μm in size in their nanocarpet, as well as numerous small ones.

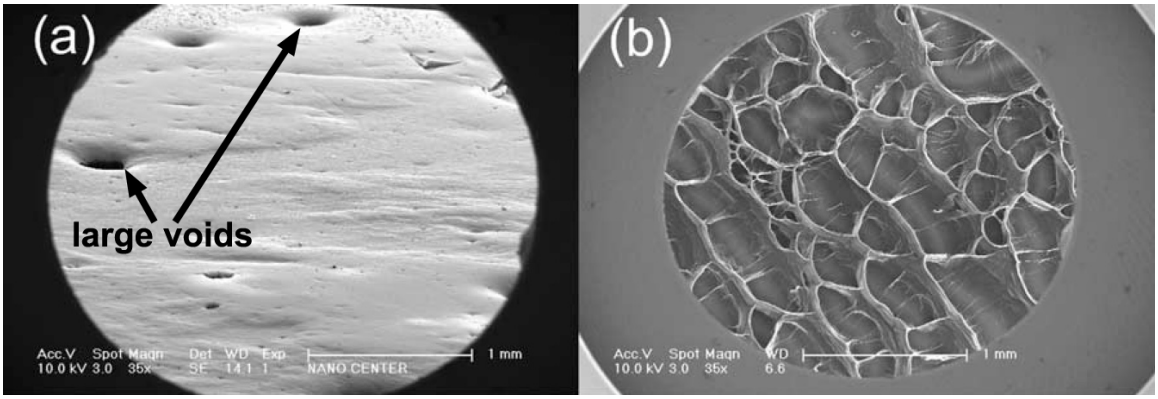

Figure 1.13: Very low magnification SEM images of nanocarpets as reported by Sheng et al. (a) Tilted view of as-grown nanocarpet, with large voids indicated. (b) Top view of patterned nanocarpet following ethanol treatment and air drying. Figures were published in Applied Surface Science, Vol 250(1–4), L. M. Sheng, M. Liu, P. Liu, Y. Wei, L. Liu, and S. S. Fan, Field emission from self-assembly structure of carbon-nanotube films, pgs 9–13, Copyright Elsevier 2005 [23]. Text and arrows added by the thesis author.

The fact that Sheng et al. observe crack formation as in Chakrapani et al., and that they formed at sparse regions (defects), supports the possibility of multiple modes of

pattern formation occurring. The relief of stresses in the wetted nanocarpet by the formation of cracks initiated at stress concentrations may be initially occurring and in conjunction with a slower surface-tension based widening of void regions. The results presented in this thesis in chapter 6, where no pattern formation occurs if nanocarpets are anchored at their base, contribute to the understanding of this situation.

1.5 Problem Statements

Several problem statements have been formulated to motivate this work and will be used throughout to focus the discussion.

1. **What is the mechanism for pattern formation in nanocarpets by a drying fluid?**
2. **What types of patterns are possible?**
3. **Can nanocarpets be anchored within a surface while remaining sufficiently functional?**
4. **What differences are there, if any, between patterns produced in anchored nanocarpets and those in unanchored nanocarpets, and what does this mean?**

The first is intricately related to the possible development of a method of fabrication via self-assembly based upon this pattern formation process, and the second is similarly motivated. The third is technologically driven but also relevant for understanding the pattern formation mechanism involved. The fourth has bearing on the prospects for success of any technology involving nanocarpets in environments where they may interact with fluids, and again is relevant to the pattern formation.

1.6 Overview of the Thesis

A brief outline of the thesis is as follows.

In chapter 2, the nanocarpet fabrication ("carbon nanotube growth") methods and experimental system used for this work are covered in detail separately from

other experimental methods. The reasons for this are simplification and emphasis. It will be seen that limitations on fabrication abilities can place strong limitations on the conclusions possible from experiments on nanocarpet pattern formation.

Chapter 3 concerns the materials, methods, and experimental setup other than the fabrication of the nanocarpets. Liquids used, sample handling protocols, microscopy, spin-coating, and the types of experiments conducted in this work are covered.

In chapter 4, results are presented from pattern formation experiments using nanocarpets that have not been anchored to a substrate, a state referred to throughout as being "as-grown." The discussion of these results will begin to address the problem statements in §1.5, while setting the stage for later chapters.

Chapter 5 concerns a method devised during the course of this work for answering the third problem statement in §1.5. It is found that it is possible to anchor nanocarpets to a surface, and the details of how this can be carried out are explored. The degree to which these anchored nanocarpets remain functional is primarily inferred from their morphology and the steps used in the anchoring process.

A return is made in chapter 6 to attempting to understand the pattern formation process described herein, this time using nanocarpets that have been anchored following the method of chapter 5.

Chapter 7 describes the application of a population balance model to pattern formation in nanocarpets, and how, if the appropriate details were known, predictions could be made and tested.

In chapter 8, detailed discussion is presented with the intention of determining the extent to which the problems stated in §1.5 are answered by the results, and what new questions are raised by the results. Implications for the mechanism of nanocarpet pattern formation as well as technological relevance are discussed. Finally, the overall findings are summarized and an outlook for future directions in this area of study are given.

The first appendix provides brief discussion of the wetting of CNTs. The second appendix contains further details about the CNT growth setup. The third appendix deals with population balance models, including an application to the well-known

problem of polyurethane foam formation. This example application is useful in comparison and development of the model applied in chapter 7 to pattern formation in nanocarpets. The final appendix contains additional results and larger versions of selected figures.

Chapter 2

Carbon Nanotube Growth

2.1 Introduction

The intention of this chapter is to cover the methods and setup used for the CNT growth separately from any other experimental methods used. The reasons for this are simplicity and emphasis. In any experimental study involving nanoscale materials, the exact details of the fabrication steps are incredibly important. This stage of projects such as the present one is generally where many problems arise, as well as being the stage where the most improvements are possible. Under conditions of limited detailed dynamic information, it is essential to have as much physical information as possible about the experimental materials before and after experiments are conducted.

The emphasis of this thesis is not on the growth of CNTs. Rather, the CNT materials (nanocarpets) are taken as a model nanoscale system in which to study phenomena of liquid-induced pattern formation. It was not practically feasible to include other potentially appropriate nanoscale systems such as arrays of metal and polymeric nanowires or silicon nanorods [24]. Similarly, simply purchasing nanocarpets "off the shelf" with specified desired properties was not only impossible, but, at this stage of the research, would not have resulted in the important observations included here that resulted from the intimate connection between material fabrication (including its inherent pathologies) and experiment.

Consequently, growth of CNTs was conducted for this study, but was carried out with the intention of replicating known methods [25, 26] for growth and with minimal

interest in optimization or varying approaches. Some iteration between experiments on nanocarpets and changes in the protocol used for their growth were necessary in order to achieve successful experimental results. This was because of pathologies in the experiments that were traced to issues in the growth process.

The experiments in Chapters 5 and 6 were conducted solely with nanocarpets grown by the thesis author using the setup described in this chapter. Many of the experiments in chapter 4 used nanocarpets generously grown for this work by Dr. Michael Bronikowski and collaborators at the NASA Jet Propulsion Laboratory, and also used methods similar to those described in this chapter.

2.2 Historical Perspective

The discovery of CNTs is attributed to Iijima [1] in 1991, but it is likely that they were first produced decades before, as part of arc-based carbon fiber production at Union Carbide in the late 50s, finally published by Bacon [27] in 1960. Indeed, it is possible that any pyrolytic process involving certain carbon-containing gases (benzene, ferrocene, xylene, acetylene, ethylene, methane, etc.) and metallic catalysts produces at least some CNTs. Probably the first high resolution transmission electron microscopy (TEM) image of what would later be called a CNT, but which at the time was described as "tubular graphite of nanometre scale," was published in 1976 [28]. Smalley and coworkers [29] discovered C_{60}, "buckminsterfullerene" or "buckyball," which garnered the Nobel Prize in chemistry in 1996 and which resulted in the name of the family of related carbon structures that includes CNTs—the "fullerenes."

Striking a DC-arc between graphite electrodes in a helium atmosphere is the oldest method of CNT production [30, 1], and is known to produce the highest quality CNTs, i.e., with the fewest structural defects in the CNTs themselves [31]. Modifications include RF fields and different gaseous atmospheres. The primary drawback to this method is random orientations of the CNTs, with bundling together of CNTs being very common. Following growth, CNTs made with this method are often used in solution.

Thermal chemical vapor deposition (CVD) in general means the use of elevated temperatures, a well-prepared substrate, and the proper gaseous mixture in order to obtain the formation (deposition) of some material, often a thin film, on the substrate. Thermal CVD has been in wide use in the semiconductor and microelectronics industry for thin film production for decades [32], attaining fine control over deposition and growth of various oxides and pure materials in thin layers. It was first applied to the growth of CNTs in 1993 by Endo's group [33]. Subsequent modifications of the basic thermal CVD idea have included microwave plasma enhancement, RF field application, careful control over the catalyst properties, and placing the catalyst material in the vicinity of the substrate during the reaction, but not directly onto it prior to beginning the process. Thermal CVD and its variants are well-suited to the growth of CNTs in patterned areas and in array configuration, and results in CNTs on a substrate, simplifying sample handling. These are the primary reasons it is used for this work.

Many of the wondrous technological applications of CNTs, both currently being developed and those envisioned, require large quantities (kilograms per day) of high-quality CNTs [34]. Arc-based and CVD-based methods will likely never be able to produce the necessary quantities, even if they can provide the quality levels desired. The high pressure carbon monoxide (HiPCO) process first developed by the Smalley group [35, 36] is designed to address this issue.

Because of the exponentially growing research interest in CNTs, many variations on their growth are being explored. For example, it has even been demonstrated that CNTs can be formed from biological material, such as blades of grass [37]. In 2004, ultratall nanocarpets of single-walled carbon nanotubes (SWNT) on the order of 2.5 mm were grown in a vertical array on a substrate by Iijima's group using water vapor–assisted thermal CVD [38]. Another impressive example of ultralong CNTs in a nanocarpet configuration are the MWNT 3.25 mm tall samples demonstrated by Eres et al. [39] using thermal CVD with the addition of ferrocene gas, also in 2004. It has even been said [40] that this group can grow 9.25 mm tall nanocarpets.

There are various advantages, disadvantages, and comparisons that can be made

between methods for CNT growth [40, 41], i.e., pattern retention and creation, aligned or nonaligned growth, degree of CNT interweaving, quantities possible, purity of resulting CNTs, amount of amorphous deposits, etc., but these are not important for this work. The method of CNT growth itself was never found to be a limiting factor for conducting the experiments in this work, and it is expected that the results of this thesis are independent of the exact *method* of CNT growth, as long as the CNTs are still in a nanocarpet configuration on a substrate. This is important because the context of this work is the technological use of CNT-based materials in realistic environments.

2.3 Description of CNT Growth by Thermal CVD

CNT growth by thermal CVD is a rather straightforward process from the perspective of experimental setup, with the focus being to provide controlled physical and chemical conditions in order for the spontaneous growth reaction to occur. Though many enhancements to the basic version of this growth process can be made, the goal of the CNT growth portion of this thesis was to produce nanocarpet samples of sufficient quality for the patterning and anchoring experiments. Consequently, the most basic thermal CVD approach was used in order to keep this stage of the work as simple as possible. Even so, it took many growth runs and iterations with the setup in order to achieve acceptable results.

A simplified schematic of the setup used for CNT growth by thermal CVD is shown in figure 2.1. Gas flow is supplied by standard compressed gas cylinders (N_2, H_2 UHP grade, C_2H_4 99.5% pure, and Ar UHP grade) equipped with stainless steel pressure regulators (3810 series, Matheson Tri-Gas, Irving, TX), passed through manual flow control equipment (ball valves, Swagelok, Solon, OH; volumetric flow meters, Aalborg, Orangeburg, NY; manifold with 1-way check valves, Atomate, Simi Valley, CA) mounted on an aluminum control panel, and delivered to the 1 in. diameter quartz tube furnace. All gas flow lines are Swagelok 1/4 in. OD stainless steel tubing or Swagelok braided steel flex-hose. Prior to a growth run, prepared substrates are

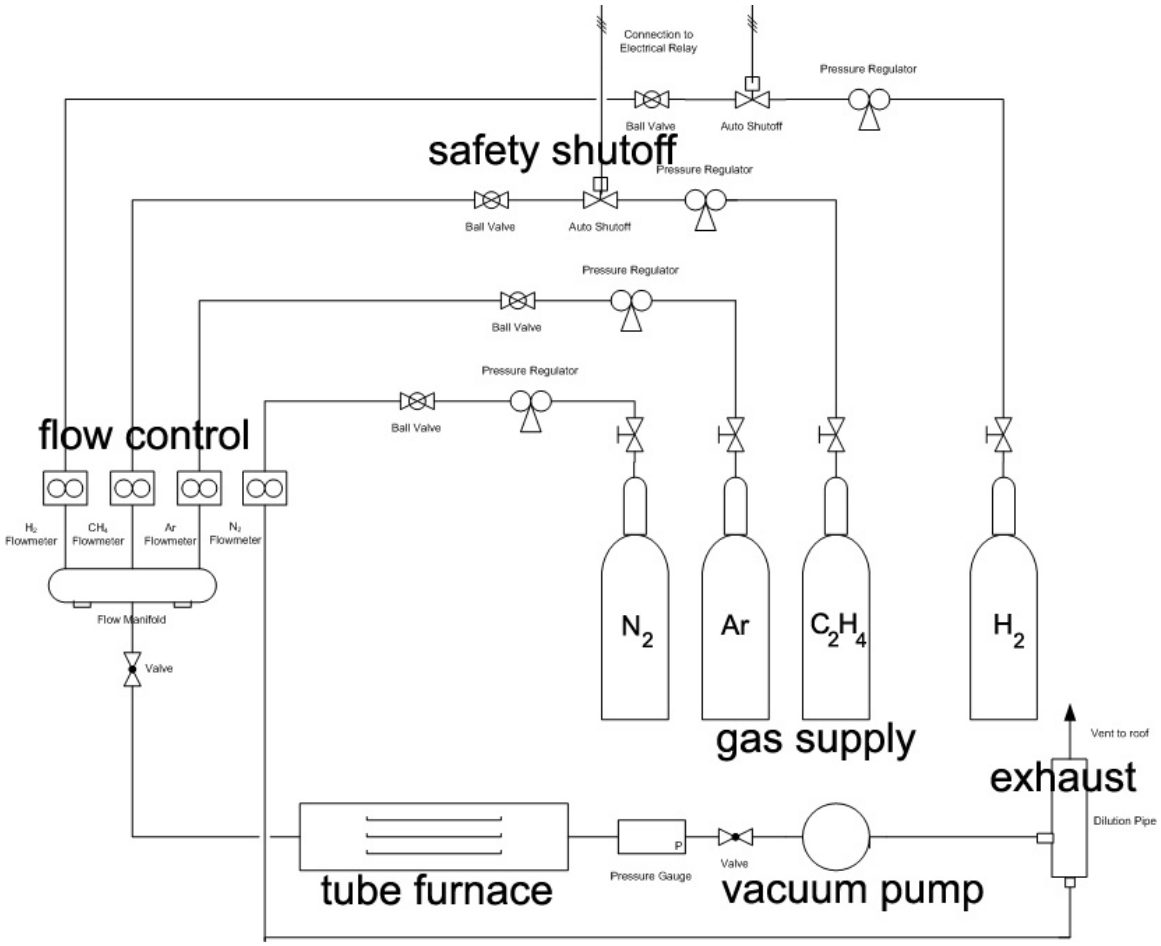

Figure 2.1: Schematic of thermal CVD setup.

set into a quartz sample holder (the "boat") and loaded into the quartz tube from one end, and the system is sealed. Custom fittings from Atomate (Simi Valley, CA) are installed on the ends of the quartz tube to make a conveniently removable leak-proof seal between the Swagelok lines and the growth chamber. The tube furnace (Mini-Mite 1100, Lindberg/BlueM, Asheville, NC) heats the reaction chamber to the run temperature (usually 725 °C) and is automatically temperature controlled to within a couple degrees Celsius. During the growth run, reaction gases are continuously exhausted from the quartz tube reaction chamber first through a Swagelok needle valve used to control chamber pressure, then a downstream mechanical vacuum pump (Leybold, Export, PA), and then into an enlarged elbow used as a mixing chamber (from Atomate) to dilute the 350 Standard Cubic Centimeter (SCCM) flow with sufficient

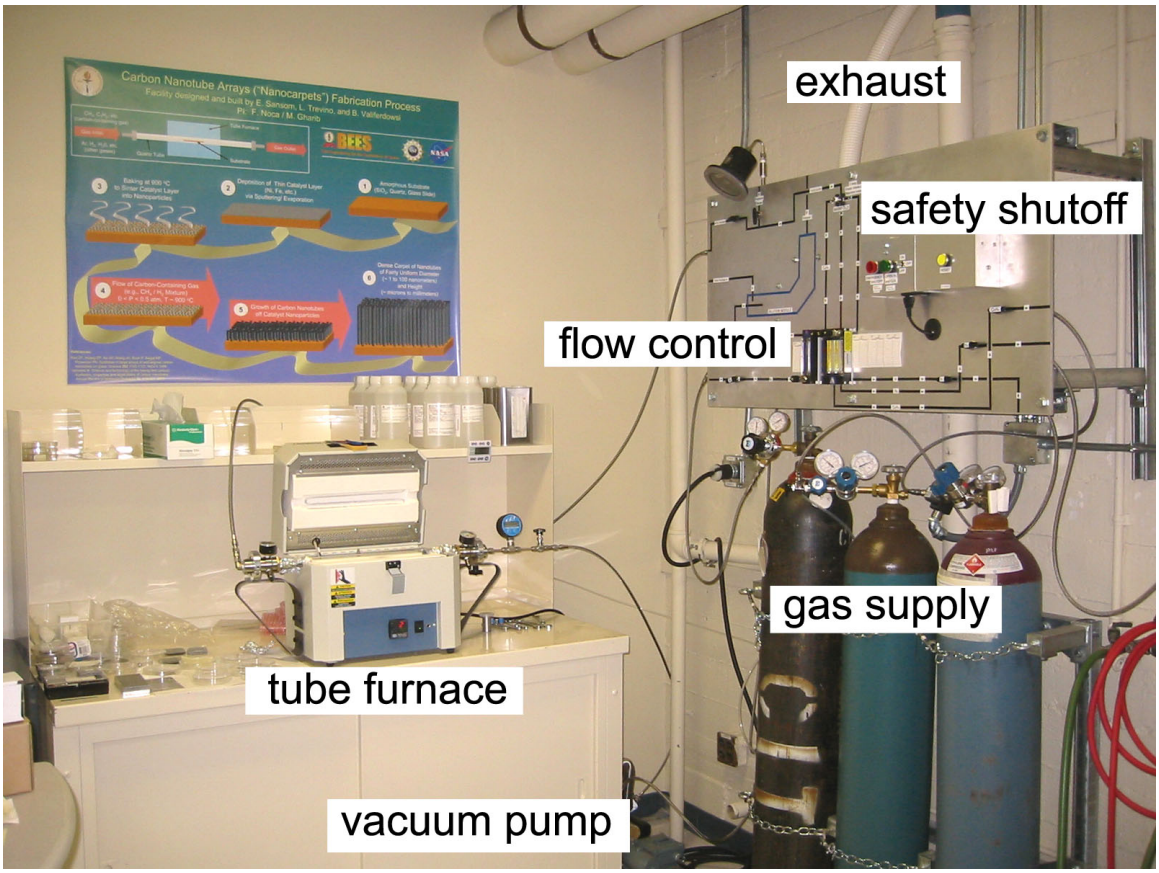

Figure 2.2: Actual picture of thermal CVD setup for CNT growth. Labels correspond to those in the schematic in figure 2.1.

nitrogen (typically 40000 SCCM) to bring the flammable gas concentration below the lower flammability limit, which is about 2.7% for C_2H_4 and 4% for H_2. This renders the flow safe enough for exhaust to atmosphere. Temperature is fixed and well-controlled during a growth run, while volumetric flowrate and total pressure are adjusted manually throughout the run to maintain target values as closely as possible. Total pressure (vacuum) is measured using a digital pressure transducer installed just upstream of the tube furnace and a readout meter (Omega, Stamford, CT). This was installed after the picture in figure 2.2 was taken.

The actual system constructed for the work of this thesis is shown in figure 2.2, with labels corresponding to the schematic in figure 2.1. Additional images and detail drawings related to the setup are given in appendix B.

2.4 Preparation of Substrates Prior to CNT Growth

Silicon wafer substrates in this work were either covered with a 200 nm layer of SiO_2 or only their native oxide layer (a couple nm in thickness). Quartz substrates were 1/16 in. thick, and were cut from a several-inch-square sheet into 1 cm square pieces prior to any other steps. This resulted in the edges of the quartz squares being rough, especially at the microscale. Consequently, nanocarpet edges were never used for experiments. The cutting process possibly also resulted in quartz dust contamination of the samples, which tended to cause problems, but whose extent of effect was only determined in the late stages of this work. In general, CNT growth from silicon wafer substrates was much more uniform, and taller nanocarpets were produced, than for quartz substrates. The greater contamination of the quartz substrates is likely the reason for this quality difference.

As in the paper of Bronikowski [26], sputter-coating of thin layers of iron was used for the catalyst material. Substrates were sputtered with either 2.5, 5, 7, or 20 nm of iron in this work. The best growths tended to be for the 5 nm thick layers. Sputter-coating of all samples was conducted in one large batch of coating runs using an Emitech K575d Peltier cooled high resolution sputter coater. It has a standard rotary vacuum pump backing a turbo-pump, and this is an important feature for sputtering oxidizing metals like iron. This allows the coating chamber to be fully evacuated of ambient air prior to iron deposition, thereby minimizing oxidation of the iron while it is being deposited. Oxidation of the iron catalyst layer can have extreme negative effects on CVD growth of CNTs, yielding very poor to no CNT growth. The quartz thickness monitor installed on the sputter-coater gives accurate readings for film thickness deposited.

Quartz squares and 3 in. silicon wafers were sputter-coated with the four thicknesses of iron. For use in a growth run, the silicon wafers were manually cleaved into small pieces that could fit on the sample holder in the tube furnace. This cleaving process with a diamond scribe did create some silicon dust contamination on the sur-

face of the coated wafers, though this was minimized as much as possible by careful scribing and blowing the dust off with canned compressed air.

All samples were sputter-coated in one set of runs at Keck Graduate Institute in Claremont, CA, courtesy of Drs. Anna Hickerson, Reza Miraghaie, and Jim Sterling. They were then stored in an in-house desiccator in the as-sputtered state until needed for use in a CNT growth run.

2.5 Safety

Because hydrogen and to a lesser extent ethylene (C_2H_4) are highly flammable, the possibility of leaks and overall safety are a concern in CNT growth by thermal CVD. Automatic and manual safety features were installed, including electrically controlled, flammable duty solenoid valves, a combustible gas sensor (Sierra Monitors, Milpitas, CA), a strobe warning light, an emergency shut-off, and an in-house built control box mounted on the panel with the flow control equipment. The gas sensor is mounted in the ceiling just above the gas cylinders, where any gas leakage is likely to accumulate. Wiring diagrams for the electrical system in several states are in appendix B. The system is electrically powered, wired 120 VAC, and designed as normally closed to account for a possible power failure. In order to enable the system for a run, a switch is thrown and a valve open button is pressed. If the gas sensor is tripped, the solenoid valves (just after the cylinder pressure regulators) on the H_2 and C_2H_4 lines will not open. If the control system is tripped and shuts the solenoid valves, the system must be reset prior to the start of another growth run.

2.6 Refinements and Improvements

Invariably, issues were encountered in achieving quality growth of nanocarpets for use in this work. Upon SEM or even optical microscope observation, CNT growth across the substrate surface could be spotty, indicating many growth defects, or have great variation in height. This was traced to either uncleanliness of the growth system and

process or contaminated substrate surfaces. After many CNT growth runs, the quartz tube becomes coated with amorphous carbon. This was removed by carrying out a run with no substrates, and using the maximum temperature of the tube furnace, 1100 °C. This burned off the carbon deposits successfully, and subsequent CNT growth runs were of much higher quality.

Dust particles from either the lab environment or handling of the samples (for example the scribing of silicon substrates) caused poor local CNT growth. Blowing off the dust particles and occasionally also rinsing the sputter-coated substrates in isopropanol and deionized water before CNT growth were used.

To ensure a more uniform temperature distribution within the tube furnace (there is only one thermocouple installed as part of the furnace's control system), the ends were packed with aluminum foil to prevent air being exchanged between the vicinity of the quartz tube and the external room air.

Ambient leaks *into* the CNT growth system were a major issue in the early development stages of the nanocarpet growth system. Because the CNT growth reaction is very sensitive to oxidizers, leakage into the system produced very poor to no CNT growth. A combustible gas sniffer (Atomate, Simi Valley, CA) was used, and the system was run without performing CNT growth, using a slightly pressurized state rather than the vacuum state normally used for CNT growth. The sniffer is very sensitive and small leaks around fittings were found in this way. Another reliable way to check for leaks and compare the system state after a change was made was to pump the system down to its maximum vacuum level (about 1 Torr), close upstream and downstream valves to isolate the system, and then take vacuum measurements over time. Plots could be constructed showing how quickly the vacuum in the system was lost, indicating leakage into the system. Ideally, the vacuum would be maintained indefinitely, but the best state obtained and used for this work was for the system to reach ambient pressure in about one day's time.

2.7 Typical CNT Growth Protocol

In the paper of Bronikowski [26], which uses thermal CVD growth on iron catalyst layers with ethylene as the carbon source gas, it is found that the best parameters for longest (tallest nanocarpets) and highest quality CNT growth of around 100 μm in length are a temperature of 725 °C, iron catalyst layer thickness of 2.5 to 5 nm, total absolute pressure of 200 Torr, and flow velocity at the substrate surface of 2 cm/s. It is also found that the ratio of H_2 to C_2H_4 (within the range of 0 to 1) is not a strong determinant for CNT growth. The final important finding of Bronikowski relevant to this work is that CNT length (nanocarpet height) is maximum for growth times of 5 minutes and constant thereafter.

For the system used in this work, the CNT growth parameters used were a total absolute pressure of 600 Torr, H_2 to C_2H_4 volumetric ratio of 1 to 4, volumetric flowrate of H_2 of 70 SCCM, volumetric flowrate of C_2H_4 of 280 SCCM, temperature of 725 °C, and a growth time of 10 minutes. The flowrates and pressure were selected to give an estimated 2 cm/s flow velocity at the substrate surface. Several iron catalyst thicknesses were used, with 5 nm being the best.

A growth run is conducted as follows. The substrates on the quartz boat are loaded (gloves were worn and samples were only touched with cleaned tweezers) into the quartz tube from one end and the tube is sealed. The system is first purged without turning on the furnace in order to remove ambient air, using alternately 500 SCCM Ar, 280 SCCM C_2H_4 (40000 SCCM of dilution N_2 was also flowed in the downstream portion of the system whenever using flammable gases), 70 SCCM H_2, and once more with Ar, each for 2 min. The system is pumped down to maximum vacuum to verify there are no leaks. 500 SCCM Ar is again flowed, the system is brought to 600 Torr absolute pressure, and the tube furnace is turned on and begins heating to 725 °C. Once growth temperature is reached, the gas flow is immediately switched to coflowing 280 SCCM C_2H_4 and 70 SCCM H_2, again with 40000 SCCM of dilution N_2 being flowed downstream prior to exhaust. Pressure in the tube furnace is maintained as accurately as possible using the needle valve at the exit. After 10 min.

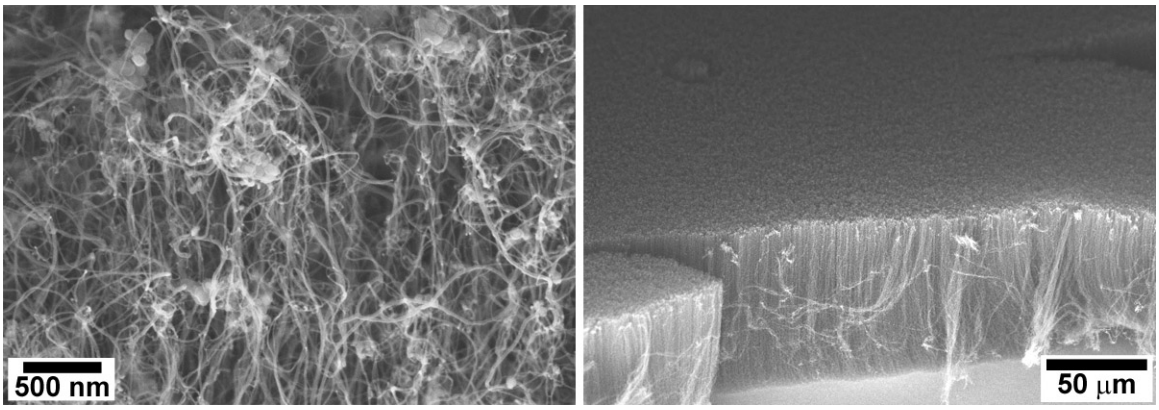

Figure 2.3: An example of a nanocarpet grown on silicon, with two 60° tilted SEM views of the same location. The left is at much higher magnification than the right. Some catalyst particles are visible at this scale.

growth time, the system is allowed to cool to room temperature under 500 SCCM Ar flow.

Occasionally additional components were added to the upstream side of the quartz boat with the growth substrates prior to CNT growth, perhaps improving the growth via mechanisms similar to those used in the iron (II) phthalocyanine pyrolysis methods in the studies described in §1.4. For example, pieces of the iron containing alloy Invar (McMaster-Carr, Santa Fe Springs, CA) were occasionally tried. Highly localized flow effects were likely involved in CNT growth as well, as the furthest downstream sample always had the tallest nanocarpet grown.

2.8 Examples of Nanocarpet Samples Grown

Following nanocarpet growth, samples were inspected visually and under an optical microscope, and carefully characterized in the SEM. A small portion of the nanocarpet was carefully scraped from the growth substrate using tweezers, in a diagonal line near a corner of the sample. This was done in order to allow a local cross-sectional view of the nanocarpet and measure its height accurately, as well as to produce some of the SEM views of experiments shown in this work. Figure 2.3 and figure 2.4 are examples of nanocarpet sample SEM characterization.

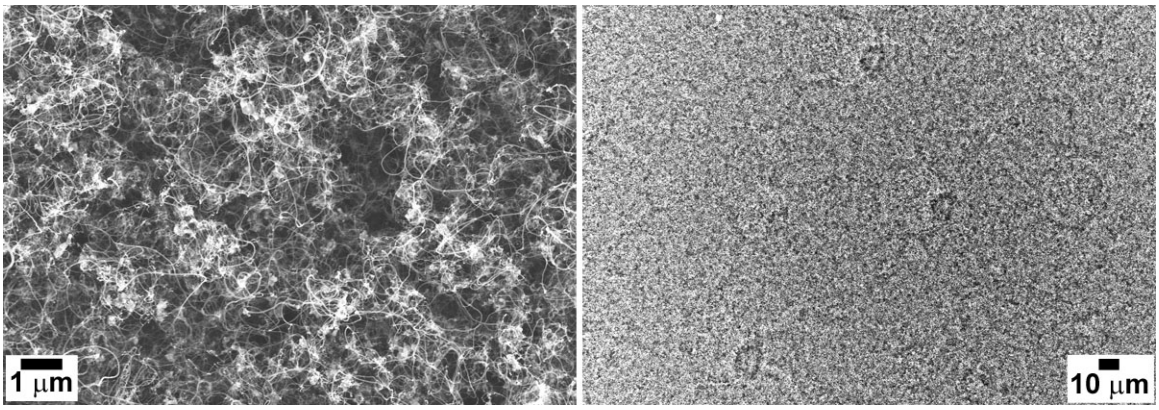

Figure 2.4: An example of a nanocarpet grown on silicon, with two top-view SEM images of the same location. The left is at higher magnification than the right.

Chapter 3

Materials and Methods

3.1 Introduction

This chapter describes the materials and methods used in this thesis in addition to the CNT growth covered in chapter 2. Basic material properties are listed and handling protocols are described. Microscopy and details about conducting liquid treatment experiments are given.

3.2 Materials

Surfactants [5] are molecules comprised of hydrophobic parts and hydrophilic parts. Consequently, they tend to aggregate into monolayers at interfaces such as the water-air interface of a solution. Common soaps and detergents are made of surfactants. A surfactant always tends to lower the surface tension of a liquid, in proportion to how many of the surfactant molecules there are attached to the surface. The most important characteristic for surfactants in solution is their critical micellar concentration (cmc), above which any increase in surfactant concentration merely results in the additional molecules ending up in micelles, which are structures within the solution made of the surfactant molecules. For a surfactant solution with concentration below the cmc, addition of surfactant results in the molecules attaching to the surface. Because surfactants are molecules in solution, diffusion and local concentration effects can significantly affect the fluid mechanics of the situation [42], especially at

the small length scales of interest in this thesis. It is primarily for this reason that a pure liquid, polydimethylsiloxane (PDMS), was preferred in the later experiments conducted for this thesis.

Sodium dodecyl sulfate (SDS) (Sigma-Aldrich, St. Louis, MO) is an anionic surfactant, common in interfacial fluid mechanics studies, and has a cmc of 8.5 mm (0.25 wt%) [43], with a molecular weight of 288.4 g/mol. The typical concentration of SDS used in this thesis is 0.5 cmc (0.123 wt%). According to Mysels' [43] empirical study, a freshly made, very pure solution of 0.5 cmc SDS has a surface tension of 52 mN/m (dyne/cm). This is only immediately after SDS is added to the pure water, however, at which point the surface immediately begins to "age," meaning that SDS molecules continue to diffuse to the surface from the bulk, thereby lowering the surface tension further. The empirical relationship Mysels determined for freshly made, pure SDS solutions (maximum surface tension at a given concentration) is

$$\gamma = 68.49 - 6.516ln(c) - 3.353ln^2(c), \tag{3.1}$$

where γ is surface tension and c is the SDS concentration. According to this relationship, a 0.75 cmc SDS solution has $\gamma = 44.9$ mN/m, and a 1.0 cmc SDS solution has $\gamma = 39.2$ mN/m. It is estimated that most solutions used in this work have surface tensions of perhaps 10 mN/m less than the pure, fresh value. An empirically measured plot of surface tension vs. time [4] for SDS shows that the surface tension levels off at its asymptotic value after one to two hours. For the 4.25 mm concentration most often used in this thesis, this means the surface tension should be about 26 or 27 mN/m, which is not much higher than that of PDMS oil described below.

Triton X-100 (Sigma-Aldrich, St. Louis, MO) is a nonionic surfactant, commonly used in biochemistry and molecular biology, and has a cmc of 0.15 wt% (0.24 mM) [44], with molecular weight of 625 g/mol. Typically 0.1 wt% (0.67c̆mc) is used for lysing biological cells, and this is a commonly used concentration in results in this thesis. Triton X-100 is referred to throughout simply as Triton-X, as no other types are used. It is referred to in the literature more commonly by weight percent than cmc

and that is done here also. Surfaces of stagnant solutions of Triton-X are expected to age, meaning the surface tension will decrease with time eventually reaching an asymptotic value, as explained for SDS.

PDMS (Dow Corning, Midland, MI) is a common polymer, with the chemical formula $(CH_3)_3$-Si-O-$[(CH_3)_2SiO]_n$-Si$(CH_3)_3$ where n indicates the number of monomer units. The siloxane (Si-O group) skeleton and the decoration everywhere with methyl groups causes PDMS to be nonpolar, hydrophobic, very thermally stable, and optically transparent. Chains are highly flexible and thus at room temperature PDMS is a fluid, and is called PDMS oil in this thesis in order to clearly distinguish it from cross-linked PDMS, which is an elastomeric form and is used in the anchoring portion of this work. PDMS oil is optically clear, nonflammable, and generally inert. As an oil, PDMS is often employed for its lubricating properties, and thus it is usually denoted by its viscosity, which is also done here. The variant of PDMS used here has kinematic viscosity of 1 cSt (1 mm^2/s), equal to that of water. Its surface tension is stated by the manufacturer to be 17.4 mN/m, much lower than water, and to have an evaporation rate similar to that of water. However, because PDMS oil is nonpolar, hydrophobic, and has very low surface tension, it spreads easily on nanocarpets, creating greater area for evaporation to occur. In experiments in this thesis, PDMS oil evaporated significantly faster than aqueous solutions. Much higher viscosity PDMS oils exist but they are nonvolatile and would only coat nanocarpets completely and permanently and thus are not used.

Cross-linked PDMS (RTV615, GE Silicones, Wilton, CT) is created in a platinum-catalyzed cross-linking reaction that is initiated by the mixing of the two manufacturer-supplied components. When mixed, the dynamic viscosity of the mixture is stated by the manufacturer to be 4000 cps (4 Ns/m^2). The rate of cross-linking is increased significantly by increasing the temperature, and in this work, cross-linked PDMS materials were baked for an hour or more at 80 °C to ensure complete cross-linking following mixing of the two components. Cross-linked PDMS is very commonly used in microfluidic devices [45, 46] because it is optically transparent, can be precisely microfabricated, has minimal chemical reactivity, and has useful mechanical proper-

ties.

Polymethylmethacrylate (PMMA) is a very common thermoplastic polymeric material used for applications as diverse as canopy covers in WWII bombers to intraocular lenses implanted directly within the cornea of the eye for permanent vision correction, as it is generally considered to be highly biocompatible. It is alternately known by the trade names Lucite, Plexiglas, and Perspex, and simply as acrylic. It is also used as a high-resolution photoresist in lithography applications. In this thesis, PMMA is used as a material for anchoring nanocarpets, both in chapter 5 in developing the method of anchoring and in chapter 6 in attempting to form patterns in nanocarpets anchored in PMMA.

PMMA has a glass transition temperature at around 100 °C and begins to depolymerize at around 150 °C. It transmits more light than glass, including UV light, and it is highly impact resistant and consequently used for hockey rinks, aquariums, and protective shielding. It is also used as a high-resolution photoresist in lithography applications, and this is the most relevant application for its use in this thesis.

3.3 Scanning Electron Microscopy

Scanning electron microscopy (SEM) is crucial to conducting experiments at the nanoscale. A high quality field-emission SEM (LEO 1550 VP, Carl Zeiss, Oberkochen, Germany) was used for this work. It has many capabilities, but was used solely in the basic "in-lens secondary electron" mode under high vacuum conditions. The capability of low accelerating voltage imaging 200 V to 5 kV was utilized in this work for imaging quartz substrates and the anchoring materials (cross-linked PDMS and PMMA) because they are insulating and cause charging in the SEM. CNTs, on the other hand, are conducting and are easily imaged with the SEM. By selecting accelerating voltages carefully and imaging areas with CNTs, the imaging of CNTs on insulating substrates was possible without resorting to coating samples with a thin layer of metal as is occasionally done for SEM imaging of insulating samples.

Many different magnifications are available in the SEM for characterizing nanocar-

pet samples, from 200 X to 500 kX, and this range was important to this work in order to characterize individual CNTs as well as entire areas of nanocarpets. To facilitate the comparison between samples and experimental conditions, certain primary magnifications (20 kX, 5 kX, 1 kX, 500 X, 200 X) were adopted as standards. When a location was selected for imaging, a series of images were captured at each of the magnifications. This was enabled by the high speed of imaging possible when a moderate scan rate was used.

The basic principle of imaging using the SEM when operated in the mode used for this thesis is that an electron beam is directed at the sample, a detector collects the secondary electrons emitted from the sample, and an image is constructed by quickly raster scanning the focused electron beam across the surface.

A very useful feature of the LEO SEM was the ability to tilt samples to a specified angle, as illustrated in figure 3.1. The two nonzero angles used in this work were 60° and 45°. This allows cross-section imaging and topology to be seen clearly. However, it also introduces working distance limitations such that only sample regions nearest the SEM objective lens could be imaged clearly. Additionally, a length correction factor of $1/\sin(\theta)$, where θ is the SEM tilt angle, must be multiplied by measured lengths within the frame in the "vertical" (implying top to bottom in the image frame) direction in order to obtain the true length. This was especially important for measuring nanocarpet heights.

3.4 Optical Microscopy

Optical microscopy was invaluable in this work, yet was primarily used only for characterizing and handling nanocarpet samples. Patterns in nanocarpets *can* be observed under the optical microscope, as they are of tens to hundreds of microns in size and appear in good contrast against the black, optically absorptive pattern ridges and unpatterned areas. Epi-illumination mode was used, as nanocarpets are completely opaque to visible light. Optical microscopy would be the method of choice for obtaining dynamic information about the nanocarpet pattern formation process, but

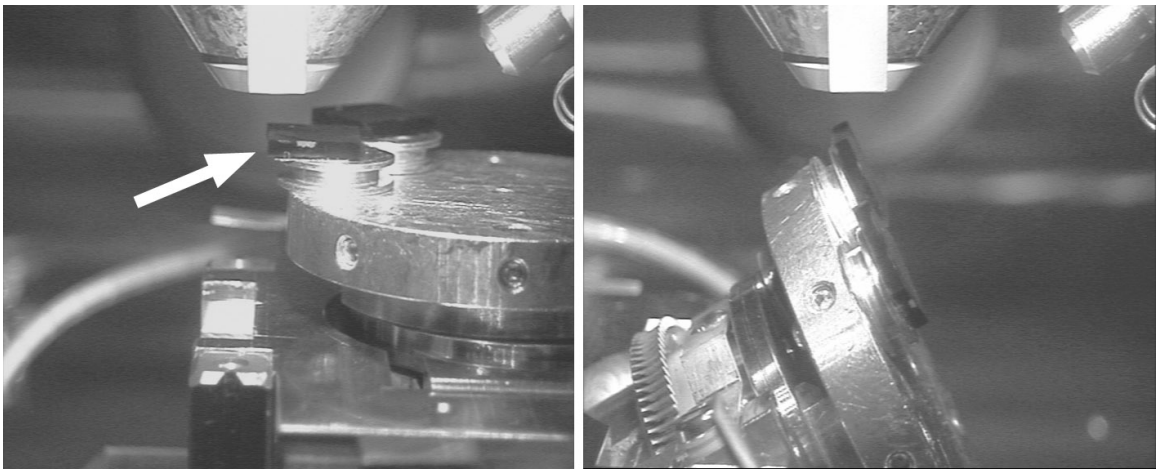

Figure 3.1: Images of two samples loaded in the SEM chamber. The left is at 0° tilt angle, the right is at 60° tilt angle. A nanocarpet grown on a quartz square (1 cm on a side) is indicated by the arrow and is mounted on carbon tape attached to aluminum mounting stubs.

requires foreknowledge of where to look at high enough magnification.

When a pattern forms in a nanocarpet, the CNTs are pulled apart from the center of the pattern elements, typically either leaving the substrate completely bare in the central region, or thinning the CNT density in the central region sufficiently for light to pass through the CNTs and reflect. To illustrate this, figure 3.2 shows an SEM image and an optical microscope image side by side. Reflected light creates bright dots corresponding to the center of pattern elements.

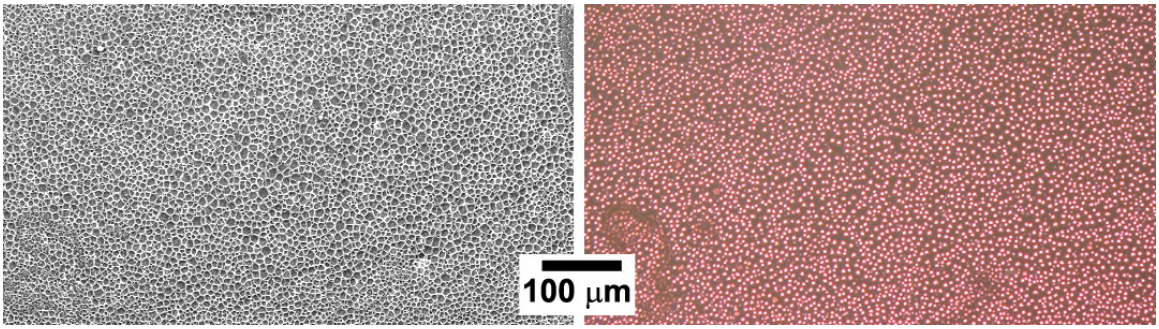

Figure 3.2: Same scale, same location comparison of SEM image (left) and optical microscope image (right) of the same nanocarpet pattern.

3.5 Drop Placement and Nanocarpet Immersion

The placement of drops in this work was carefully done using either a syringe (Hamilton, Reno, NV) or a pipette (Eppendorf, Germany). The nanocarpet sample was resting in a petri dish on a microscope stage. Impacting nanocarpets with the syringe or pipette tip was avoided as much as possible, but occasionally did occur. Additionally, the placement of drops of less wetting solutions, such as the SDS and Triton-X solutions, was sometimes done with a syringe that had a Teflon coated tip, such that the release of the drop onto the hydrophobic nanocarpet could be encouraged somewhat.

Immersion of nanocarpets was done by gripping the sides of the growth substrates carefully with flat-tipped tweezers (SPI Supplies, West Chester, PA) and quickly and completely immersing the nanocarpet including its growth substrate into the liquid. The nanocarpet was then immediately removed and set to dry. This process was much easier with the quartz substrates because they were 1/16 in. thick while the cleaved silicon wafer substrates were much thinner and tended to have nonflat edges due to the cleaving process.

3.6 Sample Organization and Tracking

In order to keep track of the large number of samples and images generated in this work, especially during development and use of the CNT growth, an in-house website was utilized. Free software was used (JAlbum) to automatically generate the website from large directories of images.

All samples were carefully labeled physically as well as within filenames, adhering to naming standards. Thousands of images were generated, mostly from SEM characterization of samples at various stages of the experiments, and from the approximately 45 growth runs completed.

Chapter 4

Pattern Formation in As-Grown Nanocarpets

4.1 Introduction

In this chapter, results are presented on pattern formation in nanocarpets that were not anchored within another material. Prior to the patterning experiments conducted, these nanocarpets were "as-grown," meaning they remained in the state they were in at the completion of the CNT growth process described in chapter 2. These results form the basis for the study of liquid-induced pattern formation in nanocarpets.

Additionally, analysis is presented of nanocarpet patterns generated in this work as well as several found in the literature. The published images were analyzed in exactly the same way as the samples from this work that were imaged in the SEM. This analysis is not intended to be exhaustive, but rather a first-order approach to characterizing the patterns and allowing their comparison.

The results of this chapter, and particularly the further defining of what is of interest in nanocarpet pattern formation, address problem statement 1 in §1.5, which was **"What is the mechanism for pattern formation in nanocarpets by a drying fluid?"** and also problem statement 2, which was **"What types of patterns are possible?"**

Figure 4.1 is an example of liquid-induced pattern formation in nanocarpets, and the sample is shown after the pattern formation process is complete. This particular

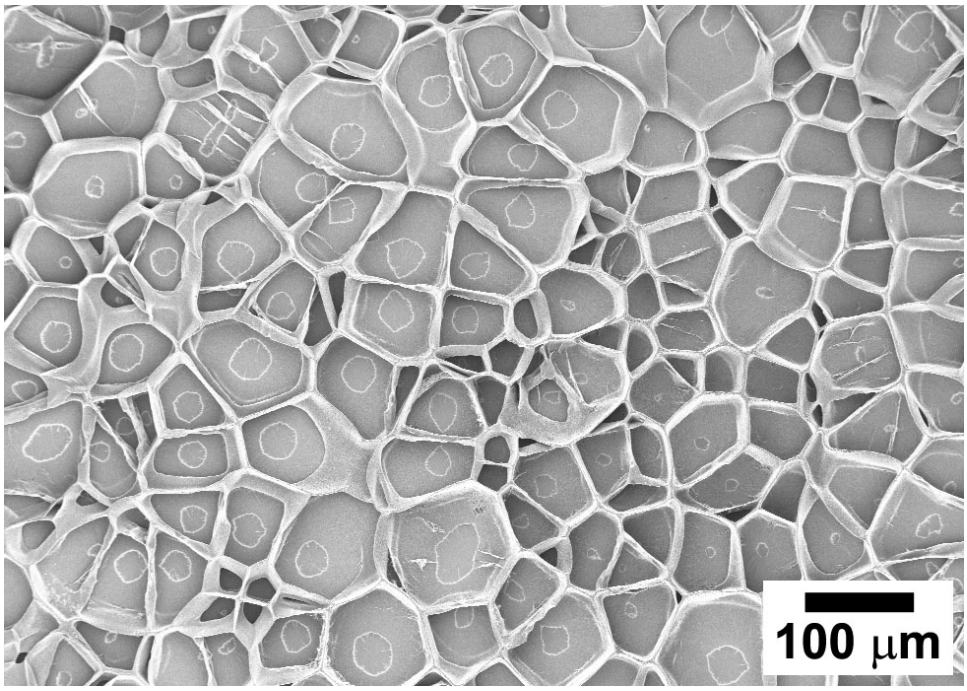

Figure 4.1: Example of liquid-induced "cellular" pattern formation in a nanocarpet, caused by 0.5 cmc SDS wetting of a 60 μm tall nanocarpet on quartz.

nanocarpet sample was 60 μm in height, on a quartz substrate, and was treated with 2 μL of 0.5 cmc SDS solution. The image was taken in the SEM under high vacuum and consequently was free of any liquid components. The pattern is fixed in this state indefinitely, as with all patterned nanocarpets once they are fully dried. The sample is imaged from directly above, and because of the way the electron beam imaging in the SEM works, brightness corresponds to higher elevation, i.e., closer to the viewer (detector). Thus the bright areas in line patterns are "ridges," while the darker central areas are "valleys" or "craters." The small, white-outlined central regions that look somewhat like biological cell nuclei are areas of bare substrate now exposed because the densely packed CNTs were pulled radially outward during the drying process. The pattern is like that of polygonal bowls touching at their edges. Figure 4.2 is an SEM image of the same sample and at the same scale, but at a 45° tilt and a slightly different location. The tilted view better illustrates the sample's topology.

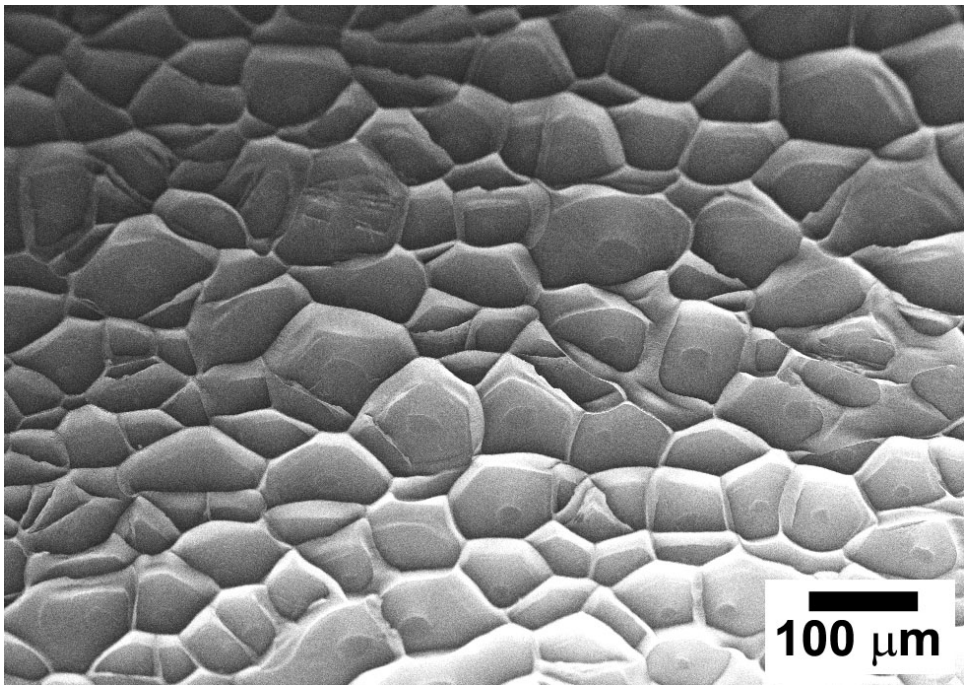

Figure 4.2: A 45° tilted view of the sample in figure 4.1, at same scale but a slightly different location.

This type of pattern is most often referred to as "cellular" in the literature, and it refers to the distinct, bounded elements that make up the pattern, which are themselves termed "cells." This is equivalent to the term "pattern element" used in this thesis. In the sense that cells are not necessarily polygonal or circular, but can even be quite elongated trenchlike structures, all nanocarpet patterns considered in this thesis could be called cellular. Figure 4.3 is another example of a pattern in a nanocarpet that would also be considered as cellular, and clearly the dominant pattern scale is much smaller than in figure 4.1.

4.2 Preliminary Observations

During the initial stage of this research, various factors that may have caused the pattern formation needed to be considered. The result shown in figure 4.4 was observed after the fact and without complete knowledge of the exact experimental details. Nanocarpet samples had been dipped in biological spore solutions as part of a paral-

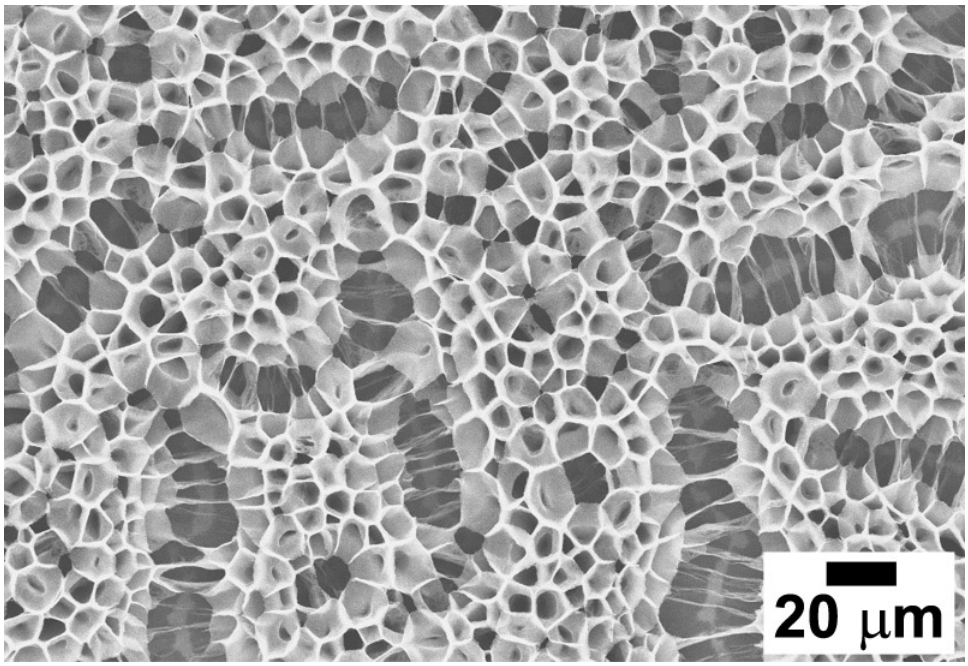

Figure 4.3: Example of a cellular pattern at a small scale, caused by acetone wetting of a nanocarpet grown on SiO_2.

lel project, and upon drying and observation in the SEM, the patterns were observed. Following this result, the ability to reproduce this pattern formation effect was sought in a series of experiments.

The initial patterns had resulted *in some cases* under the following conditions:

- DI water-spore solution
- Treatment by either sample dipping or drop application
- Drying in a dish overnight sitting in a fume hood
- Nanocarpets of ≈5 μm in height on silicon substrates

and the following were candidates for the cause:

- Hydrophobic effect
- Presence of spores
- Interfacial fluid dynamic forces

The hydrophobic effect refers to self-assembly of hydrophobic objects in an aqueous environment, thereby achieving a minimal energy state. It seemed possible that

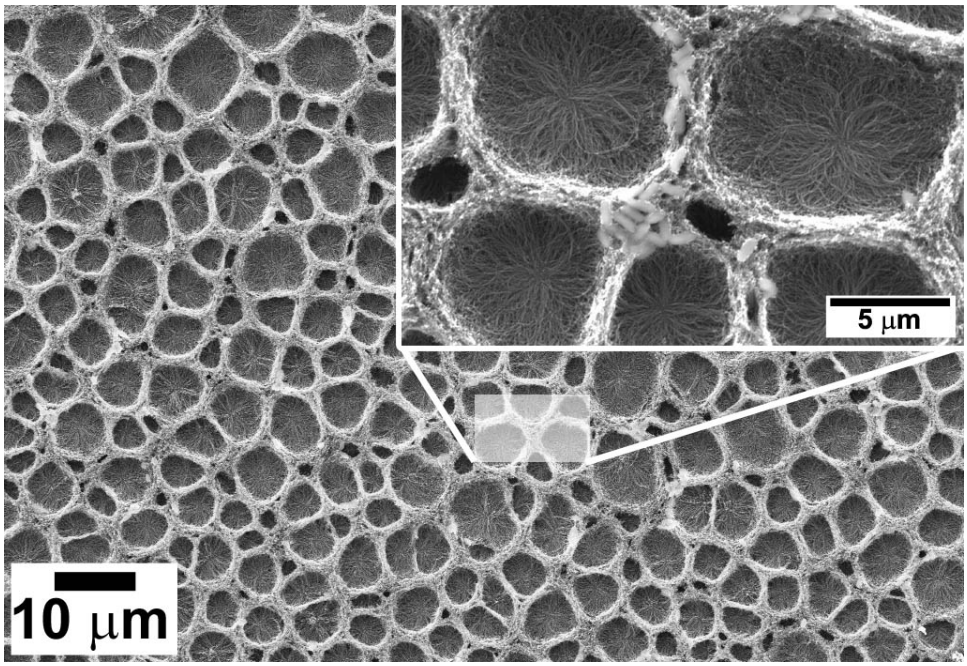

Figure 4.4: Pattern in nanocarpet formed by sample dipping and drying in a DI water and *Bacillus pumilus* spore solution. The magnified inset view is typical but is not from the location shown. The intent is to illustrate the scale.

the CNTs, known to be "hydrophobic" (though this statement has undergone significant clarification in the literature), when placed in the DI water and spore solution, could have self-assembled due to this effect. The roughly 1 μm *Bacillus pumilus* spores could have interacted in some particular way with the water-nanocarpet system, causing their rearrangement into patterns. Finally, interfacial fluid dynamics, particularly the strong effect of surface tension at these length scales, could have caused the patterns.

Follow-up experiments were conducted with other nanocarpet samples using a Hamilton syringe and drop-placement as described in §3.5. Initially, it was observed that small drops of pure DI water would not wet the nanocarpets at all, drying up atop the samples with no apparent patterning effect visible in an optical microscope. Other experiments have since shown that there is very minimal rearrangement at the top of small portions of the nanocarpet due to a drying water drop alone. Additionally, it has been reported [47] that pure water can "seep" into CNT "forests" of 10–15 μm

in height. In arguing for the necessity of polytetrafluoroethylene (PTFE) coating of the CNTs, the authors state "However, the droplets are not stable and eventually seep into the forest voids after a few minutes." In another study it was stated that "water permeates slowly into the film" [15] with the word "film" here referring to a nanocarpet of about 20 μm in height. This issue of water slowly seeping into relatively short nanocarpets helps to explain how the pattern in figure 4.4 could result from only a water and spore solution. By using the surfactant SDS in water in the follow-up experiments, it was possible to get a drop to wet an as-grown nanocarpet. Using only an optical microscope, pattern formation was eventually observed with a 0.5cmc SDS solution. By dynamically observing the pattern formation process in this way, it was clear that the patterns formed only during the final drying stage of the solution *and* that no particles were required. This result confirmed that interfacial fluid dynamic forces were the cause of the patterns.

4.3 Defining the Pattern Formation Process of Interest

Simply put, the pattern formation process that is most *reproducible*, and therefore appropriate for study, is desired. The results in this work very often served to show which processes would not be reproducible. For example, uncontrolled defects that would never be the same from sample to sample affected pattern formation strongly. Results from this work have thus been used to focus the interest in order to make the subject as tractable as possible. Given the complexity of a three-phase (air, liquid, solid) system containing nanostructures, possible defects, and experimental error, it is crucial to continually define exactly what is being studied and whether it is desired or not. The results presented in this section are used for this purpose.

4.3.1 What Part is *Not* of Interest?

It is perhaps easier to refine the definition of the pattern formation process of interest in this thesis by illustrating several examples of processes that are *not* of interest. Figures 4.5 and 4.6 show the effect of defects in nanocarpet pattern formation. These particular types of defects are termed "bald spot" defects and this means that no CNTs grew in that location, usually due to some contamination prior to the thermal CVD growth process. For example deposited dust or fibers due to not working in a cleanroom environment, or also particles from scratching or handling samples (though cleanliness was a high priority), can lead to reduced or non-existent CNT growth in the vicinity of the contaminant. These voids in the nanocarpet are then opened up and effectively amplified into (often large) pattern elements by the effect of surface tension during the wetting and drying process. In the experiment conducted with the sample in figure 4.5, the substrate with the as-grown nanocarpet on top was inverted and carefully touched to the surface of a 0.75 cmc SDS solution. The intention was to try to attain uniform and instantaneous wetting across the entire sample surface. In the right portion of figure 4.5, note the "fuzzy" appearance of the CNTs along the inner boundaries of the large features indicated by arrows. This indicates that these CNTs were never wetted as they have not been drawn together by the action of surface tension. This implies that the entire height of the nanocarpet was not filled with liquid, another issue of complication in nanocarpet pattern formation that is undesirable.

In patterned nanocarpets with obvious defect-based features like this, examination under the SEM at high magnification showed such features in all samples contained some sort of microparticle, fiber, or amorphous deposit that had affected the nanocarpet growth itself prior to the pattern formation experiment. The patterned nanocarpet sample shown in figure 4.7 is an extreme example of such contamination. Rinsing of growth substrates prior to CNT growth was attempted to eliminate particle contamination, and an example of this is shown in figure 4.8. Particle contamination is still obvious. It was generally not possible to conduct high magnification SEM char-

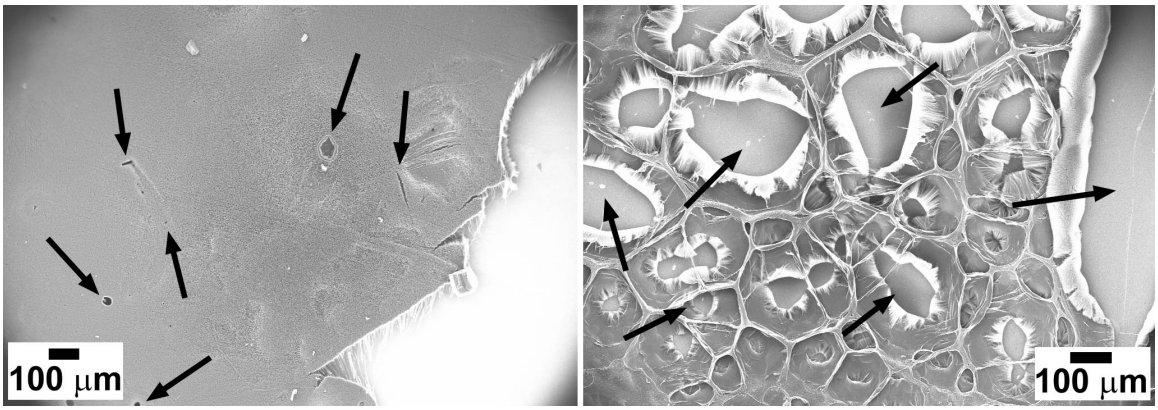

Figure 4.5: Example of large pattern elements caused by "bald spot" growth defects. The left image is before the patterning experiment, and the right image is following application of 0.75 cmc SDS solution by touching the nanocarpet into the liquid surface. Note that scales are similar but not identical, and the imaged location is not identical. Arrows in the left image indicate small voids in the nanocarpet. Arrows in the right image indicate large features that were due to preexisting defects.

acterization in specific locations both before and after experiments. Still, based on pattern morphologies, if the presence of defects were suspected to have dominated the pattern formation, results were disregarded as not reproducible and not of interest.

In addition to defects present following the nanocarpet growth process, and which then affect the pattern formation process, sample handling can damage nanocarpet samples. If a pair of tweezers accidentally brushes some of the nanocarpet surface, the delicate arrangement of the CNTs is significantly altered, with whole sections being pressed down and possibly scraped away. The sample in figure 4.9 illustrates this issue. The two features on the left in the pretreatment image, whether due to growth defects or light scratching during handling, clearly impact the pattern formation significantly and in an irreproducible manner.

In very short nanocarpets of less than 10 μm or so in height, CNTs can form bundles during liquid application and drying instead of the closed shape pattern elements that are desired for study here. This possibility is shown in figure 4.10. This nanocarpet was purchased from NanoLab (Newton, MA). CNT bundling seems to also be related to the CNT packing density, since nest-type pattern elements can also be

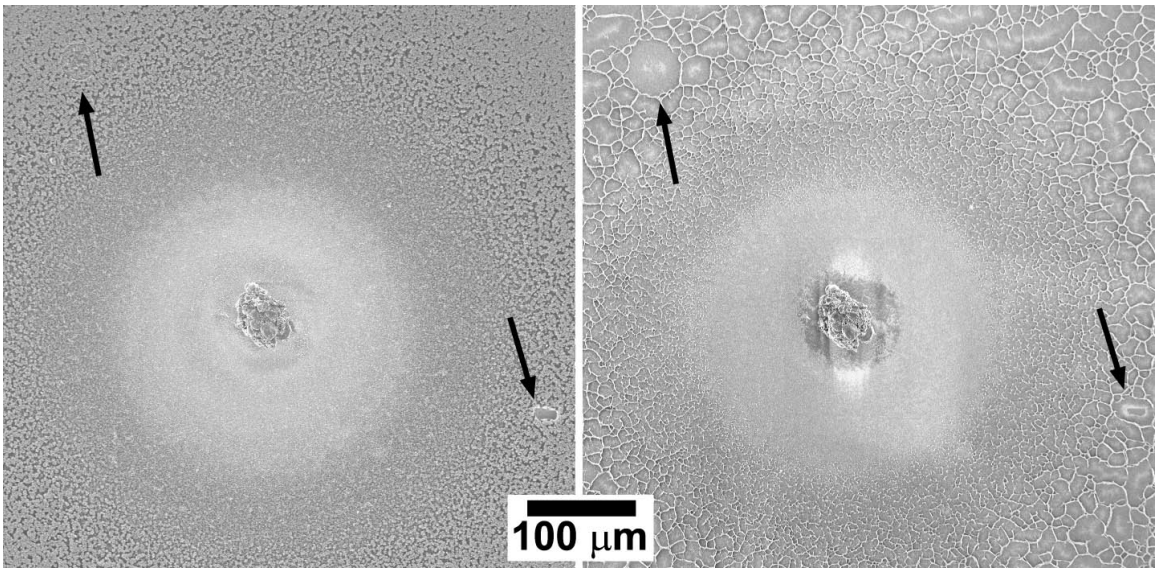

Figure 4.6: Another example of pattern elements caused by growth defects. The left image is before the patterning experiment, and the right image is following application of large drop of 0.5 cmc SDS solution. Both images are at the same scale and location. The large 50 μm contaminant particle in the center affected CNT growth within a large radius. Arrows indicate two prominent growth defects that clearly lead to pattern elements, as do all others in the sample.

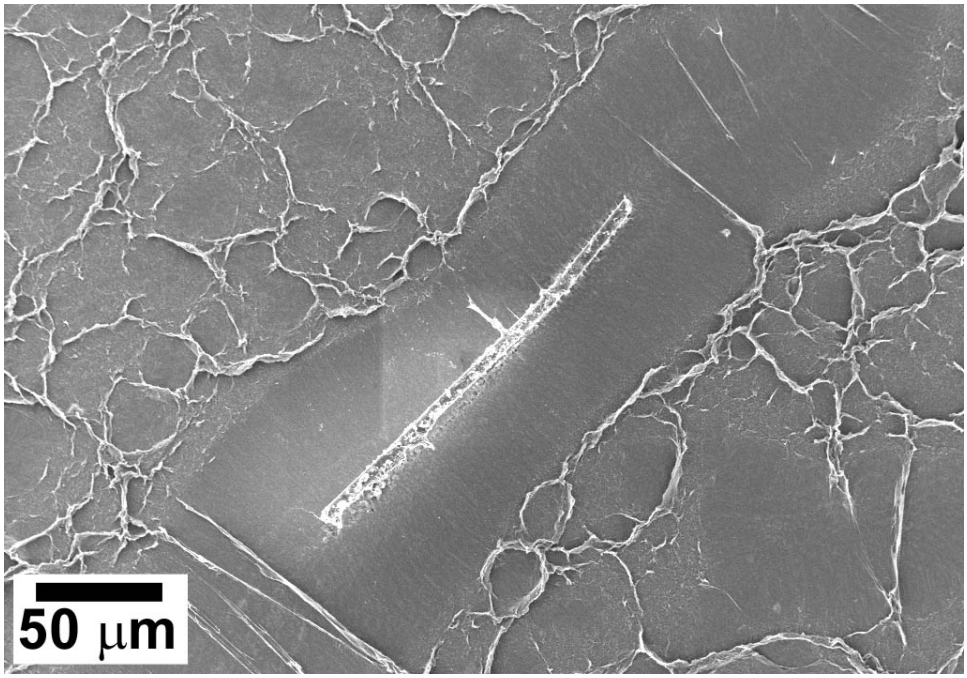

Figure 4.7: Example of a microfiber contaminant that was present prior to CNT growth and caused a line void that was amplified during wetting and drying.

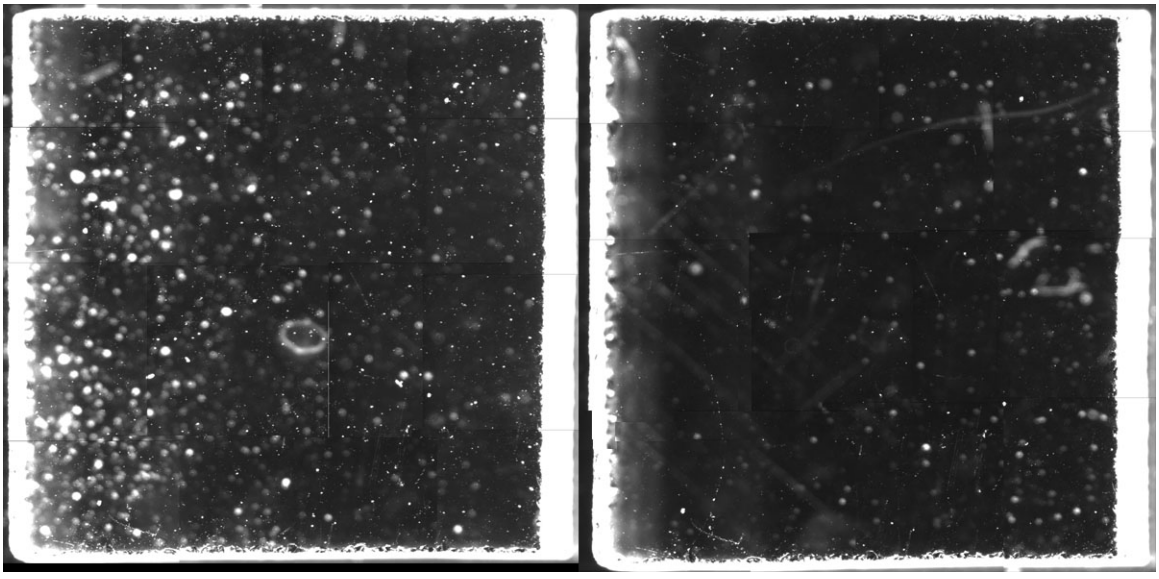

Figure 4.8: Optical microscope images showing the effect of rinsing growth substrates in isopropanol and water prior to CNT growth (but following iron sputtering). This was attempted to reduce particle contamination. Left is before, right is following rinsing. Particle contamination is still plainly visible. The iron sputtered quartz square is 1 cm on a side.

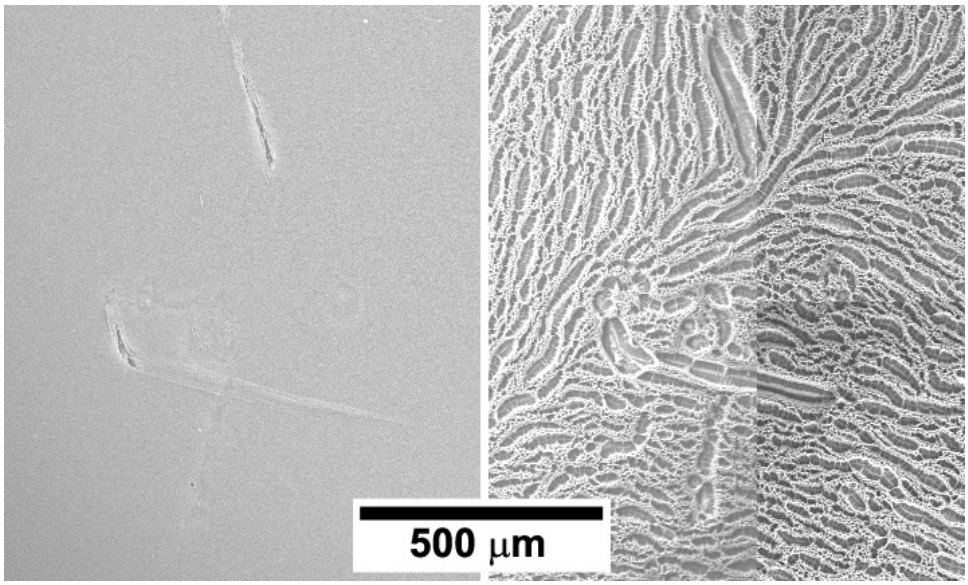

Figure 4.9: Same location, same scale, before (left) and after (right) comparison of a region of a nanocarpet on SiO_2 treated with acetone. The light scrapes due to handling that are visible on the left cause specific defects within the main pattern.

obtained in quite short nanocarpets (4 μm), for example that shown in figure 4.4. Bundling in short nanocarpets has also been reported by at least two other groups [47, 19]. Due mostly to the relatively easier growth of taller nanocarpets, the bundling effect is not of prime interest in this work. However, similar physical processes to those in closed-shape pattern element formation are expected to be involved.

It has been observed in various experiments that highly directional patterns are obtained in nanocarpets due to liquid flow effects. This means there is a moving contact line (a spreading front) within the nanocarpet. This effect is illustrated in figure 4.11, where acetone was applied to a nanocarpet on an SiO_2 substrate. The acetone was observed to flow more quickly around the edges of the nanocarpet (due to the presence of corners and the absence of CNTs) than through the main area, and the spreading flows met each other on the side opposite of where the aliquot of acetone was placed. Thus there is top-to-bottom symmetry to the pattern, in addition to the striations visible from the liquid flow. The nanocarpet regions between the large trench structures, i.e., the ridges, were patterned into very small scale structures

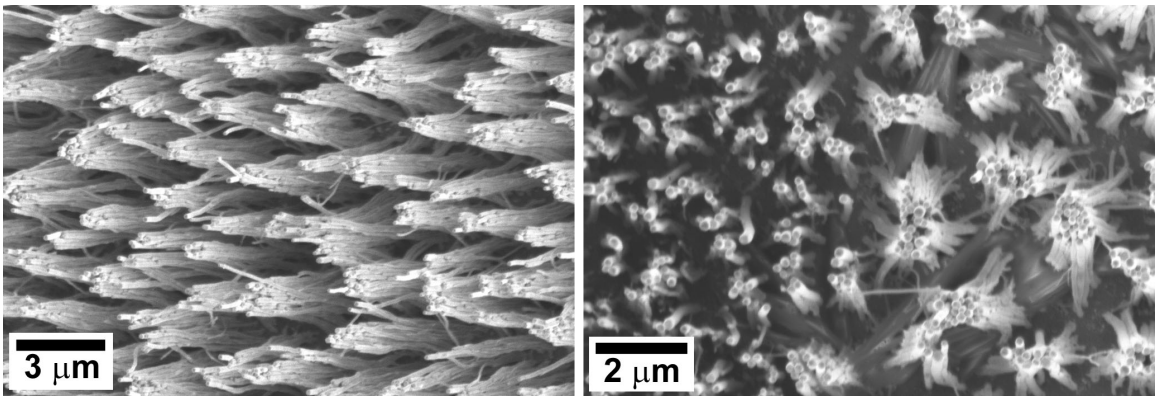

Figure 4.10: Two SEM images of a relatively short (7 μm in height), sparse nanocarpet in which CNTs have formed bundles rather than closed pattern elements. The left image is from a region that was wetted, and the right is at the boundary between the wetted (right) region and the dry (left) region. The liquid treatment was 0.1 wt% Triton-X.

that are not visible at this magnification. Although they may give reproducible pattern formation, spreading liquid fronts add further complexity to the problem, and therefore are considered to be not of interest. Directionality in patterns is taken as a marker for flow effects and thus directional patterns are also not of interest herein.

As further proof that highly directional patterns are due to spreading fronts, figure 4.12 shows the result of an experiment where 1 cSt PDMS oil was placed on a 60 μm nanocarpet grown on quartz. The 2 μL of liquid was placed in two small quantities in quick succession. The circular regions where the drops were placed are distinguished by nondirectional nests and have clear boundaries. Where the PDMS oil spread outward and then evaporated, the pattern looks similar to that of figure 4.11. Thus whether the local wetting condition of a nanocarpet is more like a sessile drop or a spreading front appears to affect the resulting pattern greatly. The region under the sessile drop where the pattern is nondirectional is the type of pattern formation of interest herein, while the spreading region is not.

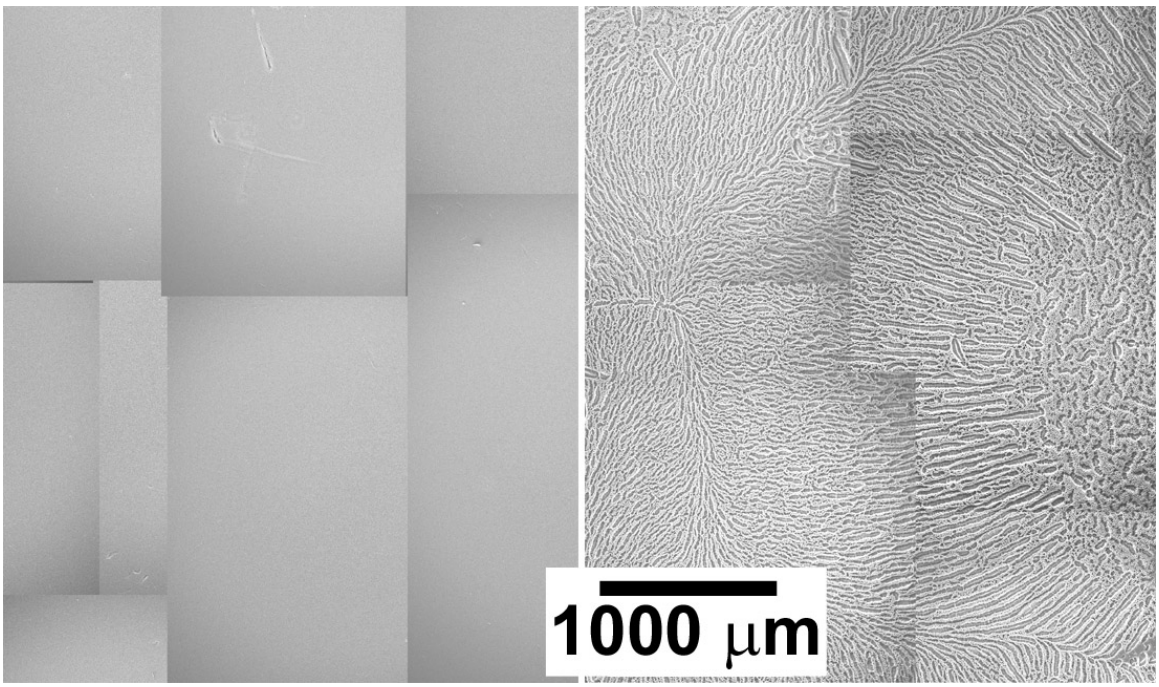

Figure 4.11: Before (left) and after (right) comparison of a nanocarpet on SiO_2 treated with acetone, shown at the same scale and location. Note the significant directionality in the pattern due to flow effects, i.e., a liquid front spreading (and retreating upon drying) within the nanocarpet. The acetone was placed just outside the visible area on the right.

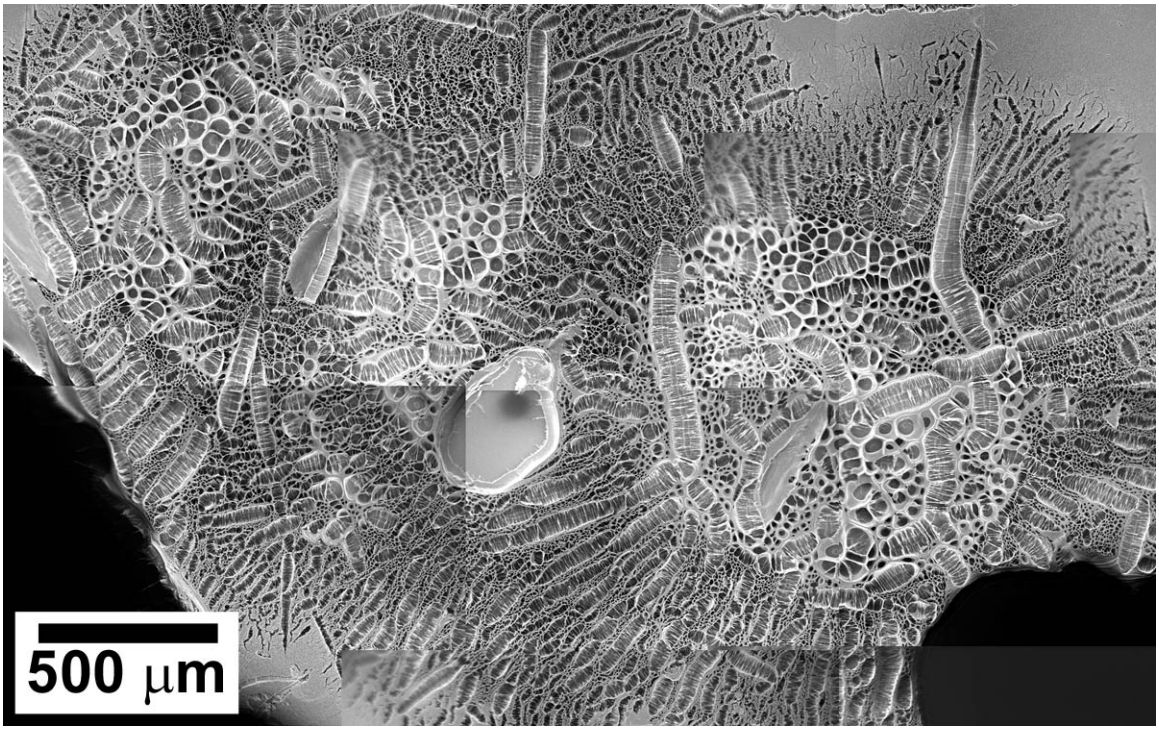

Figure 4.12: SEM composite image of a 60 μm tall nanocarpet on quartz after placing two small quantities of 1 cSt PDMS oil onto it. The areas where the drops were placed are clearly visible, as are the regions where the PDMS oil spread outward. The large bare feature in the center of the image is from impact with the pipette tip, and two additional impact locations are present within the drop placement areas.

4.3.2 What Part is of Interest?

Given the examples of the previous section, patterns of interest should clearly not be due mainly to nanocarpet growth defects or handling defects, they should not be comprised of CNT bundles, and they should not be due to liquid flow effects. They should also be the result of liquid fully impregnating the nanocarpet rather than only upper portion. Ideally, pattern elements would also be deep enough to reach the substrate fully, in order to have less complication due to effects within the height of the nanocarpet (necking off of pattern elements, say). In a nucleation and growth framework, the pattern formation process of interest would be analogous to homogeneous nucleation, if it indeed exists.

4.4 Dynamic Results

It has generally not been possible in this work to obtain dynamic results from nanocarpet pattern formation in progress. This is due to a combination of factors, but primarily to the lack of confidence that a given set of experimental conditions and a particular nanocarpet (potentially containing defects, height variation, and low quality CNTs) would, in fact, yield a pattern of interest. Some results have been obtained, however, and they are presented in this section.

figure 4.13 shows an optical micrograph time series of pattern formation in an approximately 5 μm tall nanocarpet that was grown as a strip instead of a continuous area covering the entire substrate. The strip's long axis runs left to right and continues out of the frame. In the initial image at time zero, the nanocarpet is completely soaked with 0.1 wt% Triton-X solution. In the final image, all liquid has dried up, and the entire pattern formation process took about two seconds.

figure 4.14 shows a time series of pattern formation in a 60 μm tall nanocarpet on quartz using a 0.5cmc SDS solution placed as a 2 μL drop using a pipette. A fan was directed at the microscope stage to increase convective drying. The upper left frame shows a state where the drop has spread outward following liquid wicking within the

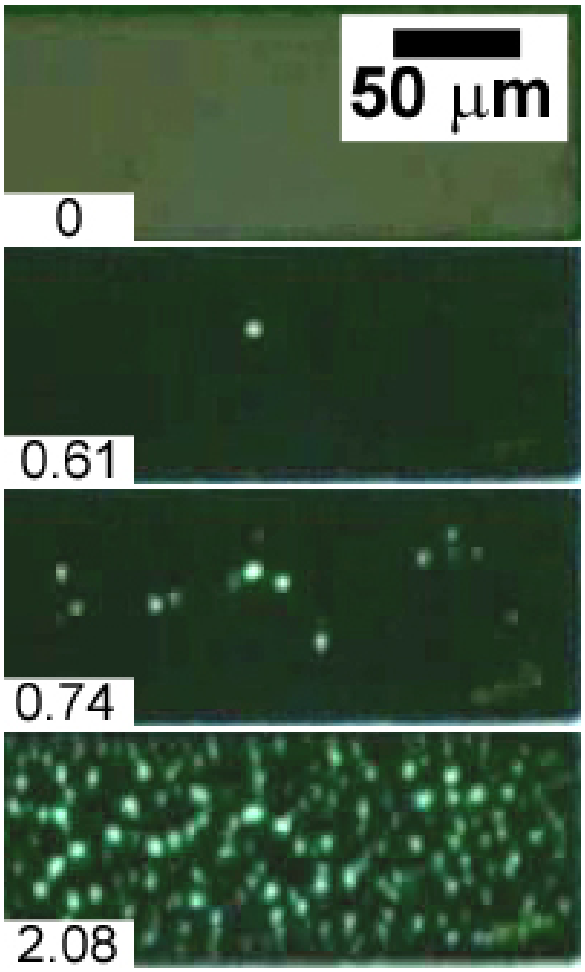

Figure 4.13: Time series of nanocarpet pattern element formation in 0.1 wt% Triton-X solution. Bright spots indicate pattern elements, allowing epi-illumination light to be reflected back to the objective. Lower left numbers are seconds.

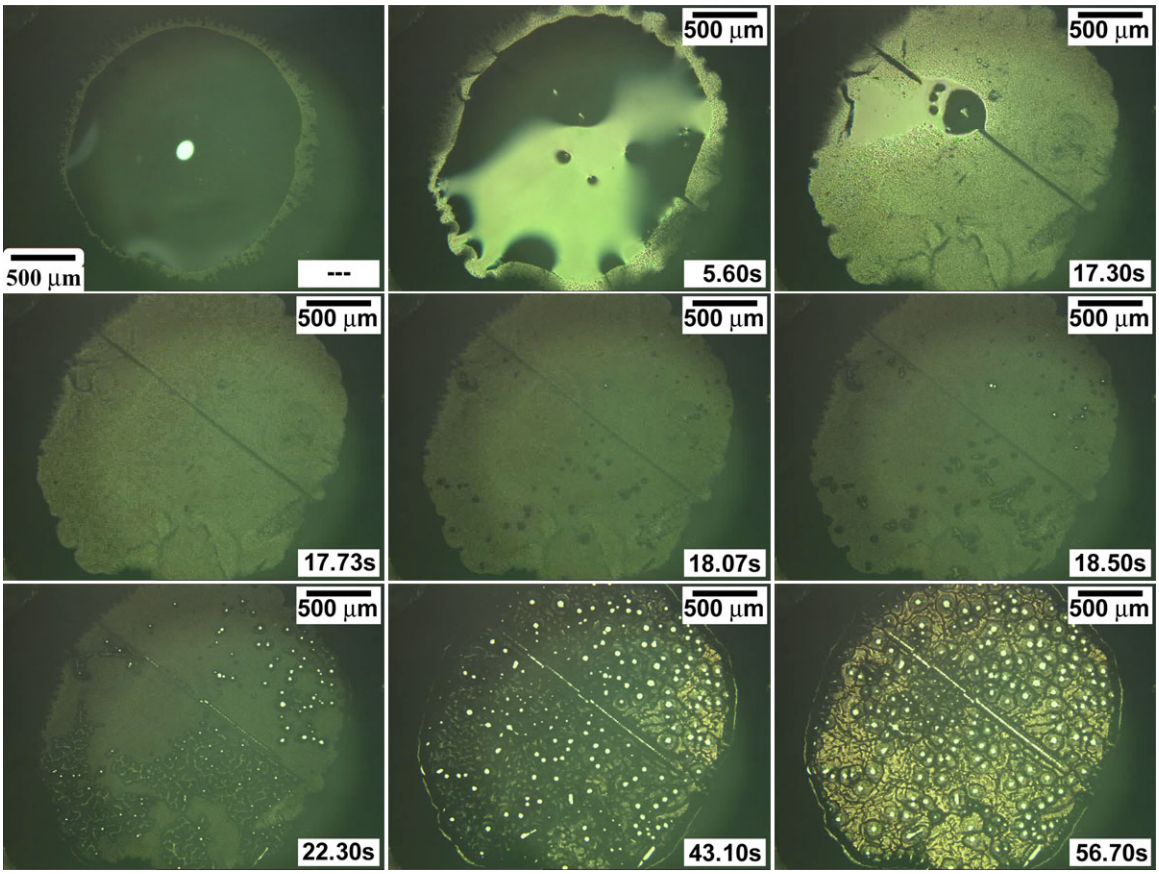

Figure 4.14: Time series showing pattern formation in a 60 µm tall nanocarpet on quartz. The solution is 0.5 cmc SDS placed with a pipette. A full-page version is shown in appendix D, figure D.10. Time in seconds shown in lower right of each frame.

nanocarpet. The drop continued to spread outward, and is no longer spreading in the second frame of the series. The liquid on top of the soaked nanocarpet evaporates first, and the fourth frame shows the soaked nanocarpet just prior to any pattern formation. Holes nucleate in some regions of the nanocarpet first but not others, and then spread outward as drying continues. The increased brightness in the eighth and ninth frames indicates the last of the liquid evaporating. The long line structure running diagonally from upper left to lower right within the wetted area is a preexisting defect.

figure 4.15 shows a time series of pattern formation in the same 60 µm tall nanocarpet as in figure 4.14 but in a separate location that was unpatterned prior to the experiment. In the experiment, 2 µL of 1 cSt PDMS oil was placed using a pipette,

but the entire volume was not placed at once, with the second quantity being quickly placed near the first. This is the same experiment that produced the image shown in figure 4.12. The white object in six of the frames is the pipette tip. The entire formation process from wetting to drying took about 7 seconds. A very important observation is that the pattern elements of interest in the area where the drops are placed do not begin to form everywhere at once, but instead appear to be seeded in certain areas. As the process proceeds, pattern elements form nearby the already existing ones, and thus the entire area is eventually covered by pattern elements that are still enlarging while liquid is present. An additional feature that is important is that a crack appears to form in the drop placement area on the right, and this is indicated by the arrow in the seventh frame. The crack (trench) grows toward the bottom of the frame. It is suspected that this type of feature is due to a preexisting defect, perhaps a scrape or a contaminant present in CNT growth, and this illustrates how greatly a defect can affect the pattern formation process.

From the results presented here and other observations during experiments, it is clear that no coalescence (joining) or breakage (splitting) of pattern elements occurs. This is an important observation for possibly discerning the mechanism of this pattern formation process.

4.5 Static Results and Distribution Analysis

Pattern formation results under various conditions have been obtained during this work. Patterns have been formed in nanocarpets by drop placement onto the nanocarpet, immersing the nanocarpet fully within a liquid and allowing the liquid to dry, touching the nanocarpet onto the liquid surface, and fully dipping the nanocarpet into the liquid. After dipping the nanocarpet fully, both setting the sample right side up to dry and also upside down to dry were tried. Both ways of drying samples were tested in order to examine the effect of confinement of the wetted nanocarpet as it is drying. Combined with difficulties in producing as-grown nanocarpets for the experiments, it has not been possible to obtain multiple sets of results under identical

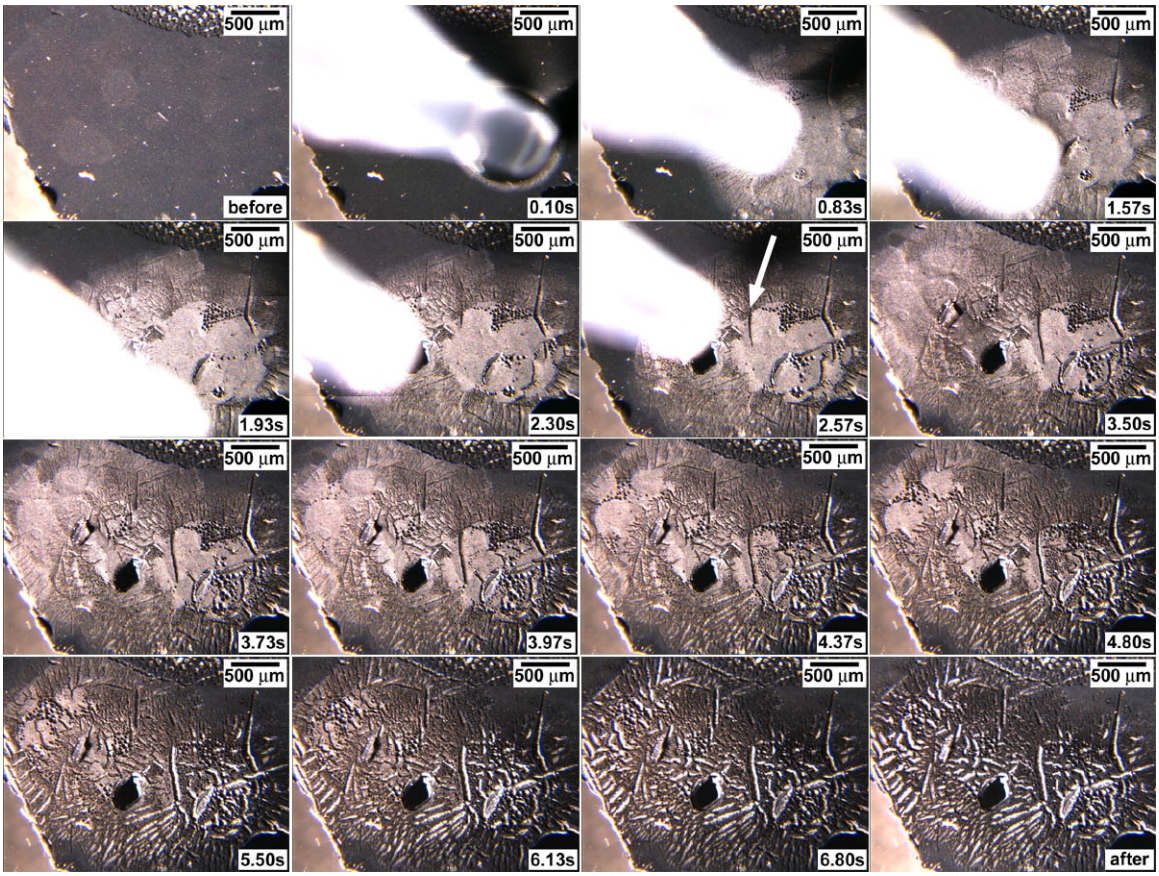

Figure 4.15: Time series showing pattern formation in a 60 µm tall nanocarpet on quartz. The liquid is 1 cSt PDMS oil placed with a pipette, and the arrow indicates the "crack" that is formed. A full-page version is shown in appendix D, figure D.11. Time in seconds shown in lower right of each frame.

conditions. The distribution analysis included in this section aims to present results from experiments under a wide range of conditions (and from the literature) in a uniform and comparable way.

4.5.1 Analysis of Individual Patterns

Often there are obvious reasons why a given sample's results should be discounted and the sample should not be considered for analysis. For example, preexisting scrapes and handling defects, particle contaminants, highly directional patterns, as well as other issues mentioned in the not-of-interest section (§4.3.1) are all sufficient reasons for excluding a given sample. Even amongst samples that are appropriate for analysis, the shape of the pattern elements vary from roughly circular to polygonal to elongated shapes. Consequently, area is chosen as a measure of pattern size, and the distribution of areas in a given pattern is desired. From the viewpoint of nucleation and growth processes, area tends to correlate (though not necessarily linearly) with the time available for growth following nucleation.

A simple measurement that can be made from pattern elements in a SEM image is diameter. If a pattern element is noncircular, the diameter of a circle with equivalent area may be used instead, which is called the hydraulic diameter in fluid mechanics. Figure 4.16 illustrates this type of measurement carried out on a nanocarpet pattern. The visible pattern elements in the lower right quarter of the image are measured, and indicated by white arrows. The distributions on the right show there is a much larger number of pattern elements with diameters around 10 and 20 μm than those with diameters of 40 μm or greater. When these diameters are converted to areas, the population is condensed further toward the smaller areas.

A nanocarpet pattern measured in this way can then be plotted and the distribution examined. Simply plotting the number vs. the area gives histogram-type data like that in figure 4.16. The number of pattern elements of within a given area range is not as important as the proportion of the total contained in the area range, so numbers in a bin can be scaled by the total population size, N. Since during the

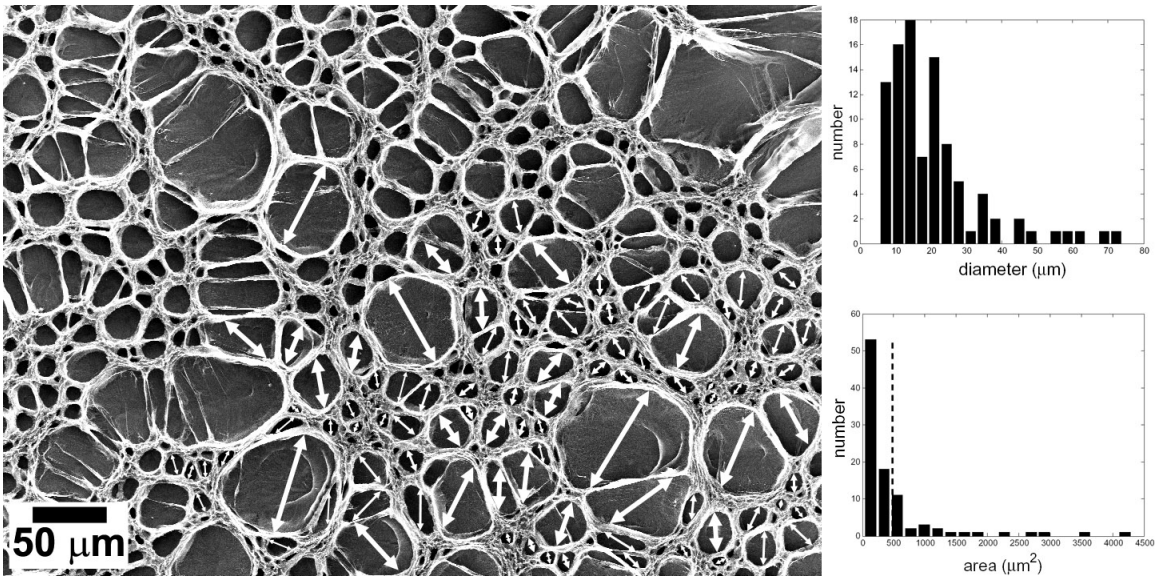

Figure 4.16: *Data set Q*. Illustration of measuring diameters from an SEM image for a pattern. White arrows indicate measurements taken, and histograms for diameter and area are shown to the right, with the dashed line indicating the mean area. This sample was approximately 90 μm in height, grown on quartz, and dipped in 1 cSt PDMS oil and left to dry upside down in a dish.

formation process N should be a function of time, it is actually $N(t)$. Similarly, the number of pattern elements in a given bin is a function of time and bin-center value, $n(x,t)$. SEM images are taken after all liquid has evaporated, and the pattern is fixed indefinitely, hence $N(\infty)$ is used to denote this state. When results from multiple patterns, with potentially large variations in areas to be compared, it is useful to normalize the areas such that all patterns will align about their mean and relative distributions within populations is clearly visible. Thus, the normalization used is

$$x^* = \frac{x - \bar{x}}{\sigma_x}, \tag{4.1}$$

where x is area of a pattern element, $\bar{x}$ is the mean area of a population of pattern elements, and σ_x is the standard deviation in the population. Plots of $n(x,t)/N(t)$ vs. x or x^* are referred to as particle size distributions (PSD). The PSD for the sample measured in figure 4.16 is shown in figure 4.17. This particular data set will

be referred to as data set "Q" as indicated in the legend, and similarly with other data sets presented in this manner.

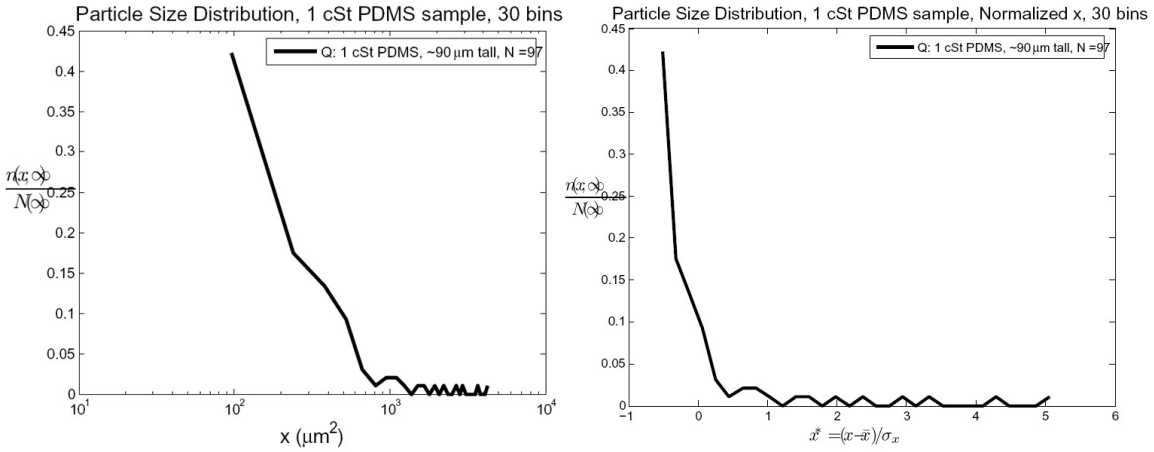

Figure 4.17: Particle size distribution (PSD) of measurements in figure 4.16. Left: log-scaled x-axis, without normalizing. Right: normalized x-axis.

It is useful to show the variation present between different nanocarpet patterns that are still considered to be of interest. Figure 4.18 shows the measurements taken from a 21 µm tall nanocarpet on quartz on which a drop of 0.36 cmc SDS with an unknown concentration of fluorescein was placed using a syringe. The syringe was impacted into the nanocarpet near the upper portion of the image, and this area is not measured as it is not of interest for pattern formation. The particle size distribution (PSD)s for this sample are shown in figure 4.19.

Another example of a different pattern and its analysis is shown in figure 4.20. An aliquot of acetone was deposited onto the 47 µm tall nanocarpet grown on SiO_2. The acetone spread instantly and dried in a couple seconds. In this case, a much larger sample size was obtained for the diameter measurements, with 530 diameters measured from the image. Consequently, 40 bins were used in the analysis. A near Gaussian distribution is obtained, centered at about 9 µm. The PSD for this sample is shown in figure 4.21. Compared to the previous samples, better resolution is obtained at the smaller length scales, which results in data points in the region of $x^* \approx -1$.

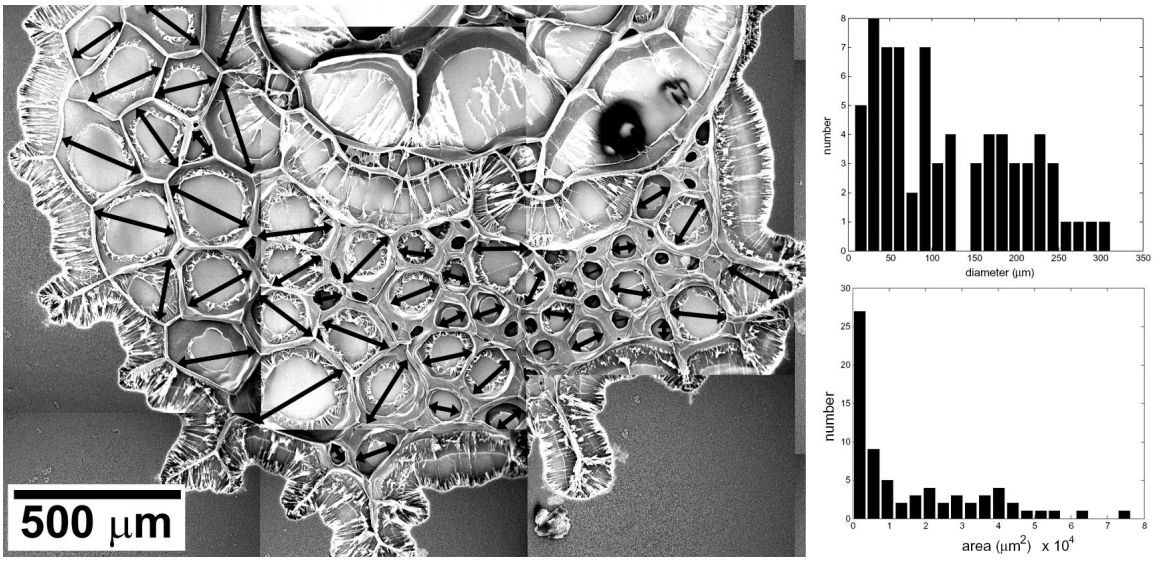

Figure 4.18: *Data set G.* Measurements for a pattern of very large "peeled back" pattern elements. The upper portion of the SEM image is due to syringe impaction during drop placement and is not measured. Unpatterned nanocarpet is visible in the lower part of the image. A 0.36 cmc SDS solution with fluorescein was used, and the nanocarpet was 21 μm tall. Black arrows indicate a measurement. Diameter and area histograms are shown to the right.

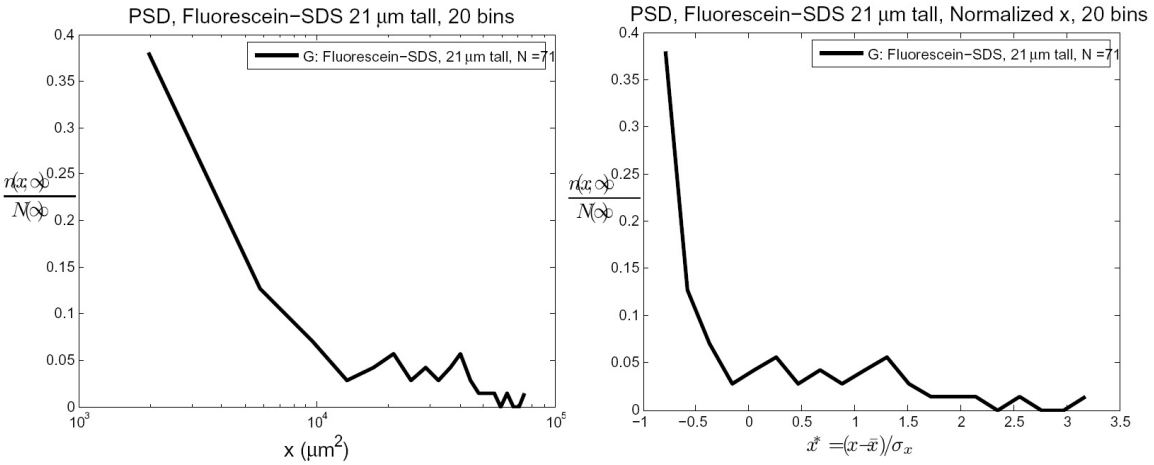

Figure 4.19: PSDs for the sample in figure 4.18.

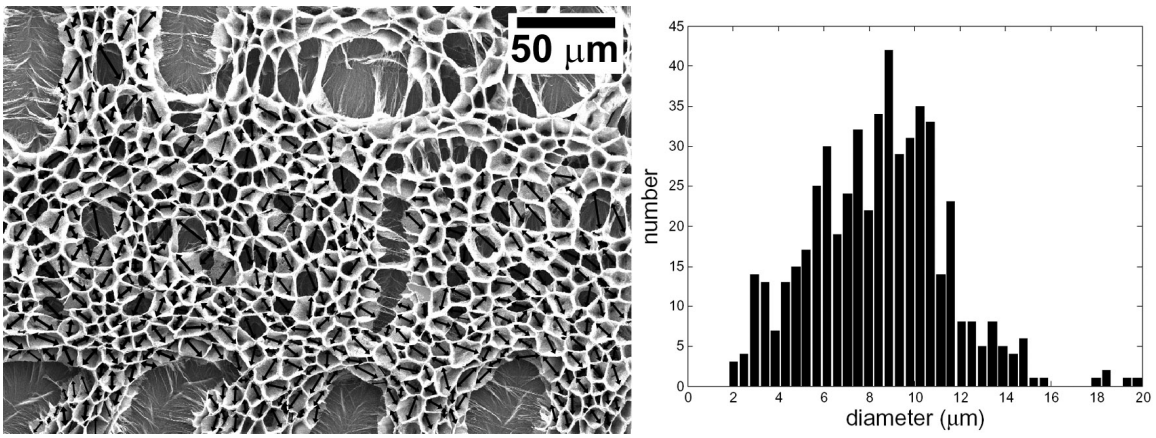

Figure 4.20: ***Data set P.*** **Measurements (black arrows) in a pattern of much smaller pattern elements. Nanocarpet was 47 μm tall on SiO_2 and treated with acetone. Diameter histogram (40 bins) is shown to the right.**

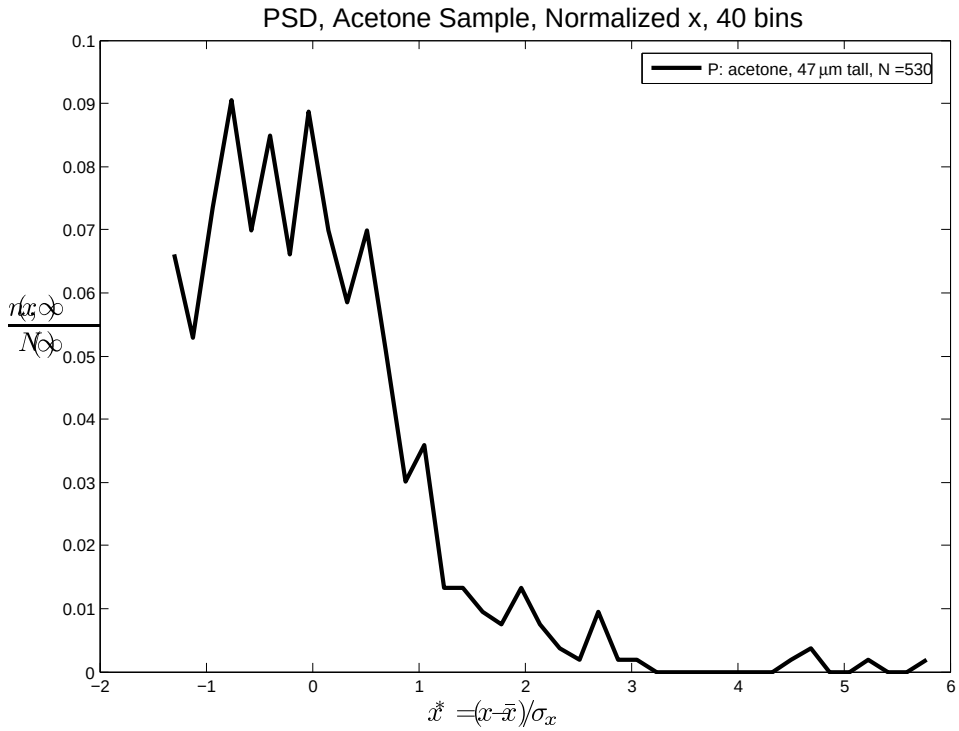

Figure 4.21: PSD for the sample in figure 4.20. Note the Gaussian-like distribution.

4.5.2 Analysis of Multiple Patterns

PSDs can be used for direct comparison between patterns obtained for different samples. This allows the consideration of experimental factors and their effect on the resulting pattern distribution. Patterns that are highly influenced by defects in the nanocarpet prior to the liquid wetting are not of prime interest in this work. However, due to limited foreknowledge and detailed characterization, it has often been impossible to determine whether growth defects (i.e., heterogeneous nucleation sites) were at play in the pattern formation process. The sample shown in figure 4.18 is suspect because of its extremely large features and the "fuzzy" appearance of the CNTs along the inner boundary of the pattern elements. In contrast to these features, the sample in figure 4.16 has well-formed rims and the pattern elements are not deep enough to reach the substrate nor peel back from it. Comparison between the PSDs for these two samples is made in figure 4.22. The SDS-fluorescein induced sample (solid line) has a more erratic distribution, and a larger population of large pattern elements, as expected. Mean pattern size differs by about one order of magnitude. The total breadth (difference between largest and smallest pattern elements) is about the same for the two patterns, with the 1 cSt PDMS oil induced sample being shifted to the right relative to its own mean in comparison with the SDS-fluorescein induced sample.

An experimental factor of interest for nanocarpet pattern formation is the rate of evaporation of the liquid. Two of the data sets analyzed come from experiments using separate pieces of the same nanocarpet. The nanocarpet substrate was broken into pieces, and regions that were not damaged during the breaking were used for the experiment. This meant that the nanocarpet itself was of identical character and height between the two samples. A 0.5 cmc SDS solution was used in a drop placement experiment on both samples. For one sample, the drop was allowed to dry under ambient conditions, and for the other, a normal house fan was directed at the microscope stage from two feet away in order to cause increased convective drying of the drop. The PSD comparisons are shown in figure 4.23. There seem to be more

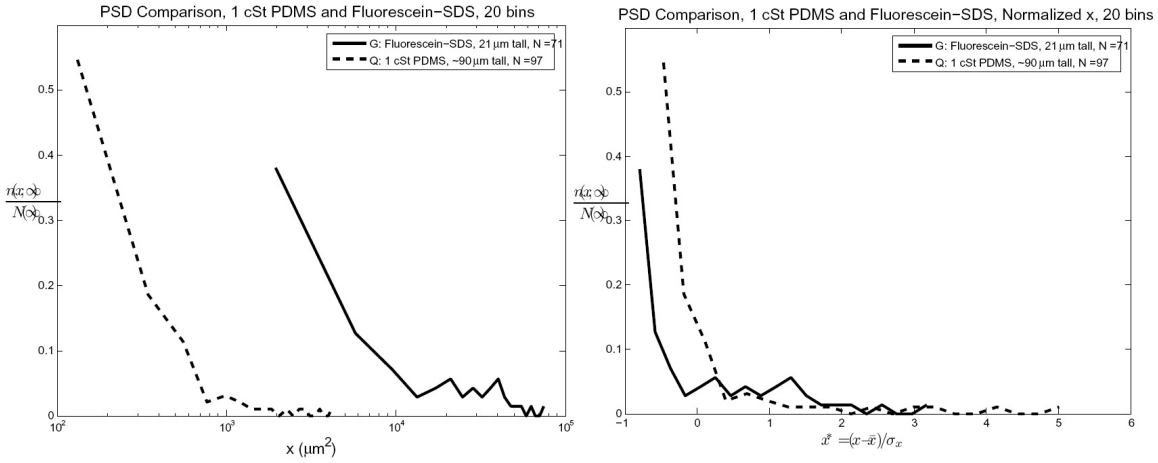

Figure 4.22: Comparison between the PSDs for the 1 cSt PDMS oil treated sample (dashed line) in figure 4.16 and the 0.36 cmc SDS (and fluorescein) treated sample (solid line) in figure 4.18.

large pattern elements in the fan dried sample than the ambient dried, but there are insufficient data for this to be conclusive.

A factor whose role is unclear in nanocarpet pattern formation is the height of the nanocarpet. To look at this, the patterns obtained from two samples treated with 0.1 wt% Triton-X solution were compared. The height of one sample was 5 µm while the height of the other was 53 µm. The PSDs are compared in figure 4.24. The taller nanocarpet has a mean pattern element area of about one order of magnitude larger than the shorter nanocarpet. The taller nanocarpet also has proportionally fewer pattern elements of small ($x^* \approx -1$) size than the shorter nanocarpet. The images for these two samples are shown in appendix D, with the shorter nanocarpet in figure D.5 and the taller nanocarpet in figure D.9. The pattern in the taller nanocarpet is more polygonal in character compared to that of the shorter nanocarpet. The pattern elements in the shorter nanocarpet are deep enough to reach the substrate, while those in the taller nanocarpet are "necked" off at some intermediate height and so do not reach the substrate.

The issue of reproducibility of patterns under the same conditions is important in order to determine whether defects or uncontrolled factors are influencing the pattern formation process. As an example of investigating reproducibility, patterns

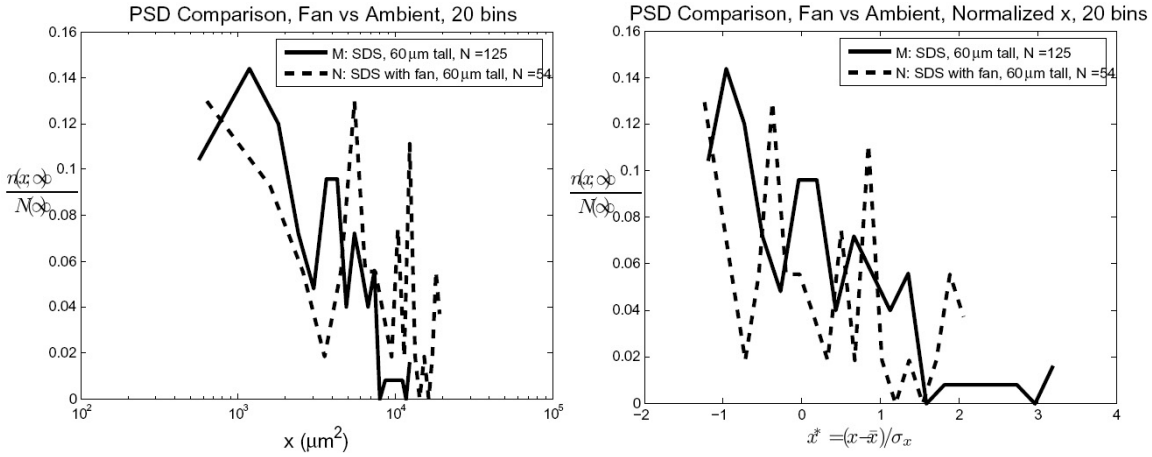

Figure 4.23: Comparison between the PSDs for two nanocarpet patterns created in an identical nanocarpet type (from breaking an as-grown sample) and using the same solution, 0.5 cmc SDS. In one sample, a fan was used (dashed line) to increase the rate of evaporation.

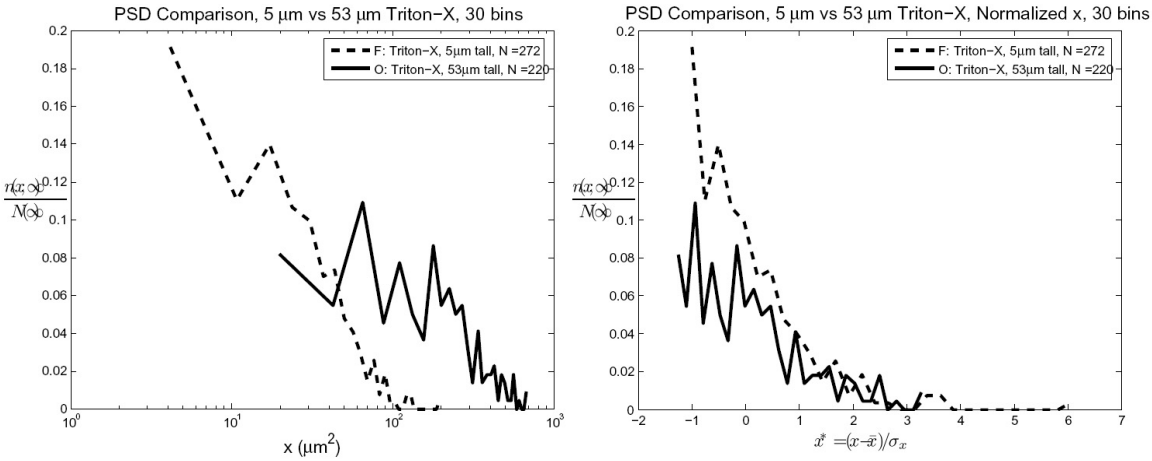

Figure 4.24: Comparison between the PSDs for two nanocarpet patterns treated with the same solution, 0.1 wt% Triton-X, but with different heights. One was 5 μm in height (dashed line) and the other was 53 μm in height (solid line).

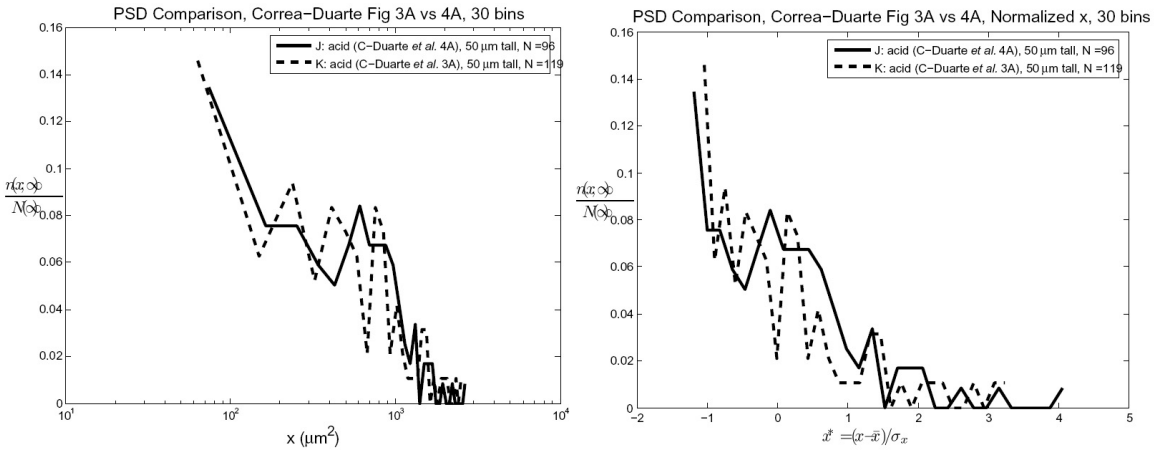

Figure 4.25: Comparison between the PSDs for two 50 μm tall nanocarpet samples treated with a nitric/sulfuric acid (1:3) solution and shown in the paper of Correa-Duarte et al. Within reasonable measurement error, the PSDs do appear to be similar.

in images from the paper of Correa-Duarte et al. [19] were analyzed, which were stated to be from nanocarpets of exactly the same height and created under the same conditions. The images from Correa-Duarte et al. that were used are their Figure 3A and Figure 4A. These patterns would be expected to have near similar PSDs, and indeed the comparison between them in figure 4.25 appears to show this is the case, within reasonable measurement error, which is unavoidable because of the available image resolutions. It is not clearly stated in their paper that the samples are distinct, separate "MWCNT-based networks" (multi-walled carbon nanotube), but the character of the patterns does appear to be different, indicating that they probably are from separate samples.

Altogether, patterns from 12 samples were analyzed in this fashion. Remaining images that are not shown in this chapter but that were analyzed are in appendix D. Additionally, images obtained from the literature were included in the analysis, naturally with somewhat limited resolution, but the images are not shown here. The five images used from the literature are as follows:

- Figure 1B from Chakrapani et al. [8] which is *Data set C*. Nanocarpet treated with water.

- Figure 1A from Liu et al. [15] which is *Data set I*. Nanocarpet treated with water.
- Figure 3A from Correa-Duarte et al. [19] which is *Data set K*. Nanocarpet treated with nitric/sulfuric acid in 1:3 ratio.
- Figure 4A from Correa-Duarte et al. [19] which is *Data set J*. Nanocarpet treated with nitric/sulfuric acid in 1:3 ratio.
- Figure 1A from Li et al. [48] which is *Data set L*. As-grown nanocarpet.

In the image from Chakrapani et al., widths were used for their large "canyon" features, as they also use in their analysis, though they neglect the small features between the canyons. In the analysis of their image included here, small features between the canyons were included and were treated similarly to other patterns here. The pattern in the image from Li et al. [48] was selected to be included in this analysis, even though the pattern is claimed to be present in the *as-synthesized* state. The pattern is remarkably similar to the nanocarpet patterns obtained in this work (and by others) by wetting with liquids and drying. Li et al. investigate super-hydrophobicity of their nanocarpets, which are grown using thermal CVD and pyrolysis of iron(II) phthalocyanine (FePc) that is placed next to the quartz glass substrates inside the furnace. In a previous paper by the same group [49] dealing with super-"amphiphobicity" of nanocarpets, the following is contained in their experimental section:

> "The pyrolysis of FePc/YPc was performed under Ar/H2 at 600–900 °C on quartz glass plates in a flow reactor consisting of a quartz glass tube and a furnace fitted with independent temperature controllers. The resulting ACNT films appeared on the quartz glass plates as a black layer. After drying the ACNT films in vacuum, they were treated with a hot concentrated mixture of H2SO4 and HNO3 (1:1, v:v) for 2 h to generate functional groups, such as hydroxyl and carboxyl, on the surface of the carbon nanotubes. The treated samples were then rinsed with pure water and dried in a vacuum again."

In [49], no SEM images of their samples following treatment with the sulfuric and nitric acid solution are given, but it is highly likely that their nanocarpets have

formed patterns due to the liquid treatment. This acid solution treatment is nearly the same as that used by Correa-Duarte et al. to form their nanocarpet patterns. The pure water rinsing step is also highly likely to form patterns in the rather short nanocarpets of Li et al. Consequently, in the paper containing the image included for analysis here [48], it is unclear whether Li et al. consider "as-synthesized" to mean the samples were just removed from the furnace or they were just removed from a rinsing step. Thus it is justified to include their pattern in the analysis.

PSDs of all 12 data sets from this work and the 5 images analyzed from the literature are shown in Figures 4.26 (non-normalized area, x) and 4.27 (normalized area, x^*. Though the plots are rather erratic and the analysis is quite likely measurement number limited (N values stated in the legend), there are some important features to be noted.

First, in figure 4.26 it is clear that nanocarpet patterns can be obtained with pattern element areas spanning four orders of magnitude. Second, there is no clear trend in nanocarpet heights in the data. Third, there is also no clear role of liquid agent used to induce the patterns. Fourth, it seems more common for samples to have a greater relative number of small pattern elements than large ones. Fifth, in figure 4.27 it is evident that the majority of pattern elements are distributed within $-1 < x^* < 1$, i.e., within one standard deviation from the mean. This is an interesting finding for possible self-assembly based manufacturing purposes. Sixth, image resolution and therefore the pattern elements that may be measured from them is preventing data in the $x^* < -1$ range. This could be alleviated by using images of the same sample taken at different scales and then analyzed. Finally, PSDs from individual samples are not Gaussian-shaped, in general. Six data sets exhibit very high numbers of small pattern elements, but the remainder have at least a near-Gaussian shape.

Reproducibly creating nanocarpet patterns was generally very difficult. The main causes of this difficulty were inability to grow nanocarpets that were uniform enough to not have a high defect density and also not having a way to apply liquids in a reproducible fashion that yielded patterns. Eventually the most reproducible exper-

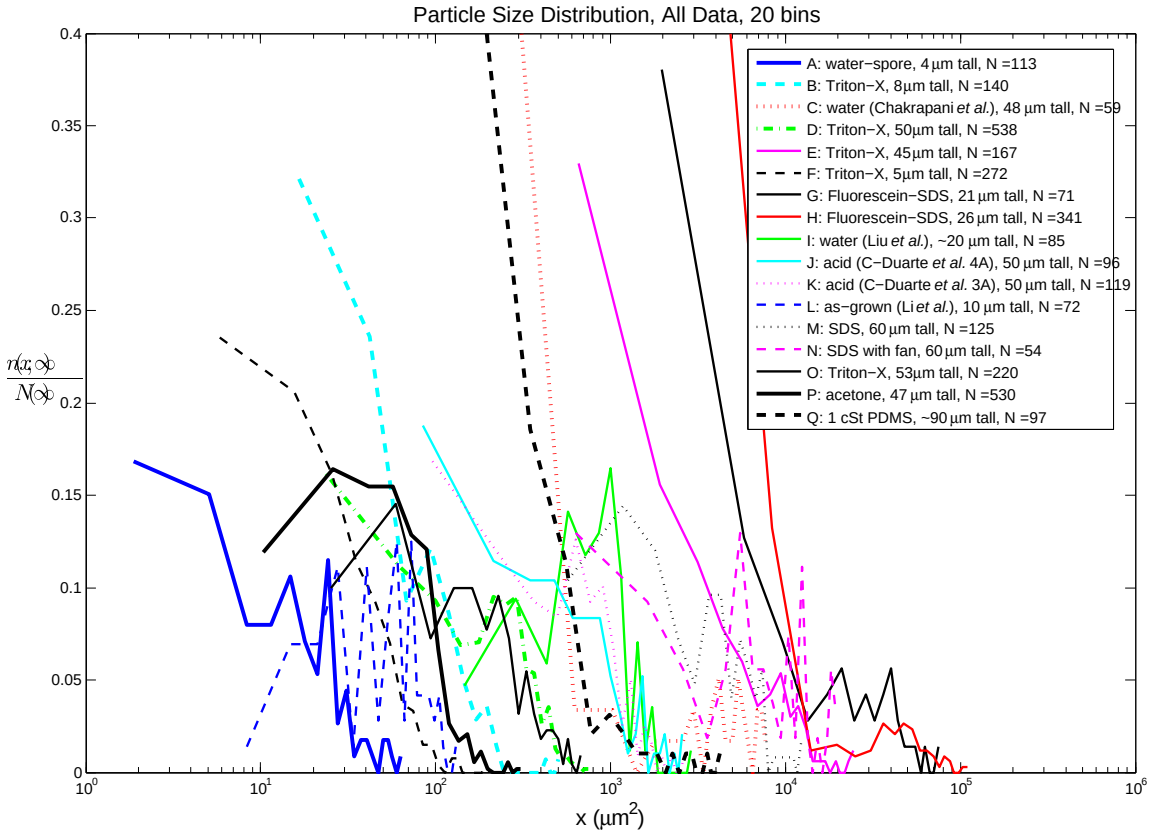

Figure 4.26: Particle size distribution using 20 bins for all data analyzed, without normalizing area, x. Note the log-scaled x-axis. A full-page version is shown in appendix D, figure D.12.

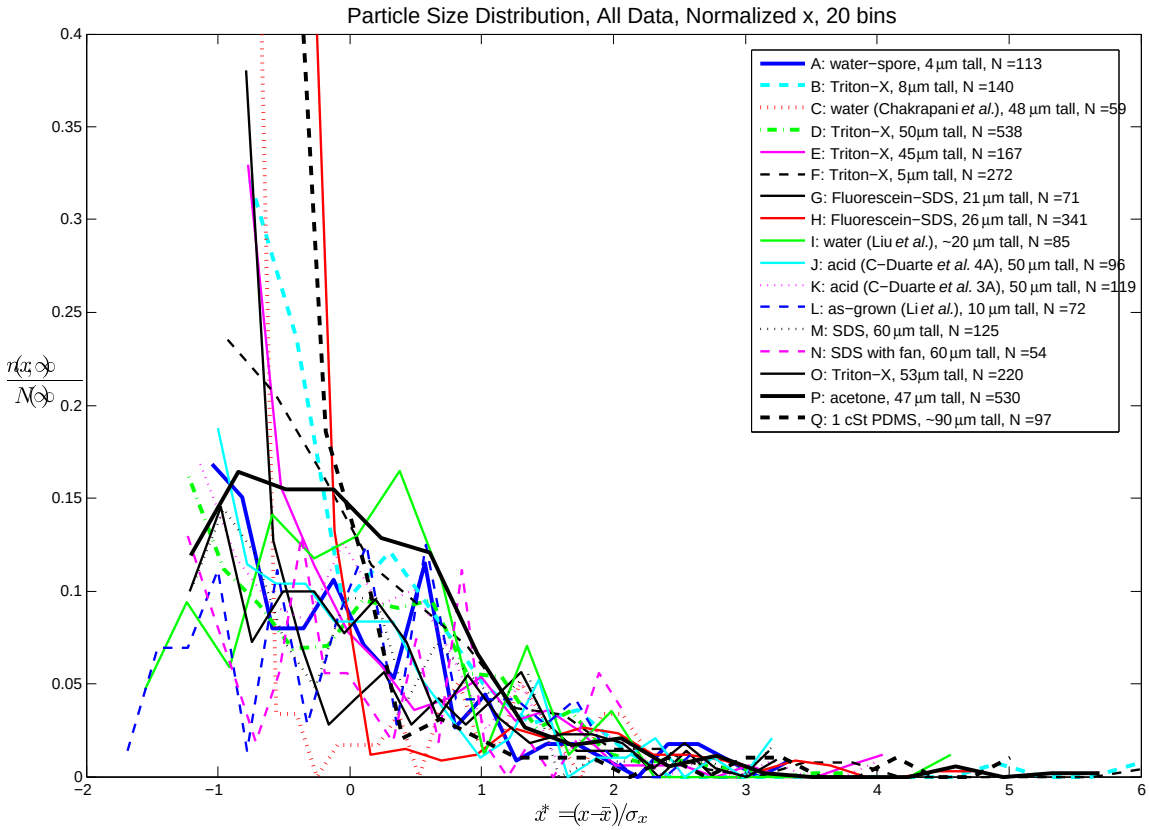

Figure 4.27: Particle size distribution using 20 bins for all data analyzed, normalizing areas so distributions align at $x^* = 0$. A full-page version is shown in appendix D, figure D.13.

imental method turned out to be nanocarpet sample dipping into a pure liquid (not a surfactant solution) and then ambient drying *upside down* in a dish. Most likely, upside down drying caused a reduced evaporation rate and coupled with sample dipping, reduced the impact of flow effects present in a drop placement experiment. The best results from attempting to create reproducible pattern formation using 1 cSt PDMS oil are shown in figure 4.28. The upper left, lower left, and lower right are from three separate samples, while the upper right is a tilted view SEM image of the sample in the lower right, though at a different location and scale. All three samples were grown in exactly the same way and dipped and dried in exactly the same way. There is no significant directionality visible in the patterns and pattern element sizes are relatively consistent. The pattern in the upper left is somewhat less "well-formed" due to the nanocarpet being shorter than in the other two samples and the growth quality being somewhat less.

4.6 Chapter Summary

In this chapter, results were presented on pattern formation in as-grown nanocarpets. Patterns with mean diameters of a few microns ranging to on the order of 100 microns were found. Generally, the type of patterns observed in nanocarpets are called "cellular" and a comparison with other cellular materials is made in chapter 8.

In the initial stages of this research, several potential causes for pattern formation were ruled out, and it was found that surface tension effects are the primary cause.

Since the situation is complex, the definition of what is of interest within this process was refined. The goal was to obtain reproducible liquid-induced pattern formation that was not due to defects, whether during nanocarpet growth or handling, the bundling together of short CNTs, nor flow effects that are marked by directional patterns. Without high resolution SEM characterization before and after experiments in identical locations, it is very difficult to ascertain whether defects were the primary cause of patterns. This issue is discussed in chapter 8.

Dynamic results were presented from nanocarpet pattern formation experiments

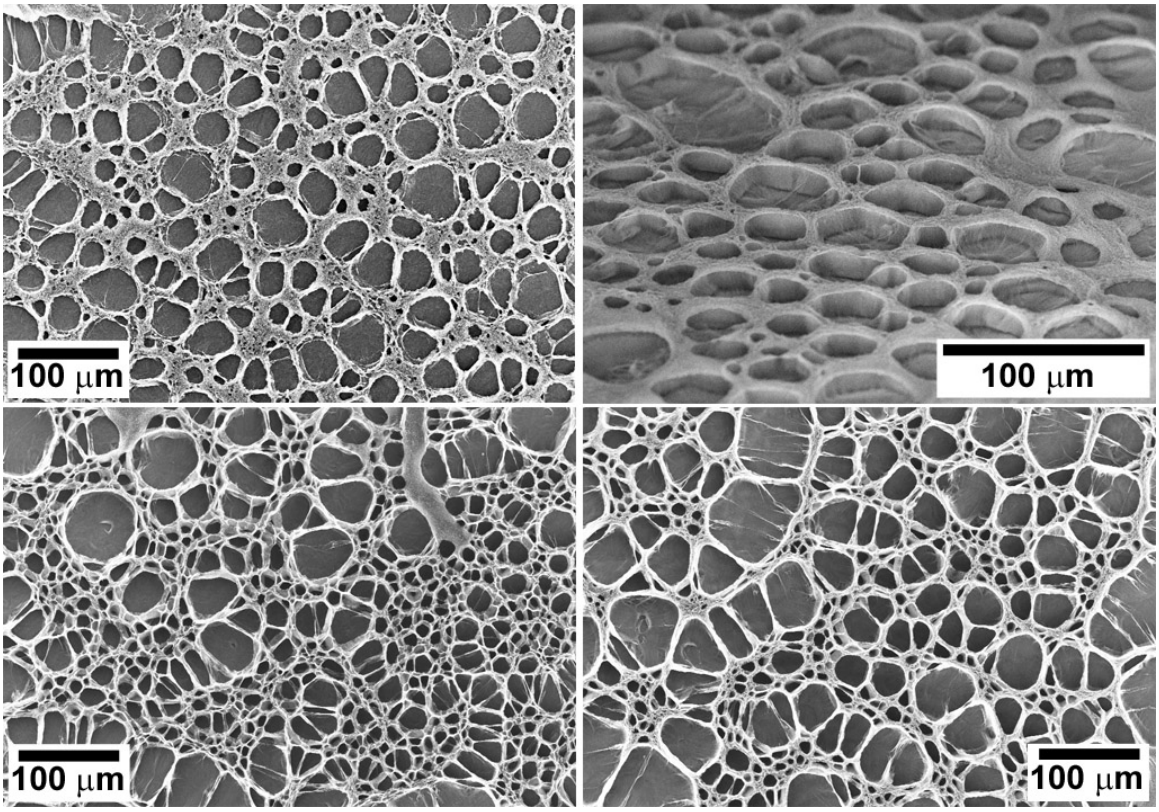

Figure 4.28: Best results from attempting to obtain reproducible pattern formation. Three samples are shown at same scale in upper left, lower left, and lower right. Upper right is 60° tilted view of lower right sample in a different location. Nanocarpets were dipped in 1 cSt PDMS oil and left to dry upside down in a petri dish.

that demonstrated the entire formation process requires a few seconds to a minute or so. It was again seen that defects play a significant role in the pattern formation process. The patterns formed under the sessile drop region in a drop placement experiments are quite different from those under the spreading region.

SEM images of several nanocarpet patterns were presented, along with pattern analysis. The "hydraulic diameter" of individual pattern elements within the patterns were measured and the entire distributions plotted and compared. By using a normalization of the area, the populations from several different samples could be aligned at their mean and compared. Similarly, the effect of experimental factors like nanocarpet height and evaporation rate can be examined by using a direct comparison of their PSDs. Potentially the effect of defects causing a pattern could be seen in the same way, though it was unclear in the comparison made here.

The analysis of 17 patterns (12 from this work and 5 from the literature) and examination of their PSDs was presented and showed that nanocarpet patterns tend to be distributed within about one standard deviation from their mean and to have a much larger number of small pattern elements than large ones.

Reproducibility in pattern formation is desired, and a comparison of two PSDs from a published study was made and seemed to illustrate reproducibility. In experiments of this work, the best conditions found for obtaining reproducible pattern formation are treatment with a pure liquid (1 cSt PDMS oil) rather than a surfactant solution and dipping the entire nanocarpet sample into the liquid, removing it, and setting it upside down to dry. The reason is unknown, but is likely related to the uniformity of conditions.

It remains unclear whether an analogue to homogeneous nucleation exists for nanocarpet pattern formation. Since even submicron defects could conceivably initiate nanocarpet pattern elements, and many other factors needed to be refined and considered, a conclusion about homogeneous nucleation cannot be made from these results.

It is clear from the results presented in this chapter that patterns of interest can be formed in as-grown nanocarpets under a wide variety of conditions and with varying

liquids and nanocarpet heights. No trends were seen in considering nanocarpet height, nor any trends due to the particular liquid used. It is unclear how the evaporation rate, surface tension, viscosity, and other properties of the liquid affect the patterns. The only necessary requirements appear to be that the liquid used wets the nanocarpet sufficiently and there are minimal defects within the nanocarpet such that the patterns are not obviously due solely to defects.

Chapter 5

Method for Anchoring Nanocarpets

5.1 Introduction

This chapter concerns a method for anchoring nanocarpets within another material in such a way that the constituent CNTs are still accessible and functional as a nanostructured material. This is in sharp contrast to other methods of creating nanocomposites that result in CNTs being fully embedded within a matrix material. The need for an anchoring method became clear in working with nanocarpets and seeing their frailty under realistic conditions. Accidental (or intentional) contact with another surface consistently removed and damaged entire sections of the nanocarpet. Attempting to use nanocarpet-based materials for any real application would require exquisite care in fabrication as well as prevention of environmental interaction with materials. By anchoring the entire nanocarpet down while still retaining the morphology of a nanocarpet, potential damage and processing difficulty will hopefully be mediated or entirely avoided.

Nanocarpets can be anchored within a single thin layer, which is spread upon some other substrate such as a glass slide, and this version of the method is called the "thin layer process." A nanocarpet can also be anchored within a thin layer that is spread upon a much thicker preexisting and already cured (hardened) layer of the same material. This results in the nanocarpet being anchored only to the depth of

the final thin layer. This version of the method is called the "thin-on-thick process." It is conceivable that more than two layers, possibly of varying material types, could be built up for various applications, with only the final thin layer used to anchor the nanocarpet.

The chapter contains a letter whose text was wholly written by the thesis author for *Nano Letters*. Following the letter, additional sections are presented that contain methodology and results that deal with creating predetermined thickness of cross-linked PDMS anchoring layers and the use of another polymeric material, PMMA, for the anchoring layer. The results of this chapter address problem statement 3 in §1.5 which was **"Can nanocarpets be anchored within a surface while remaining sufficiently functional?"**

5.2 "*Controlled Partial Embedding of Carbon Nanotubes Within Flexible Transparent Layers*"

Submitted to Nano Letters *August 28, 2006*

5.2.1 Abstract

Applications of CNTs like field emission displays, super-capacitors, and cell growth scaffolds can benefit from controllable embedding of the CNTs in a material such that the CNTs are anchored and protrude a desired length. We demonstrate a simple method for anchoring densely packed, vertically aligned arrays of CNTs into silicone layers using spin-coating, CNT insertion, curing, and growth substrate removal. CNT arrays of 51 and 120 μm in height are anchored into silicone layers of thickness 26 and 36 μm, respectively. SEM and optical microscopy are used to characterize the sample morphology and a 5.5 m/s impinging water jet is used to apply shear stress, verifying the CNTs are well-anchored.

5.2.2 Letter

A wealth of applications utilizing the properties of CNTs have been demonstrated, such as field emission displays [50, 51], enhanced surface area super-capacitors [52, 53, 54], and biological cell growth and tissue culture scaffolds [55, 56, 19]. Other applications, such as friction drag reducing surfaces in fluid flows [57, 58], have been simulated but not demonstrated. For devices that aim to directly take advantage of free and accessible CNTs, such as the above mentioned examples, it is of crucial importance to be able to fabricate the CNT-containing components so that the CNTs are partially exposed and not fully embedded within other materials. CNTs have been the subject of many studies concerned with generating composite materials with enhanced mechanical, thermal, optical, and electrical properties [59]. For the development of composite materials, it is generally not necessary that the CNTs themselves be accessible to the environment or protruding in any fashion, only that they interact favorably with the other components of the composite. Here we demonstrate how densely packed, vertically aligned CNTs can be simply and controllably anchored within a layer of curable elastomeric material (RTV615, GE Silicones, Wilton, CT). The four steps of the method are spin-coating a layer of uncured material to produce the desired thickness, vertical insertion of the CNTs, curing the entire assembly, and removal of the original growth substrate of the CNTs. This process provides straightforward control over the portion of the CNTs that is anchored within the anchoring material, and therefore also the remainder that is left free and protruding. Freestanding flexible composite films of elastomer and protruding CNTs can be obtained by peeling off the films from their substrate, whereby they can be transferred to a separate surface or device component, removing the need for final surfaces and device components to be compatible with CNT fabrication processes. The anchoring of CNTs will improve handling in further fabrication steps and robustness against being accidentally scraped, blown, or rinsed off and removed from a functional device surface. Importantly, patterns and local configurations of the original, as-grown CNTs are preserved during this anchoring process, making it compatible with stan-

dard CNT growth patterning protocols. Inversion of the as-grown CNTs, which is inherent in our method, may have additional benefits, since it is well-known that CNTs grown on a surface typically have closed ends as their tips and potentially also catalyst particles there [60]. For applications such as field emission and sensing, open ends are preferable [61], which inversion should provide.

The embedding of dispersed CNTs within polymers has been the subject of many previous studies [62, 63, 64]. It has also been demonstrated that common polymers such as PMMA and PDMS can fully wet *aligned* arrays of CNTs and be cured to form the matrix phase in the CNT-polymer composite [65, 66], where the uncured polymer material has first been deposited *onto* the CNTs. These findings suggest that anchored and protruding aligned CNTs could be made by using aligned CNTs pregrown on a substrate and controlling the thickness of the polymer layer into which they are inserted, as is demonstrated here. There are other relevant previous studies involving the deposition of materials *onto* as-grown aligned CNTs, such as gas pyrolized conformal coatings of Parylene-C [67], SiO2 via CVD[68], electrochemical deposition of the conducting polymers polypyrrole [69] and polyaniline [70], and polyvinylacetate [71] deposition from solution for the purposes of developing electrochemical sensors and field emission sources. Applying materials in this way usually requires etching back the coating or matrix if exposed CNTs are desired, the maximum thickness of conformal coatings can be significantly smaller than the thickness of the layer of aligned CNTs, and conformal coatings are deposited everywhere on the sample, including over the entire sidewalls of the CNTs. The deposition of a material by spin-coating in particular has also been used previously, for example PDMS [72], polystyrene-toluene solution [73], a spin-on-glass [74], and a polydiene rubber [75], all spin-coated on *top* of an array of aligned CNTs, but this approach will not give control over protruding lengths, if indeed any protruding CNTs are produced. Additional drawbacks to spin-coating a material on *top* of an array of CNTs, with regard to achieving controllable protruding lengths and preserving array configurations, are that growth patterns and local configurations are likely to be lost due to the local forces between the CNTs and the spun material and the entire sidewalls of the CNTs

will be coated by the spun material.

The possibility of transfer of an as-grown CNT array from its growth substrate to another surface has been demonstrated previously utilizing an HF etch to first detach the CNTs [76], however it was not possible to retain the growth patterns of the CNTs. Transfer with inherent inversion of the CNT array and retention of growth patterns has also been demonstrated using a microwave assisted hot embossing process that partially implants the CNTs into a thermoplastic polymer [77] and in another study using the screen printing of a several micron-thick-silver paste into which the CNTs are inserted and then cured [78]. However, neither of these two approaches results in simple control over the depth of anchoring of the CNTs.

In contrast to previous works, the method described here requires no material removal step because the aligned CNTs are inserted only to the depth of the anchoring material layer. Simple and direct control over the anchoring depth of the CNTs is provided by the spin-coating of the anchoring material prior to CNTinsertion. Retention of growth patterns is also an important feature of this method.

The CNT arrays used to demonstrate this anchoring method were grown by the well-known process of thermal CVD on iron sputtered quartz surfaces [40]. This growth process as used here results in densely packed arrays of multi-walled CNTs oriented perpendicular to the growth surface wherever catalyst material is present, with the height of the array on a given sample being quite uniform. Alignment is good at larger length scales, but there is entanglement present at the nanoscale. Typical CNT diameter is about 20 nm and typical internanotube spacing is about 50–100 nm. Depending on growth conditions such as growth time, feedgas flowrate (and therefore average flow velocity at the sample surface) and composition, system pressure, and thickness of the Predeposited catalyst layer, array heights can be obtained in a range from about 10 μm for shorter growth time, for example, to over 150 μm for longer growth time. Alignment and array height uniformity tends to be better for taller arrays. Because of the similarity in appearance of these aligned CNT arrays to ordinary carpets, we refer to them as "nanocarpets."

Thermal CVD-grown nanocarpets were fabricated following previously reported

methods [25, 26] in a 1 in. diameter quartz tube furnace (Lindberg/BlueM, Asheville, NC) at 725 °C on square quartz substrates (1 cm × 1 cm × 0.16 cm) that were first sputtered with 5 nm of iron. The furnace and samples were brought to growth temperature under a constant flow of 500 SCCM Ar and at a pressure of 600 Torr. Beginning immediately once growth temperature was reached, the feedgas mixture of 280 SCCM ethylene and 70 SCCM hydrogen was supplied for 10 min., keeping the total pressure constant at 600 Torr. Cool-down to ambient temperatures was achieved under 500 SCCM Ar and 600 Torr pressure. For the anchoring experiments, the final heights of the two nanocarpets were 51 and 120 μm as measured by SEM.

Two approaches were followed for anchoring a nanocarpet into an RTV layer. In the first, a thin layer of uncured RTV was spin-coated onto a flat, rigid substrate—a glass slide—and the nanocarpet was then inserted vertically, the entire assembly cured, and the nanocarpet growth substrate removed. A schematic of this "thin layer process" is shown in the upper portion of figure 5.1. In the second approach, a relatively thick layer of RTV was first created on a piece of Teflon material, and then cured, followed by the deposition of a thin layer of uncured RTV into which the nanocarpet was inserted vertically, the entire assembly cured, and the nanocarpet growth substrate removed. This "thin-on-thick process" is shown in the upper portion of figure 5.2. Because the thick layer was cured first, the nanocarpet was inserted exactly to the depth of the uncured layer that was deposited on top of the already cured layer. The fact that the two layers were of the same material, RTV, ensured good bonding at the interface between them. Cured RTV does not adhere well to Teflon, which allowed easy release of the two joined RTV layers and anchored nanocarpet.

RTV615 is comprised of PDMS and cross-linking agents. Just prior to use, the two components of the uncured RTV were mixed by manual stirring at the manufacturer recommended 10:1 ratio by weight. A glass slide was first rinsed with isopropanol (IPA) and 18.2 MΩ·cm DI water, dried with nitrogen, and secured to the bottom of a petri dish using double-sided tape. For the thin layer process, a small portion of the RTV was applied to the center of the secured glass slide, and spun at 2700 RPM

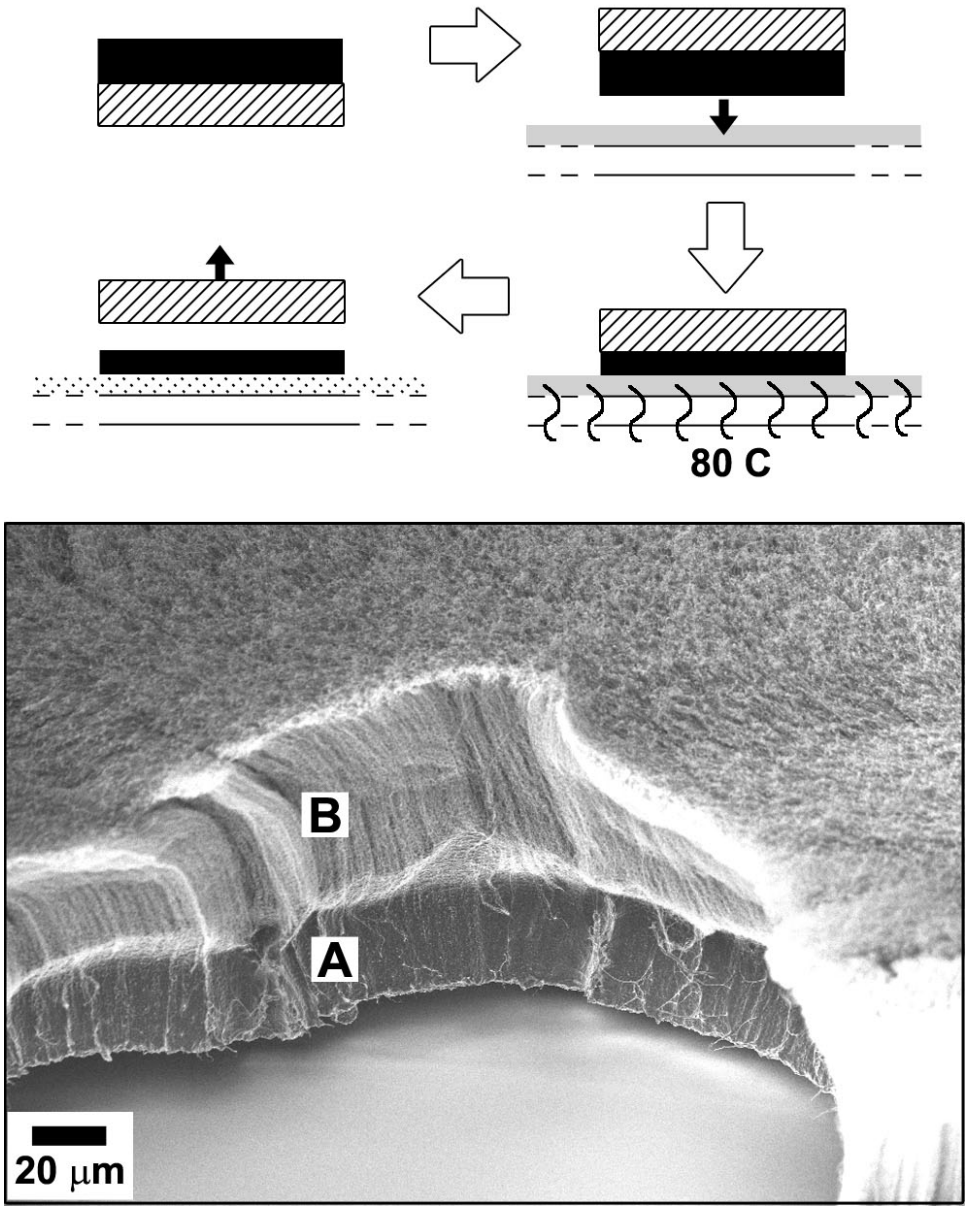

Figure 5.1: Nanocarpet anchored in RTV. **Upper**: Schematic diagram showing steps in the anchoring process for this "thin layer process" - an as-grown nanocarpet is inserted into a spin-coated layer of uncured RTV on top of a glass slide, cured at 80 °C overnight, and the growth substrate is physically removed using tweezers leaving the nanocarpet firmly anchored within the cured RTV layer. **Lower**: SEM image of a cross-section of the sample, taken at a 60° off-vertical tilt angle. **A** indicates the RTV anchoring layer, which is 30 μm thick at this location when corrected for viewing perspective, and **B** indicates the protruding, RTV-free portion of the nanocarpet, which is about 64 μm thick at this location when corrected for perspective. Scale bar is 20 μm.

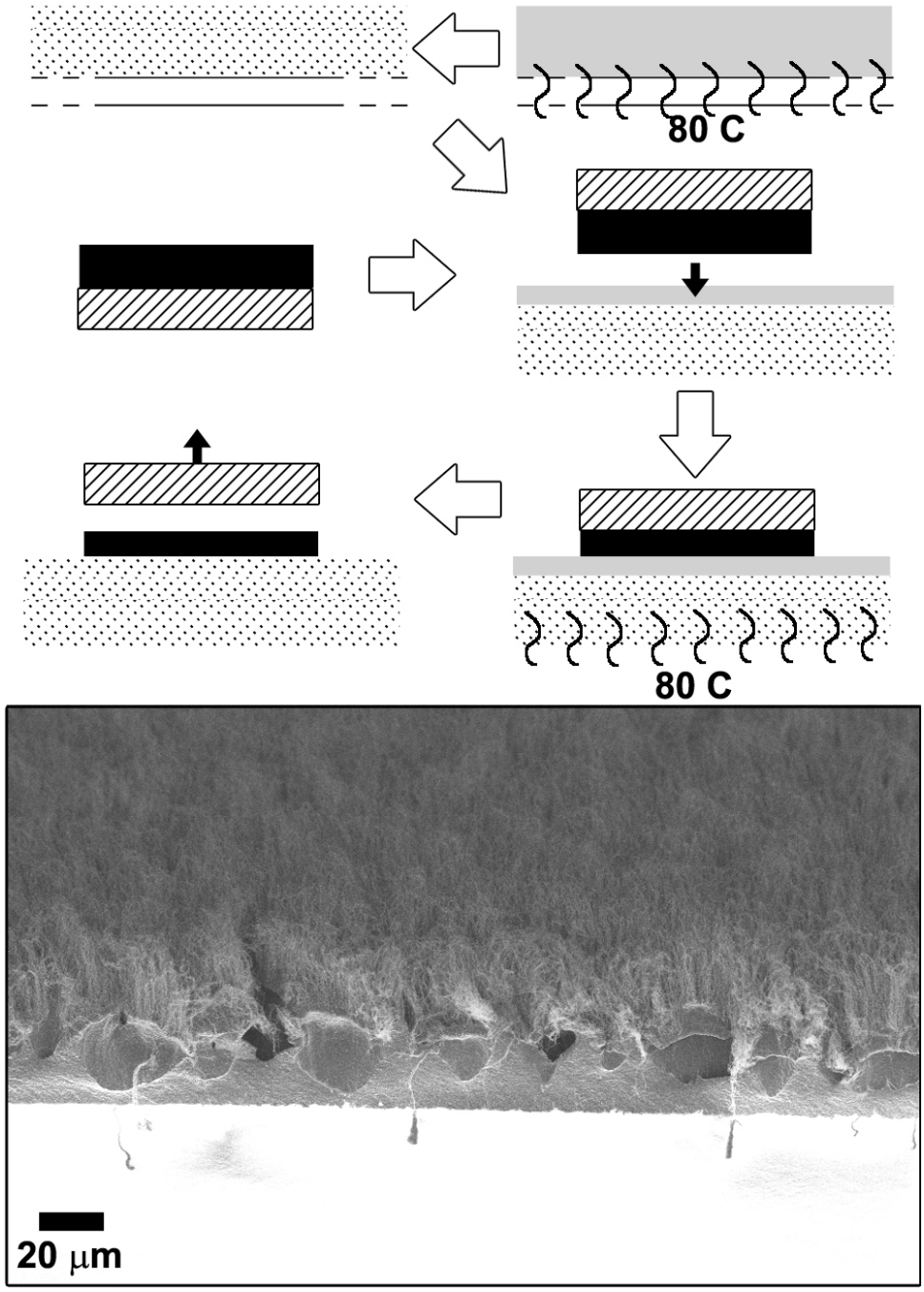

Figure 5.2: Nanocarpet anchored in RTV layer deposited on already cured underlayer of RTV. **Upper**: Schematic illustrating this "thin-on-thick process." **Lower**: SEM image showing the 51 μm thick nanocarpet protruding from the 26 μm thick second layer and anchored within it. The second layer of RTV is easily visible compared to the thick layer underneath because the high volume fraction of conductive CNTs sufficiently disperses the charge from the incident electron beam, while the underlayer has no CNTs and is accumulating charge, resulting in low contrast.

for 2 min., spreading the uncured RTV into a thin film on the glass slide. In the thin-on-thick process, a 1/32 in. thick piece of Teflon material, which had also first been IPA and DI water rinsed and nitrogen dried, was utilized to allow easy release of the RTV once the final cure was completed. A large quantity of uncured RTV mixture was spread over the Teflon surface, then baked at 80 °C. A final thin layer was then spun at 2700 RPM for 2 min. on top of the thick, cured layer still resting on the Teflon surface, followed by nanocarpet insertion and a final bake.

After spin-coating, a nanocarpet was carefully inserted into the spun layer of uncured RTV by inverting the nanocarpet without contacting the CNTs, and gently setting it into the layer. No additional force was applied to the growth substrate's backside. The entire assembly composed of the glass slide, uncured RTV layer, nanocarpet, and growth substrate (and also the Teflon piece and double-sided tape, if used) was baked at 80 °C overnight. Following baking, the quartz growth substrate was easily removed by gripping the sides using tweezers and lifting the substrate piece directly upward, releasing it from the nanocarpet now implanted in the cured RTV layer.

For the thin layer process sample, made without the Teflon piece, sections of the cured RTV layer far away from the nanocarpet implanted region were partially released and peeled up from the glass slide using a razor and tweezers, and the thickness of the RTV layer was measured to be 36 μm (± 2.5 μm) using a vernier thickness gauge, providing an average measurement over the gauge face area of 0.28 cm^2. This thickness was later confirmed in a specific location using SEM. The final result is shown in the lower portion of figure 5.1. For the thin-on-thick process sample made using the Teflon piece, the thickness of the first, thick layer of RTV was 630 μm, measured by optical microscopy, and the thickness of the second, thin layer of RTV into which the nanocarpet was anchored was 26 μm measured by SEM. This sample is shown in the lower part of figure 5.2 and in figure 5.3.

In order to verify that nanocarpets are firmly anchored within the RTV using this method and to demonstrate the feasibility of its application in experiments on friction drag reduction, the thin-on-thick process sample was placed in a 5.5 m/s

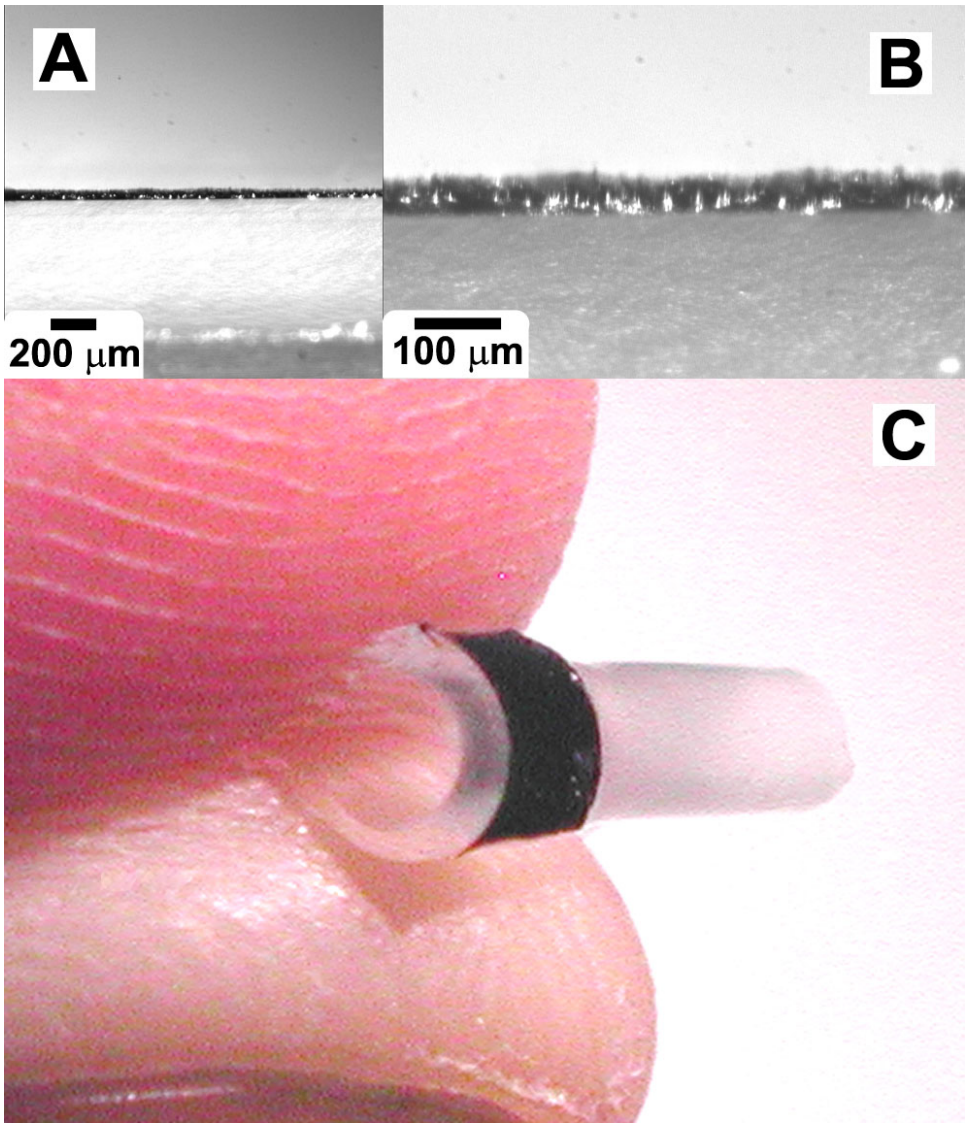

Figure 5.3: Images of a nanocarpet anchored within the top surface of a relatively thick transparent elastomeric film, using the "thin-on-thick process." (**A**) Low magnification optical micrograph of the cross-section, showing the transparent 630 μm thick RTV layer underneath the second RTV layer with the nanocarpet anchored within it. The black layer is the nanocarpet, and the dark gray region at the bottom of the image is the sample holder for the imaging. Scale bar is 200 μm. (**B**) High magnification optical micrograph of the same sample showing the black nanocarpet protruding from the 26 μm thick RTV second layer, which is joined to the thick layer underneath. The total nanocarpet thickness is about 51 μm. Some sections of the thin RTV layer reflect the incident light and appear white in the image. Scale bar is 100 μm. (**C**) The entire sample shown in panels **A** and **B** has been remounted in another RTV layer and is held between fingertips, demonstrating high flexibility of the free-standing composite, transparency of the elastomeric anchoring material, and opacity of the densely packed nanocarpet. The nanocarpet is clearly anchored solely within the upper surface of the elastomer.

water jet impinging at 45°. This experiment was designed to create a realistic wall shear stress on the anchored nanocarpet, similar to that expected for full-size ships at moderate speeds (10 knots). Though real watercraft may experience turbulent boundary layer flows at length-based Reynolds numbers of up to 10^{10}, a power-law fit to measured wall shear stress data obtained from a turbulent boundary layer with length-based Reynolds numbers of up to 2.1×10^8 predicts a wall shear stress of between 260 and 440 dynes/cm^2 for 6 m/s freestream velocity [79]. The wall shear stress caused by the 5.5 m/s impinging water jet was estimated to be 230 dynes/cm^2 using the classical Hiemenz flow solution for a plane stagnation flow [80]. The optical micrographs in figure 5.4 were taken before and after the jet experiment, and along with visual observation, they clearly indicate that no regions of the nanocarpet were removed from the RTV in which they were anchored. Thus, even at realistic levels of wall shear stress, an anchored nanocarpet produced by this method remains held within the anchoring material.

In summary, this letter has demonstrated the anchoring of nanocarpets within flexible, transparent RTV layers using a simple method of spin-coating and nanocarpet insertion followed by curing and removal of the nanocarpet growth substrate. Free-standing films and thick polymer layers with nanocarpets anchored only within the surface can easily be created. SEM and optical microscopy have been used to verify the morphology of these anchored nanocarpets, and an impinging water jet experiment has confirmed their resistance to realistic shear stresses. The key features of this anchoring method are controllability over the depth of anchoring of the constituent CNTs (and therefore the entire nanocarpet), retention of CNT growth patterns, and full scalability to larger sample areas. This method has general applicability to other anchoring materials or nanostructures, since the necessary requirements are that the anchoring material be capable of spreading into a thin film, the nanostructures be suitably embedded, and the process used for curing be nondamaging to the nanostructures. Many of the diverse applications foreseen for CNTs may benefit from the use of this method and the resulting improved utility of the anchored CNTs. Easier handling and the possibility for transfer from growth surfaces to other surfaces

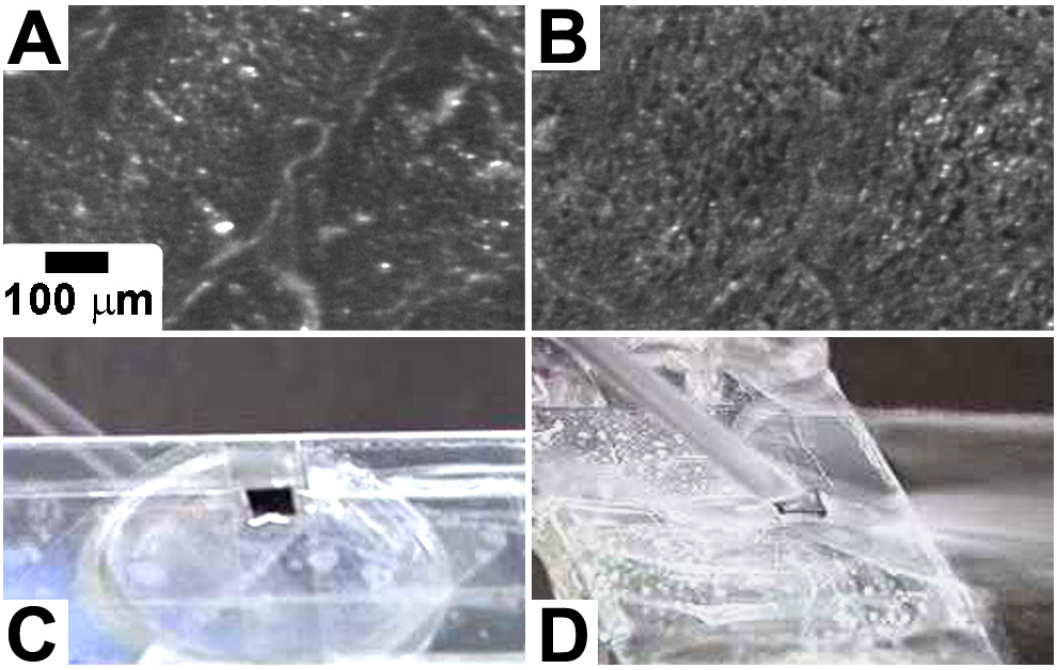

Figure 5.4: Anchored nanocarpet withstands a 5.5 m/s impinging water jet, experiencing an estimated wall shear stress of 230 dynes/cm^2, comparable to the surface of a full-size ship at a similar freestream velocity. (A) Low magnification optical micrograph of surface of the anchored nanocarpet before applying the water jet. Scale bar is 100 μm. (B) Same location and same scale as in panel A, shown after applying the water jet. Constituent nanotubes have been rearranged slightly but are clearly not removed from the anchoring layer because there are no "bald spots." (C) Image of anchored nanocarpet before applying the jet, mounted onto a glass slide. The anchored nanocarpet is black, and is 3 mm on a side. (D) Anchored nanocarpet under 5.5 m/s water jet impinging at 45°.

increases possible applications of CNTs, for example in the case of friction drag reducing surfaces in fluid flows. Further studies are needed to test this CNT anchoring method with other combinations of nanostructures and anchoring materials and to conduct detailed mechanical characterization.

5.3 Thickness of Spin-Coated Layers of Cross-Linked PDMS

One of the major advantages of the anchoring method described in §5.2 is that spin-coating can give layers of reproducible thickness. All that is required is controlling the spin-speed very accurately and allowing sufficient dwell times for spun layers to reach equilibrium thickness. For the PDMS prepolymer mix, the mix ratio is also important since it determines the viscosity of the resulting fluid mixture. Fortunately, the PDMS prepolymer components are nonvolatile so evaporation is not an issue.

A simple model exists [81] for a Newtonian liquid on a rotating disk considering a balance between viscous and centrifugal forces and predicts $h \approx \frac{1}{2}\sqrt{(3\nu/t)}\frac{1}{\omega}$, where h is film thickness, ν is kinematic viscosity, t is time the liquid layer has been spun, and ω is the rotation rate (spin-speed). It is convenient that the film thickness is independent of the radial location on the disk. If sufficient time is allowed and excess liquid at the edges can be flung off the disk while spinning, then $h \sim \omega^{-1}$ when comparing between speeds and using the same liquid.

Typically in methods using spin-coating as a step, an empirical chart is first constructed for various speeds and then used to achieve predetermined layer thicknesses in future fabrication runs. Such a chart was constructed using a high quality spin-coater (Specialty Coating Systems, Indianapolis, IN) with the cross-linked PDMS prepolymer (RTV615, GE Silicones, Wilton, CT) in the standard 10:1 ratio by weight and is shown in figure 5.5. Prior to spin-coating, the prepolymer mixture was degassed in a vacuum bell jar until all trapped bubbles were removed. Degassed prepolymer was then carefully poured onto a vacuum chuck-mounted glass slide, which had first been

rinsed in acetone, IPA, and deionized water and then nitrogen dried. The glass slide was then spun for 30 seconds at 200 RPM to spread to the prepolymer, and then spun at the desired spin speed for 60 seconds to achieve the final layer thickness. The final thickness after cross-linking is the main interest in anchoring nanocarpets rather than the thickness of the prepolymer layer. The thickness after cross-linking is also easier to measure. Each slide coated with prepolymer in the above way was immediately moved to an oven set at 80 °C and baked for an hour or more to cross-link the PDMS.

Following cross-linking, a fresh razor blade was used to carefully scrape away part of the cross-linked PDMS so that local slide thickness measurements could be made and compared to the total thickness of the slide and the cross-linked PDMS layer adhered to it. A micrometer was used and careful measurements were taken and averaged to obtain the spin-speed curve. The uncertainties of the micrometer measurements are estimated at ± 1.3 μm based on one-half the smallest graduations of 0.0001 in. The power-law fit shows the exponent on ω to be -0.86, in fair agreement with the -1 exponent predicted from theory.

This spin-speed curve was then used later to achieve desired thicknesses of cross-linked PDMS for the experiments using anchored nanocarpets in chapter 6. It is explained in detail here both for reference and the relevance to the use of spin-coating as part of the method for anchoring nanocarpets. Various similar curves could be constructed for other mix ratios of prepolymer for cross-linked PDMS, or even for other curable polymers, though volatility is a very important factor for consideration in creating spin-coated layers of reproducible thicknesses. It is important to note the range of thicknesses possible for cross-linked PDMS obtained via spin-coating. The minimum possible thickness seems to be 15–20 μm, and 160–200 μm or so seems to be the maximum. This is a limitation of the technique itself, not the equipment being used. This is also the range of possible anchoring layer thicknesses if using cross-linked PDMS as the anchoring material and spin-coating as the method of generating the layer.

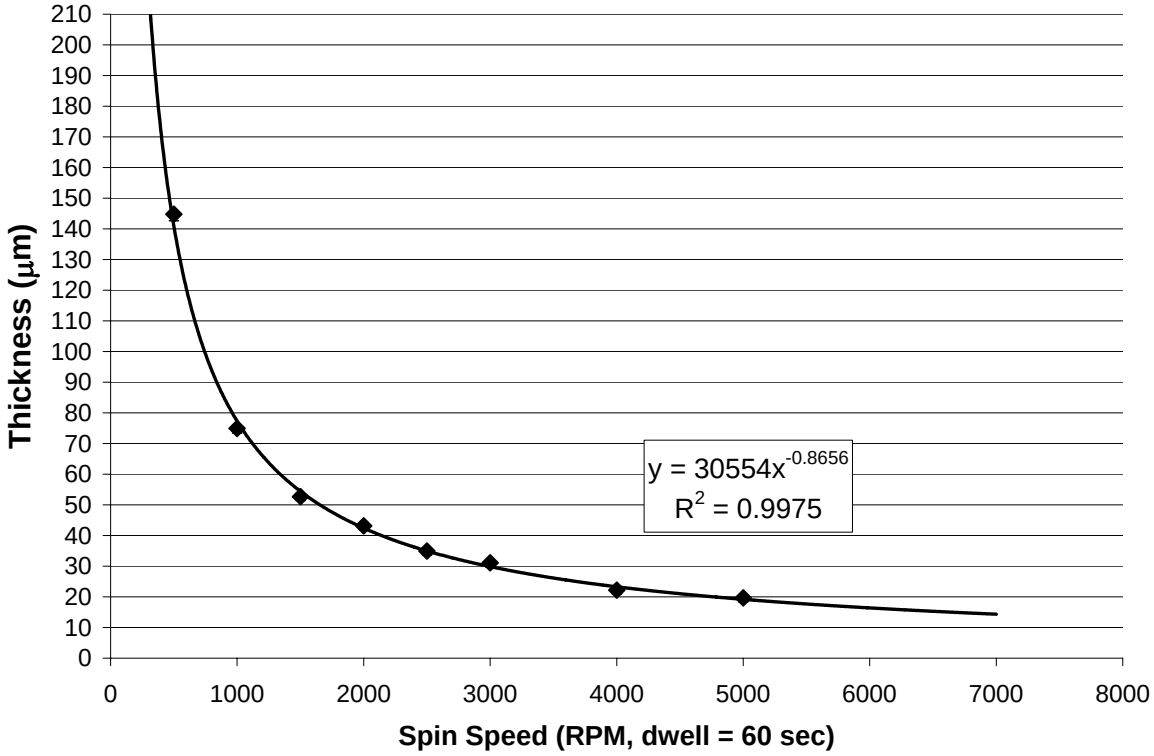

Figure 5.5: Spin-speed curve showing thickness vs. RPM for cross-linked PDMS generated using a spin-coater and GE Silicones RTV615 at the standard 10:1 mix ratio. Cross-linked PDMS films were spun on cleaned glass slides and thicknesses carefully measured using a micrometer with estimated error of ± 1.3 μm. The data are well-fit by a power-law with exponent -0.87.

5.4 Anchoring Nanocarpets in PMMA

It will be shown in the experiments described in chapter 6 that it is necessary to create anchoring layers that do not interact unfavorably with PDMS oil, which is desired for use as a liquid in pattern formation experiments. It is also valuable to demonstrate that the anchoring method of this chapter may be used with other materials. Consequently, the thermoplastic polymer PMMA was selected for use as an anchoring layer material.

Various polymers [82] have been used to infiltrate CNT sheets [83] and arrays [65, 84, 85], so it was expected that it would be possible to use PMMA for anchoring nanocarpets. From the literature [86, 87, 88, 89], it was found that PMMA can be purchased already in solvent (for example chlorobenzene or anisole, from Micro-Chem, Newton, MA) or dissolved in-house. Dissolving PMMA into solution was chosen in order to use a higher than available PMMA concentration.

PMMA is widely used as a high-resolution photoresist in photolithography applications, and nanometer resolution in feature-size is possible through its use. For application as a high-resolution photoresist, it is typically desirable to spin a uniform thin film of a micron or less in thickness. In use as an anchoring material for nanocarpets, however, it was desired to spin films of at least a few microns in order to best secure the base of the CNTs in the nanocarpet. The molecular weight of the PMMA has bearing on the thickness of spun films, but PMMA concentration used in the solution is more important.

Pure PMMA powder was used as received (Alfa Aesar, Ward Hill, MA) and dissolved under a fume hood at 40 wt% in chloroform using an erlenmeyer flask with ground glass stopper. The solution was slow to dissolve and took more than eight hours while using a magnetic stir-bar and a hot plate set at 30 °C. The 40 wt% solution was difficult to work with because it was very viscous and the highly volatile chloroform solvent evaporates very quickly from the surface of the solution. A 20 wt% solution was made instead, and later the 40 wt% solution was diluted down to somewhat less than 20 wt%. Regardless, the anchoring results obtained are not comprehensive

enough to show a dependence on PMMA concentration.

The typically fast evaporation of volatile solvents in spin-coating a solution [90] adds many complications compared to a nonvolatile mixture like PDMS prepolymer. For this work, it was desired to demonstrate that PMMA may be used for anchoring nanocarpets, but much further work would be required to demonstrate doing so controllably.

Several test cases were conducted by spinning PMMA-chloroform onto glass slides without anchoring a nanocarpet into the film. One to three 600 μL aliquots of solution were placed using a pipette as quickly as possible (a couple of seconds) onto the glass slide that was then spun at 1000-3000 RPM for 10 seconds. Following spinning, the test slides were baked on a hot plate at 150 °C for an hour to remove any remaining solvent, and then cooled to room temperature. Chloroform boils at 60 °C, and some bubbling in the PMMA film was observed, especially at the edges of the spun film, which typically did not reach fully out to the edges of the glass slide before it stopped spreading. For the nanocarpet anchoring, nanocarpets were placed as centrally as possible. Measurements were made with a micrometer and showed a PMMA film thickness of about 18 μm for the 1000 RPM speed and about 13 μm thickness for the 2000 RPM speed. The measurement on the 3000 RPM speed case was inconclusive.

1000 RPM and 10 seconds total spin time (as fast a ramp up as possible) were used for all nanocarpet anchoring results. The method described in §5.2 was followed, but it was done more quickly to account for the fast evaporation of solvent. Additionally, no extra layers such as Teflon pieces were required because it was desired to adhere the PMMA anchoring layer directly to the glass slide with the nanocarpet anchored within it. A razor blade was used to attempt to scrape off PMMA from the glass slides in the test cases, and the PMMA was verified to be very firmly adhered to the glass.

Immediately following the spinning of the PMMA-chloroform film onto the glass slide, a nanocarpet on its growth substrate was inverted and placed into the film by holding the sides of the growth substrate using tweezers. The entire assembly was then moved to a hot plate at 150 °C for an hour or more to bake off any remaining

solvent. After cooling, the growth substrate was removed by gripping it at the edges with tweezers and lifting directly upward, leaving the nanocarpet anchored in a few micron thick PMMA film on glass.

A same scale comparison between the edge region of an as-grown nanocarpet and a nanocarpet anchored in PMMA using this procedure is shown in figure 5.6. The effect of anchoring and the presence of the PMMA in the anchored sample is clearly visible. Further PMMA anchored nanocarpet results are shown in Figures 5.7, 5.8, 5.9, and 5.10. In general, due to charging effects (and its consequent low imaging contrast in the SEM), working distance limitations (the glass slide is rather large for the SEM), and unavailability of clearly visible edges, it was very difficult to obtain SEM measurements of the anchored depth within the PMMA. Occasionally the upper surface of the anchored nanocarpet would have nonvertical directionality, indicating the growth substrate had not been lifted directly upward. Large height variations or bald spot defects in the original as-grown nanocarpets were translated as void regions in the anchored nanocarpets, as the tips of the as-grown nanocarpets did not reach the PMMA layer. Blowing on the anchored nanocarpets using compressed air did not dislodge any CNTs nor visibly disturb the nanocarpets.

5.5 Chapter Summary

In this chapter, results were presented demonstrating a method of anchoring nanocarpets within another material. There are many reasons for doing this, most notably ease of handling and for specific applications that require CNTs to be held down, such as in electronics and on surfaces in contact with fluids.

Two versions of the method were demonstrated using cross-linked PDMS, those being the single layer "thin layer process" and the multi-layer "thin-on-thick process." Particularly with the thin-on-thick process, freestanding materials containing well-anchored and exposed CNTs can be created. It seems possible that, were the nanocarpets originally grown in a pattern rather than one large continuous area, the pattern could be retained through the inversion transfer process and the result would

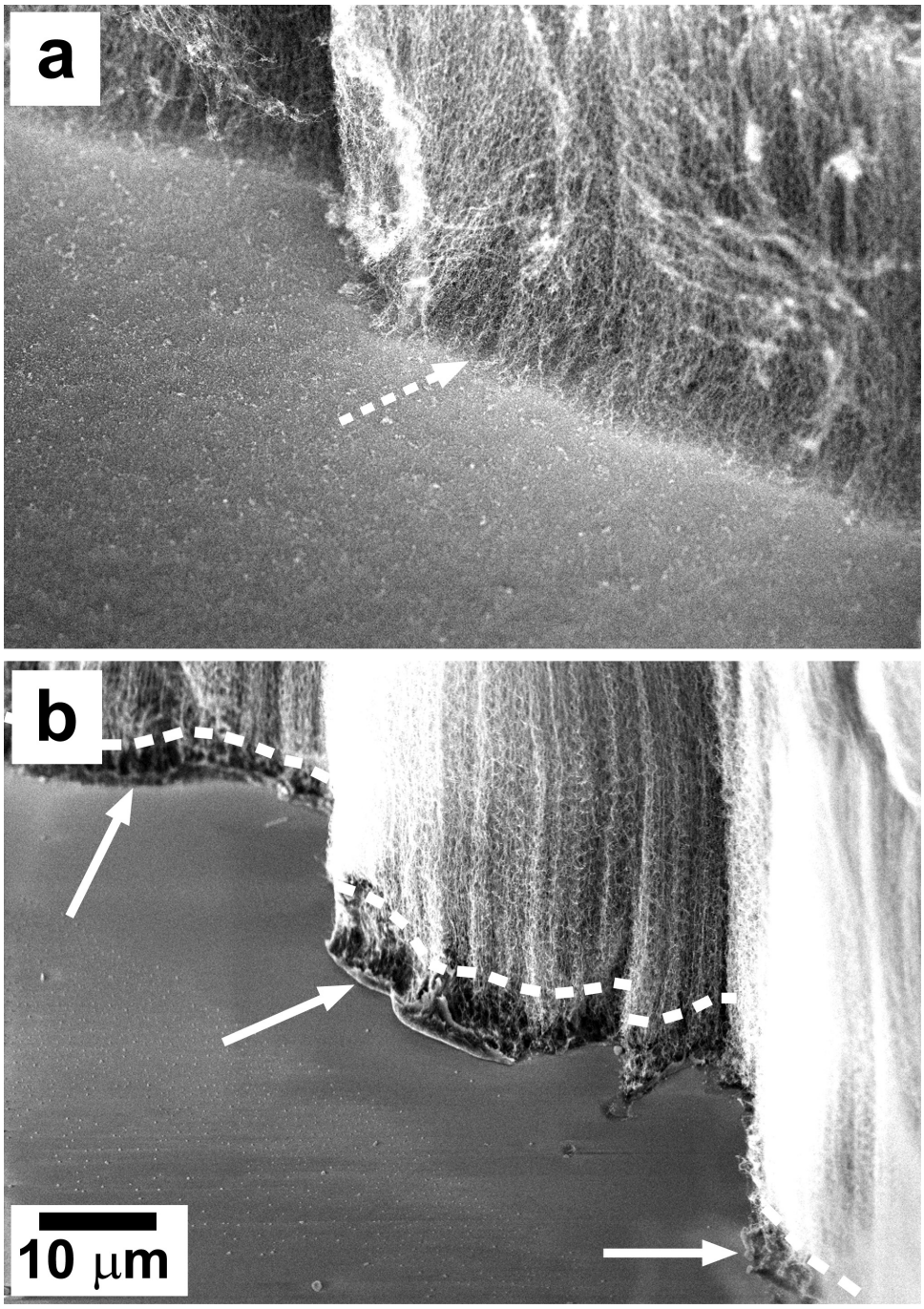

Figure 5.6: SEM images comparing the base of an as-grown nanocarpet to a similar location in a PMMA anchored nanocarpet. (a) As-grown nanocarpet, 40 μm tall, on silicon growth substrate, viewed at a 60° tilt angle. The unanchored base is indicated by the dashed arrow. (b) Anchored nanocarpet, 163 μm tall, on glass slide, viewed at a 45° tilt angle. The PMMA anchoring layer at the base is indicated by the arrows, and separated from the protruding portion of the nanocarpet by the dashed line. Both images are at the same scale.

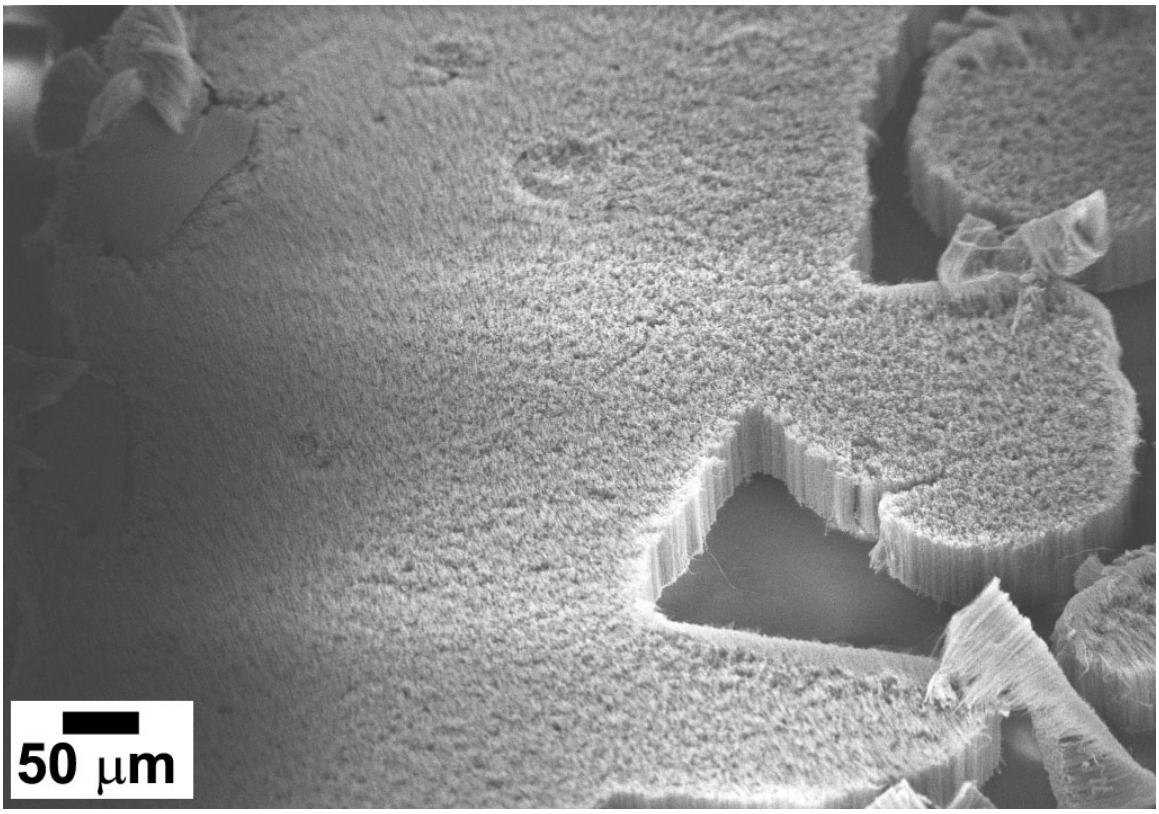

Figure 5.7: Example 1 of a nanocarpet anchored in PMMA. The nanocarpet is 79 μm tall and viewed at a 45° tilt angle. The anchoring depth was not measurable.

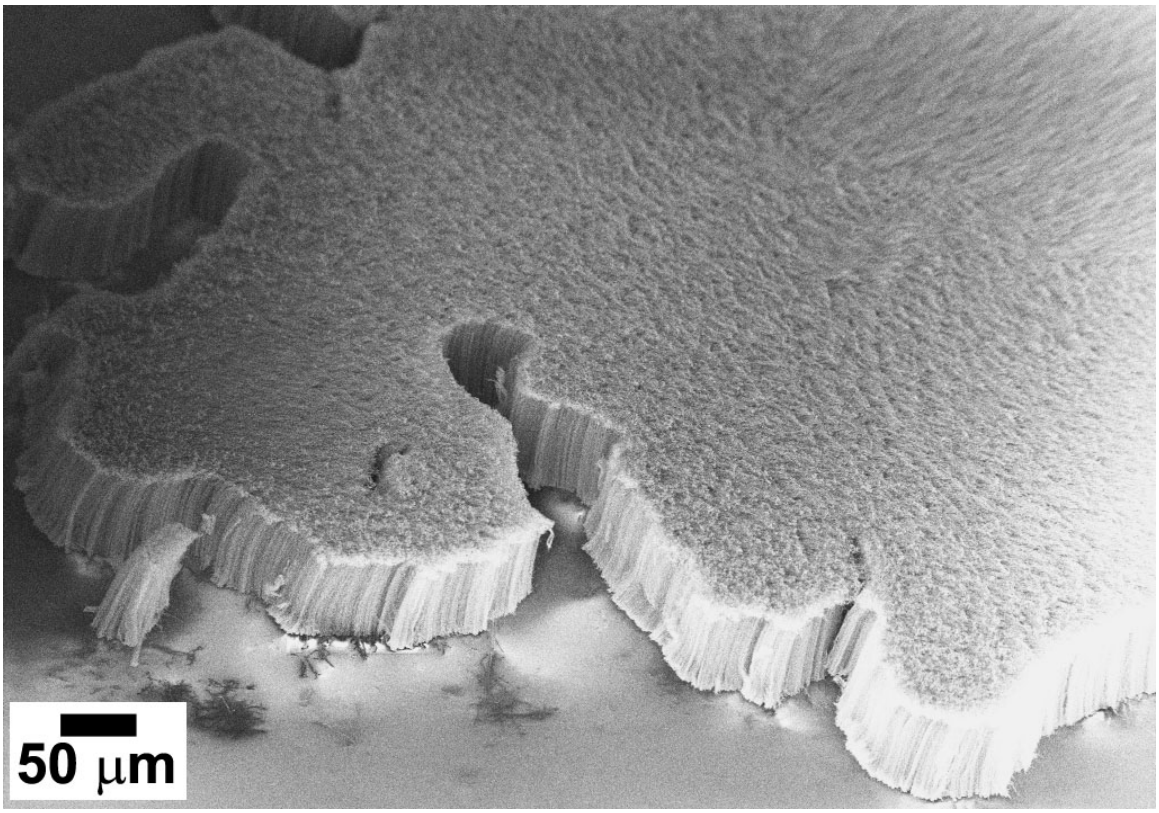

Figure 5.8: Example 2 of a nanocarpet anchored in PMMA. The nanocarpet is 81 μm tall and viewed at a 45° tilt angle. The anchoring depth was not measurable.

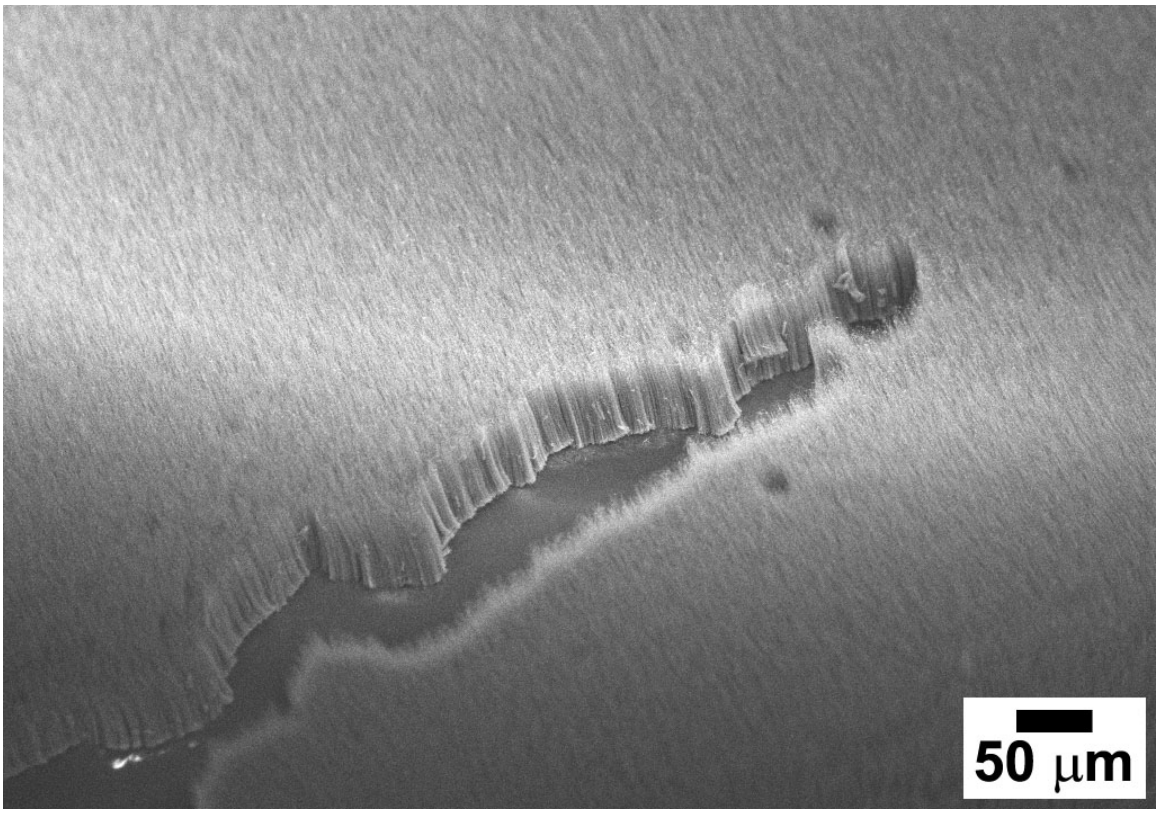

Figure 5.9: Example 3 of a nanocarpet anchored in PMMA. The nanocarpet is 61 μm tall and viewed at a 45° tilt angle. The anchoring depth was not measurable.

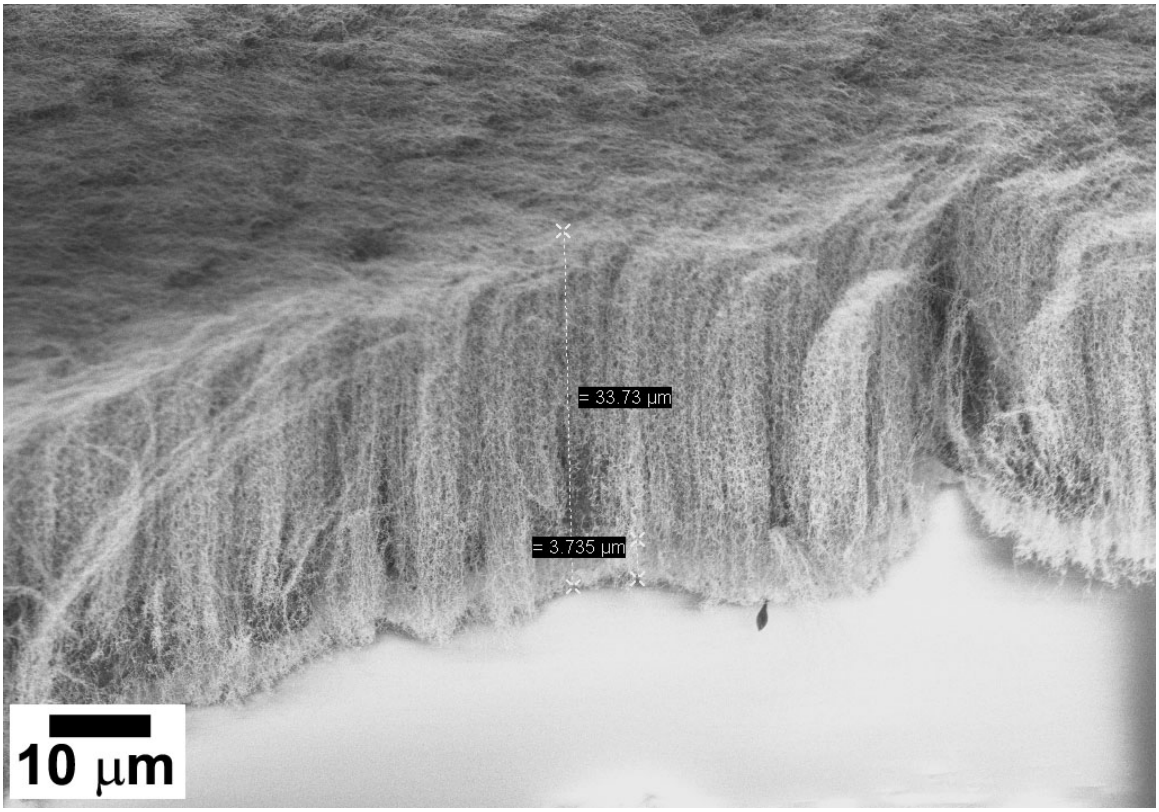

Figure 5.10: Example 4 of a nanocarpet anchored in PMMA. The nanocarpet is 48 µm tall and viewed at a 45° tilt angle. The anchoring depth was about 5 µm.

be a freestanding, easy-to-handle material with patterns of exposed nanocarpets.

The method for anchoring was compared to other methods of forming composites with CNTs. Common contrasting methods include gaseous (CVD) or solution-based deposition of a material *onto* the CNTs, simply pouring material onto them, or spin-coating material on *top* of the CNTs. None of these other methods have possibility for control over the length of CNTs left exposed following the application of the other material, while the method presented in this chapter does have such potential.

A spin-speed curve for cross-linked PDMS in the standard 10:1 ratio was generated that compares favorably to theory and indicates that 15–200 μm is the range of possible thicknesses that may be reproducibly obtained for use in anchoring nanocarpets.

The method for anchoring was also demonstrated using PMMAfor the anchoring material, though this was more involved due to a volatile solvent (chloroform). It was difficult to measure the anchoring layer thickness (anchored depth), but it was estimated to be less than 10 μm but more than 1 μm. Anchoring with PMMA was done using only the thin layer process, not the thin-on-thick process.

The results presented in this chapter show that nanocarpets *can* be anchored within a surface, but their functionality can only be inferred from the method used and the morphology observed. It seems that none of the steps used would cause significant change in the properties of the nanocarpet, aside from the mechanical support provided by the anchoring material. The fact that nanocarpets anchored in this way are inverted from their as-grown orientation may alter their functionality as well, but this is not intended to be addressed by these results.

Chapter 6

Pattern Formation in Anchored Nanocarpets

6.1 Introduction

The method described in chapter 5 for anchoring CNTs within another material while leaving some portion of their length exposed allows for pattern formation experiments to be carried out that are distinct from those using unanchored nanocarpets in chapter 4. By conducting the experiments as similarly as possible, a direct comparison can be made, and further insight into the pattern formation process is gained. This chapter is for presenting results from these experiments. These results directly address problem statement 4 in §1.5, which was **"What differences are there, if any, between patterns produced in anchored nanocarpets and those in unanchored nanocarpets, and what does this mean?"**

6.2 Preliminary Results

Before development of the anchoring method, it was found that a simple strip of double-sided carbon tape, commonly used in SEM as a conductive adhesive for securing samples to the stage, could cleanly remove large areas of as-grown nanocarpets by adhering to them more strongly than they adhere to their growth substrates. The small strip of carbon tape (a few mm on a side) was first carefully affixed to a several-times-larger piece of silicon wafer (cm on a side) in order to give the tape rigidity

and keep it very flat. An attempt was made to avoid bubbles by flattening the tape carefully with tweezers prior to peeling off its backing. Then, using the silicon wafer for handling, the whole piece was gently laid flat on top of an as-grown nanocarpet. The backside of the silicon was then lightly tamped with tweezers. Finally, the silicon was lifted directly up by its edges using tweezers, and the carbon tape was observed to be covered by the nanocarpet, which was now removed from its original substrate, and inverted relative to its orientation following growth. SEM observations of the sample from directly above show that the nanocarpet is still composed of densely packed CNTs and that the entire area is indeed covered. An SEM image is shown in figure 6.1. The circular regions that appear to be cracked are presumably sitting atop bubbles trapped between the underlying carbon tape and the silicon backing piece. These are not really cracks as in a solid material, but rather line discontinuities in the nanocarpet's morphology. Aside from these cracked regions, the as-grown nanocarpet morphology was retained, with CNTs being vertically aligned and densely packed.

According to the manufacturer (SPI Supplies, West Chester, PA), the carbon tape is composed of an acrylic-based adhesive glue filled with particles of carbon black. It has the consistency of a very tacky goo and is solid black in color. Unfortunately, high-magnification SEM images of the edge of the nanocarpet were not taken. Thus the extent of "anchoring" of the nanocarpet within the carbon tape material cannot be verified, but it is reasonable to assume that it was anchored somewhat. Gentle airflow from a compressed air can did not dislodge any CNTs.

A several microliter aliquot of acetone was applied to the carbon-tape anchored nanocarpet, and spread immediately, wetting the entire surface, then evaporated within a few seconds. Acetone was one of the liquids being tested in patterning experiments at the time. Following the experiment, the sample was imaged in the SEM and the composite is shown in figure 6.2. For ease of comparison, both the before and after images are shown side by side in figure 6.3. The structured regions in the after image correspond directly to preexisting cracks and deformations in the before image. Aside from this defect-based patterning, there is no significant pattern formation observed.

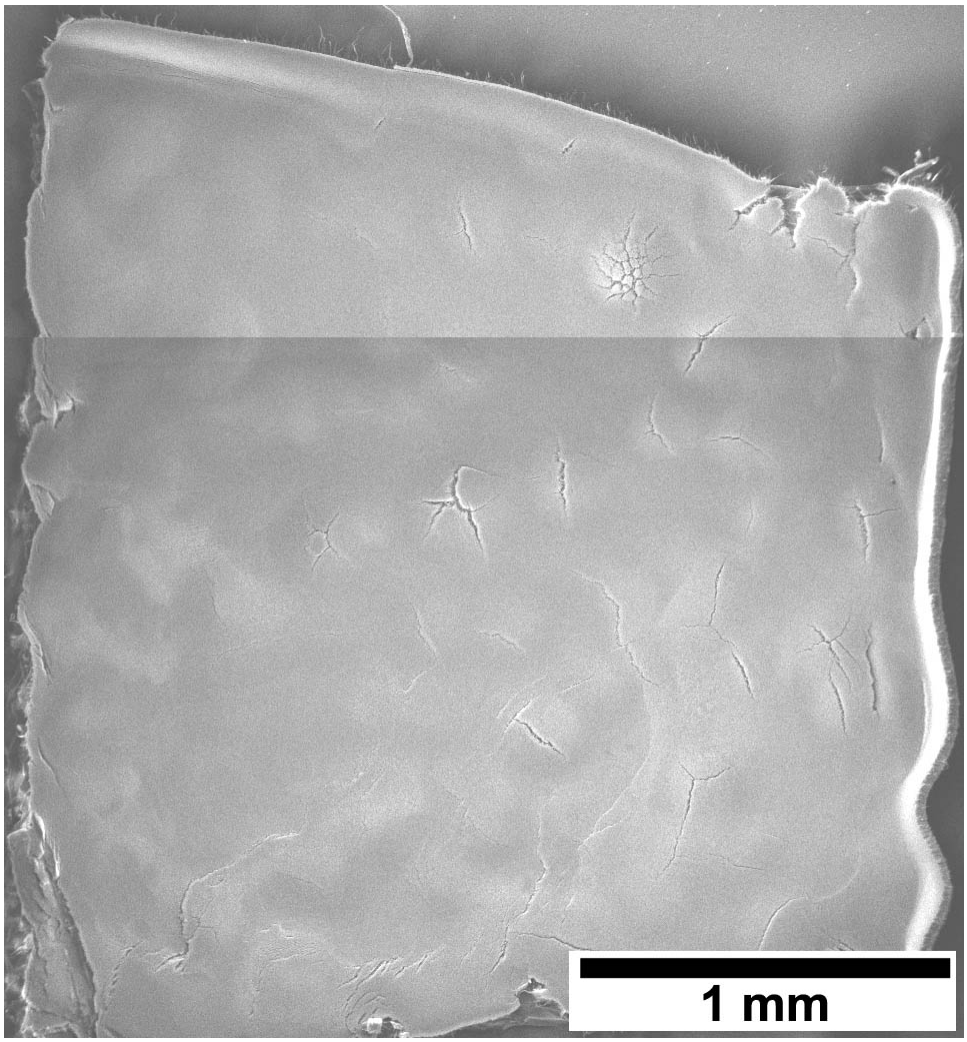

Figure 6.1: Composite SEM image of untreated nanocarpet lifted-off from its growth substrate using a piece of double-sided carbon tape adhered on its other side to a silicon backing piece. This results in inverted orientation of the nanocarpet, meaning the bottom of the as-grown nanocarpet is now the upper surface, visible in the image.

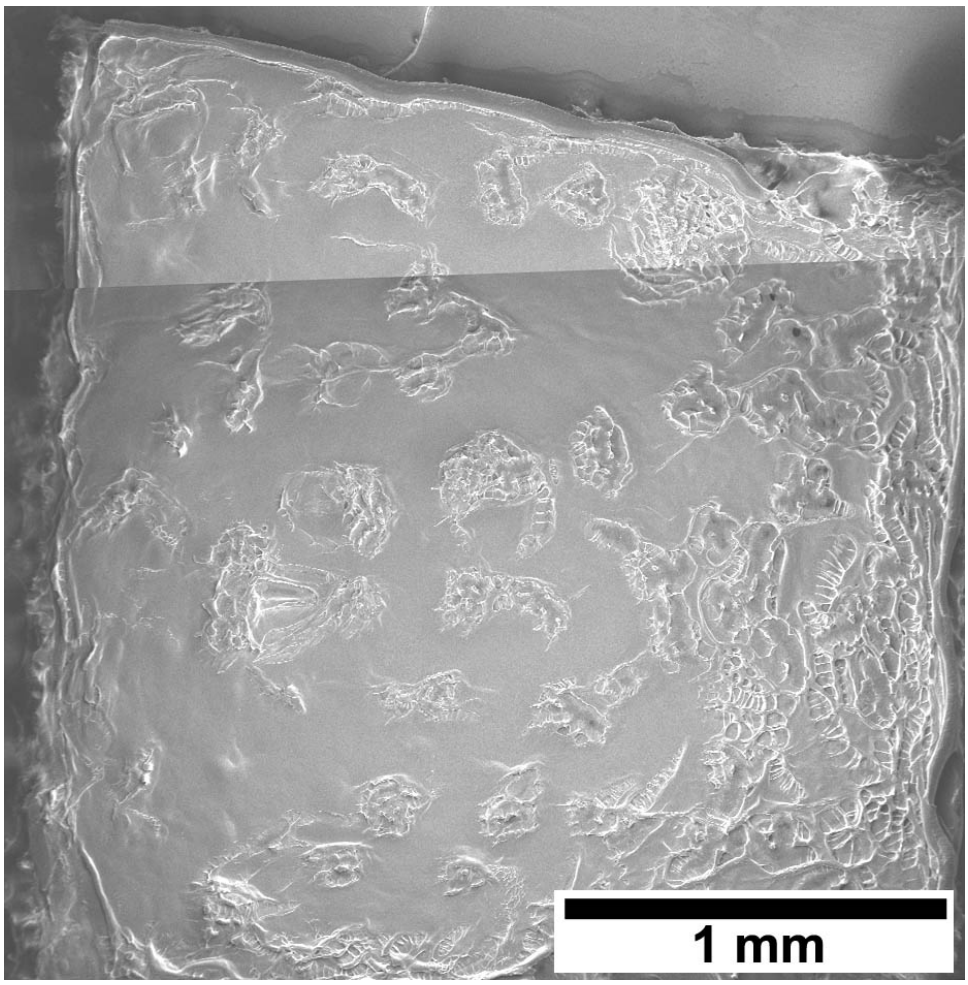

Figure 6.2: Composite SEM image of the carbon-tape anchored nanocarpet after treatment with acetone.

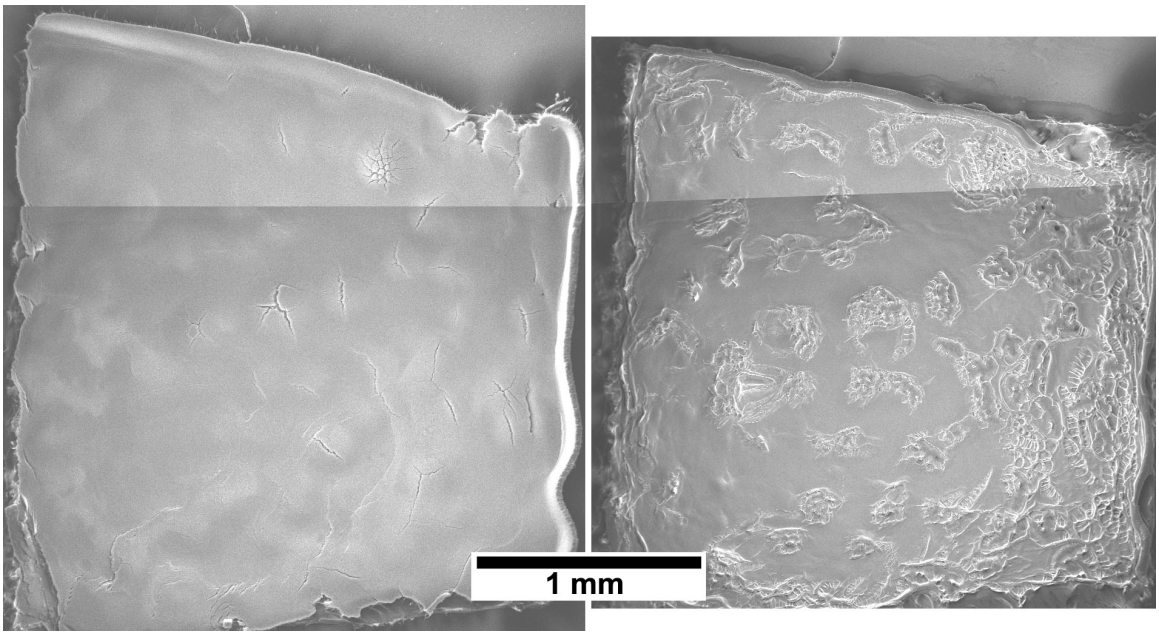

Figure 6.3: Composite SEM images comparing the before and after states of the carbon-tape anchored nanocarpet treated with acetone, shown at same scale. Left: before. Right: after.

Because the primary component of the carbon tape is an acrylic-based adhesive, it is expected that the acetone degraded and dissolved the acrylic somewhat, though not the carbon nanotubes, which are quite chemically robust to a solvent like acetone. This is a similar reaction as that used in removing nail polish, where the primary component of the nail-polish remover is acetone. Indeed, in-plane shrinkage of the carbon-tape substrate of the nanocarpet, and thus the whole sample, is observed. Comparing the before width at a given point, 2.48 mm, and the after width at the same point, 2.31 mm, as measured from the images, the shrinkage is 6.9%. Obviously the anchoring material in this experiment—the carbon tape—does not successfully withstand the liquid used, and thus no firm conclusions can be drawn. However, this remains an instructive result from the standpoint of a preliminary experiment toward understanding patterning of anchored nanocarpets. It raises the important question of whether it is at all even *possible* to obtain non-defect-based patterns in anchored nanocarpets, and highlights the importance of liquid compatibility with the anchoring material.

6.3 Patterns in Nanocarpets Anchored in Cross-Linked PDMS

The samples created in the experiments for demonstrating the method of anchoring presented in chapter 5 were exclusively made in cross-linked PDMS. Using the spin-speed curve for making layers of cross-linked PDMS with desired thickness, which was generated in the development of the anchoring method, new samples of nanocarpets anchored in cross-linked PDMS were made to be used in patterning experiments.

The first was a ≈60 μm tall (average of two measurements) nanocarpet grown on silicon, which is shown in figure 6.4. The "thin-on-thick process" multi-step anchoring approach was used for creating this anchored sample. The primary reason is ease of handling since if only a thin layer of tens of microns in thickness is used without a thick underlayer, it is very difficult to remove the layer from the surface on which it is spun and it is likely to tear during handling (dunking in liquid, moving to a dish to dry, etc.). Further, liquid surface tension will have a much greater effect on a very thin solid layer, potentially deflecting and deforming it, regardless of its material properties. Following the formation of a thick layer of cross-linked PDMS of a few hundred microns to be used as the underlayer, a spin speed of 3000 RPM was selected for the thin layer to be spun on top of the thick layer in order to give a layer of ≈30 μm final thickness, according to the empirical relationship plotted in figure 5.5.

The result of the anchoring of this sample is shown in figure 6.5. The total height of the nanocarpet at this location is about 60 μm, the thickness of the anchoring layer is about 38 μm, and thus the protruding portion of the nanocarpet is 22 μm. This is a rather inaccurate measurement however, since the cross-section of the anchoring layer is probably not a perfectly vertical sheer surface but is sloping away from the viewer, making it appear thicker in the tilted view than its actual thickness. Also, the removal of the silicon growth substrate was apparently not in a perfectly upward direction, since the entire area of the nanocarpet has a nonupward directionality to it. This makes the measurement of total height less accurate than if it were perfectly

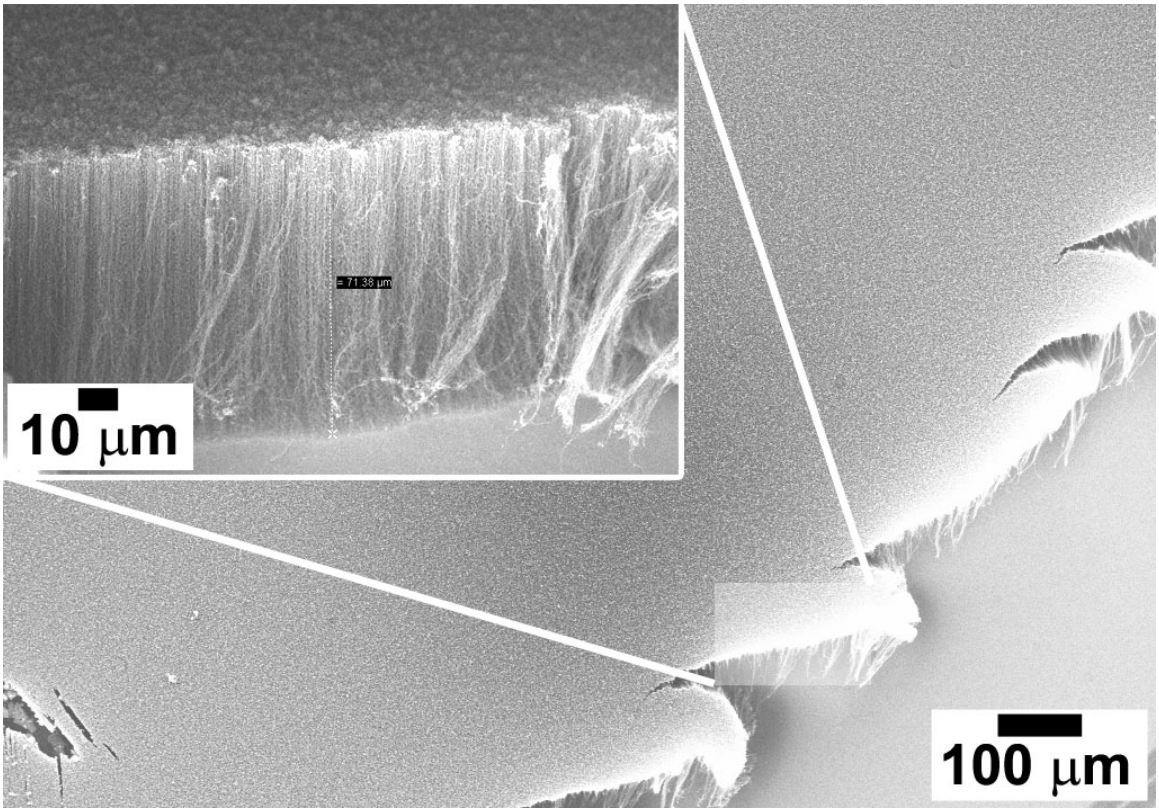

Figure 6.4: Characterization SEM images of as-grown nanocarpet with height ≈60 µm. Inset is magnified view at a 60° tilt angle.

upward.

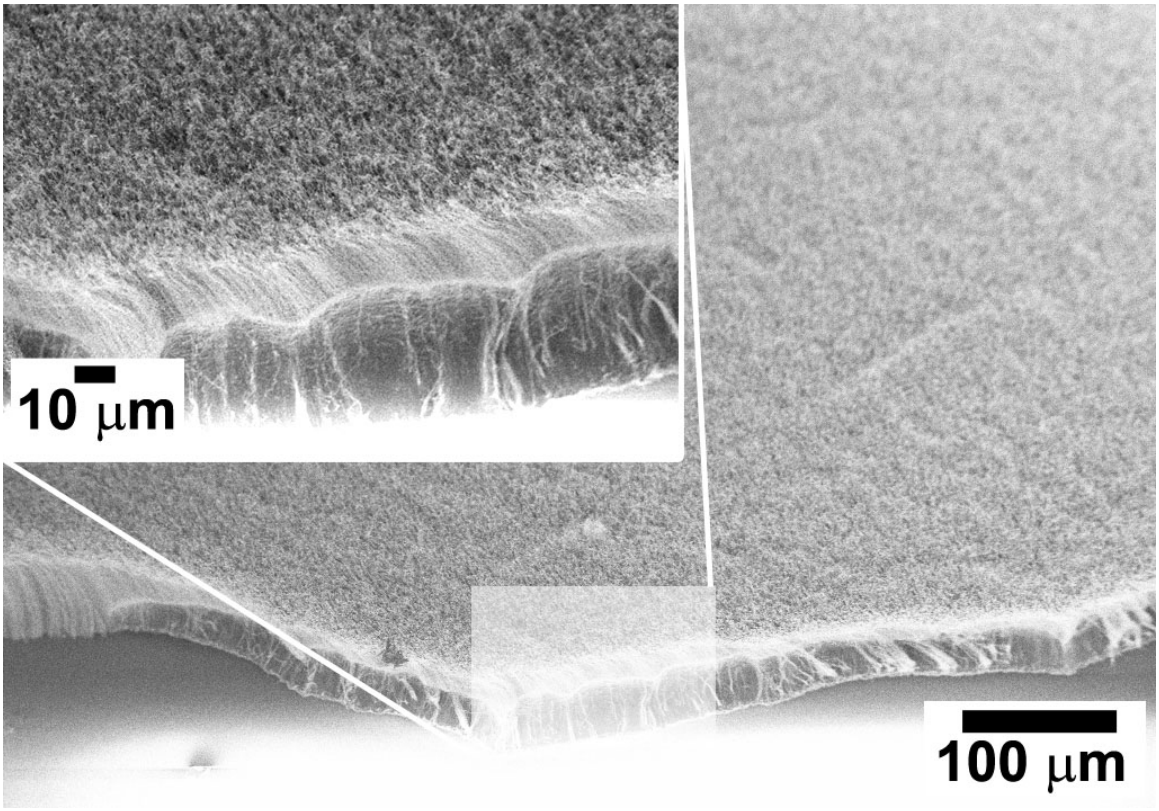

Figure 6.5: Characterization SEM images at a 45° tilt angle of the sample in figure 6.4 after anchoring in cross-linked PDMS.

As determined in chapter 4, patterning experiments by dipping in the liquid followed by upside down drying in a dish seem to give the most reproducible results. This is probably due to a combination of factors, such as reduced evaporation rate, uniformity of evaporation and uniform initial application of liquid to the nanocarpet. Consequently, this method was used for the nanocarpet anchored in cross-linked PDMS, with 1 cSt PDMS oil as the liquid. However, during the experiment it was observed that the entire piece of cross-linked PDMS with the nanocarpet anchored in its surface flexed upward very significantly while it was sitting in the petri dish during drying. Images of this behavior are shown in figure 6.6.

Though unexpected at the time of the experiment, this turns out to be an observation of a well-known phenomenon in polymer physics called swelling and deswelling

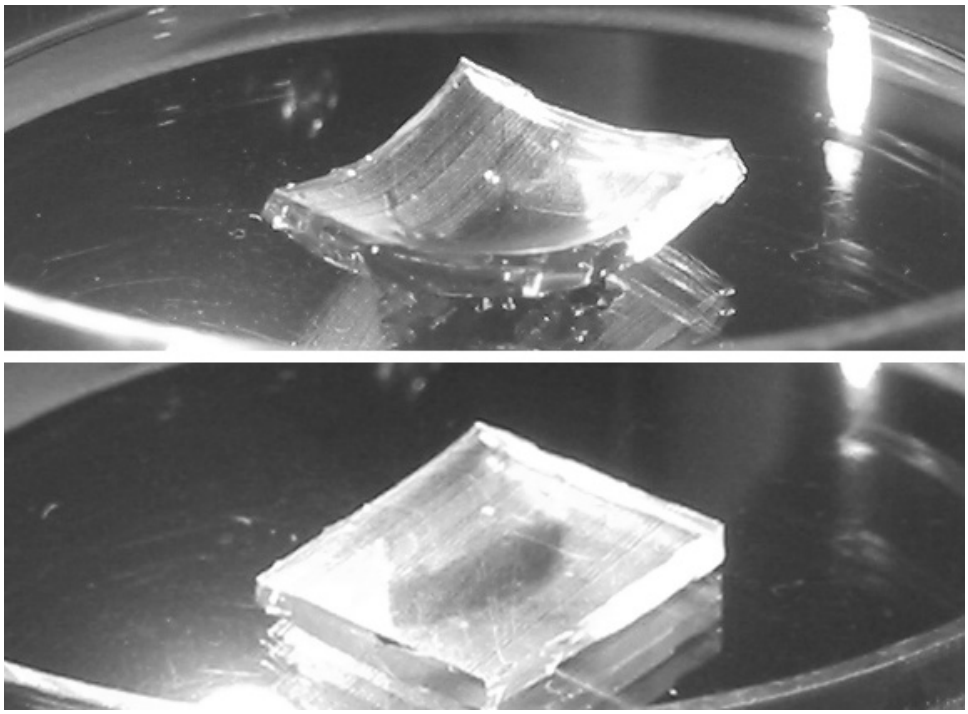

Figure 6.6: Nanocarpet sample anchored in the top layer of cross-linked PDMS was dipped in 1 cSt PDMS oil, and is shown during (above) and following (below) upside down drying in a petri dish. The sample is about 1 cm in width and 1 mm in thickness.

[91]. Cross-linked PDMS is a very common polymer used in making microfluidic devices in particular. As such, its compatibility with various solvent liquids has been investigated. In a paper by Lee et al. [46] it is stated that "a greater degree of swelling is observed with solvents that have a value of δ [the solubility parameter] similar to that of PDMS." It also makes intuitive sense that the un-cross-linked liquid form of a polymer would interact with its cross-linked form. This is understood to occur by intercalation of the liquid molecules between the cross-linked molecules, but without actually breaking any of the cross-linkages. Thus the appropriate concept is solubility of liquid PDMS oil in the cross-linked PDMS, and not dissolution of the cross-linked PDMS into the liquid PDMS oil. Lee et al. note the usefulness of the swelling effect for removing undesirable components within the cross-linked polymer and for changing surface properties such as hydrophobicity, but for the purposes of the present investigation it is an undesirable effect because of the mechanical conditions it applies to the surface in which the nanocarpet is anchored. Lee et al. further explain that the inherently uneven evaporation, and thus uneven deswelling, of a solvent from a piece of cross-linked PDMS that is set on a surface and dried in air causes an unbalanced tensile stress on the wet side. This causes buckling in the sample, and this is exactly what was observed here in the experiment with the anchored nanocarpet sample.

Once all of the 1 cSt PDMS oil has evaporated, there is no longer any source of tension on the underside of the drying sample, and the piece of cross-linked PDMS returns to its flat, unstressed state. However, because the underside has been strained rather significantly, and the strain has then been removed, permanent inelastic deformations in the surface are likely, especially at length scales relevant to nanocarpets. This turns out to be the case, and is clearly visible in the SEM images taken after this experiment and presented in figure 6.7. This effect of "wrinkling" in the surface of cross-linked PDMS has even been used to intentionally produce self-similar wrinkle patterns [92].

Following the result of the swelling, deswelling, and buckling of the cross-linked PDMS anchoring layer, an additional attempt was made using a similar approach, except this time attaching the cross-linked PDMS anchoring layer to a glass slide

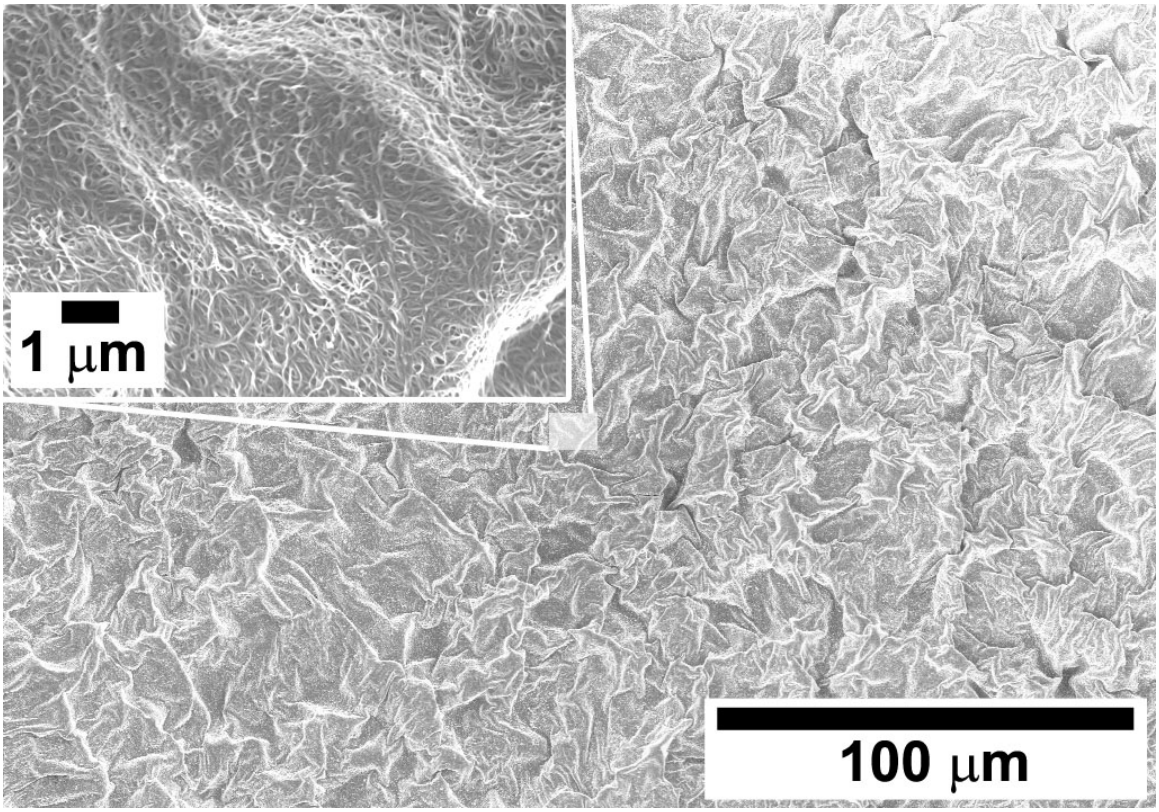

Figure 6.7: SEM images of nanocarpet anchored in cross-linked PDMS following dunking in PDMS oil and drying in a petri dish.

in order to provide rigid support. The as-grown nanocarpet sample used is shown in figure 6.8. Similar to before, the PDMS prepolymer was spun at 3000 RPM for 60 sec in order to get a ≈30 μm film following cross-linking, and it was spun onto a several-hundred-micron thick layer of already cross-linked PDMS. Following insertion of the nanocarpet and cross-linking by baking the entire sample, the section of the sample containing the nanocarpet was cut out. Another layer of PDMS prepolymer was spun onto a glass slide at 3000 RPM for 60 sec in order to obtain a ≈30 μm thick layer to join the sample containing the nanocarpet to the glass slide. The cutout section of cross-linked PDMS containing the nanocarpet was then placed into this layer, with PDMS side down and nanocarpet side up, and the entire assembly was baked overnight at 80 °C to cure. Joining two already cured layers of cross-linked PDMS by annealing in an additional baking step is known to result in attachment between the layers with interfacial strength equal to that of the bulk material [45] if excess of one prepolymer component is originally used in one layer and excess of the other component is used in the other layer. Excesses of components was not used here, but rather the curing of the prepolymer layer while in contact with the already cured layer was expected to create a strong joint and affix the entire sample to the glass slide.

Since swelling and deswelling, and therefore buckling, is essentially a chemical effect, it was expected that the surface of the nanocarpet sample would still be wrinkled following the patterning experiment, even with the addition of the rigid support provided by the glass slide. The entire assembly was dunked in 1 cSt PDMS oil and set upside down to dry in a petri dish. The sample surface containing the nanocarpet was indeed wrinkled due to the swelling and deswelling. Because of foreknowledge of the effect, careful SEM characterization was carried out before and after, allowing nanoscale comparison in the exact same location. These images are shown in figure 6.9 and clearly illustrate the wrinkling at a length scale of tens of microns, but also the interesting feature that there is almost no rearrangement of the CNTs themselves at a length scale of a few microns. No patterns of the sort we are interested in were found anywhere in the sample.

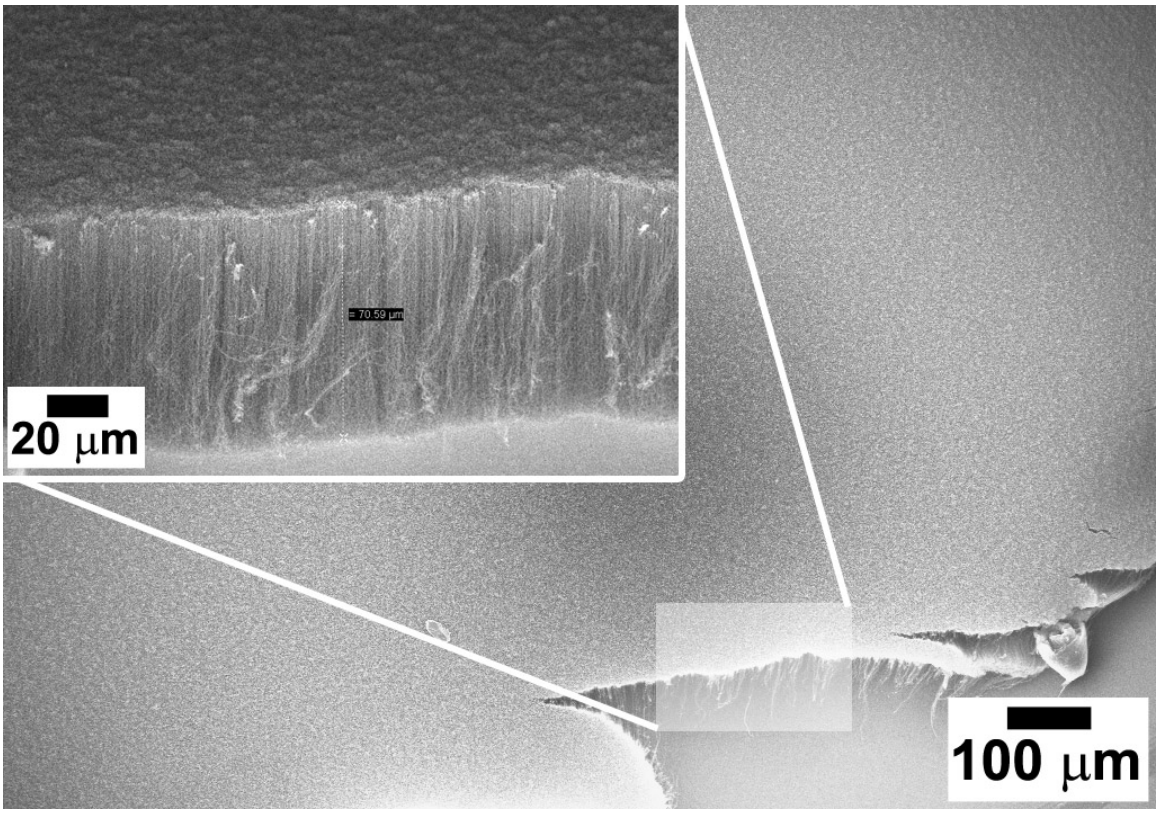

Figure 6.8: Characterization SEM images of as-grown nanocarpet with height ≈81 μm. Inset is magnified view at a 60° tilt angle.

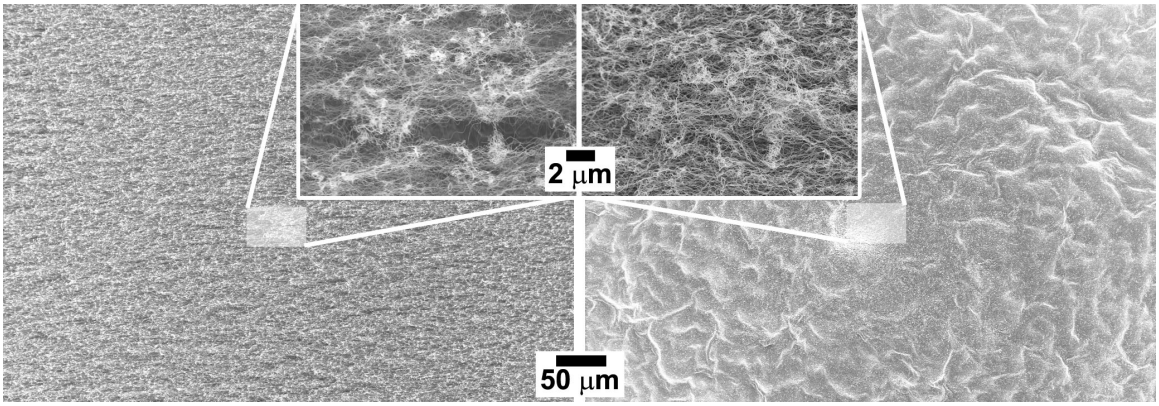

Figure 6.9: Carefully obtained SEM images of a nanocarpet anchored in cross-linked PDMS and attached to a rigid support (a glass slide) and then dunked in 1 cSt PDMS oil and dried upside down in a petri dish. The images are at exactly the same scale and location. The inset are magnified views of the centers of each of the lower magnification images. Left: before dunking and drying, Right: after dunking and drying.

6.4 Patterns in Nanocarpets Anchored in PMMA

A material was sought that could be used in the same anchoring approach but that would not swell in PDMS oil. PDMS oil was retained as the required liquid for the patterning experiments in order to best compare to previous results with unanchored nanocarpets and to continue to avoid issues with surfactants. As mentioned previously, PDMS oil has the two very important properties of being highly wetting on almost all solids, including CNTs, and of volatility similar to water if its molecular weight (which varies directly with viscosity) is very low, i.e., the 1 cSt viscosity PDMS oil used here.

The thermoplastic polymer PMMA was considered as an anchoring material. PMMA is also used for intraocular lenses to be implanted directly into the cornea of the eye, and silicone oils are sometimes used in treatment. In a published study [93], no swelling of PMMA lenses was found (by gravimetric methods) following extended contact with silicone oils. PMMAwas selected as an anchoring material and used as described in § 5.4. Two samples were anchored in PMMA and each was used in a patterning experiment. Here the samples will be termed "PMMA-1" and "PMMA-2" in order to refer to them. In the images that were obtained for the two samples, shown in figure 6.10 and figure 6.11, it is clear that the anchoring layer is more than 1 μm, but less than 10 μm.

Measuring the anchoring layer thickness in the SEM was difficult, in general, because of the high degree of image distortion from charging (due to both the PMMA and glass slide being insulating materials) and because of the rarity of unobscured visible edges in the correct orientation and near enough proximity to the sample edge for angled viewing. The total working distance of the LEO SEM used in this work is limited to about 15 mm, and care must be taken in order to avoid impacting the SEM lens with the glass slide edge. This puts a limitation on the maximum distance from the slide (or other substrate) edge that can be imaged clearly.

Similar to the thickness measurements that were made for generating the spin-speed curve for cross-linked PDMS described in § 5.3, thickness measurements of

the PMMA layers were carefully made using a micrometer by taking the difference between the glass slide thickness in an uncoated region and the total thickness in a PMMA coated region but at a location away from the nanocarpet. The glass slides used have length and width dimensions of 3" x 1" and the as-grown nanocarpets are only about 1 cm square at most, leaving a large portion of the glass slide unused. The micrometer measurements gave total PMMA layer thicknesses of 26 and 31 μm for the PMMA-1 sample and 13 and 18 μm for the PMMA-2 sample. The uncertainty in the micrometer measurements is estimated to be 1.3 μm (half the smallest graduation indicating 0.0001 in.). One explanation for why the directly measured *local* PMMA layer thicknesses in the SEM images differ significantly (e.g., 8 μm compared to 28 μm) from the micrometer measurements is that the chloroform solvent evaporates very quickly from the spun film so that the film is barely soft enough for the CNTs to be embedded under their own weight (and their growth substrate on top), resulting in a short anchoring depth within the PMMA layer. The micrometer measurement, however, is measuring the entire PMMA film thickness. Another explanation could be that the constituent CNTs of the nanocarpet do not embed at all into the PMMA film immediately following spin-coating because it is solidified too much, but during the baking on the hot plate the PMMA layer softens enough for some sinkage into the upper part of the layer. Yet another explanation could be that since the film dries so quickly upon spinning, and it is deposited from a pipette tip, the resulting film has varying thickness across the area of the glass slide substrate.

Prior to conducting the patterning experiments, a test case was conducted in which a glass slide with a spun-on PMMA film was dunked in 1 cSt PDMS oil and left to dry. No displacement of the edges of the film was visible that would have indicated swelling, and no detachment from the glass substrate was apparent. Even scraping with a razor blade could not remove the PMMA film, which indicated it was firmly adhered to the glass. In the patterning experiments using the PMMA-1 and PMMA-2 samples, the entire glass slide on which the PMMA and nanocarpet was attached was dunked in 1 cSt PDMS oil and then left to dry upside down in a petri dish. The location and length scale in the images in figure 6.12 (PMMA-1 sample)

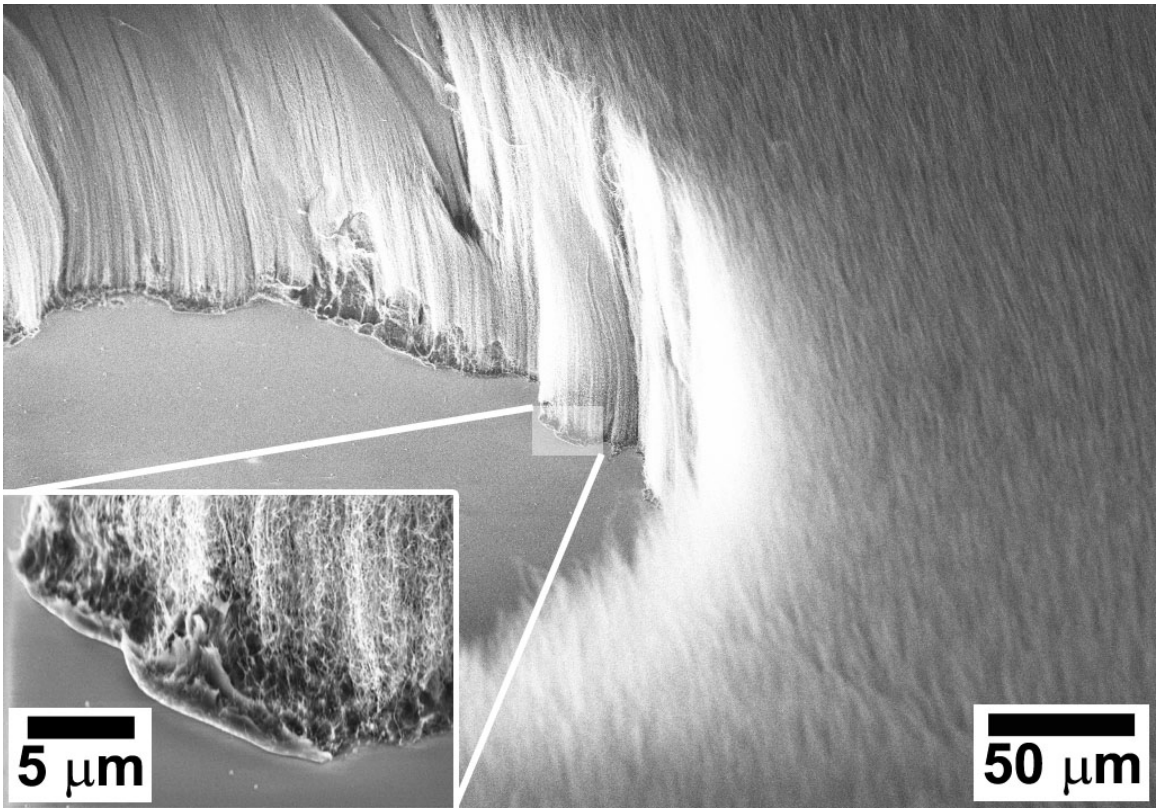

Figure 6.10: Characterization SEM images of the "PMMA-1" sample anchored in PMMA to a depth of less than about 10 μm. The total nanocarpet height is 163 μm. Both views are at a 45° tilt angle.

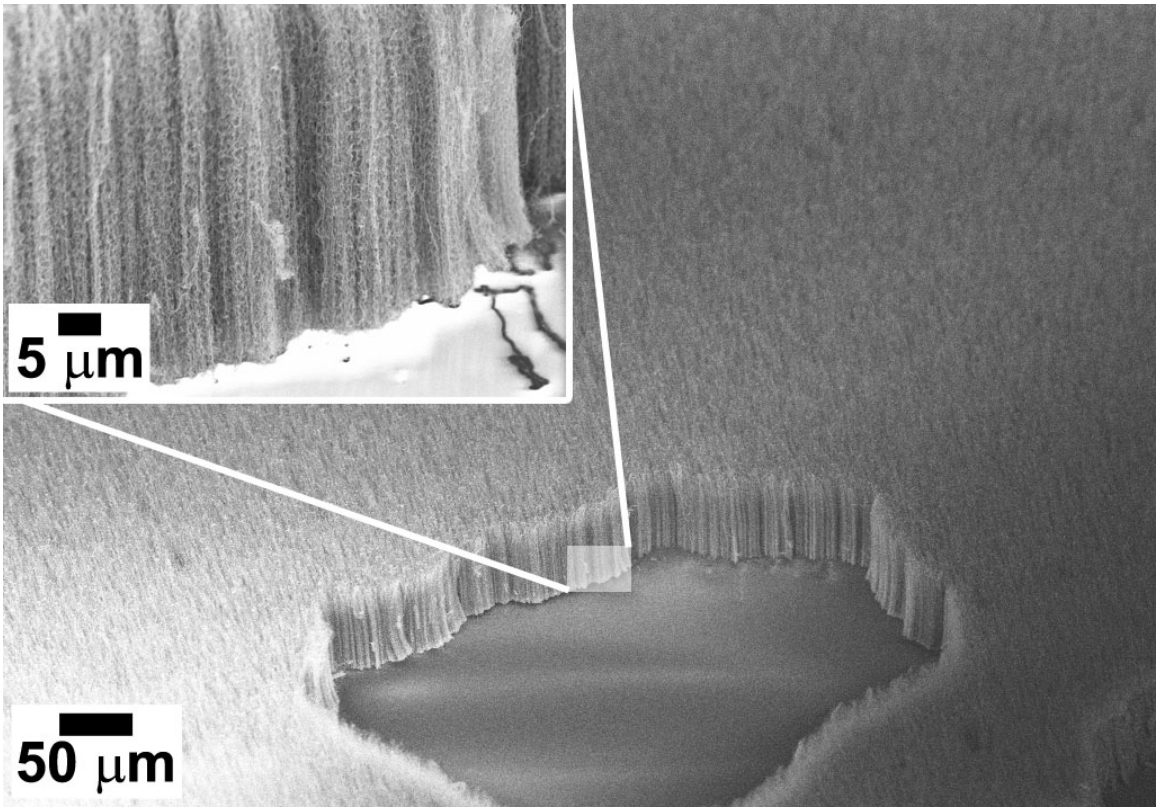

Figure 6.11: Characterization SEM images of the "PMMA-2" sample anchored in PMMA to a depth of less than about 10 μm. The total nanocarpet height is 68 μm. Both views are at a 45° tilt angle.

and figure 6.13 (PMMA-2 sample) correspond exactly to the characterization images taken before the experiment.

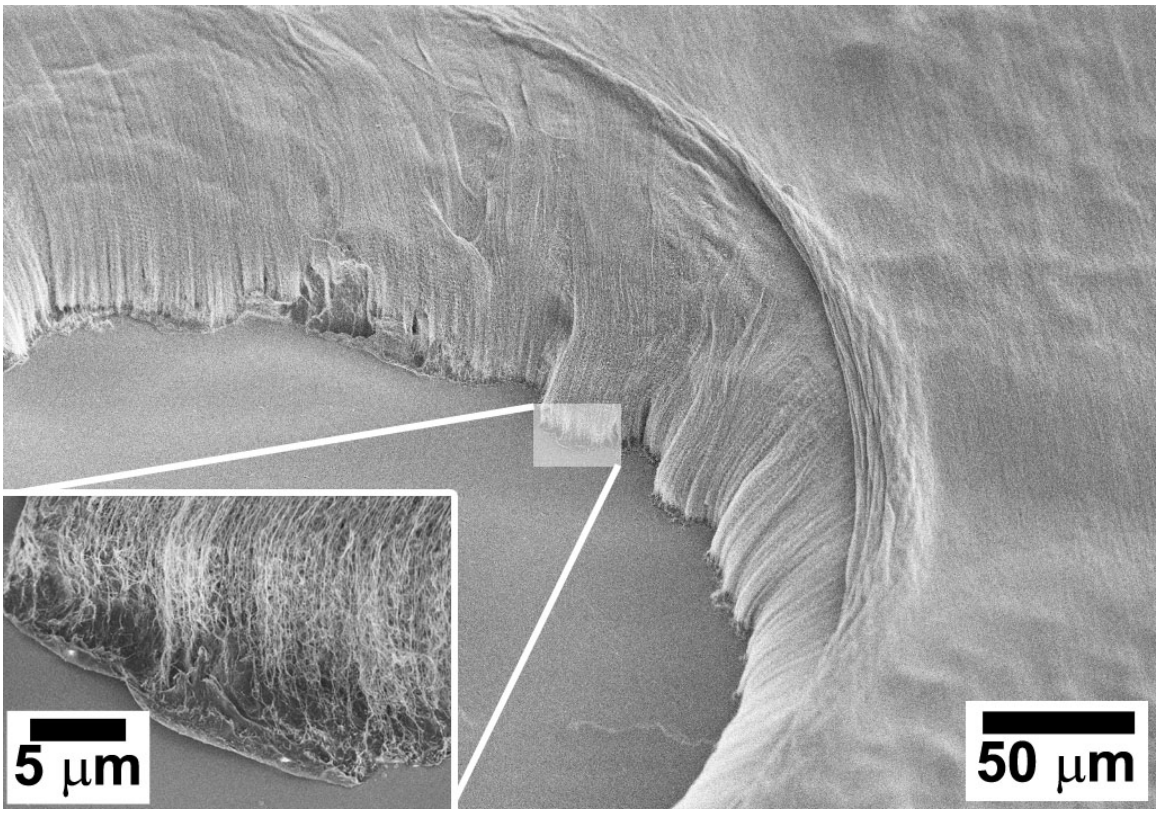

Figure 6.12: SEM images following the patterning experiment on the "PMMA-1" sample, which was anchored in PMMA to a depth of less than about 10 μm. Both views are at a 45° tilt angle and correspond identically to the images from before the experiment.

The comparison between the before and after state is important so the images for the two experiments are shown again side by side in figure 6.14 for the PMMA-1 sample and figure 6.15 for the PMMA-2 sample.

It should be immediately obvious that there is *no pattern formation* in these experiments. That is to say there are no cavity-like pattern element formations that are of interest in this thesis, even though there is some topology variation of the upper surface in the after view of the nanocarpets. An additional caveat is that in the after view of the PMMA-2 sample, there are about 8 holes visible *but*, importantly, there were darker gray spots visible in the exact same locations in the before views,

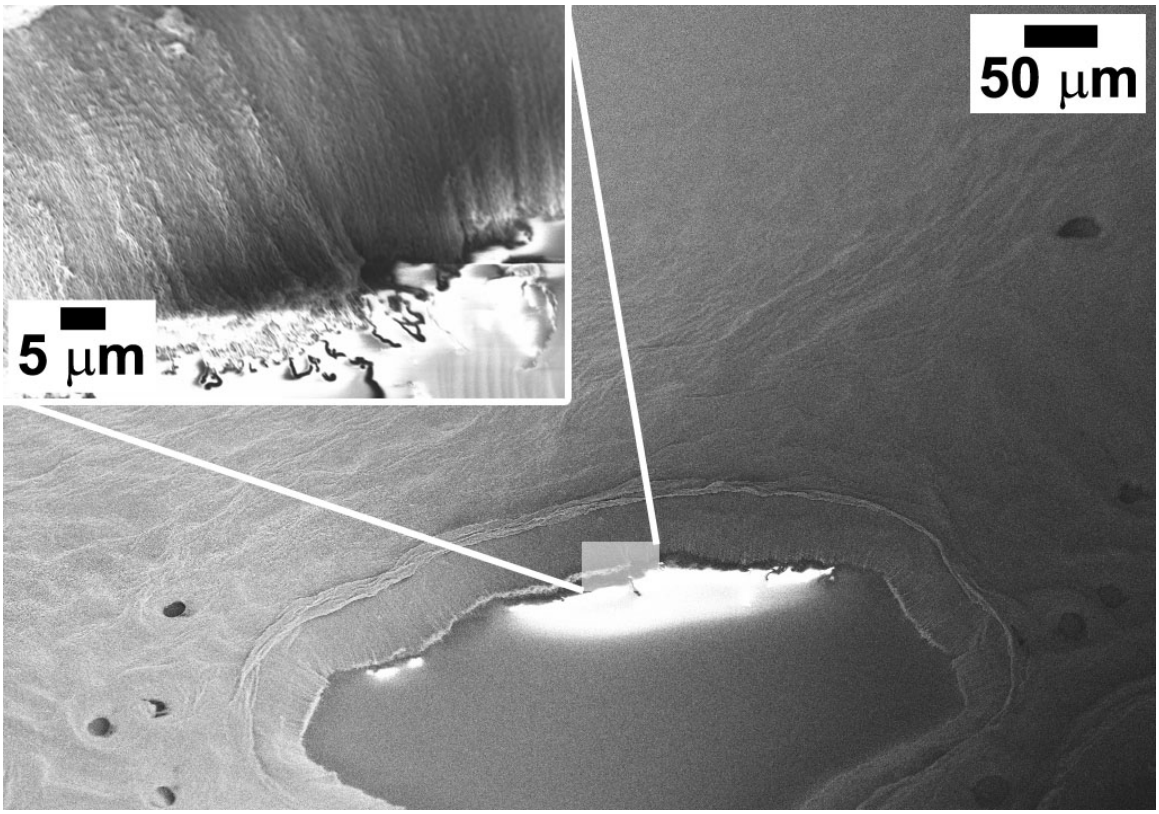

Figure 6.13: SEM images following the patterning experiment on the "PMMA-2" sample, which was anchored in PMMA to a depth of less than about 10 μm. Both views are at a 45° tilt angle and correspond identically to the images from before the experiment.

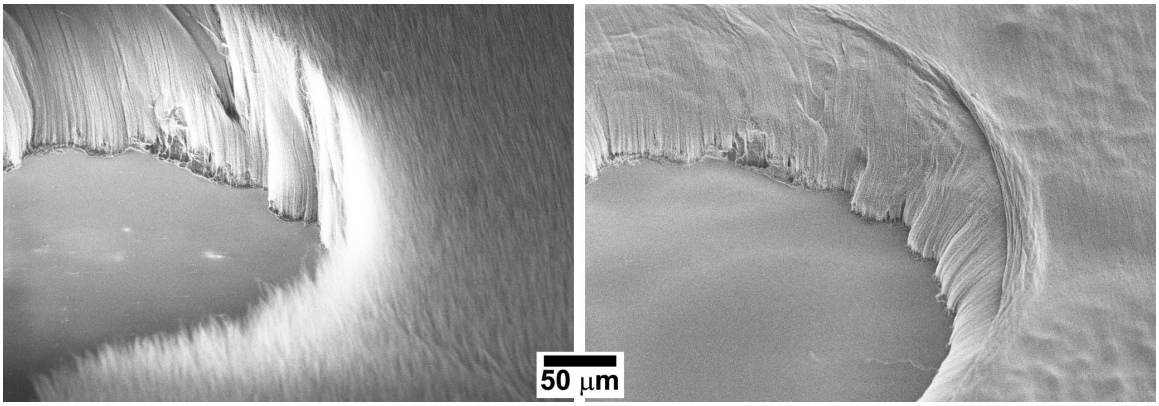

Figure 6.14: Same scale, same location, side-by-side comparison of 45° tilted view SEM images for before and after a patterning experiment using 1 cSt PDMS oil and the "PMMA-1" sample. Left: before, Right: after.

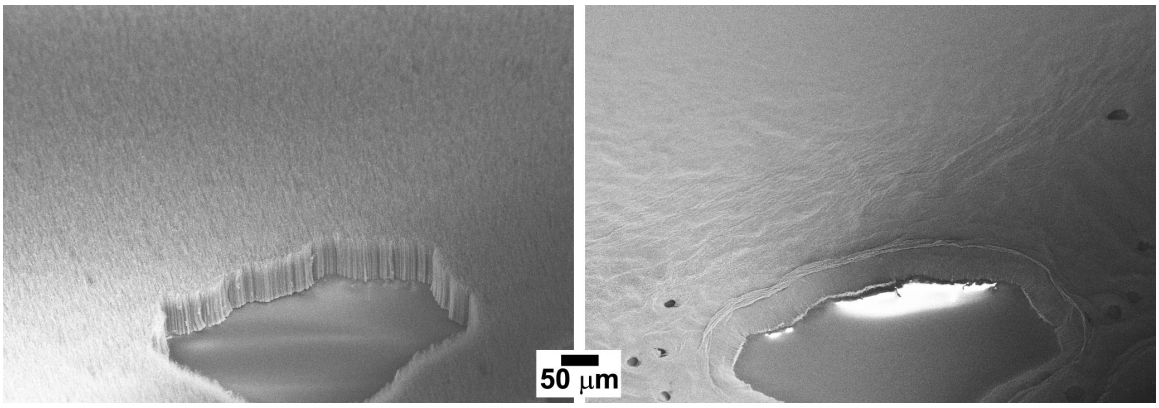

Figure 6.15: Same scale, same location, side-by-side comparison of 45° tilted view SEM images for before and after a patterning experiment using 1 cSt PDMS oil and the "PMMA-2" sample. Left: before, Right: after.

indicating these are density defect points. Thus, these are not the sort of non-defect-based patterns of interest.

This observation held true for both samples and over their entire surface. Not a single pattern element was found that could not be attributed to a preexisting defect. As further reinforcement of this point, a large area comparison view of a central region (away from any edges) for the PMMA-2 sample is shown in figure 6.16. The CNTs clearly "lay down" due to the PDMS oil wetting and drying, but no spreading apart of the CNTs has occurred.

From these results, it seems that the pattern formation of interest is not possible in anchored nanocarpets. The meaning of this will be discussed in chapter 8. Briefly, it would appear that the altering of the mechanical boundary conditions of the CNTs that make up the nanocarpet prevents their deformation and rearrangement such that they cannot spread apart and form into the patterns of interest in this thesis.

Another result that addresses the possibility of pattern formation in anchored nanocarpets is shown in figure 6.17 where, following 1 cSt PDMS oil wetting and drying of both samples, an unanchored nanocarpet is directly compared to an anchored nanocarpet. Even though the surface of the anchored nanocarpet appears to tend toward a pattern similar to that in the unanchored nanocarpet, the anchoring of the CNTs constrains their deflection and translation sufficiently to prevent the actual

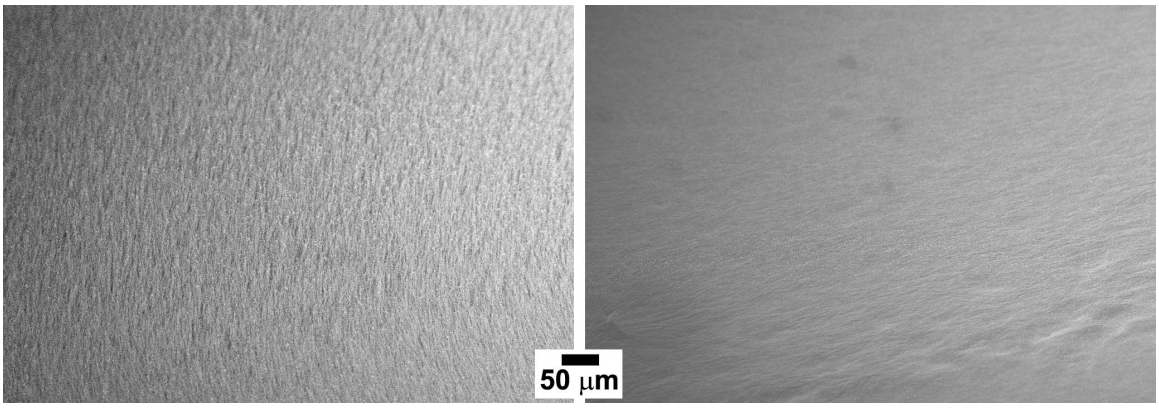

Figure 6.16: Same scale, similar but not identical location, side-by-side comparison of 45° tilted view SEM images for before and after a patterning experiment using 1 cSt PDMS oil and the "PMMA-2" sample. Left: before, Right: after.

opening of pattern elements.

6.5 Chapter Summary

In this chapter, results were presented from pattern formation experiments conducted with nanocarpet samples that had been anchored within another material. In an initial experiment, a nanocarpet stuck to double-sided carbon tape and wetted with acetone seemed to show that pattern formation did not occur except from some large discontinuities in the anchored nanocarpet.

The use of cross-linked PDMS as the anchoring material and 1 cSt PDMS oil as the liquid agent resulted in swelling and deswelling of the cross-linked PDMS layer, and buckling of the surface in which the nanocarpet was anchored. Because of this, no conclusions could be drawn about pattern formation in the nanocarpet anchored in cross-linked PDMS.

By using PMMA as the anchoring material, which did not swell upon treatment with PDMS oil, it was found in two experiments that pattern formation of interest did not occur. A few preexisting defects opened slightly but the sample surface in general was devoid of any pattern elements. The experiments were conducted in exactly the

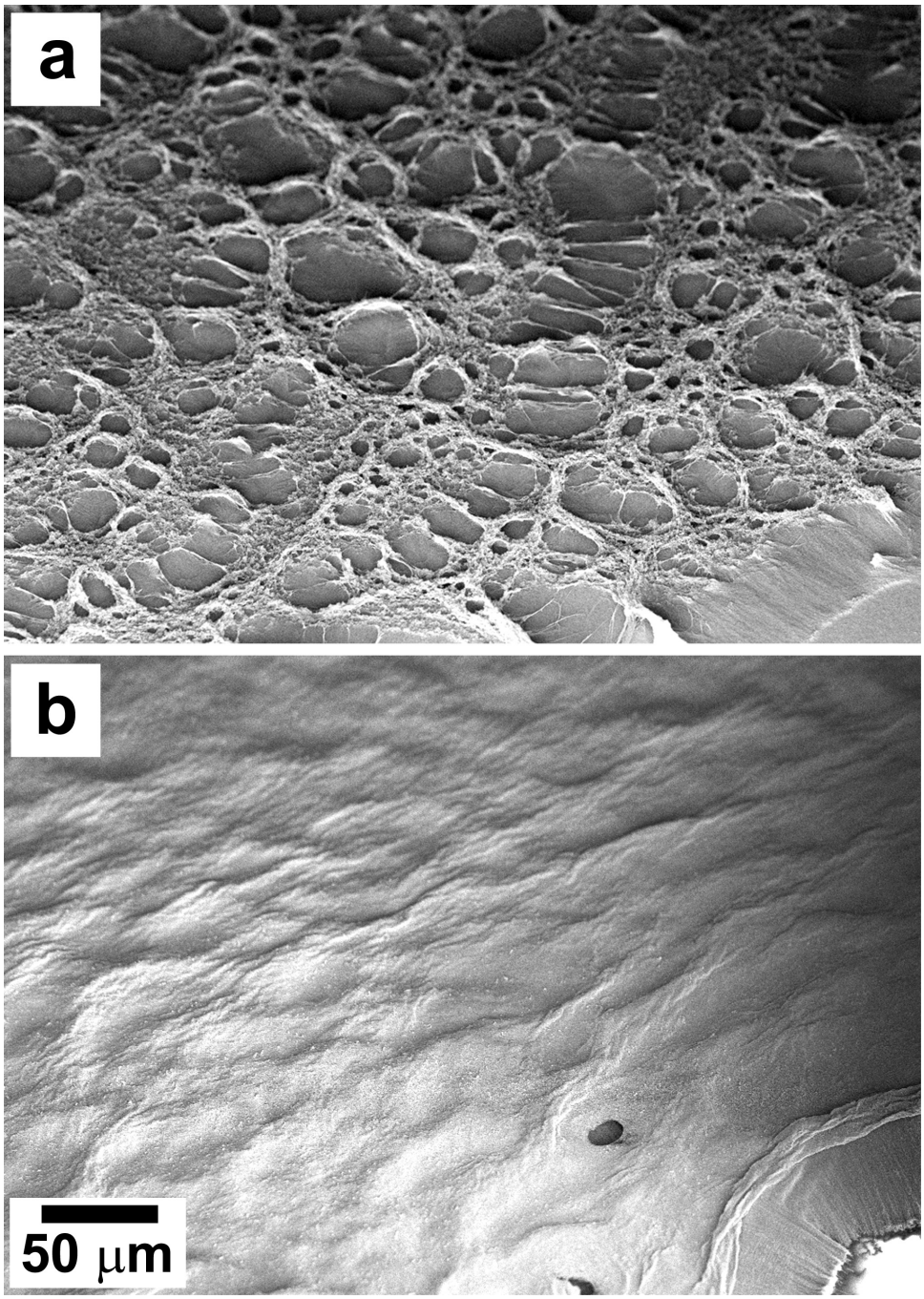

Figure 6.17: Low magnification SEM images showing pattern formation in a 73 μm tall unanchored nanocarpet in (a) and the lack of pattern formation in a 117 μm tall PMMA anchored nanocarpet in (b). Both samples were imaged following immersion in 1 cSt PDMS oil and drying. The upper surface of the anchored nanocarpet is undulated but is still continuous, while CNTs in the unanchored nanocarpet have separated and opened up into pattern elements. Both images are at the same scale and at a 45° tilt angle.

same manner as those using 1 cSt PDMS oil in chapter 4 that did yield extensive patterns. Thus, the difference between patterns produced in anchored nanocarpets and unanchored nanocarpets is that there are none at all in anchored nanocarpets, while there is a variety of possible patterns (circular, polygonal, elongated) in unanchored nanocarpets. The meaning of this is considered in chapter 8.

Chapter 7

Population Balance Model for Pattern Formation in Nanocarpets

7.1 Introduction

The objective of this chapter is to begin the process of formulating a model for pattern formation in nanocarpets and to begin to identify where further work would be needed to create a functional understanding of the physics involved. The basic idea is that pattern elements nucleate and grow within a 2-D plane, and total area is conserved, with unpatterned area being converted to area within pattern elements over time. This is considered while keeping track of the number of pattern elements of various areas.

An important fundamental distinction is being made here between the nanoscale physical processes involved in CNT deformations and rearrangements, which generally occur at length scales several orders smaller than those of the pattern elements (nests, craters, valleys, trenches, etc.), and the gross description of the sizes and distributions of the pattern elements themselves. This allows a general population balance approach to the dynamics of the microscale pattern elements. The form of the nucleation and growth rates of these pattern elements is necessary and are based on the dynamics of the (unknown) specific interactions between the liquid and CNTs.

A population balance model [94] is a means of describing systems involving populations of "particles" within a separate phase, called the "continuous phase," and

which are possibly subject to convective motion, birth, death, and growth. Population balances are useful in many fields, and are frequently applied to diverse problems such as crystallization, many types of dispersions, emulsions, and biological cell populations. More details about their formulation and features are given in appendix C. In this chapter, an attempt is made to apply the population balance approach to pattern formation in nanocarpets.

7.2 1-D Population Balance Model Applied to Nanocarpet Pattern Formation

Population balance models can be quite complex, however, the intention here is to keep the model as simple as possible while still having some descriptive power. We first define the geometry by restricting ourselves completely to 2-D, and choose the horizontal plane coincident with the upper surface of the fully wetted nanocarpet as our system. We define a "particle" in this system as a contiguous in-plane area that is devoid of liquid and CNTs and that is bounded by adjacent CNT tips. Thus, a particle is a constituent pattern element within the nanocarpet patterns, by definition. As liquid evaporates and the nanocarpet deforms (shrinks or collapses) in the height dimension as well as in-plane, the planar system in the model is allowed to move vertically with the nanocarpet upper surface (defined by the CNT tips) such that at any time t a particle (nanocarpet pattern element) is defined in the plane by the closed shape made by its upper rim intersecting the planar system. This geometry is illustrated in figure 7.1. The "continuous phase," as it is termed in a population balance, is the area in the plane not occupied by particles and will be called the "non-particle area" in this model.

Though the physical geometry being considered is 2-D, the location of the particles in the plane is ignored, and their behavior is said to be independent of "external coordinates." This is equivalent to stating that the particles are uniformly distributed within the plane and there is no relative motion of the particles or the nonparticle

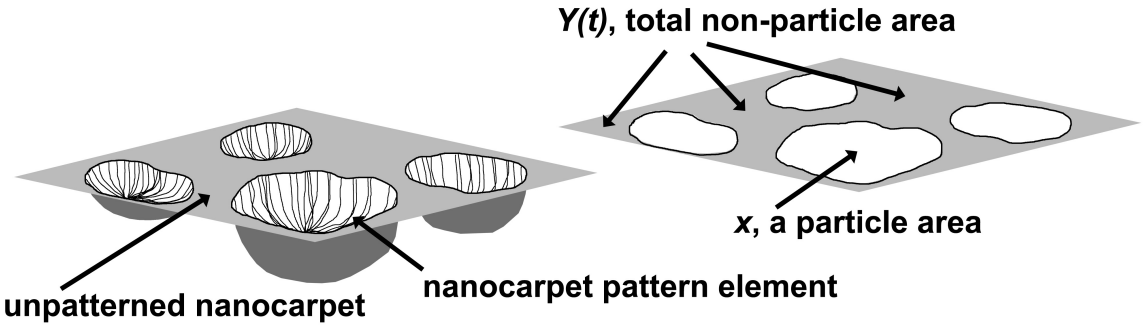

Figure 7.1: Illustration of geometry used in formulating the population balance model.

area. The only property considered of the particles themselves is their *area*, and is a scalar, and the area "dimension" represents the "internal coordinates." This further implies the model will only be a 1-D model in particle state space, with the physical property x representing a particle area.

To further simplify the model, the assumptions in table 7.1 are also made.

Table 7.1: Population Balance Model Assumptions

1. Particle formation is assumed to occur through the process of nucleation (birth) and growth.
2. Nucleation is assumed to be homogeneous.
3. No particles are present initially (this could be relaxed through the initial condition).
4. No coalescence or disappearance (death) of particles is considered.
5. No relative motion (convection) exists between the particles and the nonparticle area.
6. All physical properties are assumed constant.
7. Total area, that is the sum of all particle area and nonparticle area, is constant (closed system).

The typical formulation of a population balance in three dimensions is essentially

a statement of conservation of mass or size, while keeping track of all members of the population. The current formulation is essentially a statement of conservation of area within a spatially 2-D system, while keeping track of population members' areas but not their locations. As particles increase in number and area, the available nonparticle area decreases accordingly, such that the total area remains constant. One caveat to this model is that it does not account for interactions between particles. When particles, which here are nanocarpet pattern elements, grow and eventually begin to run into each other, whatever effect this has on the restricted ability of particles to continue to grow is not included in this model. In order to include this, the locations of population members would need to be accounted for, complicating the model.

The goal will be to obtain a PSD and its time evolution. This could be compared with experimentally obtained dynamic measurements of pattern formation in nanocarpets, were such measurements available. The general case of a simplified 1-D population balance is described in appendix C and is restated here for convenience,

$$\frac{\partial f_1(x,t)}{\partial t} + \frac{\partial}{\partial x}(\dot{X}(x,Y,t) f_1(x,t)) = 0, \tag{7.1}$$

where

$f_1(x,t) =$ number density of particles as a function of a particle property, x, and time, t,
$\dot{X}(x,t) =$ growth rate of particle with property value of x,
$Y = Y(t)$, a scalar quantity describing the continuous phase.

Following the general case, we define variables for the present model in Table 7.2.

As in the general case, newly formed particles have area zero, and the nucleation rate can be considered as an influx at $x = 0$, making it the boundary condition. Thus, the population balance equation reads

$$\frac{\partial}{\partial t} f(x,t) + \frac{\partial}{\partial x}\left(\dot{X}(x,Y,t) f(x,t)\right) = 0, \tag{7.2}$$

and the influx boundary condition is

Table 7.2: Population Balance Model Definition of Variables

x = particle area, with units $[L^2]$
$\dot{X}(x, Y, t)$ = area growth rate of particle with area x, with units $[\frac{L^2}{t}]$
$f(x, t)$ = number density of particles as a function of area and time, t, defined as a number per unit area, with units $[\frac{1}{L^2}]$
$f(x, t)dx$ = number of particles in the interval $(x, x + dx)$, with units [1]
$Y(t)$ = total nonparticle area in the system as a function of time, with units $[L^2]$
$\dot{n}_0(Y)$ = particle nucleation rate as a function of total nonparticle area, with units $[\frac{1}{t}]$
$N(t)$ = total number of particles within the system, with units [1]
A_T = fixed total area in the system, with units $[L^2]$

$$\dot{X}(0, Y, t)f(0, t) = \dot{n}_0(Y), \tag{7.3}$$

or, equivalently

$$f(0, t) = \frac{\dot{n}_0(Y)}{\dot{X}(0, Y, t)}. \tag{7.4}$$

Eq. (7.3) is stating that the growth rate for particles of area zero times the number density at area zero is equal to the nucleation rate of new particles (of area zero). Nucleated particles are immediately subject to growth. This is considered an "influx" because under the current assumptions this is the only way for new particles to enter the system. Thus, this is the boundary condition. The rate of change of total particles in the system is

$$\frac{dN}{dt} = \frac{d}{dt}\int_0^\infty f(x, t)dx = \dot{X}(0, Y, t)f(0, t) - \dot{X}(\infty, Y, t)f(\infty, t) = \dot{n}_0(Y). \tag{7.5}$$

The so-called regularity condition is

$$\dot{X}(\infty, Y, t)f(\infty, t) = 0, \tag{7.6}$$

which means either the growth rate or the number density must vanish for arbitrarily large particle area.

The relationship coupling the total nonparticle area to the particles is written by using the assumption of constant total area,

$$A_T = Y(t) + \int_0^\infty x f(x,t) dx. \tag{7.7}$$

Eq. (7.7) states that the total area is the sum of the total nonparticle area and the total area occupied by particles. We take the time derivative and note that the total area is fixed,

$$0 = \frac{dY}{dt} + \frac{d}{dt} \int_0^\infty x f(x,t) dx, \tag{7.8}$$

and rearrange and carry out the product rule,

$$\frac{dY}{dt} = -\int_0^\infty \dot{X}(x,Y,t) f(x,t) dx - \int_0^\infty x \frac{d}{dt} f(x,t) dx. \tag{7.9}$$

Eq. (7.9) states that the total nonparticle area, $Y(t)$, is decreasing due to the growth rate of existing particles within the system, $\dot{X}(x,Y,t)$, which itself may depend upon the total nonparticle area. $Y(t)$ is also decreasing due to a term representing the sum over all particle areas of the product of particle area and the rate of change of number density at that particle area. This second term is not present in the general case described in appendix C in eq. (C.13) because $Y(t)$ in that case was taken to be a scalar quantity such as the supersaturation level of a solution in considering crystal growth. The supersaturation level is depleted solely in proportion to crystals' growth rates (in mass). However, the decrease in supersaturation level would not correspond to a decrease in volume of solution as crystals grow. In the present model, however, $Y(t)$ is depleted both by the growth rate of particles in the area "dimension" *and* by the number density change multiplied by their actual areas, and this is represented by the second term in eq. (7.9).

The initial condition on $Y(t)$ uses the assumption of no particles present initially,

$$Y(0) = A_T. \tag{7.10}$$

We begin the method of characteristics by assuming x and t may be parameterized by the characteristic Z and write

$$f = f(x(Z), t(Z)). \tag{7.11}$$

We take the total derivative of f,

$$\frac{df}{dZ} = \frac{\partial f}{\partial x}\frac{dx}{dZ} + \frac{\partial f}{\partial t}\frac{dt}{dZ}. \tag{7.12}$$

The population balance equation, eq. (7.2), may be expanded and reorganized as

$$\dot{X}\frac{\partial f}{\partial x} + \frac{\partial f}{\partial t} = -f\frac{\partial}{\partial x}\dot{X}. \tag{7.13}$$

By inspection, we see that the characteristics should be defined by letting

$$\frac{dt}{dZ} = 1, \tag{7.14}$$

$$\frac{dx}{dZ} = \dot{X}, \tag{7.15}$$

and the population balance equation is now transformed to be

$$\frac{df}{dZ} = \dot{X}\frac{\partial f}{\partial x} + \frac{\partial f}{\partial t} = -f\frac{\partial}{\partial x}\dot{X}. \tag{7.16}$$

This can be compactly written as

$$\frac{d}{dZ}ln(f(Z)) = -\frac{\partial}{\partial x}\dot{X}. \tag{7.17}$$

Eq. (7.14) may be integrated to give

$$t = Z + r, \tag{7.18}$$

where r is the start time of a given characteristic, Z. Eq. (7.15) is integrated to give,

$$\int_{Z=0,r}^{Z,r} dx = x(Z,r) - x(0,r) = \int_{z=0}^{Z} \dot{X}\left(x(z,r), Y(t(z,r)), t(z,r)\right) dz, \tag{7.19}$$

where z is a dummy variable of integration, and the notation $x(z,r)$ is used to denote that this is on the characteristic defined by r. If the area at the lower bound (the smallest particles), $x(0,r)$, is simply taken as 0, the equation is then

$$x(Z,r) = \int_{z=0}^{Z} \dot{X}\left(x(z,r), Y(t(z,r)), t(z,r)\right) dz. \tag{7.20}$$

This means that there is no analogue to "critical size" for a nucleated particle being considered here. If there were, then there would be some nonzero area for which all particle number densities below this area would be zero since particles could not grow unless they are at least of critical area. Any particle area will be allowed to grow under the current assumptions. Eq. (7.20) states that the area of the particle with characteristic value, Z, and start time, r, is equal to the integral over Z of its area growth rate, $\dot{X}$. This gives the relationship between x and Z and r, whereas eq. (7.18) gave the relationship between t and Z and r. Clearly, the form of the area growth rate for particles is needed here in order to proceed further.

The transformed population balance equation, eq. (7.17), can be integrated,

$$\int_{Z=0,r}^{Z,r} d(ln(f(Z))) = -\int_{z=0}^{Z} \frac{\partial}{\partial x}\dot{X}\left(x(z,r), Y(t(z,r)), t(z,r)\right) dz, \tag{7.21}$$

$$ln\left(\frac{f(Z,r)}{f(0,r)}\right) = -\int_{z=0}^{Z} \frac{\partial}{\partial x}\dot{X}\left(x(z,r), Y(t(z,r)), t(z,r)\right) dz. \tag{7.22}$$

Referring back to eq. (7.4), which was true for all t, we note that

$$f(0,r) = \frac{\dot{n}_0(Y)}{\dot{X}(0,Y,r)}, \tag{7.23}$$

and this is the boundary condition for eq. (7.22).

Thus we have a completed a formal outline to the solution of the initial population

balance equation, eq. (7.2), including the relationship to the total nonparticle area, definition of characteristics, boundary condition, and initial condition (no particles present). These equations are summarized in table 7.3.

In order to go further with the solution, and begin to think of numerically solving the set of equations, more details about the physics are required. As an example, the details are needed for how the area growth rate, $\dot{X}$, depends upon physical characteristics of the nanocarpet, the liquid involved (its evaporation rate, surface tension, and perhaps even viscosity), and possible interaction between the nanocarpet pattern elements. For comparison, the population balance modeling of bubble formation in a polyurethane foam, which is described in appendix C, considers the mass of particles (bubbles) with their mass growth rate dependent on surface area and a concentration difference. It could turn out for nanocarpet pattern elements, for example, that their growth rate may be independent of their size but highly dependent upon liquid properties and nanocarpet properties. Regardless of these unresolved issues, the framework outlined above in this section shows how such details could be implemented into an overall model for nanocarpet pattern formation.

7.3 Particle Size Distribution (PSD)

The goal of the population balance model formulated above, if additional physical details were available, would be to obtain PSDs and their time evolution, thus describing entire populations of nanocarpet pattern elements. By achieving this, results from pattern formation experiments could be directly compared to predictions from the model, the model could then be refined, and greater understanding of the nanocarpet pattern formation problem would be achieved. The purpose of this section is to emphasize the particle size distribution and describe how it could be used.

The relationship between number density and particle area (the "size" coordinate here) is the PSD. There will be a mean particle area and some range (spread) of particle areas for which there are nonzero number densities. This results from nucleation and growth occurring simultaneously for at least some portion of time. The shape

Table 7.3: Population Balance Model Solution Equations

$\frac{\partial}{\partial t}f(x,t) + \frac{\partial}{\partial x}\left(\dot{X}(x,Y,t)f(x,t)\right) = 0$	Original form of population balance equation
$t = Z + r$	Relating t to characteristics
$x(Z,r) = \int_{z=0}^{Z} \dot{X}\left(x(z,r), Y(t(z,r)), t(z,r)\right) dz$	Relating x to characteristics
$ln\left(\frac{f(Z,r)}{f(0,r)}\right) = -\int_{z=0}^{Z} \frac{\partial}{\partial x}\dot{X}\left(x(z,r), Y(t(z,r)), t(z,r)\right) dz$	Final form of population balance equation
$f(0,r) = \frac{\dot{n}_0(Y)}{\dot{X}(0,Y,r)}$	Boundary condition
$f(Z,0) = 0$	Initial condition
$\frac{dY}{dt} = -\int_0^\infty \dot{X}(x,Y,t)f(x,t)dx - \int_0^\infty x\frac{d}{dt}f(x,t)dx$	Equation describing change of nonparticle area as particles grow
$Y(0) = A_T$	Initial condition for $Y(t)$

of a PSD is usually like that of a downward opening parabola. For the nanocarpet pattern formation situation, growth is constantly occurring as long as some pattern elements have been nucleated and there is still liquid present. The difference between the smallest area with nonzero number density and the largest area with nonzero number density is called the breadth, and is related to the time between the nucleation of the first particles and the last particles. It is conceivable that nucleation could occur continuously as long as there is liquid present, and the lower bound of the breadth would be determined by the last of the liquid evaporating, at which point the nanocarpet pattern is fixed.

In considering processes modeled as nucleation and growth processes such as the current model of nanocarpet pattern formation, there is generally a significant variation (orders of magnitude) between distributions obtained under different conditions. It is helpful to define a length scale that will allow easy comparison between distributions. An example dividing by variance is given in Niyogi et al. [95], however, here it is preferred to use

$$x^* = \frac{x - \bar{x}}{\sigma_x}, \tag{7.24}$$

where σ_x is the standard deviation in x and $\bar{x}$ is the mean of x. The number density $f(x,t)$ can then be normalized by the total number of particles in the system $N(t)$ and plotted against x^*. This aligns the centers of the distributions being compared at $x^* = 0$ and scales the number densities to be independent of their total system size. A PSD scaled in this way should generally look like a Gaussian. Thus entire distributions should fall primarily within $(-3 < x^* < +3)$. The time evolution of PSDs can also be followed using this scaling. A sketch illustrating this is shown in figure 7.2. The effect of various factors on the PSD is of great interest, both for understanding the physics as well as using a pattern formation process for manufacturing purposes.

7.4 Chapter Summary

The model formulated in this chapter is based upon considering nanocarpet pattern elements in two dimensions only and neglecting their spatial locations. Total area in the system is conserved, and the population balance is a way to keep track of the growth of all the pattern elements. A distinction is made between the length scales relevant to the pattern elements themselves (microns and larger) and the individual CNTs that define them (much less than a micron). The interactions of the CNTs with each other and the liquid would be included in an appropriate form for the growth rate.

The following are outstanding issues in being able to make predictions from the model:

1. Form of the growth rate law for individual particles
2. Form of the nucleation rate
3. Accounting for interaction between particles, if it is to be included
4. Influence of any other factors which affect nucleation and growth rates

The first and second issues are obviously needed for solutions and would result from an understanding of system behavior at the nanoscale.

The third issue is currently left out of the model, and because of this, nanocarpet pattern elements (particles) are only allowed to grow until just before they begin to "run into each other." Thus the patterns obtained from the model as it is would be uniformly distributed, noncontacting circles. The interaction of nanocarpet pattern elements with each other after they contact one another is what creates polygonal cellular patterns, and they would not occur within this model. The limiting case for what may be describable by a model without including particle interaction is perhaps exemplified by the pattern shown in figure 1.1. At the time the pattern is fixed by the loss of liquid, the pattern elements (particles in the model terminology) are mostly near-circular, but are beginning to be warped and affected by the presence of

neighbors. For particle interaction to be included in the model, it is expected that location of particles (external coordinates) would need to be included. Additionally, the growth rate would likely be directionally dependent, as growth of a portion of a particle that is not in contact with another particle should be different than a portion that is in contact.

The last issue pertains to a possible analogue to a "blowing agent," which is an additional component in the polyurethane foam system [95, 96] that influences the PSD via the growth rate and the nucleation rate. It is unclear whether there should be an analogous factor in nanocarpet pattern formation, but it remains a possibility.

The underlying assumption of homogeneous nucleation in this model is very important. Classically, homogeneous nucleation depends on the free energy change associated with the formation of a nucleus of critical size. In a real system with defects that serve as heterogeneous nucleation sites, the activation energy for heterogeneous nucleation is lower than that for homogeneous nucleation, and thus heterogeneous nucleation can occur earlier during the formation process. Modeling heterogenous nucleation, however, is more complicated than homogeneous nucleation and that is why a simple model such as this assumes only homogeneous nucleation. Because heterogeneous nucleation occurs earlier in the process, there is a longer time available for growth, and this tends to increase the mean particle size. The rate of heterogeneous nucleation is dependent on the number of sites available. It is perhaps best to think of both heterogeneous nucleation and homogeneous nucleation occurring simultaneously. If the number of heterogeneous nucleation sites is sufficiently large, then they will cause many nuclei to be formed in a short period of time, which will then damp out homogeneous nucleation (assuming it is due to some concentration-like property). The result of a formation process with heterogeneous nucleation, then, is a narrower distribution in particle sizes than would be obtained for pure homogeneous nucleation. Significant heterogeneous nucleation should also result in a larger mean particle size. If quantification of heterogeneous nucleation sites (e.g., "bald spot" defects) were experimentally carried out, these effects should be evident in properly scaled PSD plots.

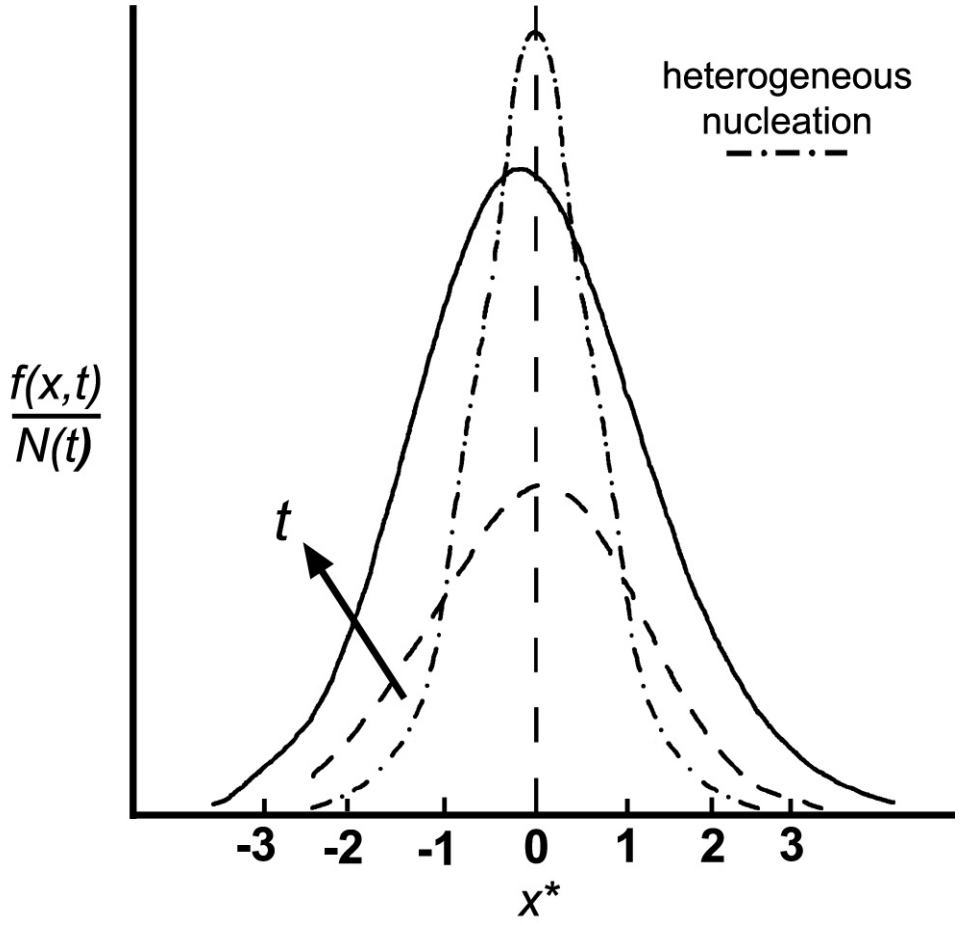

Figure 7.2: Sketch illustrating idealized particle size distributions plotted on scaled axes. In general, distributions will not be symmetric, and broaden with time. Maximum in normalized number density will depend upon the competition between nucleation of new particles and growth of existing ones. Heterogeneous nucleation causes a larger mean size (not evident in this scaling) and narrower distribution compared to pure homogeneous nucleation.

Chapter 8

Discussion

8.1 Introduction

The objective of this chapter is to discuss the extent to which the problem statements set out in §1.5 are answered by the results of this thesis, as well as to discuss several underlying issues in this work. A view is adopted of pattern formation in nanocarpets as being a nucleation and growth process. This provides convenient terminology as well as being the basis of the model of chapter 7.

The results of this thesis have demonstrated that pattern formation is common in as-grown nanocarpets, but once the CNTs in nanocarpets are fixed at their base using the anchoring method demonstrated herein, pattern formation does not occur at all, even under identical conditions as those that do form patterns in as-grown nanocarpets. This result is in stark contrast to all known prior studies [15, 8, 21, 23, 19] that include pattern formation of nanocarpets in some way. What this finding means about the pattern formation process is considered in this chapter.

The role of defects in pattern formation is considered. The presence of defects, whether incidental or intentional, has been detected in prior studies as well as in this work. A discussion of the importance of the physical boundary conditions on CNTs is given, using basic beam mechanics. This is used to understand the results from the patterning experiments on anchored nanocarpets given in chapter 6 and to address problem statement 4 in §1.5 dealing with the meaning of differences in patterns formed in anchored and unanchored nanocarpets.

Aspects of controllability in the anchoring method and how the experimental results relate with the population balance model are also considered. A brief comparison with cellular foams is made, as they are a very common structure in which pattern formation is a primary characteristic.

8.2 Role of Defects/Voids/Vacancies

Both Chakrapani et al. and Liu et al. demonstrate pattern formation nucleated by forced vacancies as part of their studies. It has been found in this thesis that "bald spot" defects from the CNT growth lead to the formation of often large pattern elements. In this section, growth defects such as this and forced vacances, whether by predetermined patterns of CNT growth (Chakrapani et al.) or destruction of regions of as-grown CNTs (Liu et al.), are considered to be similar. Any of these defects may be considered as a void in a densely packed CNT array, with the void having larger spacing than the normal edge-to-edge spacing of the CNTs in the array.

If it is assumed that such an array with a single defect is wetted by a liquid making contact angle θ with the CNTs, for example PDMS oil, which is evaporating and whose surface is just dropping below the top of the array, the situation would look something like the sketch in figure 8.1. The diameter of the defect, D, is taken to be larger than the spacing between the CNTs, d. Atmospheric pressure is P_a and the capillary underpressure on the liquid side of the interface within the defect is P_1 and within the gap between CNTs is P_2.

If it is assumed for convenience that the liquid-air interface within the defect and within the gap between CNTs is spherical, Laplace's law applied within the defect is

$$P_a - P_1 = \frac{4\gamma \cos\theta}{D}, \tag{8.1}$$

and within the gap between CNTs is

$$P_a - P_2 = \frac{4\gamma \cos\theta}{d}. \tag{8.2}$$

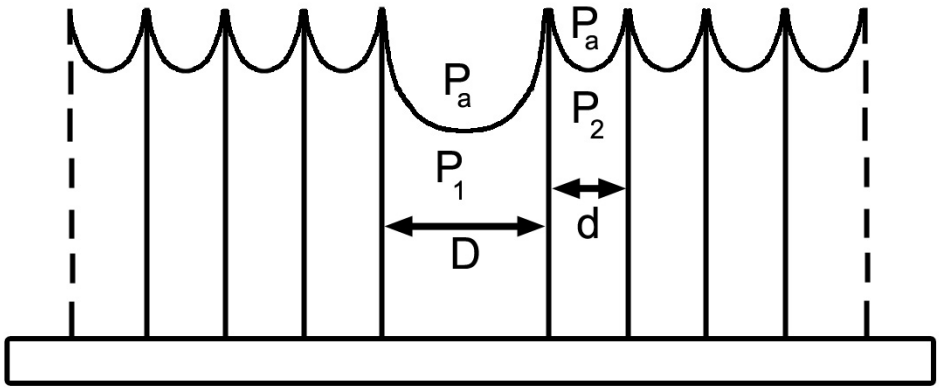

Figure 8.1: Sketch of the side-view of an idealized defect in an infinite nanocarpet wetted by a liquid.

Substituting eq. (8.2) into eq. (8.1) gives

$$P_1 - P_2 = 4\gamma \cos\theta \left(\frac{1}{d} - \frac{1}{D}\right). \tag{8.3}$$

Because D was defined to be larger than d, both sides of eq. (8.3) are greater than zero. This means that there is a net outward pressure on the CNT at the edge of the defect. If this pressure is sufficient to deflect or displace the CNTs surrounding the defect (due to not being anchored at their base), then the defect should grow. As it enlarges, the gap between the surrounding CNTs would decrease, and the net capillary pressure on CNTs surrounding the defect would increase further.

An estimate can be made of the dependence of the deflection of the CNTs on the net outward pressure due to the defect in figure 8.1. The same approximate value for elastic modulus of CNTs, $E = 1$ TPa, as in Chakrapani et al., a nanocarpet height of 100 μm, and CNT diameters of 20 nm (which is more realistic for nanocarpets in this work) are assumed. The defect size remains as D, and a gap between CNTs of 100 nm (also more realistic for this work) is also assumed. A reasonable value for γ is taken as 18 mN/m (for 1 cSt PDMS oil), and contact angle is chosen as $\theta = 0$ (for 1 cSt PDMS oil), the net outward pressure on the CNT at the edge of the defect is

given by the expression

$$\Delta P = 4\gamma \left(\frac{1}{d} - \frac{1}{D} \right). \tag{8.4}$$

For a cantilevered beam, which is not necessarily true at all for unanchored nanocarpets, and a uniformly distributed (also not necessarily true) load W, the deflection at the free end from small deflection (linear) beam mechanics is given by $\delta = WL^3/8EI$. The load is taken to be $W = (\Delta P) d_{CNT} L$ where L is the height of the nanocarpet or the length of an individual CNT, d_{CNT} is the CNT diameter, and ΔP is the net pressure. The hydrostatic pressure within the liquid is neglected. The CNT deflection expression can now be written,

$$\delta = \frac{\Delta P d_{CNT} L^4}{8EI}, \tag{8.5}$$

and substituting in eq. (8.4) gives,

$$\delta = 4\gamma \left(\frac{1}{d} - \frac{1}{D} \right) d_{CNT} L^4 \frac{1}{8EI}. \tag{8.6}$$

Eq. (8.6) can be rearranged to give

$$\frac{1}{D} = \frac{1}{d} - \frac{2EI\delta}{\gamma d_{CNT} L^4}, \tag{8.7}$$

which is inverted to give

$$D = \frac{d\gamma d_{CNT} L^4}{\gamma d_{CNT} L^4 - 2dEI\delta}. \tag{8.8}$$

Now for a deflection of 100 nm at the free end of the cantilevered CNT, the defect size is given by eq. (8.8) to also be 100 nm. The second moment of inertia $I = \pi d_{CNT}^4/64$ for the CNT cross-section is dominating the expression. This is taken to mean that net pressures due to capillary forces are very significant for CNTs because of their small size, thus any net pressure at all (due to a defect of greater size than CNT gaps) will cause significant deflections.

Gross approximations are being used in this model, such as spherical interfaces between regularly spaced 1-D objects (CNTs), capillary pressures acting on the entire

length of the 1-D objects, and linear beam mechanics. Still, it indicates that preexisting defects can effectively nucleate the formation of pattern elements. As long as liquid and therefore surface tension and capillary pressure are present in the system, the nucleated pattern element should grow. In an ideal system with perfectly regular CNTs and only a single defect, the pattern element nucleated by the defect would grow outward as long as liquid is present, flattening the CNTs as it grows. However, if there are many distributed defects in the system, then each nucleated pattern element would grow outward, and eventually the deflecting CNTs at the edges of the growing pattern elements will face equal and opposite forces due to neighboring pattern elements. This means that even if liquid remains in the system, the overall pattern will be fixed once it reaches this point.

This also may give insight into the possibility of homogeneous nucleation within this system. Suppose there were no actual defects as drawn above or as detectable in a typical high magnification SEM image of a nanocarpet. Rather, that the CNT packing density (and possibly also the height and topology) varied within the plane. Then there would be a constant competition between all the net outward pressures (due to capillarity) in the system, with the minimum packing density locations corresponding to "sources" of largest net outward pressure. These sources would then nucleate the pattern elements and originate the final patterns.

The notion of the lateral capillary force [12], which is due to overlapping menisci of objects piercing a liquid-air interface, may be applied to the CNTs in the nanocarpet. The lateral capillary force is such that like objects are drawn together, and drawn together more strongly the closer they get to each other. The above description was based solely on capillary pressure due to Laplace's law, and does not require that the CNTs ever pierce the liquid-air interface, which is claimed by Chakrapani et al. to not be the case. However, it was shown in this thesis (see for example figure 4.14) that the liquid-air interface does appear to drop below the CNT tips. If this is occurring, then the existence of the lateral capillary force would serve to pull CNTs closer together to each other, further encouraging the growth of pattern elements nucleated by defects as considered above. Also, if the liquid-air interface does drop below the CNT tips and

lower toward the substrate, then the outward net pressure at the edge of the defect should continually deflect the CNTs outward. The final curvature of the CNTs would then be collapsed downward and outward from the defect. A possible cantilevered boundary condition could affect this significantly, however.

Thus defects serve as heterogeneous nucleation sites for pattern elements. A careful, high magnification mapping of defects within a nanocarpet made before patterning with liquids should be compared directly to the resulting pattern that otherwise would appear to be "of interest" as defined in this thesis. Without this type of comparison in careful experiments, it is very difficult to conclude whether a given pattern is due to preexisting, possibly submicron defects in the nanocarpet. This type of comparison could help to determine if an analogue to homogeneous nucleation exists for nanocarpet pattern formation. If a nanocarpet were created with sufficiently few defects, and carefully characterized, then a model considering something like minimums in packing density mentioned above and applied by Liu et al. could perhaps be detected.

8.3 Importance of CNT Boundary Conditions

The pattern formation experiments conducted with anchored nanocarpets in chapter 6 show some very interesting behavior. No pattern formation is observed under conditions identical to those in other experiments in this thesis. In order to verify that no experimental conditions had changed, an experiment was conducted at the same time and in the same way using an unanchored nanocarpet from the same growth run as was used to fabricate the anchored nanocarpets. Significant pattern formation over the entire surface was observed.

In the previous section, the role of defects in pattern formation was considered. Because the anchored nanocarpets were made from nanocarpets grown in the same way and at the same time as the control experiment that *did* result in pattern formation, the extent of defects within the anchored nanocarpets should be the same. The anchoring process, essentially an inversion of the nanocarpet and adhesion within a

hard plastic layer, should not alter the number nor the location of defects from the growth. The sample shown in figure 6.13 does appear to have about nine visible defects following the wetting and drying. Still no pattern formation over the bulk of the surface is caused.

Figure 8.2 shows high magnification comparisons between the before wetting and after wetting (and drying) states at exactly the same locations in two nanocarpets from similar growth runs—one that was anchored and one that was not. Importantly, the shape of the edge of the anchoring layer in the anchored nanocarpet does not change due to the wetting and drying. This means that no slipping or deformation of the anchoring layer occurs. It is clear that the CNTs anchored in PMMA experience a cantilevered boundary condition at their base. The unanchored nanocarpet does *not* have a cantilevered boundary condition, and the unanchored CNTs are pulled flush with the substrate by the action of surface tension. A closer look at the boundary condition of the CNTs is provided in figure 8.3, which shows a same scale comparison between the edge of the unanchored nanocarpet and the PMMA anchored nanocarpet. Lower magnification images also showed that the entire boundary of the unanchored nanocarpet had been pulled in toward the nanocarpet covered area by surface tension. The boundary condition at the base of the unanchored CNTs is thus more like a pinned, sliding condition where the only degree of freedom that is prevented is vertical translation.

In the framework of Chakrapani et al. [8], adhesion to the substrate at the base of CNTs should result in inhomogeneous shrinkage of the entire nanocarpet during wetting and the formation of cracks to relieve stresses. This effect is not observed in the present anchored nanocarpets that are strongly fixed at their base unlike those of Chakrapani et al. This is true even though there are clearly some void defects present, which according to Sheng et al. [23] are the origination point of cracks. As first mentioned in §1.4.1, Chakrapani et al. also assume a cantilever boundary condition for their CNTs but the expected corresponding curvature is not exhibited following wetting and drying. The insets of figure 8.3 are intended to illustrate the curvatures for the unanchored and anchored cases in the figure, with the unanchored

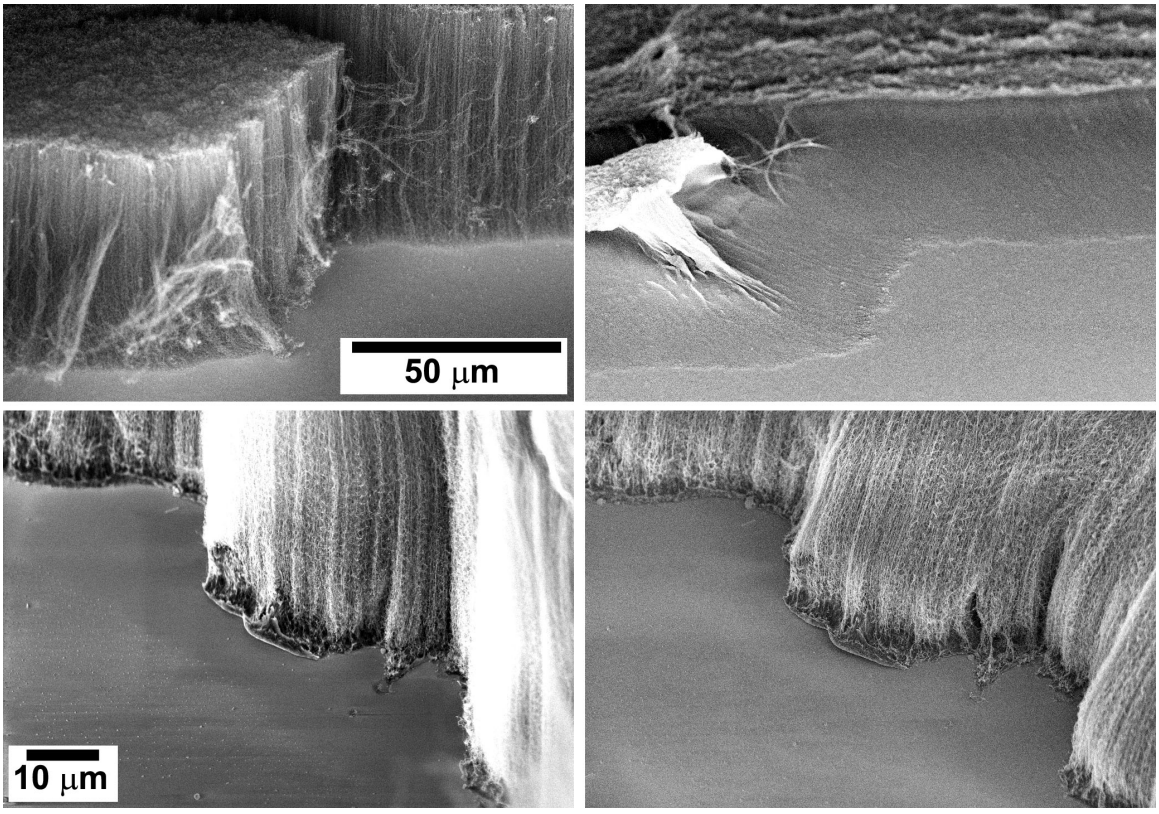

Figure 8.2: Effect of wetting and drying in a pattern formation experiment for an unanchored (top row, same scale, same location) and anchored (bottom row, same scale, same location) nanocarpet. The edge of the two nanocarpets is imaged in the SEM at high magnification to look at the boundary conditions. Left images are before treatment with 1 cSt PDMS oil. Right images are following treatment and upside down drying. The nanocarpet in the top row was 77 μm tall and is viewed at a 60° tilt angle, while the nanocarpet in the bottom row is 163 μm tall, viewed at a 45° tilt angle, and is the same sample as in figure 6.12.

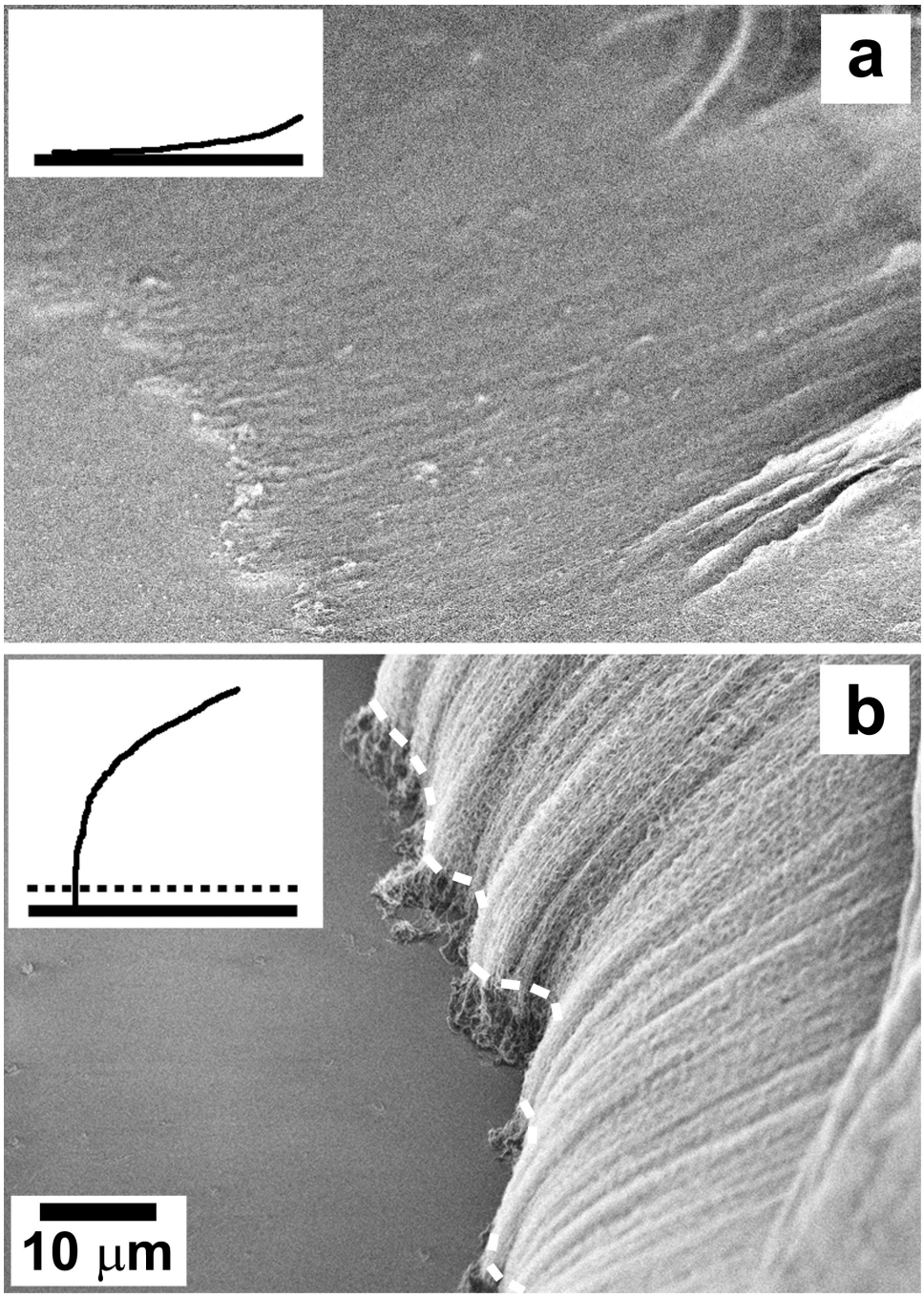

Figure 8.3: The edge of unanchored and anchored nanocarpets following wetting by 1 cSt PDMS oil and drying. a: Unanchored CNTs (viewed at a 60° tilt angle) lie flush against the substrate at the boundary. b: Anchored CNTs (viewed at a 45° tilt angle) are cantilevered and cannot lie flush. These CNTs have the opposite bending curvature of the unanchored CNTs. Both images are at the same scale, and insets are schematics of an individual CNT under each of the two conditions.

case matching that observed by Chakrapani *et al* and the anchored case corresponding to a true cantilever boundary condition.

The formation of neither cracks nor distributed pattern elements in the anchored nanocarpets means that the boundary condition at the base of nanocarpets is a primary factor in determining if pattern formation occurs or does not occur. If nanocarpets are considered as a continuous material and not a large discrete set of CNTs, it is speculated that pattern formation in nanocarpets may require an overall decrease in contact area between the nanocarpet and its substrate. It also seems that for pattern formation to occur, the CNTs must be able to lie flush against the substrate, particularly in the central regions of pattern elements. Anchoring prevents this possibility, and therefore also pattern formation.

A feature of the anchored nanocarpets that is also quite different from the unanchored nanocarpets is the flatness of the upper surface of the anchored nanocarpets. Following the anchoring process, which inverts the nanocarpet from its as-grown state, the upper surface should be very flat, though not necessarily perfectly horizontal. It should in fact be exactly as flat as the substrate surface it was grown upon. This property may be subtly involved in addition to the boundary conditions discussed above. This could have bearing on the possible triggering and damping of instabilities in the system, but it is unclear at this time.

8.4 Controllability of Anchoring

The anchoring method presented in chapter 5 should allow controllability over the anchoring depth for a nanocarpet. However, demonstration of controllability, i.e., specifying a desired anchoring depth and obtaining it, has not been shown as part of this work. The spin-speed curve for cross-linked PDMS generated in §5.3 and the theory governing it imply that spin-coating layers of specified thickness should be possible, within a range of perhaps a couple of microns. In fact, the thickness of the spin-coated layer of cross-linked PDMS predicted by the empirical curve is about 32 μm, and the the two thicknesses obtained in the nanocarpets that were anchored

were measured (locally) as 26 μm and 30 μm. These values are somewhat less than predicted, but the setup used for creating the two anchored nanocarpets shown was less reliable than the spin-coater used for the spin-speed curve. Even though the spin-coating itself should be controllable, demonstration of controllability of nanocarpet anchoring would have to be provided by data comparing the thickness of spin-coated layers (after cross-linking) and the final thickness of anchoring layers within nanocarpets. There is expected to be some difference between these thicknesses because of capillary suction of the PDMS mixture (even though it is very viscous compared to 1 cSt PDMS oil, for example) up into the interstices within the nanocarpet. The degree of thickness difference in the anchoring layer due to this effect is very speculative without measurements.

De Gennes et al. [5] derive an expression that is analogous to the classical Jurin's law for capillary rise but that is for a porous medium. The final form is

$$h = \frac{\sum_V (\gamma_{SO} - \gamma_{SL})}{\rho_L \Phi_g}, \tag{8.9}$$

where h is the equilibrium height of the capillary rise, $\sum_V$ is the surface area per unit volume for the porous medium, γ_{SO} is the solid-air surface energy, γ_{SL} is the solid-liquid surface energy, ρ_L is the liquid density, and Φ_g is void fractional volume. This relationship could possibly be applied to the study of imbibition of liquids, such as the PDMS prepolymer, by nanocarpet material. This capillary rise into a nanocarpet is what may be considered to be "suction" into the interstices. However, even making an estimate for the value of h would be premature.

The fact remains that anchored nanocarpets with 26 and 30 μm thick anchoring layers of cross-linked PDMS were produced, and large portions of the nanocarpet did not appear to be invaded by PDMS prepolymer.

The other anchoring material demonstrated in this work, PMMA, was used in solution form so that it could be spin-coated in order to apply the anchoring method. In this approach, the volatile solvent is lost so quickly that the PMMA layer is likely too solidified for any capillary suction to occur, which is beneficial from the viewpoint

of controllable anchoring. However, the spin-coating of micron-thick PMMA layers in this way was unreliable for producing controlled thicknesses in these results. Another possible approach to anchoring nanocarpets could be using commercially available polymeric sheets, such as 50 μm thick PMMA (Goodfellow, Oakdale, PA), which has been demonstrated as a material for fabricating microstructures [97]. Nanocarpets could simply be inverted and set on such a sheet, applying heating so that a temperature greater than the glass transition temperature of PMMA is reached. The nanocarpets should sink somewhat and be anchored within the softened PMMA by this process followed by cooling. This could perhaps yield a more controllable method for using PMMA as the anchoring material.

8.5 Experimental Results and the Population Balance Model

The population balance model of chapter 7 was based on nucleation and growth, with the assumptions of homogeneous nucleation and uniformly distributed pattern elements in a 2-D system. It was speculated that ideal distributions of areas would be Gaussian-like, and the influence of heterogeneous nucleation could be seen by an increase in mean area and a narrowed distribution. The pattern analysis results of §4.5, however, tended to show a very large relative number of smaller areas for almost all patterns analyzed. This could mean that nucleation is continuous as long as there is liquid present (because the pattern is fixed once all liquid is gone). It could also mean that there are multiple modes of pattern formation occurring with different growth rates, i.e., one mode produces pattern elements with a very low growth rate, yielding small pattern elements, and another mode produces pattern elements with a high growth rate, yielding large pattern elements. Similarly, only one mode of pattern formation could be present with a nonlinear growth rate. Still another possibility could be that interaction between pattern elements is very significant, which is not considered in formulating the population balance model.

The inclusion of external coordinates within the model, and also possibly in the measurements, would be necessary to investigate the local effects of the presence of large pattern elements. A region of few large pattern elements could also have a different number of small pattern elements compared to a region of many large pattern elements.

The fact that large pattern elements occupy a large proportion of the system area would seem to imply that they should damp out the tendency for more large pattern elements to form. This effect could possibly be taken into account by weighting the analysis to better show the influence of large pattern elements. As the distributions are presented in §4.5, there are naturally smaller numbers of large pattern elements included because only one area (in one image) has been considered. Area weighting could also potentially mask the real effect that in an area based process such as this, there will likely always be a large number of small elements if nucleation levels are sufficient.

The possibility of nucleation and growth occurring in nanocarpet pattern formation is thrown out by Chakrapani et al. [8] because their cellular patterns are not polygonal. However, as clearly seen in the population balance model of Niyogi et al. [95] applied to bubble formation in polyurethane foams, nucleation and growth does not have to yield polygonal patterns if the process is arrested prior to cells interacting with each other. Both polygonal pattern formation, for example Figures 4.1 and 4.3, and nonpolygonal pattern formation, for example figure 4.28, were observed in this work. The nonpolygonal pattern formation was presumably do to the 1 cSt PDMS oil evaporating before polygonal patterns could form.

The form of the growth rate law for individual pattern elements is required to complete the model of chapter 7. In the planar system considered, the central regions of pattern elements would simply be empty spaces corresponding to where CNTs have been pulled flush to the surface or deflected outward. Thus it seems that a possible growth rate law should not be area dependent, but circumferentially dependent. This is further supported by the fact that surface tension is the driving force for pattern formation.

The results presented in §4.5 were obtained with limited sample sizes. This prevents strong conclusions from being possible. If a large amount of data were obtained from nanocarpet pattern formation with no significant influence of growth defects, more significant conclusions could be drawn. Additionally, detailed, high magnification dynamic results could greatly help the formulation of the growth rate law, which should be due to the effects of surface tension on the CNTs bordering the pattern elements.

8.6 Brief Comparison to Cellular Foams

The purpose of this section is to speculate briefly on the relationship between nanocarpet patterns and cellular foams, and this is motivated simply by their obvious similarity in appearance. This is the reason Chakrapani et al. [8] refer to their nanocarpet patterns as "two-dimensional cellular carbon nanotube foams."

There is a large quantity of literature dealing with cellular materials [98, 99, 100, 101, 102, 103]. Gibson and Ashby [101] define a cellular solid as a material made up of an interconnected network of solid struts or plates that form the edges and faces of cells. By this definition, nanocarpet patterns are actually *not* a cellular material, because the bottoms of pattern elements are collapsed and possibly flush with the substrate. Nanocarpet patterns are 2-D cellular foams only if the upper surface of the final pattern is considered, i.e., the ridges between pattern elements. Additionally, most cellular foams are comprised of a continuous liquid phase between the cells, which allows the direct application of Laplace's law, whereas CNTs are actually adjacent solid bodies. The physical relationships describing growing pattern elements in a nanocarpet pattern should be different than those for true cellular materials with only a liquid and gas phase.

The final patterns observed in cellular foams give great insight into their formation, and the same may be true for nanocarpet patterns. For example, in the situation of bubble nucleation in a liquid, if the bubbles nucleate randomly in space but all at the same time, and all bubbles grow with the same linear growth rate, the resulting

pattern is called a random Voronoi honeycomb (in 2-D only) [101]. Euler's law for convex polyhedra is a topological relationship and applies to the usual cellular foams with only a liquid and gas phase, and states in 2-D that $F - E + V = 1$, where F is the number of faces (each entire cell is a single face in 2-D), E is the number of edges, and V is the number of vertices. This can be used to show the average number of cell edges should be 6, if the average number of edges that meet at vertices is 3. The number of edges and how many edges connect at vertices are very important values for cellular foams. The number of edges of some pattern elements in a nanocarpet pattern from this work was measured from an SEMimage and is shown in figure 8.4. This is the same nanocarpet pattern presented in figure 4.1. The number of edges that connect at vertices is clearly not 3, however, so the meaning of the disagreement with the Euler's law prediction of 6 being the average is unclear.

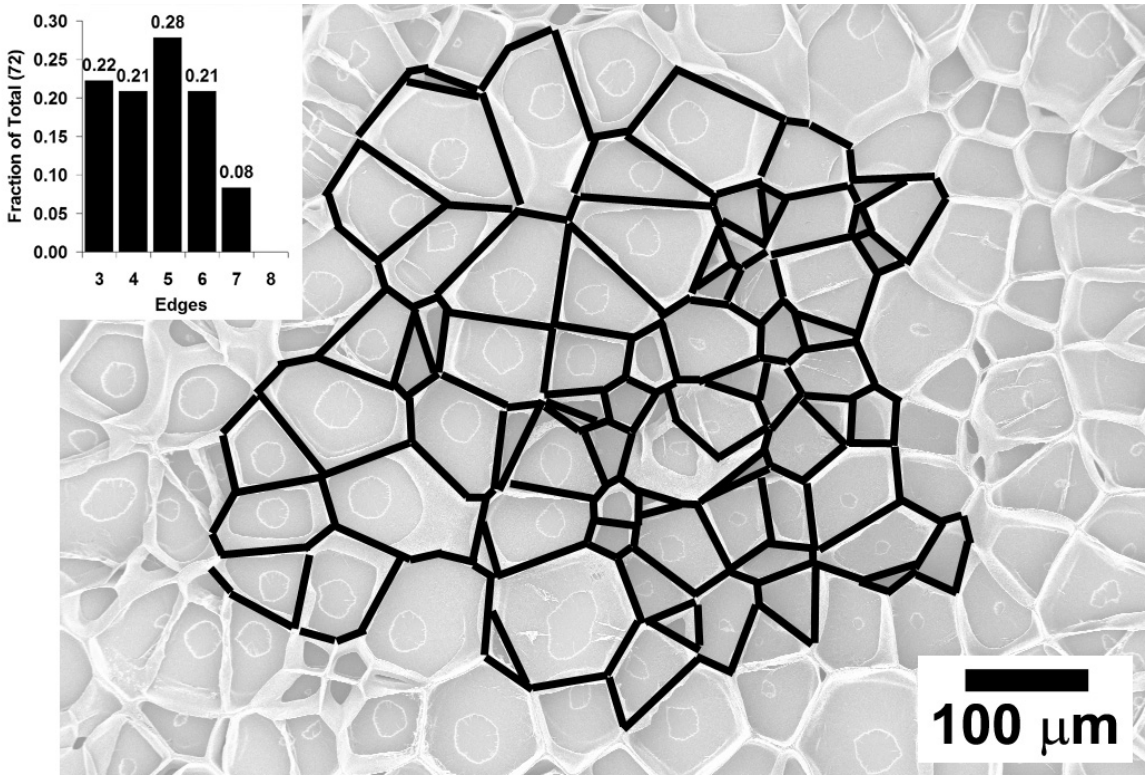

Figure 8.4: Outline of cell borders in a nanocarpet pattern. Inset: Distribution of number of cell edges for the marked cells.

This type of analysis could possibly be used as another way to show that hetero-

geneous nucleation due to defects (which would cause randomly nucleated pattern elements) is causing nanocarpet patterns. It would also contribute greatly to determining the growth rate law that should be used in the population balance model in chapter 7. However, the 3-D nature of nanocarpet pattern formation, which is highly evident in the complete lack of pattern formation in anchored nanocarpets, makes the problem quite complicated.

8.7 Future Work

The question of whether or not homogeneous nucleation of pattern elements in nanocarpets can even exist has been raised throughout this thesis. Unfortunately, it has not been clearly answered by the results. Given these results, and those of the prior works discussed in §1.4, it seems that homogeneous nucleation cannot exist, as heterogeneous nucleation is simply too prevalent. This issue remains an open question.

Proper formulation of the growth rate law and nucleation rate for use in the population balance model of chapter 7 is still necessary. Alternatively, another model for pattern formation could be formulated. If predictions from a model were possible, whether the model begun in this thesis or a separate one, the predictions would need to be compared to experimental results, preferably dynamic pattern formation measurements.

Further development of the anchoring method and demonstration of its controllability remains to be carried out. Extension to nanostructures other than CNTs is also an interesting possibility.

Force of adhesion measurements comparing both as-grown nanocarpets and anchored nanocarpets could help to elucidate the mechanical properties of nanocarpets, which could also improve understanding of their pattern formation. If the anchoring method were developed sufficiently, varying degrees of anchoring could be provided, possibly finding a range in which pattern formation is possible in anchored nanocarpets. This would be interesting for understanding CNT mechanics in general, as well as nanocarpets.

High quality mappings of void defect locations before pattern formation and direct comparison with the resulting patterns would be useful for further understanding the role of defects.

Technological applications of nanocarpets could be attempted using the understanding gained from this work. For example, the multiple demonstrations of field emission from patterned nanocarpets [23, 21] seem to show it can be used in an application, as does the demonstration of biological cell growth on patterned nanocarpets [19]. It would be very interesting to use anchored nanocarpets for the variety of applications mentioned in chapter 5. The evidence that patterns do not form within them following wetting and drying should improve their technological value.

Chapter 9

Summary and Conclusions

In this thesis, the objective was to obtain and study pattern formation in nanocarpets by the application of liquids and their subsequent evaporation. In this way, no matter how the liquid was applied (drop placement, nanocarpet and entire substrate immersion, touching a nanocarpet into a liquid surface), the ≈100 μm tall nanocarpets themselves were subjected to liquid immersion. The study of the pattern formation process was greatly facilitated by the development as part of this work of a method for anchoring nanocarpets within another material.

Four problem statements were used to guide this thesis, and they are used here also to summarize.

What is the mechanism for pattern formation in nanocarpets by a drying fluid? The results in chapter 4 showed that the presence of surface tension at liquid-air interfaces in contact with CNTs is the source of pattern formation, regardless of the particular liquid used. Pattern formation times are on the order of tens of seconds. Neighboring CNTs within the nanocarpet are mutually drawn together, which has the effect of pulling them away from regions where no CNTs are present. This was shown to invariably occur in any locations where there were never any CNTs grown, which are called defects in this thesis, and also from other disturbances of the nanocarpets prior to wetting. The question of whether these types of patterns may also form in the absence of any preexisting defects remains unanswered. It was speculated that even very small variations in spacings between CNTs may be sufficient to nucleate the formation of pattern elements. The evaporation of the last remaining

liquid was shown to fix the patterns, and they remained indefinitely in the patterned state, which was attributed to van der Waals forces between the contacting CNTs. It was also speculated that loss of liquid may not be the only way in which patterns are constrained or fixed, but that the interaction between neighboring pattern elements could stop their growth and be a source of pattern fixation.

What types of patterns are possible? The many images presented and the pattern analysis in chapter 4 showed that several primary types of patterns are possible. Patterns of distributed circles or nearly circular shapes seem to indicate that pattern elements have not had sufficient growth time to contact each other and mature into polygonal patterns. Larger-scale striated patterns superposed with patterns of much smaller average length scale are possible when liquid spreading flows are present. The patterns created under a sessile drop region were shown to be significantly different than within a liquid spreading flow region. Very large pattern elements are possible when CNTs are translated outward from the center of the pattern elements by the action of surface tension, exposing the bare substrate underneath. Reproducibility of patterns appears to be possible, as demonstrated by a visual comparison of SEM images from upside down dried nanocarpets that were first immersed in 1 cSt PDMS oil. By using an analogue to the hydraulic diameter in fluid mechanics, images of patterns were analyzed, and resulted in plots of distributions. These plots of 17 data sets under a wide variety of treatment conditions indicated that all nanocarpet patterns fall within about one standard deviation of the mean within a given pattern. Comparing mean pattern sizes between populations, however, showed they can vary over four orders of magnitude.

Can nanocarpets be anchored within a surface while remaining sufficiently functional? By inverting nanocarpets and carefully inserting them into spin-coated layers of curable polymers in chapter 5, it was demonstrated that nanocarpets can be anchored within another material to a depth of less than the height of the nanocarpet. Both cross-linked PDMS and PMMA were demonstrated as anchoring materials using this method. Spin-coating provides a controllable method of creating a thin layer of liquid, and therefore controllability over the thickness of the nanocarpet

anchoring layer should be possible.

What differences are there, if any, between patterns produced in anchored nanocarpets and those in unanchored nanocarpets, and what does this mean? It was found in chapter 6 that nanocarpet patterns are, in fact, not possible in PMMA anchored nanocarpets. This was true in spite of the presence of the same types and numbers of defects and same experimental conditions as those that created the patterns in chapter 4. This was attributed to mean that enforcing a cantilevered boundary condition by creating an anchoring layer at the base of the CNTs in the nanocarpets prevents the necessary degrees of freedom for patterns to form.

Some overall conclusions may also be drawn from the results of this thesis. Pattern formation in nanocarpets has been shown to often be dominated by the presence of significant heterogeneities in the morphologies of the nanocarpets themselves. Pattern formation observed by other workers is most likely due to this finding as well. Because of the significance of surface tension forces acting on nanoscale structures (CNTs), any unbalanced effects create an unstable situation and growth of pattern elements will occur. This indicates that the prospect for controllability over this type of pattern formation is not good, unless heterogeneities can be significantly minimized. If the model for pattern formation were developed further, prediction of patterns that would be obtained might be possible, and this pattern formation process could be used for convenient fabrication by self-assembly.

The development of the anchoring method for nanocarpets expands their possible use in many technological applications, and should increase their ease of handling and robustness.

The demonstration in this thesis of the effect of enforcing a cantilevered boundary condition means that strength of adhesion of nanocarpets to their substrates is crucially important when considering pattern formation.

The findings of this thesis could potentially all be applied to the consideration of pattern formation in any type of packed and aligned 1-D nanostructures, the possibility of anchoring them, and the necessity of consideration of boundary conditions.

Appendix A

Wetting of CNTs

In this appendix, general wetting and particularly the wetting of CNTs is discussed. This is done here because it has not been of prime importance to this work, but is relevant to working with liquids and CNTs.

The subject of wetting is considered to be the study of the behavior of a liquid, particularly its spreading, in contact with a solid (or another liquid) and a gas, usually air [5]. Thus it is the mutual contact of three phases that is of interest. In the nanocarpet (including its substrate) and liquid system (in an air atmosphere) one thinks of the wetting of the liquid upon the CNTs themselves and also the nanocarpet substrate, which in this work is either a silicon dioxide coated silicon wafer, quartz glass, or an anchoring layer of cross-linked PDMS or PMMA.

There is an impressive body of work being built currently that deals with the wetting (and very often the *non*wetting) of physically and chemically structured and multiscaled surfaces [104, 105, 106]. In particular, the so-called lotus effect has been of interest in the literature in recent years, and it refers to the super-hydrophobicity and self-cleaning exhibited by lotus leaves [107, 108, 109]. Nanocarpets have also been shown to exhibit similar behavior, with near 180° water drop contact angles [47, 110]. The subject is quite involved, however, and considering its many subtleties is not relevant to the scope of this thesis because the aim in creating patterns in nanocarpets is for the liquid to first completely wet the nanocarpet.

The Young-Dupré law (sometimes simply called Young's Law) describes a force

balance at equilibrium along the contact line of the three phases and is

$$\gamma \cos\theta_E = \gamma_{SO} - \gamma_{SL}, \tag{A.1}$$

where γ is the liquid-air surface tension, θ_E is the equilibrium contact angle measured within the liquid, and γ_{SO} and γ_{SL} are the solid-vapor and solid-liquid interfacial tensions, respectively. The sign of $\cos\theta_E$ determines whether a liquid in a given system is said to be "mostly wetting" (for $0 < \theta_E \leq \pi/2$) or "mostly nonwetting" (for $\pi/2 \leq \theta_E \leq \pi$). If $\theta_E = 0$ then there is complete wetting, and a drop of that liquid would spread completely to a film of molecular thickness on that particular solid surface. Also, if $\theta_E \leq \pi/2$, the liquid will spontaneously invade a capillary (a small diameter tube), a porous medium, or a sponge-like structure. This is very important in this work because nanocarpets are similar to a porous medium with regards to wetting. It is noted that this description does not include dynamic interactions, which can be very complicated indeed. The advancing contact angle that is present when a contact line is moving away from the liquid side is typically larger than the equilibrium contact angle, and the receding contact angle that is present during the movement of a contact line toward the liquid side is typically smaller than the equilibrium contact angle. The contact lines of droplets sliding on a smooth solid surface exhibit this behavior.

Contact angles can be measured in many ways, but since it was desired in this work for the liquid to wet nanocarpets fully, it was not necessary to measure contact angles.

For individual CNTs, theoretical predictions were made [111] for water contact angles on carbon fibers of various diameters (surface curvatures) down to the nanoscale. The surface energy of CNTs can be considered to be similar to that of graphene, a planar form of graphite, as they have the same chemical structure of hexagonally bonded carbon. For a CNT of 20 nm diameter, a water contact angle of 82° was predicted. In a highly related study [112], clever experiments were conducted by attaching a CNT to an atomic force microscope (AFM) tip and carefully dipping the

CNTs into various liquids (PDMS polyethylene-glycol, glycerol, water) and recording the force jump during retraction of the CNT from the liquid. By considering the CNT tip to be a cylinder with a hemispherical cap, the geometry can be used to derive a relationship between force and contact angle. For a 20 nm diameter CNT a water contact angle of 80° was found. More importantly for this work, it was directly verified that PDMS oil with surface tension of 25.1 mN/m (the PDMS oil in this work was specified to have surface tension 17.4 mN/m) has a contact angle of 0°, which was deduced from the fact that it completely wetted the CNT tip up to and including the AFM probe, regardless of the length of CNT used. PDMS oil is prominently used for the experiments in this thesis, and thus it has been shown to fully wet individual CNTs.

Appendix B

CNT Growth Setup

Additional figures and diagrams of the CNT growth setup used in this work are given here.

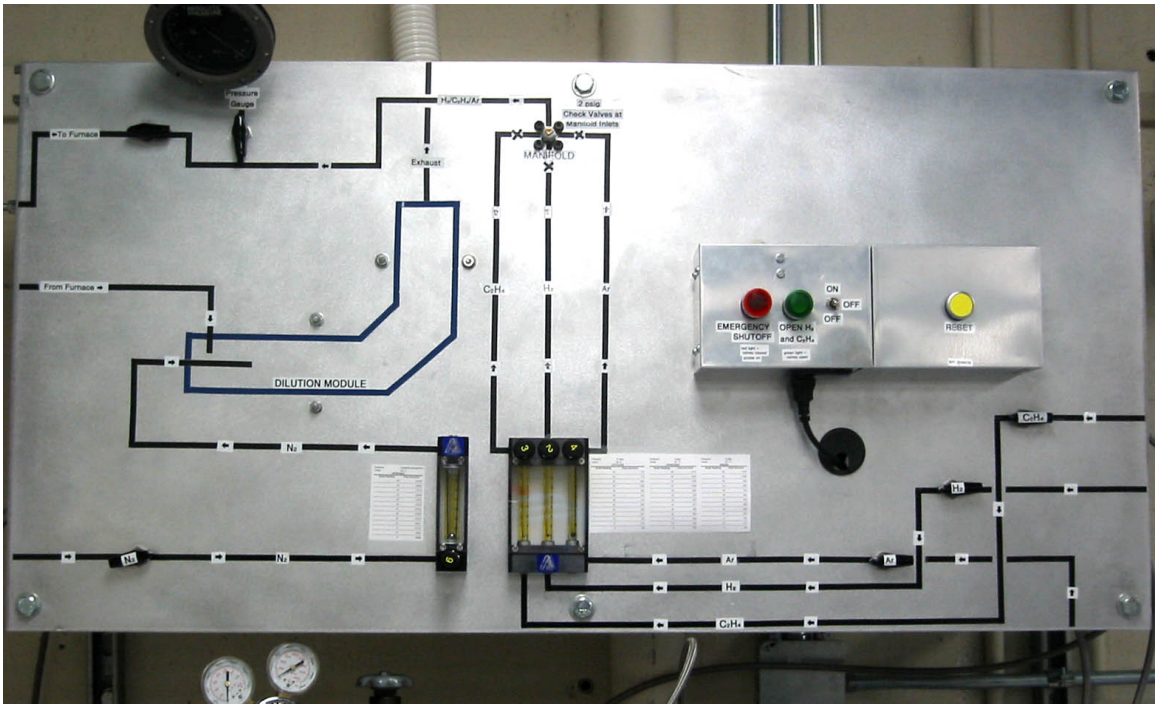

Figure B.1: View of the front of the control panel showing the ball valves, rotameters (manual volumetric flow controllers), labeling, and control boxes.

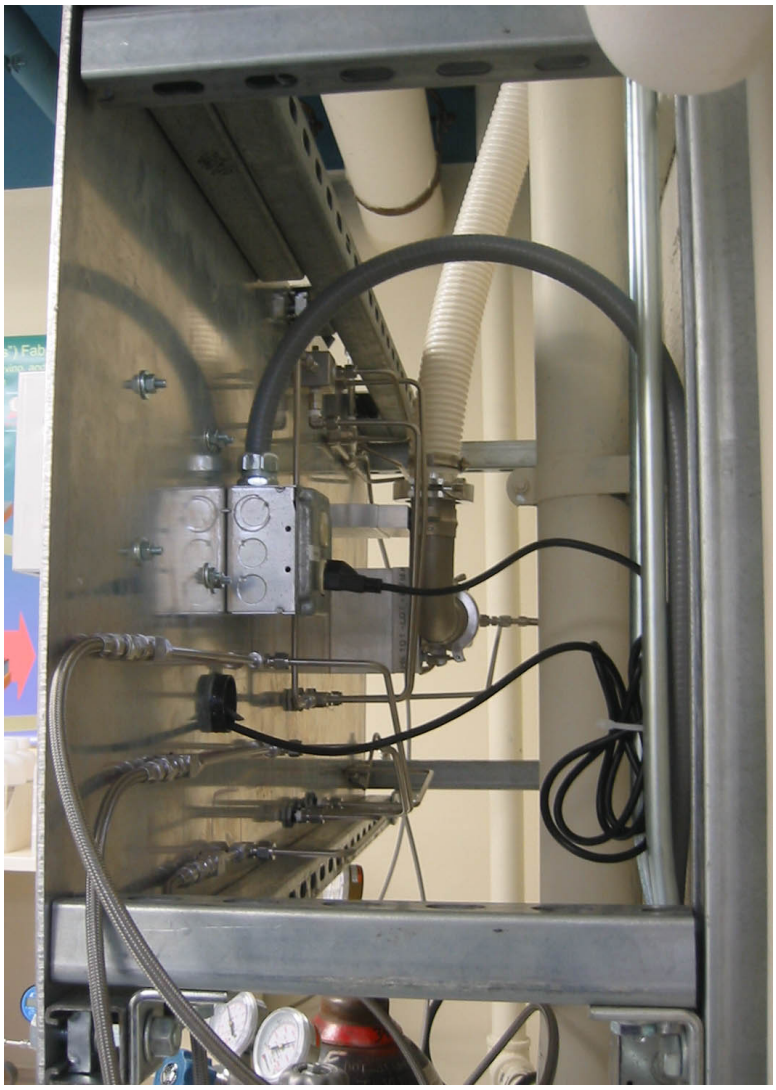

Figure B.2: View of the back of the control panel showing the Swagelok lines, and the unistrut mounting of the panel to the wall, allowing sufficient working space.

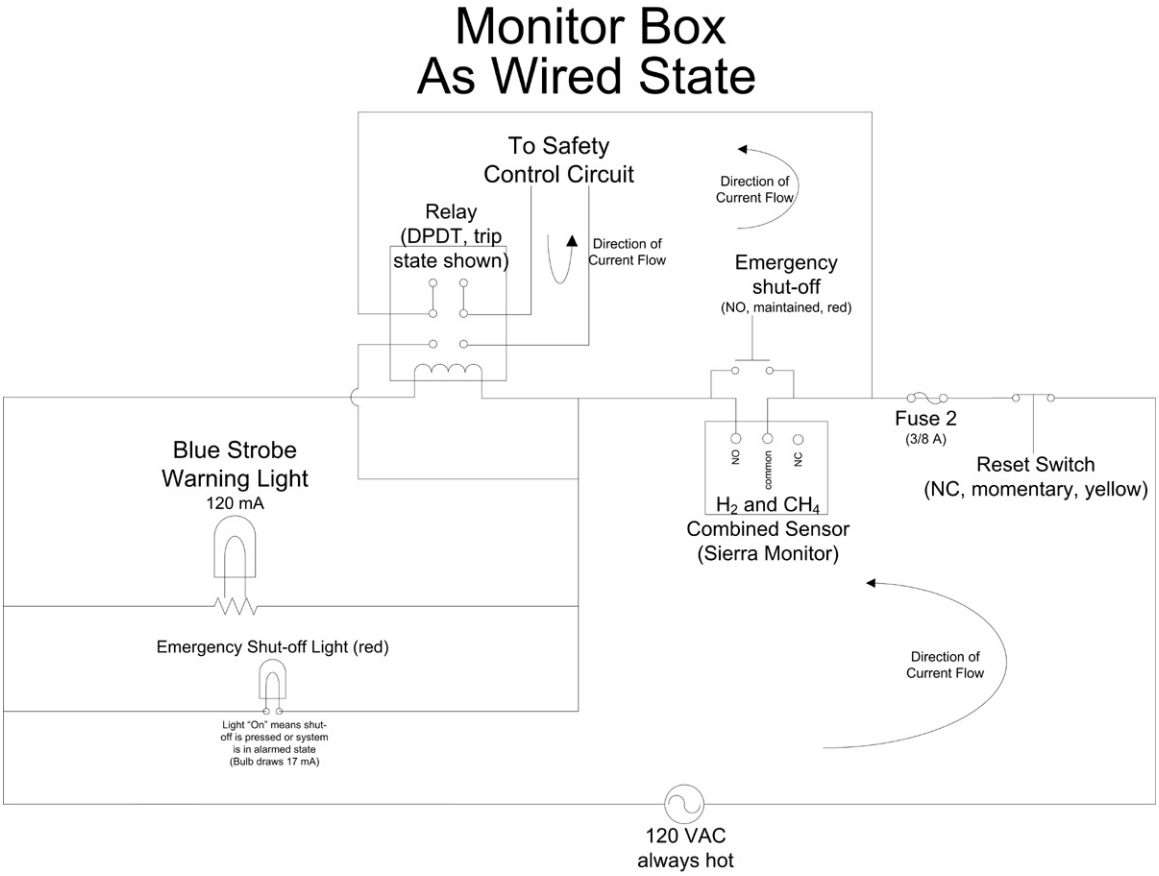

Figure B.3: Wiring diagram for the monitor box and external components (warning light and gas sensor) in the as-wired state.

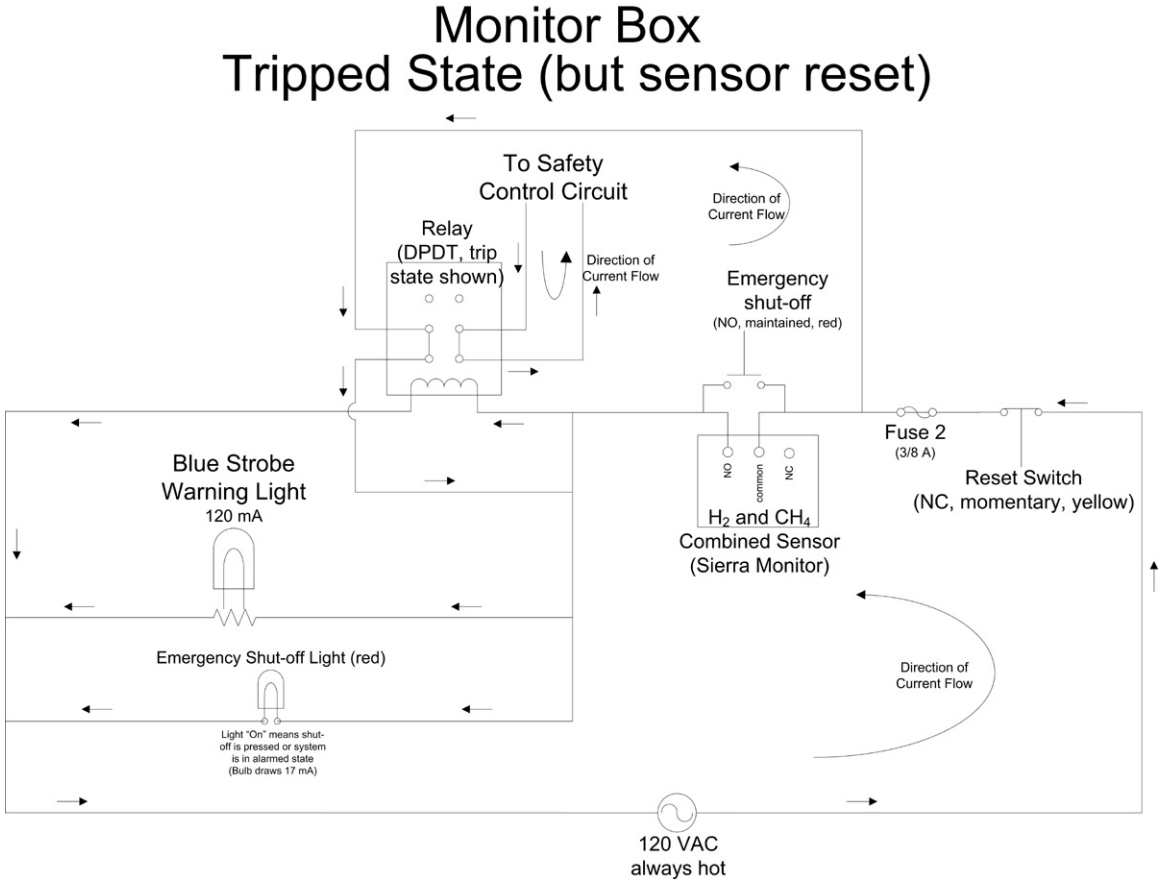

Figure B.4: Wiring diagram for the monitor box and external components (warning light and gas sensor) in the tripped state.

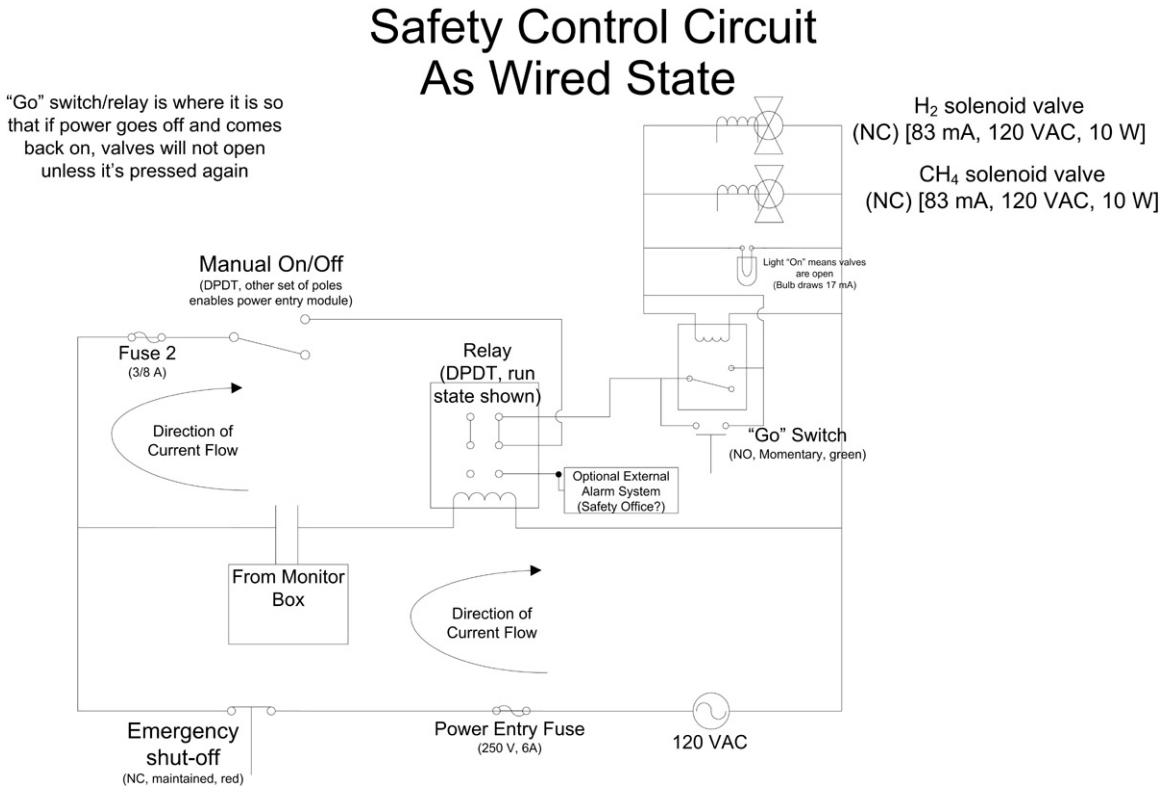

Figure B.5: Wiring diagram for the control box and flow system components (solenoid valves and control switches) in the as-wired state.

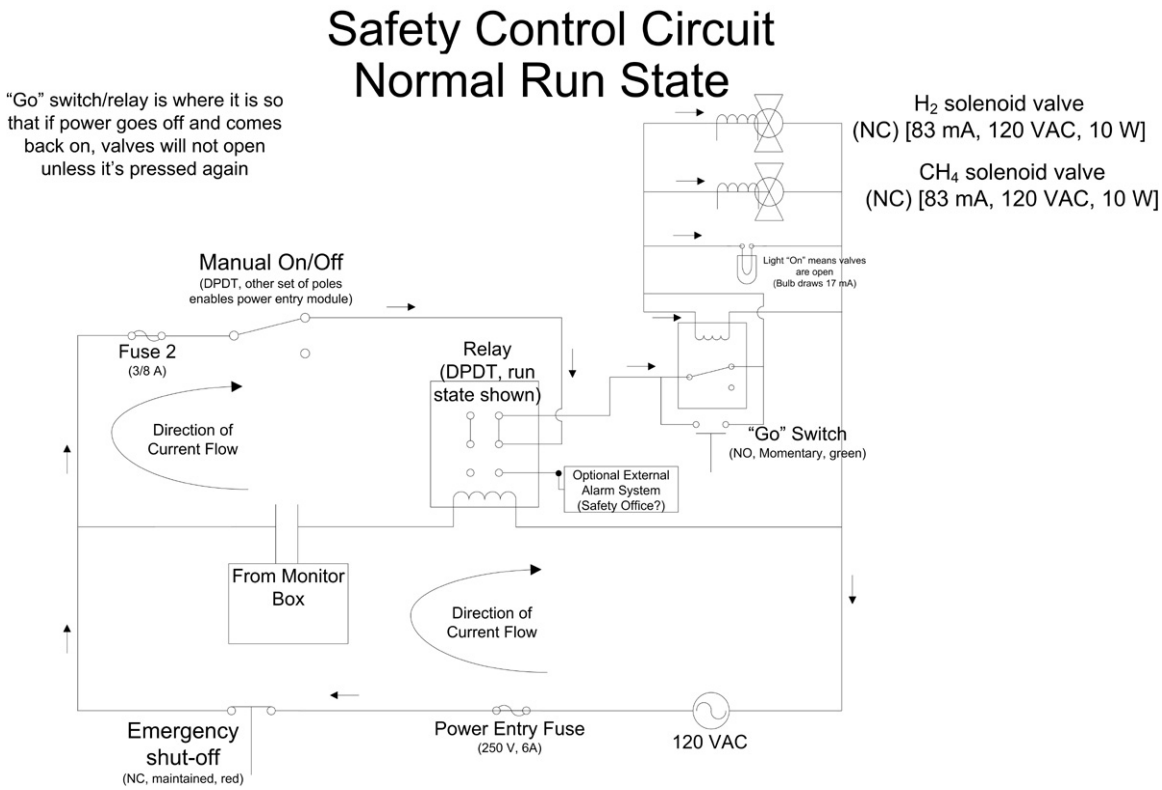

Figure B.6: Wiring diagram for the control box and flow system components (solenoid valves and control switches) in the run state.

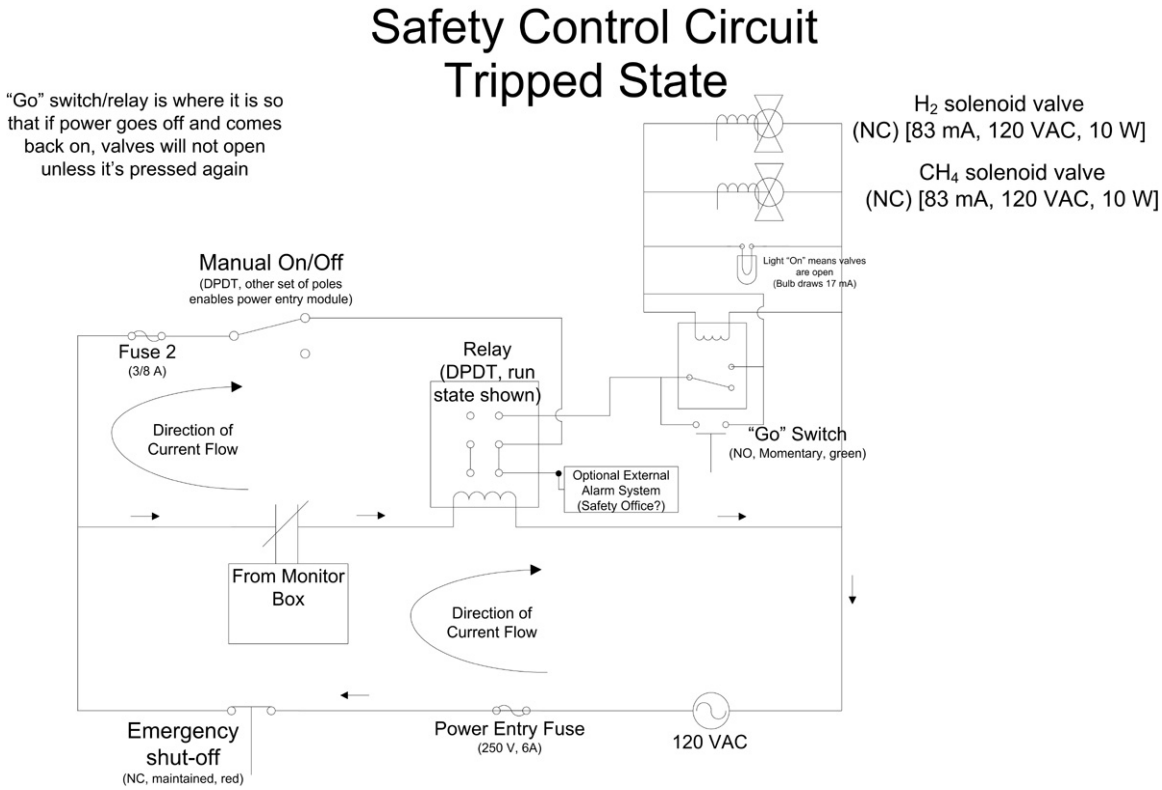

Figure B.7: Wiring diagram for the control box and flow system components (solenoid valves and control switches) in the tripped state.

Appendix C

Population Balance Modeling

C.1 The General 1-D Population Balance

A population balance model [94] is a means of describing systems involving populations of "particles" within a separate phase, called the "continuous phase," and which are possibly subject to convective motion, birth, death, and growth. The continuous phase is the environment in which the particles exist, and its behavior is treated separately from that of the particles themselves. One set of coordinates, often scalar in nature, is used to describe particle properties that are of interest, such as size, and these are termed the "internal coordinates." Another set of coordinates may be used to describe particle centroid positions relative to some fixed spatial coordinate system, and these are termed the "external coordinates." If the system being considered happens to be an open system, for example, external coordinates would be important for describing the particle fluxes in and out of the system and how particle properties may depend on the spatial gradients. Alternatively, the two assumptions that particles are uniformly spatially distributed within the system and there is no convective behavior within the system eliminates the need for external coordinates altogether. This does not mean, however, that nothing needs to be known about the continuous phase, since as particles grow, the surrounding continuous phase may very well be affected.

Most often, we are interested in the *growth* of particles in a system, focusing on either their size or mass. Considering the particle state space as a continuum

consisting of both internal and external coordinates, the Reynolds transport theorem may be used to derive the general N-dimensional case of the population balance equation,

$$\frac{\partial}{\partial t} f_1 + \nabla_x \cdot (\dot{\mathbf{X}} f_1) + \nabla_r \cdot (\dot{\mathbf{R}} f_1) = h, \tag{C.1}$$

where

$\mathbf{x}$ = internal coordinates,
$\mathbf{r}$ = external coordinates,
$\mathbf{Y} = \mathbf{Y}(\mathbf{r}, t)$, the "continuous phase vector,"
t = time,
$f_1 = f_1(\mathbf{x}, \mathbf{r}, t)$, the number density of particles,
$\dot{\mathbf{X}} = \frac{d}{dt}\mathbf{X}(\mathbf{x}, \mathbf{r}, \mathbf{Y}, t)$, growth rate in internal coordinates of particle $\mathbf{X}$ that has property values of $\mathbf{x}$,
$\dot{\mathbf{R}} = \frac{d}{dt}\mathbf{R}(\mathbf{x}, \mathbf{r}, \mathbf{Y}, t)$, time rate of change in external coordinates of particle $\mathbf{X}$,
$h = h(\mathbf{x}, \mathbf{r}, \mathbf{Y}, t)$, the *net* birth rate of particles per unit volume of particle state space,

and initial and boundary conditions are required, as well as an equation describing the relationship between the continuous phase vector $\mathbf{Y}(\mathbf{r}, t)$ and the particles in the system.

For simplicity, we now restrict ourselves to one dimension in internal coordinates, a uniform spatial distribution of particles, and no convection such that external coordinates are no longer needed. Additionally, particle interaction is neglected, meaning that particles cannot break or aggregate within the system. They are still, however, allowed to nucleate and begin to grow within the system. The allowance of nucleation is handled in the lower boundary condition but no longer appears as a nonhomogeneous $h(x, Y, t)$ term.

Under these simplifications, the general 1-D population balance equation including a spatially uniform scalar quantity describing the continuous phase, $Y(t)$, as given in Ramkrishna [94] is

$$\frac{\partial f_1(x,t)}{\partial t} + \frac{\partial}{\partial x}(\dot{X}(x, Y, t) f_1(x, t)) = 0, \tag{C.2}$$

where

$f_1(x,t)$ = number density of particles as a function of a particle property, x, and time, t,
$\dot{X}(x,t)$ = growth rate of particle with property value of x,
$Y = Y(t)$, a scalar quantity describing the continuous phase,

and initial and boundary conditions are required as well as the relationship between $Y(t)$ and the particles. Eq. (C.2) is a first-order, linear, nonhomogeneous hyperbolic partial differential equation. It is like an advection equation, for which the general form is usually written

$$\frac{\partial \psi}{\partial t} + \nabla \cdot (\psi \mathbf{u}) = 0. \tag{C.3}$$

Eq. (C.2) can also be expanded and rearranged to look like a one-way wave equation

$$\frac{1}{\dot{X}} \frac{\partial}{\partial t} f_1(x,t) + \frac{\partial}{\partial x} f_1(x,t) = -\frac{1}{\dot{X}} f_1(x,t) \frac{\partial}{\partial x} \dot{X}. \tag{C.4}$$

The standard form of a nonhomogeneous one-way wave equation with constant wave speed c and forcing $f(x,t)$ (with x being a spatial variable here, not a particle property as elsewhere) is

$$\frac{1}{c} \frac{\partial u}{\partial t} + \frac{\partial u}{\partial x} = f(x,t). \tag{C.5}$$

The above features indicate that the method of characteristics may be applied to find solutions to simple population balance equations such as eq. (C.2).

For eq. (C.2), if the initial condition is *no* particles, then $f_1(x,0) = 0$. The nucleation rate is taken to be a function of Y and is $\dot{n}_0(Y)$ particles per unit time, new particles have $x = 0$, and $\dot{n}_0(Y)$ is taken to be a "flux" in at $x = 0$. This defines the boundary condition for the problem and is written

$$\dot{X}(0,Y,t) f_1(0,t) = \dot{n}_0(Y). \tag{C.6}$$

Eq. (C.2) can be integrated over all x,

$$\int_0^\infty \left(\frac{\partial f_1(x,t)}{\partial t} + \frac{\partial}{\partial x} (\dot{X}(x,Y,t) f_1(x,t)) \right) dx = 0, \tag{C.7}$$

$$\int_0^\infty \frac{\partial f_1(x,t)}{\partial t}dx + \int_0^\infty \frac{\partial}{\partial x}(\dot{X}(x,Y,t)f_1(x,t))dx = 0, \tag{C.8}$$

$$\frac{d}{dt}\int_0^\infty f_1(x,t)dx + \dot{X}(\infty,Y,t)f_1(\infty,t) - \dot{X}(0,Y,t)f_1(0,t) = 0, \tag{C.9}$$

$$\frac{d}{dt}\int_0^\infty f_1(x,t)dx = \dot{X}(0,Y,t)f_1(0,t) - \dot{X}(\infty,Y,t)f_1(\infty,t), \tag{C.10}$$

and if N is the total number of particles per unit physical space in external coordinates (volume, area, length), then

$$\frac{dN}{dt} = \frac{d}{dt}\int_0^\infty f_1(x,t)dx = \dot{X}(0,Y,t)f_1(0,t) - \dot{X}(\infty,Y,t)f_1(\infty,t) = \dot{n}_0(Y), \tag{C.11}$$

where the right-hand side means the number of particles can only increase by nucleation. Eqs. (C.6) and (C.11) imply that

$$\dot{X}(\infty,Y,t)f_1(\infty,t) = 0, \tag{C.12}$$

which is termed the *regularity* condition and which means that either the number density $f_1(\infty,t)$ or the growth rate $\dot{X}(\infty,Y,t)$ must vanish for arbitrarily large x.

The last missing piece in the formulation of the problem is the relationship between the continuous phase, described by $Y(t)$, and the particles. It is expected that $Y(t)$ will be depleted with time due to the growth of particles. If this happens in proportion to the growth rate of particles, and with the proportionality factor itself being dependent on size, then

$$\frac{dY}{dt} = -\int_0^\infty \alpha(x)\dot{X}(x,Y,t)f_1(x,t)dx, \tag{C.13}$$

with $\alpha(x)$ being the size-dependent proportionality factor. All that remains is specifying an initial condition for $Y(t)$.

C.2 Instructive Population Balance Model for Polyurethane Foams

A "particle" in a population balance model does not have to be a physical particle, but rather only must behave as one within the model. Thus a bubble (or a pattern element in a nanocarpet pattern) can be considered to be a particle and a population balance can be used to predict the bubble size distribution and its time evolution in polyurethane foam formation.

A population balance model based solely on nucleation and growth has been used [96, 95] to predict the bubble size distribution in polyurethane foam formation within a cylindrical container under "free rise" (the foam itself is not physically confined but is free to rise) conditions. The reason a distribution in bubble sizes results is that nucleation and growth both occur simultaneously for a portion of the total reaction time. Some of the basic assumptions of the model used that are relevant are given in Table C.1.

Table C.1: Polyurethane Foam Model Assumptions

1. Bubble formation is assumed to occur only through nucleation and growth.
2. Nucleation is assumed to be *homogeneous*.
3. No coalescence or breakage of bubbles occurs.
4. The blowing agent in its vapor phase behaves as an ideal gas.
5. No relative motion exists between the bubbles and the liquid.
6. No loss of liquid or vapor by evaporation occurs (i.e., a system of fixed total volume).
7. All physical properties such as specific heats and densities are assumed constant, and volume changes in the liquid are neglected.

These assumptions and the following model are instructive in considering a model for nanocarpet pattern formation. They especially help to identify what the important components of such a model would be.

The general formulation of a 1-D population balance was given in §C.1, and the 1-D population balance equation as written by Niyogi et al. is

$$\frac{\partial}{\partial t}(fV_L) + \frac{\partial}{\partial l}(fGV_L) = 0, \tag{C.14}$$

for bubbles with diameter l, associated number density fV_L, and bubble growth rate $G = dl/dt$. Eq. (C.14) can be expanded and rearranged to obtain

$$\frac{1}{G}\frac{\partial}{\partial t}(fV_L) + \frac{\partial}{\partial l}(fV_L) = -\frac{1}{G}\frac{\partial G}{\partial l}fV_L. \tag{C.15}$$

If this were considered as a one-way wave equation, the "wave speed" would be related to the bubble growth rate G. The method of characteristics may be used to find solutions. As in §C.1, external coordinates are not needed because the bubble distribution is assumed uniform in space and there is no convection included.

The initial condition is just an arbitrary distribution (possibly zero),

$$t = 0, f = f(0, l) \ for\ all\ l \tag{C.16}$$

and the boundary condition for the number density at the critical nucleus size l_N is

$$l = l_N, fV_L(t, l_N) = \frac{J(t)V_L(t)}{G(l_N, t)} \ for\ all\ t, \tag{C.17}$$

where $J(t)$ is the rate of nucleation of new bubbles and $V_L(t)$ is the liquid volume.

The boundary condition states that, for all t, the number density of bubbles of diameter equal to the critical nucleus diameter, l_N, is equal to the nucleation rate times the liquid volume divided by the growth rate of bubbles of this diameter. This means that if nucleated bubbles grow very quickly, the number density of bubbles at the critical nucleus diameter will be small, but this can be counteracted by either a high nucleation rate (which is *independent* of diameter) or a large available liquid volume. This is effectively a "lower" boundary condition, since it is inherent that there are no bubbles of diameter less than l_N.

Since Niyogi et al. are considering the formation of spherical gaseous bubbles within a liquid prepolymer mixture, they assume the gas in the bubble behaves as an ideal gas. The growth rate of a bubble of diameter l is obtained from a mass-balance for a bubble as

$$\frac{d}{dt}\left[\frac{\pi}{6}l^3\frac{P}{RT}\right] = k_m\pi l^2\Delta C_B. \tag{C.18}$$

This equation states that the rate of change of the mass of the bubble is proportional, via the size-dependent mass-transfer coefficient k_m, to its surface area times the difference, ΔC_B, between the actual concentration and the equilibrium concentration of blowing agent. Applying the derivative, rearranging, and defining the growth rate G,

$$G \equiv \frac{dl}{dt}, \tag{C.19}$$

$$G = \frac{2k_m RT\Delta C_B}{P} + \frac{l}{3T}\frac{dT}{dt}. \tag{C.20}$$

It is seen that the growth rate is dependent on the environment of the bubbles, i.e., the continuous phase, primarily through the scalar-valued concentration difference and the temperature. Comparing with discussion in §C.1 about handling the continuous phase, it is clear that coupling relationships will be necessary in this polyurethane bubble formation to relate the bubbles with the continuous phase variables. The original population balance equation, eq. (C.14), can be expanded and rearranged to obtain

$$\frac{1}{fV}\frac{\partial}{\partial t}(fV_L) + \frac{G}{fV_L}\frac{\partial}{\partial l}(fV_L) = -\frac{\partial G}{\partial l}, \tag{C.21}$$

and substituting eq. (C.20) into eq. (C.21),

$$\frac{1}{fV_L}\frac{\partial}{\partial t}(fV_L) + \frac{G}{fV_L}\frac{\partial}{\partial l}(fV_L) = -2\frac{RT}{P}\Delta C_B\frac{dk_m}{dl} - \frac{1}{3T}\frac{dT}{dt}. \tag{C.22}$$

As previously expected, the method of characteristics can now be used to solve

eq. (C.22) with the characteristics identified as part of the coefficients in eq. (C.22),

$$\frac{dt}{dZ} = 1, \tag{C.23}$$

$$\frac{dl}{dZ} = G. \tag{C.24}$$

Using these characteristics to transform eq. (C.22), we have

$$\frac{d}{dZ} ln(fV_L T^{1/3}) = -2\frac{2RT}{P}\Delta C_B \frac{dk_m}{dl}. \tag{C.25}$$

Integration of the first characteristic, eq. (C.23), gives

$$t = Z + r, \tag{C.26}$$

with r as the start time of a given characteristic. Thus, fV_L can now be recast as a function of Z and r. The boundary condition at the starting point of all characteristics, $l = l_N$, must be specified in terms of Z and r. Eq. (C.24) can be integrated as follows,

$$\int_{Z=0,r}^{Z,r} dl = l(Z,r) - l_N = \int_{Z=0,r}^{Z,r} G dZ, \tag{C.27}$$

$$l(Z,r) - l_N = \int_{t'=r}^{t'=t} \left[\frac{2k_m RT}{P}\Delta C_B + \frac{l}{3T}\frac{dT}{dt}\right] dt', \tag{C.28}$$

where eq. (C.20) has been used to substitute for G, and eq. C.26 has been used to replace Z as the integration variable on the right-hand side. Finally, the transformed population balance equation, eq. (C.25), can be integrated,

$$\int_{Z=0,r}^{Z,r} d(ln(fV_L T^{1/3})) = -\int_{t'=r}^{t'=t} \left[\frac{2RT}{P}\Delta C_B \frac{dk_m}{dl}\right] dt', \tag{C.29}$$

$$ln\left[\frac{(fV_L T^{1/3})|_{Z,r}}{(fV_L T^{1/3})|_{Z=0,r}}\right] = -\int_{t'=r}^{t'=t} \left[\frac{2RT}{P}\Delta C_B \frac{dk_m}{dl}\right] dt'. \tag{C.30}$$

In the above, $(fV_L)|_{Z=0,r}$ equals the value of fV_L at the lower bound $l = l_N$ and start time r of the characteristic, and can be obtained from the original statement

of the boundary condition, eq. (C.17). Once Z and r are specified, eqs. (C.26), C.28, and C.30 can be used to obtain fV_L as a function of l and t, and thus the above constitutes the formal solution to the population balance equation posed in eq. (C.14). Eqs. (C.26), (C.28), and (C.30) have to be integrated numerically and simultaneously with coupling equations relating the bubbles to the continuous phase. These equations govern heat or other energy exchange, polymerization chemistry, and mass transfer into the bubbles. The coupling equations would be achieving the same goal as eq. (C.13) in the general case of §C.1. The bubble size distribution can thus be obtained using the above procedure and starting the characteristics, Z, at different points of time (for different values of r).

C.3 Discussion

The example model in §C.2 required knowledge of the growth rate law, which was taken to be a mass-transfer coefficient model, which itself was diffusive in nature. This means that if the diffusion coefficient were constant, bubble radii would grow as the square root of time. It was also necessary to include in the boundary condition, eq. (C.17), the nucleation rate of new bubbles, $J(t)$, the total liquid volume as a function of time, $V_L(t)$, and the critical nucleus diameter, l_N. In principle, the model procedure of Niyogi et al. could accommodate any growth rate law in place of the diffusive mass-transfer model used. Correct forms for nucleation rate and other model components would also be needed. This is of importance here because their correlates are desired for understanding and modeling nanocarpet pattern formation, namely growth rate, nucleation rate, critical size (if it exists), and total "liquid volume" as a function of time. For nanocarpet patterns considered in 2-D, a better metric for liquid volume would likely be nonpatterned area.

A major caveat of the volumetric model of Niyogi et al. is that interaction between bubbles is not considered. It was stated in the model assumptions in table C.1 that coalescence or breakage of bubbles is not allowed to occur. Because they are bubbles, any contact between them would eventually result in coalescence. This effectively

means that bubbles are not allowed to contact each other in their model. However, this has serious implications for an analogous model applied to nanocarpet pattern formation. If the Niyogi et al. model were applied directly, then nanocarpet pattern elements would only be allowed to grow until just before they begin to "run into each other." Thus the patterns obtained would be uniformly distributed, non-contacting circles. There is no allowance in the Niyogi et al. framework for a growth rate law dependent upon location within the bubble, for example angular dependence. The interaction of nanocarpet pattern elements with each other is what creates polygonal cellular patterns, so it is apparent that an appropriate growth rate law for nanocarpet pattern formation would need to account for this and it is of high interest in this thesis. In Niyogi et al. [95], it is stated that:

> "Thus, the morphology of the foam has to change from that of a froth of spherical bubbles to cellular polyhedral structure, when the gas-phase volume fraction becomes very high (for uniform-sized bubbles in FCC packing, this value is 0.74). Beyond this value, the bubbles can no longer be spherical, and the calculation of mass transfer based on spherical bubbles will not yield correct values. It will require a separate treatment (not attempted in this work), since liquid will be present in the form of thin films and plateau borders."

Some useful features of the Niyogi et al. model [95] are exhibited in their results, and are helpful in considering nanocarpet pattern formation. It is found that a lower initial concentration of blowing agent (to be converted into bubbles) results in a larger nucleation rate, and the rise time to peak nucleation rate is faster than for higher initial blowing agent concentrations. This effect is highly related to the temperature of the system, which has the same behavior. The exothermic polymerization reaction creating the polyurethane causes a higher temperature, and earlier than for higher initial blowing agent concentrations, therefore causing a higher nucleation rate. For nanocarpet pattern formation, there should be no "blowing agent," per se, but the existence of factors that could cause increased nucleation rate is possible. The total

number of bubbles in the polyurethane foam system reaches a higher final value, and rises faster, for lower initial blowing agent concentration. This makes sense in conjunction with the increased nucleation rate. For nanocarpet pattern formation, it is also expected that for a higher nucleation rate, a larger number of pattern elements should be formed. In the polyurethane foam, the mean bubble diameter is found to increase nearly linearly with the initial blowing agent concentration, and is primarily an effect of the increased rise time of nucleation rate seen for the higher concentrations. Not as many nuclei are formed as for lower concentrations, but the longer rise time allows them to grow to larger diameter during the simulation time period. If the appropriate analogue for blowing agent were identified in nanocarpet pattern formation, this would be an important relationship to consider. It is important to note that in the second paper by Niyogi et al. [96], they find that these trends are reversed when water is used as the blowing agent (a chemical blowing agent, whereas Freon is a physical blowing agent). That is, lower initial concentration of water leads to smaller nucleation rate with longer rise time and fewer total bubbles in the system with larger mean diameter. For water as blowing agent, a near-linear decrease in mean-diameter with initial concentration is found.

The relationship between the number density and the bubble diameter is the bubble size distribution (or more generally, the particle size distribution), and is a very important measure of a cellular system. In Niyogi et al. [95] it is found that the distributions are shaped like parabolas opening downward. The spread in possible bubble diameters widens, the mean bubble diameter increases, and the maximum number density decreases as the initial blowing agent (in this case Freon) concentration increases. Thus for a low initial blowing agent concentration, there is a higher density of smaller bubbles (with smaller spread), while for a high initial blowing agent concentration, there is a somewhat (e.g., one to two orders of magnitude) lower density of larger bubbles (with larger spread). Again, these trends are reversed when water is used as the blowing agent [96], with a low initial concentration causing a lower density of larger bubbles (and larger spread) and a high initial concentration causing a higher density of smaller bubbles (and smaller spread). Niyogi et al. define

"breadth" to be the difference in diameter between the largest and smallest bubbles. This obviously depends on the time between when the first bubble is born (and begins to grow) and when the last bubble is born. For nanocarpet pattern formation, this would be the time difference between when the first pattern element begins to form, and when the last of the liquid has evaporated. In general, increased rise times and length of nucleating periods would tend to increase the breadth of the particle size distribution, but this may be mediated by a size-dependent growth rate. Finally, Niyogi et al. define a useful normalized length scale for comparing different particle size distributions,

$$l^* = \frac{l - \bar{l}}{\sigma_l^2}, \tag{C.31}$$

where σ_l^2 is the variance in l and $\bar{l}$ is the mean of l. The number density fV_L can then be normalized by the total number of particles in the system $f_0 V_L$ and plotted against l^*. This has the effect of aligning the centers of the distributions being compared at $l^* = 0$ and scaling the number densities to be independent of their total system size. If dynamic information is available, the time evolution of the distribution can also be followed in this way.

Appendix D

Additional Data

D.1 Images Used in Distribution Analysis in §4.5

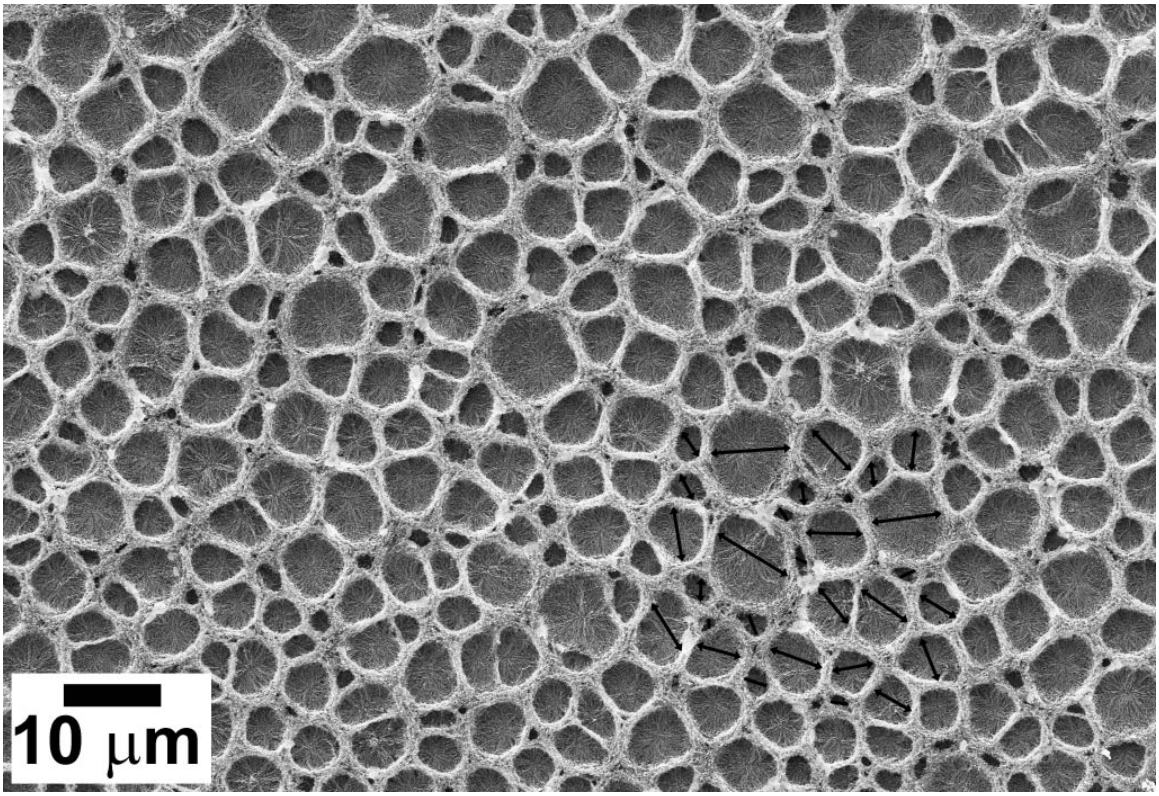

Figure D.1: *Data set A*. Image used in analysis. Sample was 4 μm tall, treated with solution of water and *Bacillus pumilus* spores. More measurements were taken than are shown.

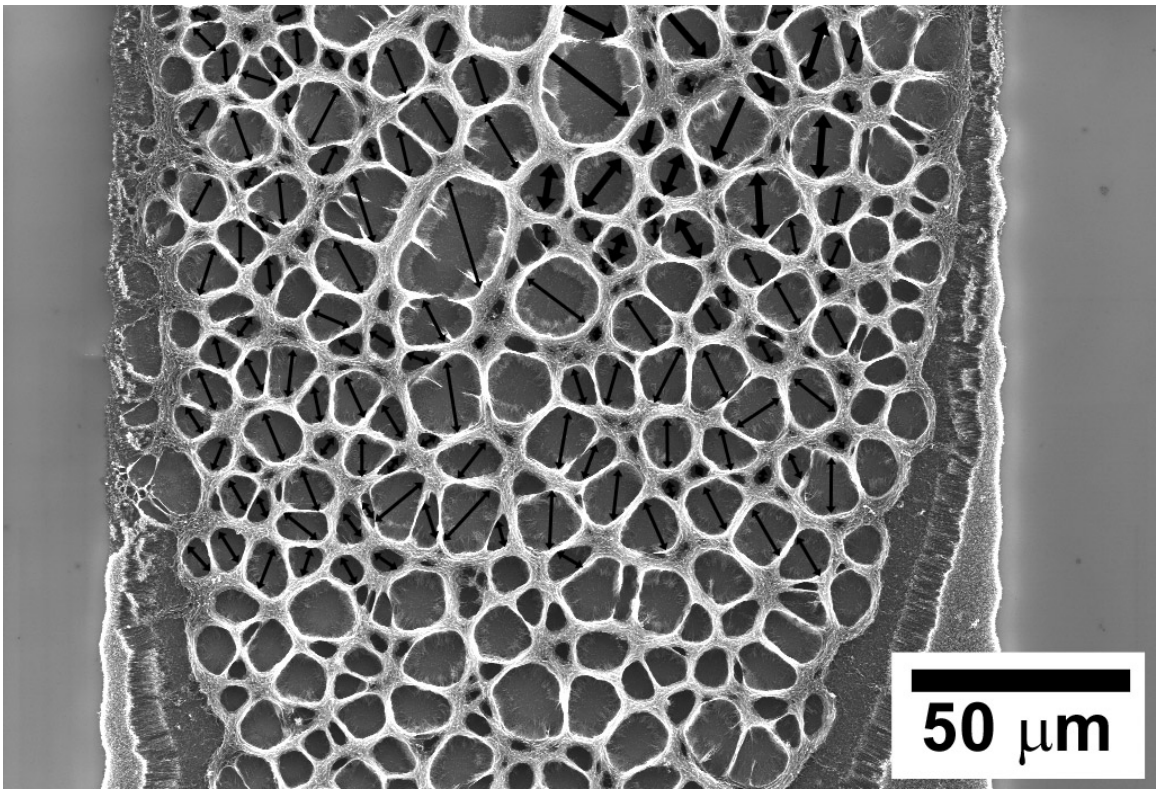

Figure D.2: ***Data set B*****. Image used in analysis. Sample was 8 μm tall, treated with 0.1 wt% Triton-X.**

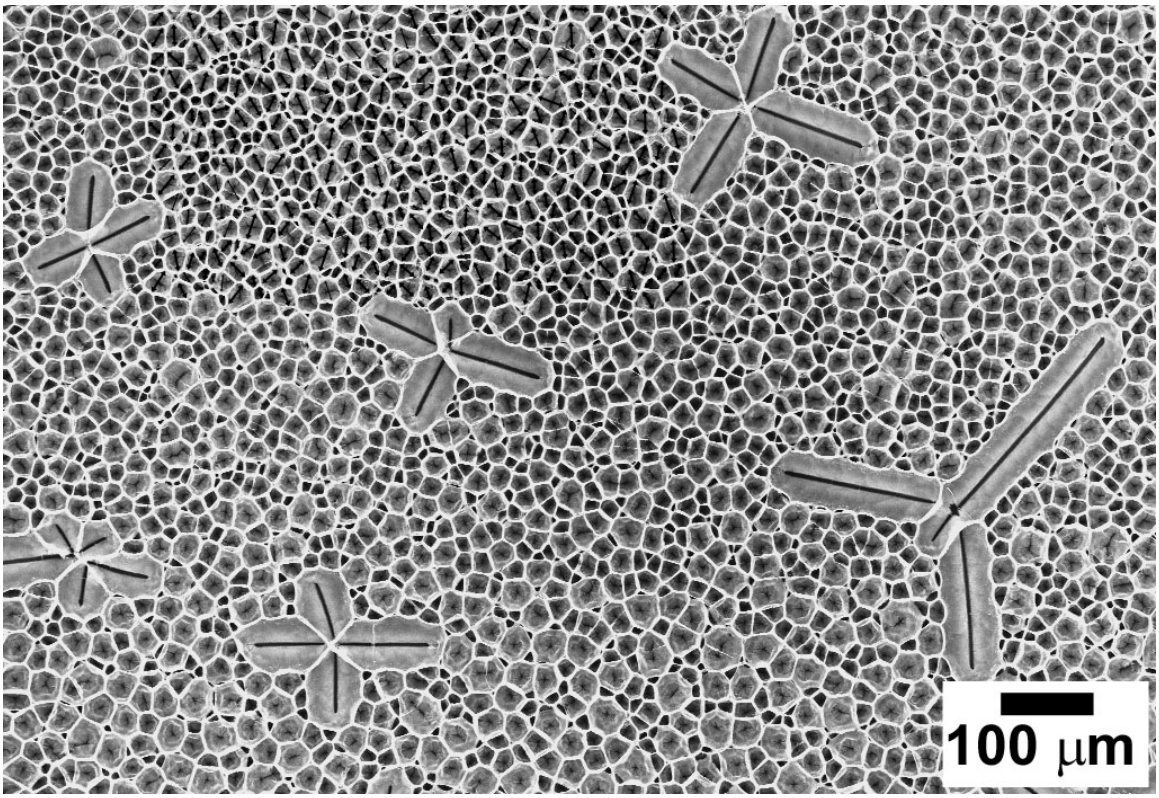

Figure D.3: ***Data set D.*** **Image used in analysis. Sample was 50 μm tall, treated with 0.1 wt% Triton-X.**

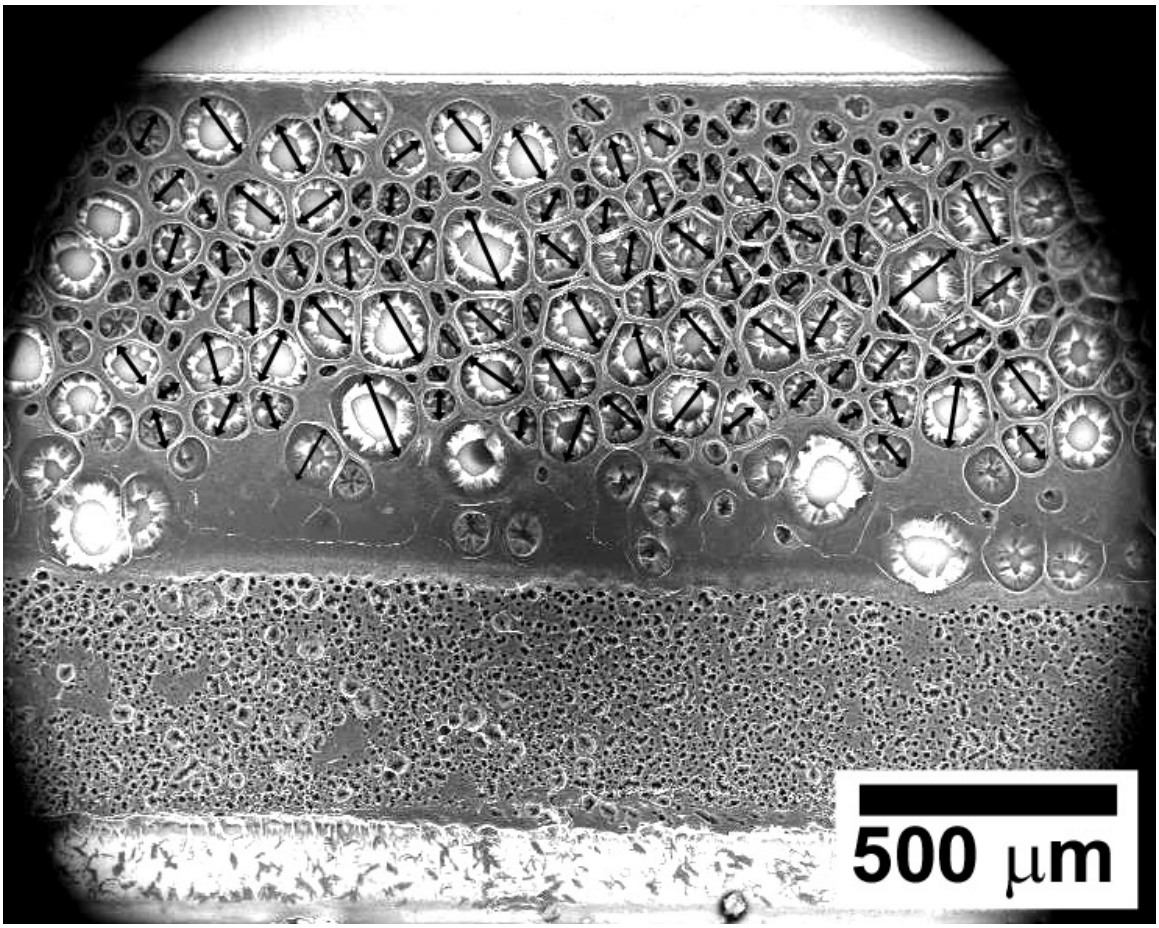

Figure D.4: ***Data set E.*** **Image used in analysis. Sample was 45 μm tall, treated with 0.1 wt% Triton-X. Only the pattern elements in the upper portion were considered.**

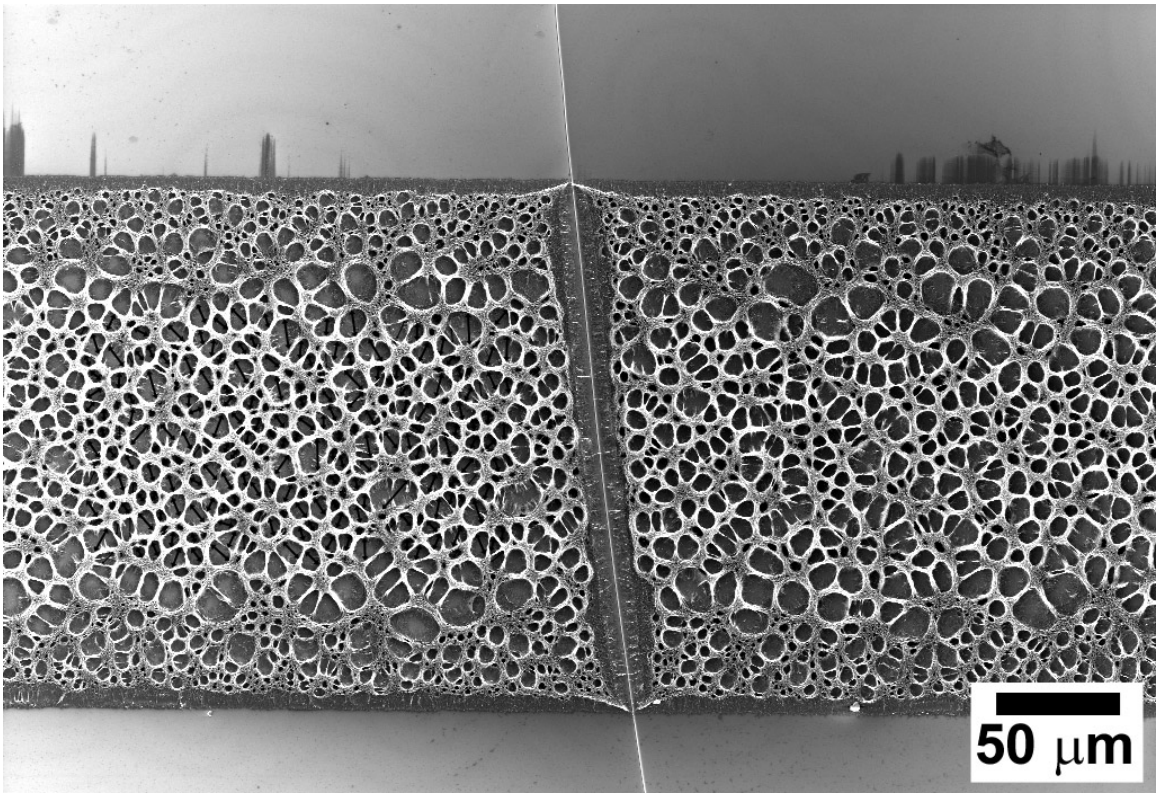

Figure D.5: ***Data set F.*** **Image used in analysis. Sample was 5 μm tall, treated with 0.1 wt% Triton-X.**

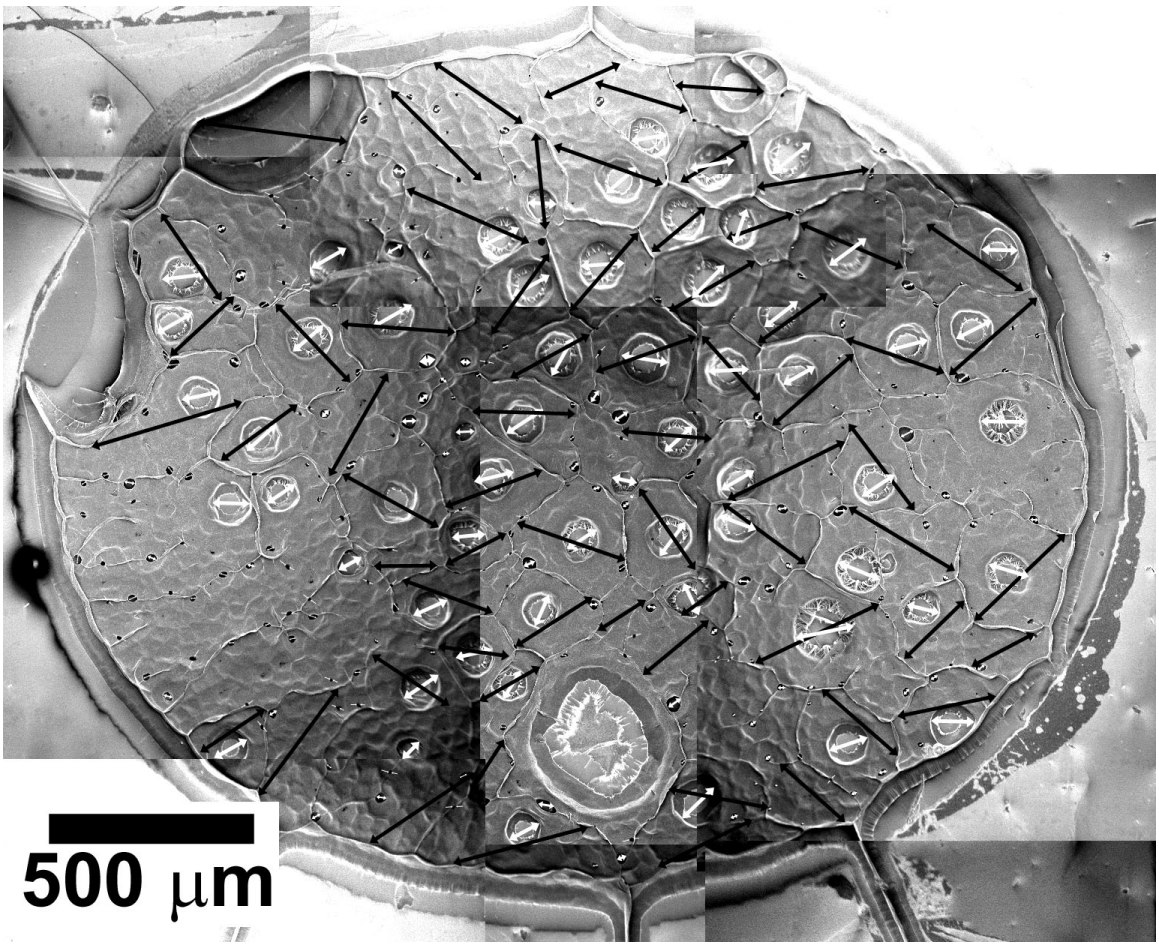

Figure D.6: ***Data set H.*** **Image used in analysis. Sample was 26 μm tall, treated with 0.36 cmc SDS and unknown concentration of fluorescein. Feature in the bottom center is due to syringe impact and was not measured.**

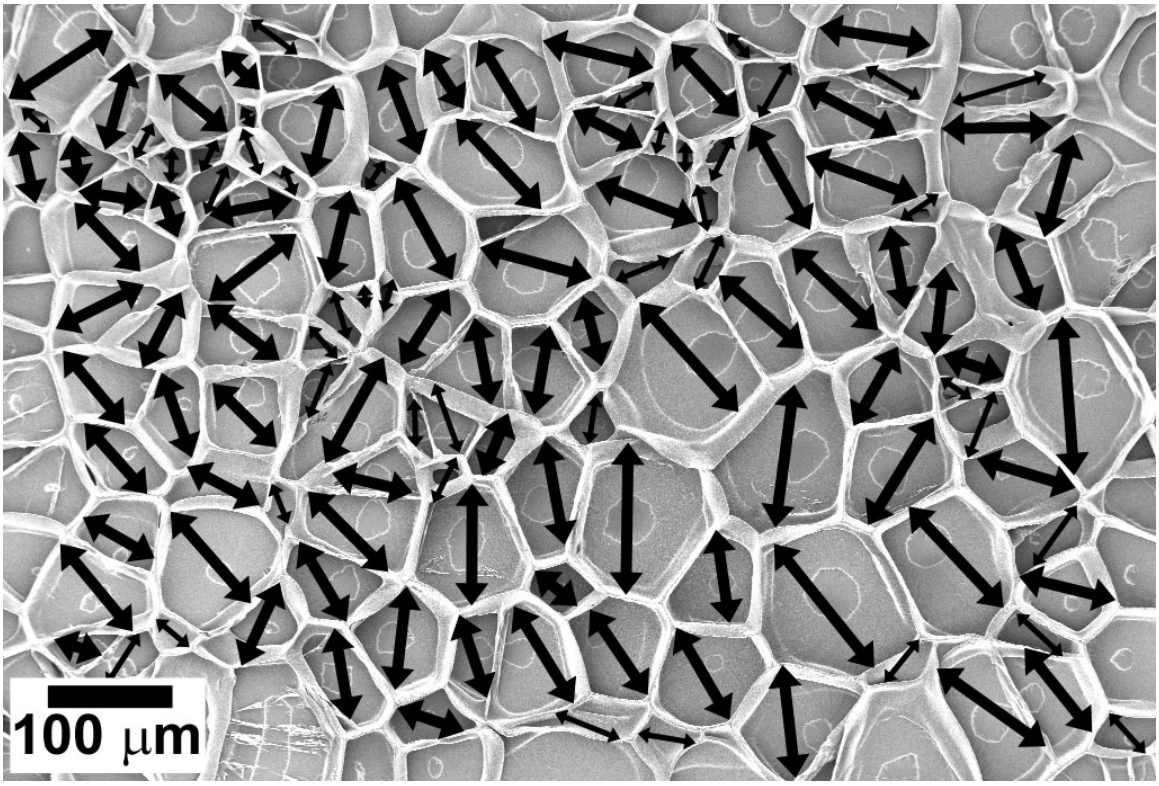

Figure D.7: ***Data set M.*** **Image used in analysis. Sample was 60 μm tall, treated with 0.5 cmc SDS.**

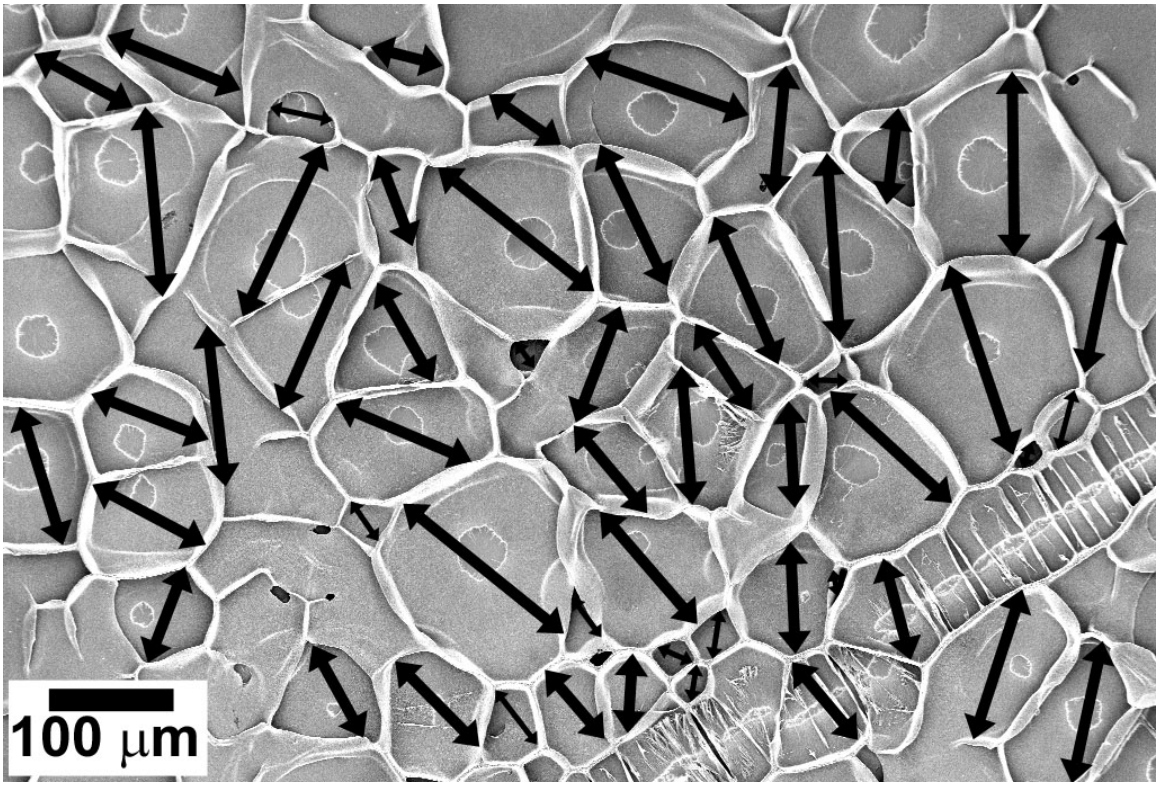

Figure D.8: ***Data set N*****. Image used in analysis. Sample was 60 μm tall, treated with 0.5 cmc SDS. A fan was used to increase convective drying.**

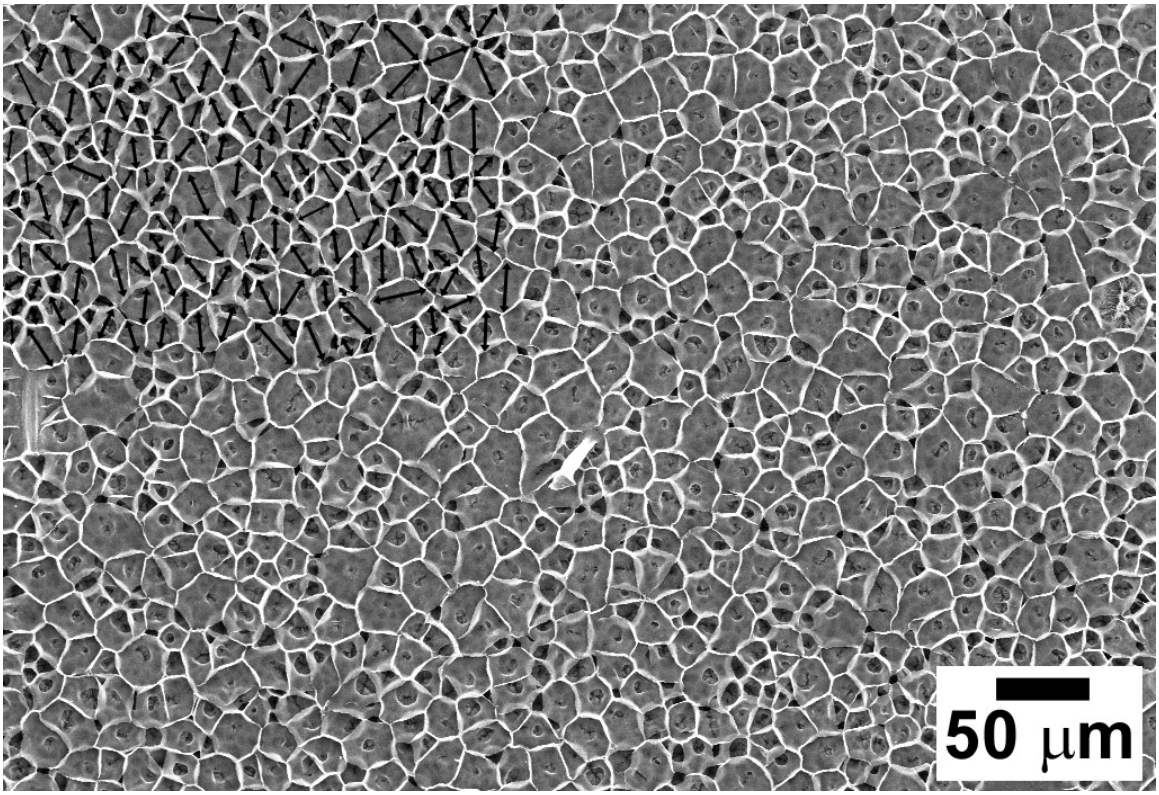

Figure D.9: ***Data set O.*** **Image used in analysis. Sample was 53 μm tall, treated with 0.1 wt% Triton-X.**

D.2 Full-Page Versions of Selected Figures

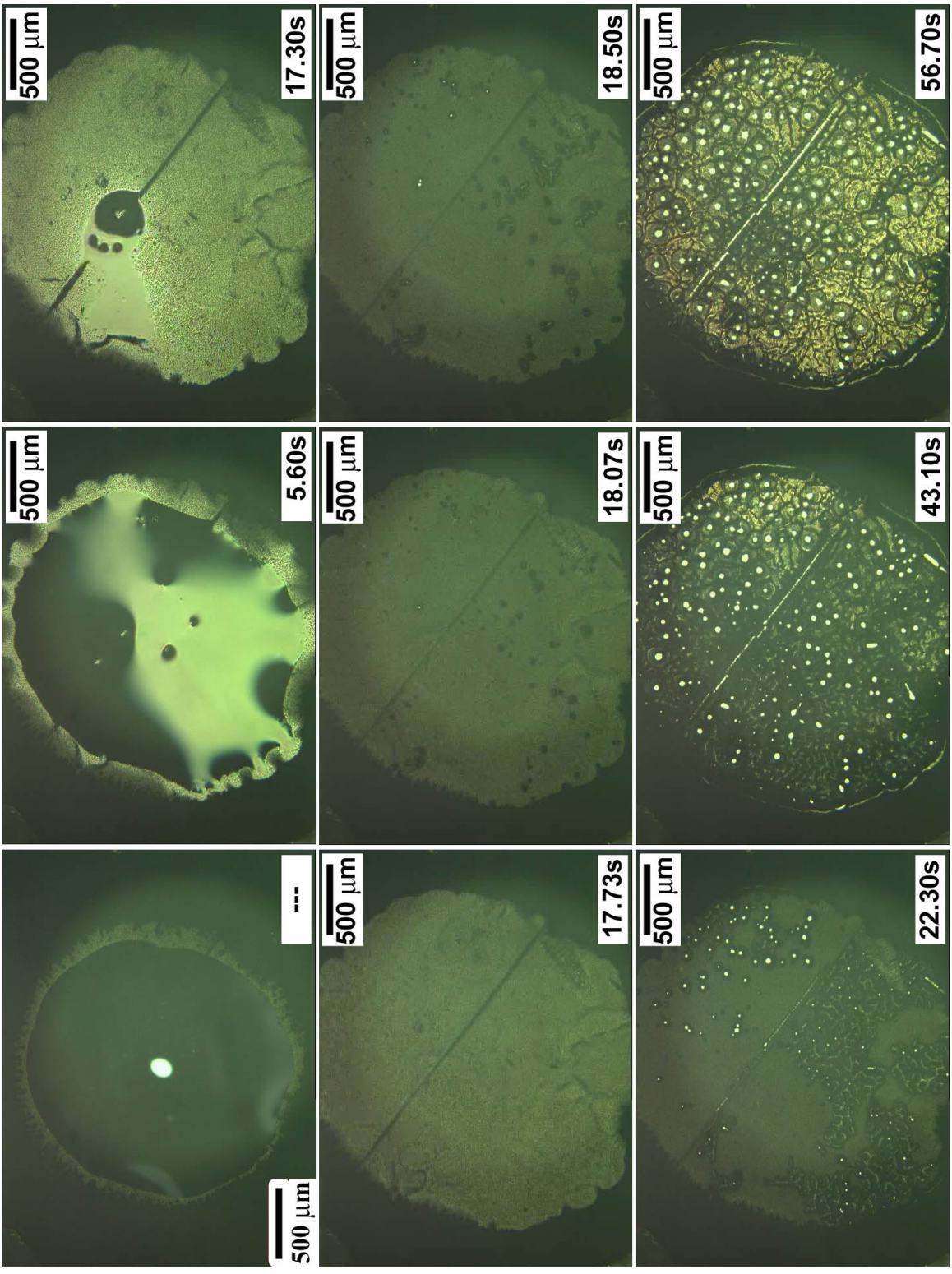

Figure D.10: Large version of figure 4.14. Time series of applying 0.5 cmc SDS to as-grown 60 µm nanocarpet on quartz.

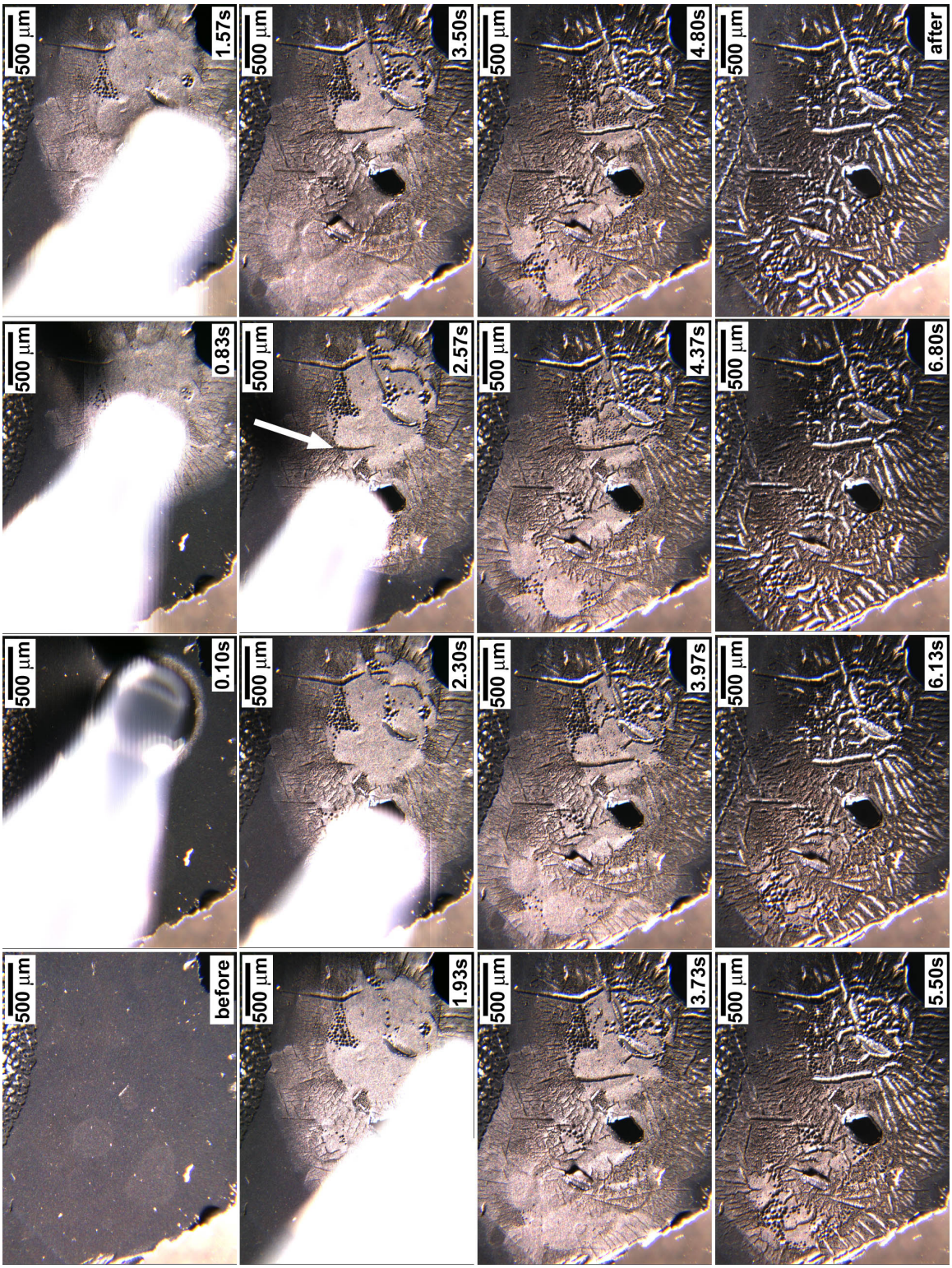

Figure D.11: Large version of figure 4.15. Time series of applying 1 cSt PDMS oil to as-grown 60 µm nanocarpet on quartz.

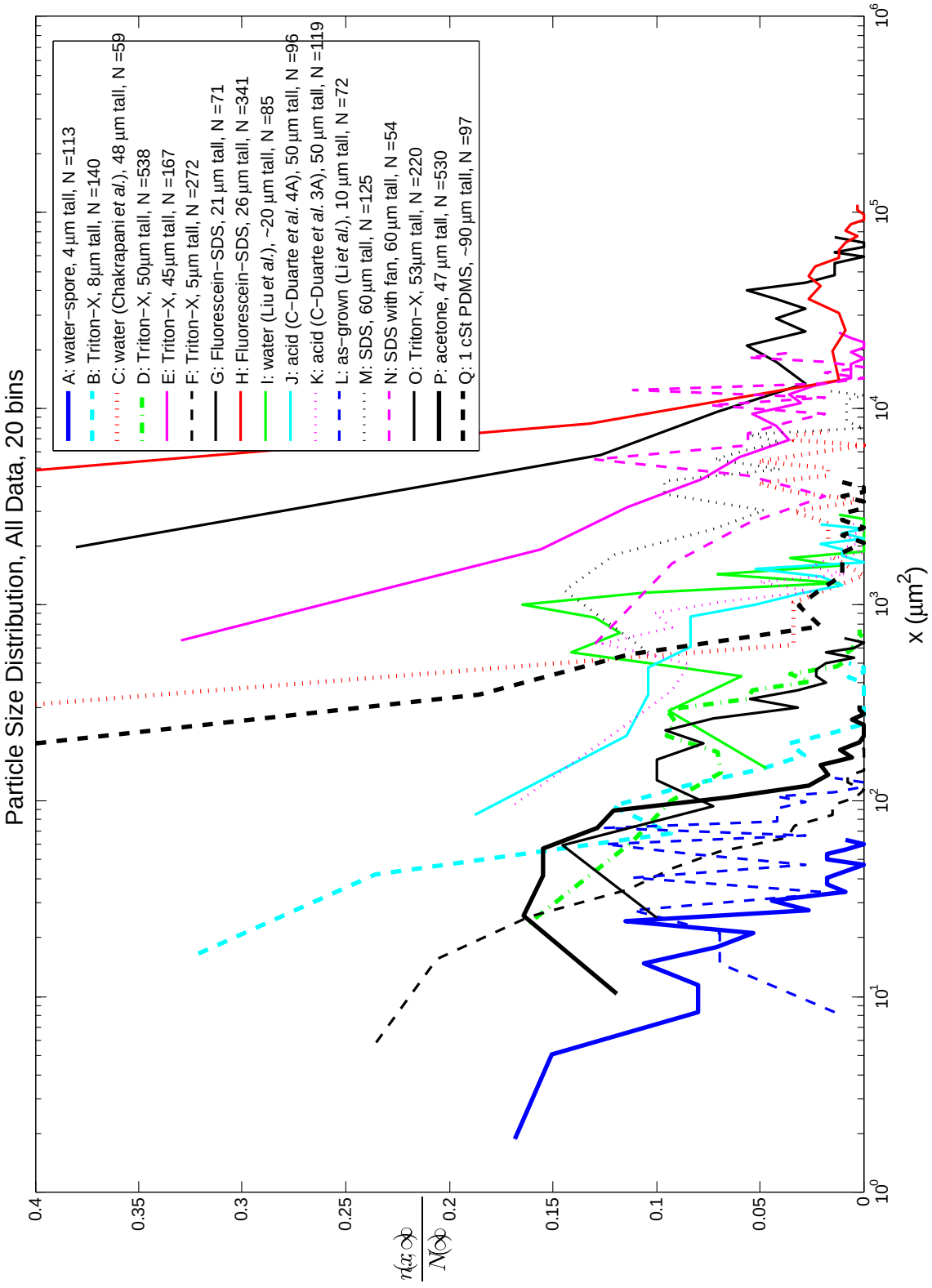

Figure D.12: Large version of figure 4.26. Particle size distribution using 20 bins for all data analyzed, without normalizing area, x. Note the log-scaled x-axis.

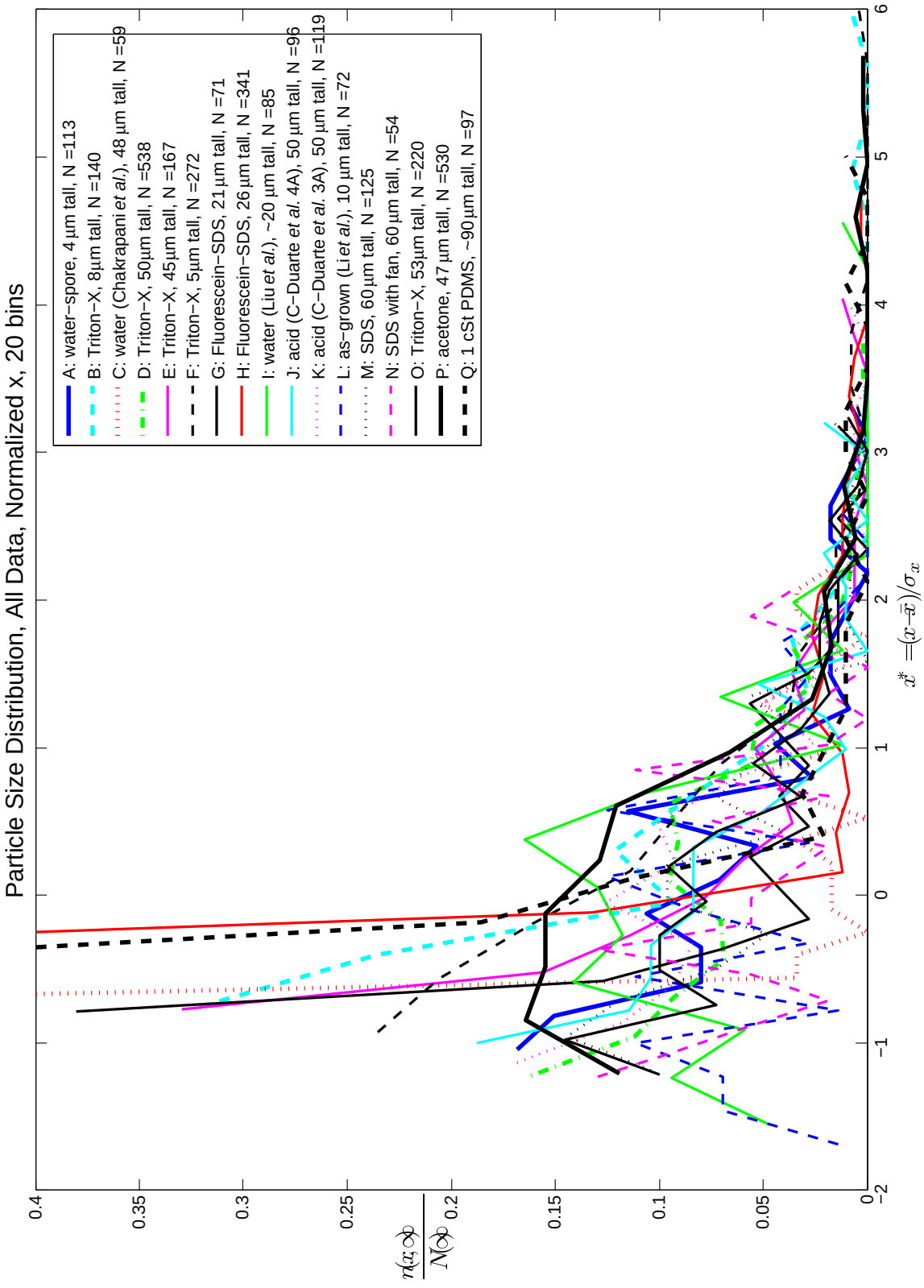

Figure D.13: Large version of figure 4.27. Particle size distribution using 20 bins for all data analyzed, normalizing areas so distributions align at $x^* = 0$.

Glossary

AFM

atomic force microscope A.0

cmc

critical micellar concentration 3.2, 4.1, 4.2, 4.4

CNT

carbon nanotube 1.1–1.4, 1.6, 2.1–2.3, 2.6, 2.7, 3.3, 3.4, 3.6, 4.1–4.4, 5.1, 5.2, 5.5, 6.1, 6.2, 7.1, 7.2, 7.4, 8.2, 8.5, 8.6, 9.0, A.0, B.0

cross-linked PDMS

elastomer of PDMS following a cross-linking reaction, commonly known by the GE Silicones trade name RTV, or generically as simply silicone 3.2, 3.3, 5.1, 5.3, 5.5, 6.3, 6.5, 8.4, A.0

CVD

chemical vapor deposition 1.4, 2.2, 2.3, 2.7, 5.2, 5.5

external coordinates

in population balance models, a set of coordinates used to describe particle centroid positions relative to a fixed spatial coordinate system 7.2, C.1, C.2

internal coordinates

in population balance models, a set of usually scalar coordinates used to describe particle properties which are of interest 7.2, C.1

IPA

isopropanol 5.2, 5.3

MWNT

multi-walled carbon nanotube 1.2, 2.2

nanocarpet

densely packed and vertically aligned array of carbon nanotubes resembling an ordinary carpet in appearance 1.3, 2.1, 4.1, 5.2

nanocarpet pattern

a whole set of pattern elements spatially distributed in a nanocarpet 1.3, C.2, C.3

pattern element

individual elements comprising the patterns formed in nanocarpets and defined as contiguous areas surrounded by a border of adjacent CNT tips; alternately called cells, nests, craters, valleys, or cavities 1.3, 7.1, 7.2, C.2, C.3

PDMS

polydimethylsiloxane 3.2, 5.2, 9.0, A.0

PDMS oil

polydimethylsiloxane in liquid form, commonly called silicone oil 3.2, 4.3, 4.4, 5.4, 6.3–6.5, 8.4, 8.5, 9.0, A.0

PMMA

polymethylmethacrylate 3.2, 3.3, 5.1, 5.2, 5.4, 5.5, 6.4, 6.5, 8.3, 8.4, 9.0, A.0

population balance

mathematical description of a system involving populations of "particles" within a separate, continuous phase, and which are potentially subject to convective fluxes, birth, death, and growth 7.1, C.1

PSD

particle size distribution 4.5, 4.6, 7.2–7.4

PTFE

polytetrafluoroethylene, also the DuPont trade name of Teflon 4.2

SCCM

standard cubic centimeter 2.3, 2.7, 5.2

SDS

sodium dodecyl sulfate 3.2, 4.1, 4.2, 4.4, 4.5

SEM

scanning electron microscopy or scanning electron microscope 1.4, 2.6, 2.8, 3.3, 3.6, 4.1–4.3, 4.5, 4.6, 5.2, 5.4, 6.2, 8.6

SWNT

single-walled carbon nanotube 2.2

TEM

transmission electron microscopy 2.2

thin layer process

a single layer process results in a nanocarpet anchored in one thin layer spread on a substrate 5.2, 5.5

thin-on-thick process

multiple layer creation steps are used to anchor a nanocarpet within a thin layer that is in turn joined to a much thicker layer 5.2, 5.5, 6.3

References

[1] S. Iijima. Helical microtubules of graphitic carbon. *Nature*, 354(6348):56–58, 1991.

[2] M. Terrones. Science and technology of the twenty-first centure: Synthesis, properties, and applications of carbon nanotubes. *Annual Review of Materials Research*, 33:419–501, 2003.

[3] W. A. de Heer. Nanotubes and the pursuit of applications. *MRS Bulletin*, 29 (4):281–285, 2004.

[4] A. W. Adamson and A. P. Gast. *Physical Chemistry of Surfaces*. Wiley, New York, 6th edition, 1997.

[5] P. G. de Gennes, F. Brochard-Wyatt, and D. Quere. *Capillarity and Wetting Phenomena: Drops, Bubbles, Pearls, Waves*. Springer, New York, 2004.

[6] J. Israelachvili. *Intermolecular and Surface Forces*. Academic Press, London, 2nd edition, 1992.

[7] M. R. Falvo, G. J. Clary, R. M. Taylor, V. Chi, F. P. Brooks, S. Washburn, and R. Superfine. Bending and buckling of carbon nanotubes under large strain. *Nature*, 389(6651):582–584, 1997.

[8] N. Chakrapani, B. Q. Wei, A. Carrillo, P. M. Ajayan, and R. S. Kane. Capillarity-driven assembly of two-dimensional cellular carbon nanotube foams. *Proceedings of the National Academy of Sciences of the United States of America*, 101(12):4009–4012, 2004.

[9] B. Q. Wei, R. Vajtai, Y. Jung, J. Ward, R. Zhang, G. Ramanath, and P. M. Ajayan. Assembly of highly organized carbon nanotube architectures by chemical vapor deposition. *Chemistry of Materials*, 15(8):1598–1606, 2003.

[10] L. A. Girifalco, M. Hodak, and R. S. Lee. Carbon nanotubes, buckyballs, ropes, and a universal graphitic potential. *Physical Review. B, Condensed Matter*, 62 (19):13104–13110, 2000.

[11] H. Namatsu, K. Kurihara, M. Nagase, K. Iwadate, and K. Murase. Dimensional limitations of silicon nanolines resulting from pattern distortion due to surface-tension of rinse water. *Applied Physics Letters*, 66(20):2655–2657, 1995.

[12] O. D. Velev, N. D. Denkov, V. N. Paunov, P. A. Kralchevsky, and K. Nagayama. Direct measurement of lateral capillary forces. *Langmuir*, 9(12):3702–3709, 1993.

[13] N. D. Denkov, O. D. Velev, P. A. Kralchevsky, I. B. Ivanov, H. Yoshimura, and K. Nagayama. Mechanism of formation of 2-dimensional crystals from latex-particles on substrates. *Langmuir*, 8(12):3183–3190, 1992.

[14] N. D. Denkov, O. D. Velev, P. A. Kralchevsky, I. B. Ivanov, H. Yoshimura, and K. Nagayama. 2-dimensional crystallization. *Nature*, 361(6407):26–26, 1993.

[15] H. Liu, S. H. Li, J. Zhai, H. J. Li, Q. S. Zheng, L. Jiang, and D. B. Zhu. Self-assembly of large-scale micropatterns on aligned carbon nanotube films. *Angewandte Chemie International Edition*, 43(9):1146–1149, 2004.

[16] X. B. Wang, Y. Q. Liu, and D. B. Zhu. Honeycomb-like alignments of carbon nanotubes synthesized by pyrolysis of a metal phthalocyanine. *Applied Physics. A, Materials Science and Processing*, 71(3):347–348, 2000.

[17] Z. J. Zhang, B. Q. Wei, and P. M. Ajayan. Self-networking of carbon nanotubes. *Chemical Communications*, (9):962–963, 2002.

[18] H. Liu, J. Zhai, and L. Jiang. Wetting and anti-wetting on aligned carbon nanotube films. *Soft Matter*, 2(10):811–821, 2006.

[19] M. A. Correa-Duarte, N. Wagner, J. Rojas-Chapana, C. Morsczeck, M. Thie, and M. Giersig. Fabrication and biocompatibility of carbon nanotube-based 3d networks as scaffolds for cell seeding and growth. *Nano Letters*, 4(11):2233–2236, 2004.

[20] W. Z. Li, J. G. Wen, Y. Tu, and Z. F. Ren. Effect of gas pressure on the growth and structure of carbon nanotubes by chemical vapor deposition. *Applied Physics A, Materials Science and Processing*, 73(2):259–264, 2001.

[21] A. Patil, R. Vaia, and L. Dai. Surface modification of aligned carbon nanotube arrays for electron emitting applications. *Synthetic Metals*, 154(1-3):229–232, 2005.

[22] L. Feng, Z. Y. Zhang, Z. H. Mai, Y. M. Ma, B. Q. Liu, L. Jiang, and D. B. Zhu. A super-hydrophobic and super-oleophilic coating mesh film for the separation of oil and water. *Angewandte Chemie International Edition*, 43(15):2012–2014, 2004.

[23] L. M. Sheng, M. Liu, P. Liu, Y. Wei, L. Liu, and S. S. Fan. Field emission from self-assembly structure of carbon-nanotube films. *Applied Surface Science*, 250 (1-4):9–13, 2005.

[24] J. G. Fan, D. Dyer, G. Zhang, and Y. P. Zhao. Nanocarpet effect: Pattern formation during the wetting of vertically aligned nanorod arrays. *Nano Letters*, 4(11):2133–2138, 2004.

[25] M. J. Bronikowski, H. M. Manohara, and B. D. Hunt. Growth of carbon nanotube bundle arrays on silicon surfaces. *Journal of Vacuum Science and Technology, A: Vacuum, Surfaces, and Films*, 24(4):1318, 2006.

[26] M. J. Bronikowski. Cvd growth of carbon nanotube bundle arrays. *Carbon*, 44 (13):2822–2832, 2006.

[27] R. Bacon. Growth, structure, and properties of graphite whiskers. *Journal of Applied Physics*, 31(2):283–290, 1960.

[28] A. Oberlin, M. Endo, and T. Koyama. Filamentous growth of carbon through benzene decomposition. *Journal of Crystal Growth*, 32(3):335–349, 1976.

[29] H. W. Kroto, J. R. Heath, S. C. Obrien, R. F. Curl, and R. E. Smalley. C60: Buckminsterfullerene. *Nature*, 318(6042):162–163, 1985.

[30] T. W. Ebbesen and P. M. Ajayan. Large-scale synthesis of carbon nanotubes. *Nature*, 358(6383):220–222, 1992.

[31] R. G. Ding, G. Q. Lu, Z. F. Yan, and M. A. Wilson. Recent advances in the preparation and utilization of carbon nanotubes for hydrogen storage. *Journal of Nanoscience and Nanotechnology*, 1(1):7–29, 2001.

[32] A. Sherman. *Chemical vapor deposition for microelectronics: principles, technology, and applications*. Noyes Publications, Park Ridge, NJ, 1987.

[33] M. Endo, K. Takeuchi, S. Igarashi, K. Kobori, M. Shiraishi, and H. W. Kroto. The production and structure of pyrolytic carbon nanotubes (pcnts). *Journal of Physics and Chemistry of Solids*, 54(12):1841–1848, 1993.

[34] R. H. Baughman, A. A. Zakhidov, and W. A. de Heer. Carbon nanotubes—the route toward applications. *Science*, 297(5582):787–792, 2002.

[35] M. J. Bronikowski, P. A. Willis, D. T. Colbert, K. A. Smith, and R. E. Smalley. Gas-phase production of carbon single-walled nanotubes from carbon monoxide via the hipco process: A parametric study. *Journal of Vacuum Science and Technology, A: Vacuum, Surfaces, and Films*, 19(4):1800–1805, 2001.

[36] P. Nikolaev, M. J. Bronikowski, Bradly, F. Rohmund, D. T. Colbert, K. A. Smith, and R. E. Smalley. Gas-phase catalytic growth of single-walled carbon nanotubes from carbon monoxide. *Chemical Physics Letters*, 313(1-2):91–97, 1999.

[37] Z. H. Kang, E. B. Wang, B. D. Mao, Z. M. Su, L. Chen, and L. Xu. Obtaining carbon nanotubes from grass. *Nanotechnology*, 16(8):1192–1195, 2005.

[38] K. Hata, D. N. Futaba, K. Mizuno, T. Namai, M. Yumura, and S. Iijima. Water-assisted highly efficient synthesis of impurity-free single-waited carbon nanotubes. *Science*, 306(5700):1362–1364, 2004.

[39] G. Eres, A. A. Puretzky, D. B. Geohegan, and H. Cui. In situ control of the catalyst efficiency in chemical vapor deposition of vertically aligned carbon nanotubes on predeposited metal catalyst films. *Applied Physics Letters*, 84 (10):1759–1761, 2004.

[40] A. V. Melechko, V. I. Merkulov, T. E. McKnight, M. A. Guillorn, K. L. Klein, D. H. Lowndes, and M. L. Simpson. Vertically aligned carbon nanofibers and related structures: Controlled synthesis and directed assembly. *Journal of Applied Physics*, 97(4):041301, 2005.

[41] M. Terrones. Carbon nanotubes: synthesis and properties, electronic devices and other emerging applications. *International Materials Reviews*, 49(6):325–377, 2004.

[42] A. M. Cazabat, F. Heslot, S. M. Troian, and P. Carles. Fingering instability of thin spreading films driven by temperature gradients. *Nature*, 346(6287): 824–826, 1990.

[43] K. J. Mysels. Surface-tension of solutions of pure sodium dodecyl-sulfate. *Langmuir*, 2(4):423–428, 1986.

[44] A. McPherson. *Crystallization of Biological Macromolecules*. Cold Spring Harbor Laboratory Press, Cold Spring Harbor, NY, 1999.

[45] M. A. Unger, H. P. Chou, T. Thorsen, A. Scherer, and S. R. Quake. Monolithic microfabricated valves and pumps by multilayer soft lithography. *Science*, 288 (5463):113–116, 2000.

[46] J. N. Lee, C. Park, and G. M. Whitesides. Solvent compatibility of poly(dimethylsiloxane)-based microfluidic devices. *Analytical chemistry*, 75(23): 6544–6554, 2003.

[47] K. K. S. Lau, J. Bico, K. B. K. Teo, M. Chhowalla, G. A. J. Amaratunga, W. I. Milne, G. H. McKinley, and K. K. Gleason. Superhydrophobic carbon nanotube forests. *Nano Letters*, 3(12):1701–1705, 2003.

[48] S. H. Li, H. J. Li, X. B. Wang, Y. L. Song, Y. Q. Liu, L. Jiang, and D. B. Zhu. Super-hydrophobicity of large-area honeycomb-like aligned carbon nanotubes. *Journal of Physical Chemistry B*, 106(36):9274–9276, 2002.

[49] H. J. Li, X. B. Wang, Y. L. Song, Y. Q. Liu, Q. S. Li, L. Jiang, and D. B. Zhu. Super-"amphiphobic" aligned carbon nanotube films. *Angewandte Chemie International Edition*, 40(9):1743–1746, 2001.

[50] S. S. Fan, M. G. Chapline, N. R. Franklin, T. W. Tombler, A. M. Cassell, and H. J. Dai. Self-oriented regular arrays of carbon nanotubes and their field emission properties. *Science*, 283(5401):512, 1999.

[51] W. A. de Heer, A. Chatelain, and D. Ugarte. A carbon nanotube field-emission electron source. *Science*, 270(5239):1179, 1995.

[52] C. M. Niu, E. K. Sichel, R. Hoch, D. Moy, and H. Tennent. High power electrochemical capacitors based on carbon nanotube electrodes. *Applied Physics Letters*, 70(11):1480, 1997.

[53] C. F. Zhou, S. Kumar, C. D. Doyle, and J. M. Tour. Functionalized single wall carbon nanotubes treated with pyrrole for electrochemical supercapacitor membranes. *Chemistry of Materials*, 17(8):1997, 2005.

[54] C. Liu and H. M. Cheng. Carbon nanotubes for clean energy applications. *Journal of Physics D: Applied Physics*, 38(14):231, 2005.

[55] M. Firkowska, I. Olek, N. Pazos-Perez, J. Rojas-Chapana, and M. Giersig. Highly ordered mwnt-based matrixes: Topography at the nanoscale conceived for tissue engineering. *Langmuir*, 22(12):5427, 2006.

[56] R. A. MacDonald, B. F. Laurenzi, G. Viswanathan, P. M. Ajayan, and J. P. Stegemann. Collagen-carbon nanotube composite materials as scaffolds in tissue engineering. *Journal of Biomedical Materials Research, Part A*, 74A(3):489, 2005.

[57] J. H. Walther, T. Werder, R. L. Jaffe, and P. Koumoutsakos. Hydrodynamic properties of carbon nanotubes. *Physical Review E: Statistical, Nonlinear, and Soft Matter Physics*, 69(6):062201, 2004.

[58] A. N. Ford and D. V. Papavassiliou. Flow around surface-attached carbon nanotubes. *Industrial and Engineering Chemistry Research*, 45(5):1797, 2006.

[59] Y. H. Hu, O. A. Shenderova, Z. Hu, C. W. Padgett, and D. W. Brenner. Carbon nanostructures for advanced composites. *Reports on Progress in Physics*, 69(6): 1847, 2006.

[60] S. M. Huang and L. M. Dai. Plasma etching for purification and controlled opening of aligned carbon nanotubes. *Journal of Physical Chemistry B*, 106 (14):3543, 2002.

[61] A. Patil, L. C. Li, L. M. Dai, M. Casavant, and K. Strong. Carbon-nanotube electron emitters for display applications. *Journal of the Society for Information Display*, 13(9):709, 2005.

[62] P. M. Ajayan, O. Stephan, C. Colliex, and D. Trauth. Aligned carbon nanotube arrays formed by cutting a polymer resin-nanotube composite. *Science*, 265 (5176):1212, 1994.

[63] H. D. Wagner, O. Lourie, Y. Feldman, and R. Tenne. Stress-induced fragmentation of multiwall carbon nanotubes in a polymer matrix. *Applied Physics Letters*, 72(2):188, 1998.

[64] L. Jin, C. Bower, and O. Zhou. Alignment of carbon nanotubes in a polymer matrix by mechanical stretching. *Applied Physics Letters*, 73(9):1197, 1998.

[65] N. R. Raravikar, A. S. Vijayaraghavan, P. Keblinski, L. S. Schadler, and P. M. Ajayan. Embedded carbon-nanotube-stiffened polymer surfaces. *Small*, 1(3): 317, 2005.

[66] Y. J. Jung, S. Kar, S. Talapatra, C. Soldano, G. Viswanathan, X. S. Li, Z. L. Yao, F. S. Ou, A. Avadhanula, R. Vajtai, S. Curran, O. Nalamasu, and P. M. Ajayan. Aligned carbon nanotube-polymer hybrid architectures for diverse flexible electronic applications. *Nano Letters*, 6(3):413, 2006.

[67] S. Miserendino, J. Yoo, A. Cassell, and Y. C. Tai. Electrochemical characterization of parylene-embedded carbon nanotube nanoelectrode arrays. *Nanotechnology*, 17(4):23, 2006.

[68] J. Li, R. Stevens, L. Delzeit, H. T. Ng, A. Cassell, J. Han, and M. Meyyappan. Electronic properties of multiwalled carbon nanotubes in an embedded vertical array. *Applied Physics Letters*, 81(5):910, 2002.

[69] J. H. Chen, Z. P. Huang, D. Z. Wang, S. X. Yang, W. Z. Li, J. G. Wen, and Z. F. Ren. Electrochemical synthesis of polypyrrole films over each of well-aligned carbon nanotubes. *Synthetic Metals*, 125(3):289, 2001.

[70] M. Gao, S. M. Huang, L. M. Dai, G. Wallace, R. P. Gao, and Z. L. Wang. Aligned coaxial nanowires of carbon nanotubes sheathed with conducting polymers. *Angewandte Chemie International Edition*, 39(20):3664, 2000.

[71] C. Wei, L. M. Dai, A. Roy, and T. B. Tolle. Multifunctional chemical vapor sensors of aligned carbon nanotube and polymer composites. *Journal of the American Chemical Society*, 128(5):1412, 2006.

[72] E. Lahiff, C. Y. Ryu, S. Curran, A. I. Minett, W. J. Blau, and P. M. Ajayan. Selective positioning and density control of nanotubes within a polymer thin film. *Nano Letters*, 3(10):1333, 2003.

[73] B. J. Hinds, N. Chopra, T. Rantell, R. Andrews, V. Gavalas, and L. G. Bachas. Aligned multiwalled carbon nanotube membranes. *Science*, 303(5654):62, 2004.

[74] C. V. Nguyen, L. Delzeit, A. M. Cassell, J. Li, J. Han, and M. Meyyappan. Preparation of nucleic acid functionalized carbon nanotube arrays. *Nano Letters*, 2(10):1079, 2002.

[75] L. C. Li, J. B. Yang, R. Vaia, and L. M. Dai. Multicomponent micropatterns of carbon nanotubes. *Synthetic Metals*, 154(1-3):225, 2005.

[76] S. M. Huang, L. M. Dai, and A. W. H. Mau. Patterned growth and contact transfer of well-aligned carbon nanotube films. *Journal of Physical Chemistry B*, 103(21):4223, 1999.

[77] E. Sunden, J. K. Moon, C. P. Wong, W. P. King, and S. Graham. Microwave assisted patterning of vertically aligned carbon nanotubes onto polymer substrates. *Journal of Vacuum Science and Technology, B: Microelectronics and Nanometer Structures: Processing, Measurement, and Phenomena*, 24(4):1947, 2006.

[78] C. C. Chiu, T. Y. Tsai, and N. H. Tai. Field emission properties of carbon nanotube arrays through the pattern transfer process. *Nanotechnology*, 17(12): 2840, 2006.

[79] W. C. Sanders, E. S. Winkel, D. R. Dowling, M. Perlin, and S. L. Ceccio. Bubble friction drag reduction in a high-reynolds-number flat-plate turbulent boundary layer. *Journal of Fluid Mechanics*, 552(-1):353–380, 2006.

[80] F. M. White. *Viscous Fluid Flow*. McGraw-Hill, New York, 2nd edition, 1991.

[81] A. G. Emslie, F. T. Bonner, and L. G. Peck. Flow of a viscous liquid on a rotating disk. *Journal of Applied Physics*, 29(5):858–862, 1958.

[82] J. N. Coleman, U. Khan, and Y. K. Gun'ko. Mechanical reinforcement of polymers using carbon nanotubes. *Advanced Materials*, 18(6):689–706, 2006.

[83] J. N. Coleman, W. J. Blau, A. B. Dalton, E. Munoz, S. Collins, B. G. Kim, J. M. Razal, M. Selvidge, G. Vieiro, and R. H. Baughman. Improving the mechanical properties of single-walled carbon nanotube sheets by intercalation of polymeric adhesives. *Applied Physics Letters*, 82(11):1682–1684, 2003.

[84] N. R. Raravikar, L. S. Schadler, A. S. Vijayaraghavan, Y. P. Zhao, B. Q. Wei, and P. M. Ajayan. Synthesis and characterization of thickness-aligned carbon nanotube-polymer composite films. *Chemistry of Materials*, 17(5):974–983, 2005.

[85] Z. J. Jia, Z. Y. Wang, C. L. Xu, J. Liang, B. Q. Wei, D. H. Wu, and S. W. Zhu. Study on poly(methyl methacrylate)/carbon nanotube composites. *Materials Science and Engineering. A, Structural Materials*, 271(1-2):395–400, 1999.

[86] D. E. Bornside, C. W. Macosko, and L. E. Scriven. Spin coating of a pmma chlorobenzene solution. *Journal of the Electrochemical Society*, 138(1):317–320, 1991.

[87] C. B. Walsh and E. I. Franses. Thickness and quality of spin-coated polymer films by two-angle ellipsometry. *Thin Solid Films*, 347(1-2):167–177, 1999.

[88] C. Ton-That, A. G. Shard, and R. H. Bradley. Surface feature size of spin cast ps/pmma blends. *Polymer*, 43(18):4973–4977, 2002.

[89] W. W. Flack, D. S. Soong, A. T. Bell, and D. W. Hess. A mathematical model for spin coating of polymer resists. *Journal of Applied Physics*, 56(4):1199–1206, 1984.

[90] A. Oztekin, D. E. Bornside, R. A. Brown, and P. K. Seidel. The connection between hydrodynamic stability of gas-flow in spin-coating and coated film uniformity. *Journal of Applied Physics*, 77(6):2297–2308, 1995.

[91] G. Rossi and K. A. Mazich. Macroscopic description of the kinetics of swelling for a cross-linked elastomer or gel. *Physical Review. E, Statistical Physics, Plasmas, Fluids, and Related Interdisciplinary Topics*, 48(2):1182–1191, 1993.

[92] K. Efimenko, M. Rackaitis, E. Manias, A. Vaziri, L. Mahadevan, and J. Genzer. Nested self-similar wrinkling patterns in skins. *Nature Materials*, 4(4):293–297, 2005.

[93] J. A. Khawly, R. J. Lambert, and G. J. Jaffe. Intraocular lens changes after short- and long-term exposure to intraocular silicone oil—an in vivo study. *Ophthalmology*, 105(7):1227–1233, 1998.

[94] D. Ramkrishna. *Population balances: theory and applications to particulate systems in engineering*. Academic Press, San Diego, 2000.

[95] D. Niyogi, R. Kumar, and K. S. Gandhi. Modeling of bubble-size distribution in free rise polyurethane foams. *AIChE Journal*, 38(8):1170–1184, 1992.

[96] D. Niyogi, R. Kumar, and K. S. Gandhi. Water blown free rise polyurethane foams. *Polymer Engineering and Science*, 39(1):199–209, 1999.

[97] A. C. Henry, R. L. McCarley, S. S. Das, and C. G. K. Malek. Characteristics of commercial pmma sheets used in the fabrication of extreme high-aspect-ratio microstructures. *Journal of the Electrochemical Society*, 146(7):2631–2636, 1999.

[98] D. Weaire and M. A. Fortes. Stress and strain in liquid and solid foams. *Advances in Physics*, 43(6):685–738, 1994.

[99] D. Weaire and N. Rivier. Soap, cells, and statistics—random patterns in two dimensions. *Contemporary Physics*, 25(1):59–99, 1984.

[100] F. A. Shutov. Foamed polymers—cellular structure and properties. *Advances in Polymer Science*, 51:155–225, 1983.

[101] L. J. Gibson and M. F. Ashby. *Cellular Solids: Structure and Properties*. Cambridge University Press, Cambridge, 2nd edition, 1997.

[102] G. Schliecker. Structure and dynamics of cellular systems. *Advances in Physics*, 51(5):1319–1378, 2002.

[103] D. L Weaire and S. Hutzler. *The Physics of Foams*. Oxford University Press, New York, 1999.

[104] D. Oner and T. J. McCarthy. Ultrahydrophobic surfaces. effects of topography length scales on wettability. *Langmuir*, 16(20):7777–7782, 2000.

[105] L. Zhai, M. C. Berg, F. C. Cebeci, Y. Kim, J. M. Milwid, M. F. Rubner, and R. E. Cohen. Patterned superhydrophobic surfaces: Toward a synthetic mimic of the namib desert beetle. *Nano Letters*, 6(6):1213–1217, 2006.

[106] B. Krasovitski and A. Marmur. Drops down the hill: Theoretical study of limiting contact angles and the hysteresis range on a tilted plate. *Langmuir*, 21 (9):3881–3885, 2005.

[107] R. Furstner, W. Barthlott, C. Neinhuis, and P. Walzel. Wetting and self-cleaning properties of artificial superhydrophobic surfaces. *Langmuir*, 21(3):956–961, 2005.

[108] W. Barthlott and C. Neinhuis. Purity of the sacred lotus, or escape from contamination in biological surfaces. *Planta*, 202(1):1–8, 1997.

[109] Y. T. Cheng and D. E. Rodak. Is the lotus leaf superhydrophobic? *Applied Physics Letters*, 86(14):144101, 2005.

[110] L. Feng, S. H. Li, Y. S. Li, H. J. Li, L. J. Zhang, J. Zhai, Y. L. Song, B. Q. Liu, L. Jiang, and D. B. Zhu. Super-hydrophobic surfaces: From natural to artificial. *Advanced Materials*, 14(24):1857–1860, 2002.

[111] A. V. Neimark. Thermodynamic equilibrium and stability of liquid films and droplets on fibers. *Journal of Adhesion Science and Technology*, 13(10):1137–1154, 1999.

[112] A. H. Barber, S. R. Cohen, and H. D. Wagner. Static and dynamic wetting measurements of single carbon nanotubes. *Physical Review Letters*, 92(18): 186103, 2004.